Low attenuation microwave waveguides

Al-Hariri, Ali Mohammed Bakir

LOW ATTENUATION MICROWAVE WAVEGUIDES

by

Ali Mohammed Bakir AL-HARIRI

A thesis submitted to the University of London

for the degree of Doctor of Philosophy.

Department of Electrical and Electronic Engineering,

Queen Mary College

University of London

October 1974

TO MY PARENTS

ABSTRACT

An investigation of the dispersion and attenuation characteristics of cylindrical structures supporting guided electromagnetic waves with low attenuation is described. The object of the investigation is to understand how the cross-sectional shape and the nature of the boundary conditions affects the propagation characteristics. Attention is directed towards structures supporting the least number of propagating modes under the conditions which yield low attenuation over a reasonable bandwidth. Elliptical waveguides with both smooth walls and corrugated walls are studied in detail. This reveals errors in previous theories which are corrected. Some aspects of corrugated rectangular and circular waveguides are considered. Potential low attenuation waveguides such as the dielectric lined and dielectric waveguides are evaluated.

ACKNOWLEDGEMENTS

The author would like to express his most sincere thanks to:

Professor M.W. Humphrey Davies for his permission to undertake the research in the Department of Electrical and Electronic Engineering, Queen Mary College.

His supervisors, Professor P.J.B. Clarricoats and Dr. A.D. Olver, who initiated the project and for their constant interest and guidance, with whom many helpful discussions were held.

Professor L. Lewin who took an active interest in part of the project during his stay at Q.M.C. and for his encouragement and advice.

Dr. G. Poulton and Dr. D. Ross for their helpful suggestions.

The Electromagnetics Group, Queen Mary College, especially S.L. Chong, for their advice and help.

The University of London who provided financial support throughout the duration of this work.

Mrs. Sylvia Reading for typing this manuscript.

CONTENTS

CHAPTER ONE

INTRODUCTION

During a general research programme on corrugated waveguides and horns, Clarricoats and Saha < 1 >, observed the presence of a low-loss linearly polarised hybrid mode in corrugated circular waveguides, Figure (4.1). In their analysis, a surface impedance model was used to represent the corrugated region of the waveguide and the power-losses on the metal surfaces were calculated. The low-loss phenomenon of the waveguide was later confirmed theoretically by Clarricoats and Olver < 2 > and experimentally by Olver, Clarricoats and Chong < 3 >. In the latter analysis, a space harmonic representation of the field was used and field matching techniques were employed to derive the characteristic equation of the structure < 4 >. The attenuation results thus obtained were lower than those of either the TE_{11} mode or the TE_{01} mode of a comparable size smooth wall circular waveguide.

It was recognised that the presence of the corrugated boundary acts to reduce the field intensity near the metal surfaces and thus lowering the power-losses at these surfaces. The physical picture that emerges when the corrugation depth is nearly one quarter of a wavelength is that the boundary so created acts to maintain the azimuthal component of current while reducing the dominant axial current component.

In a dielectric lined circular waveguide, Figure (6.1), the field intensity near the metal surface

of a circular waveguide is reduced, as demonstrated by Carlin and D'Agostino < 5 >, < 6 > for circularly symmetric modes and by Clarricoats et al <38> for the azimuthally dependent modes. The presence of the lining near the metal surface provides the circular electric modes with an electric wall boundary, while the circular magnetic modes are provided with a magnetic wall boundary, as either the frequency or the lining thickness increases. For the hybrid mode TM conditions predominate and low-loss occurs for a thickness near to $\lambda/4$.

The above effects are not restricted to circular cross-section waveguides, Bryant < 7 >, investigated the propagation characteristics of a square waveguide, containing transverse periodic corrugations. He identified the presence of two types of propagating modes, one of which is characterised by low field intensity at the corrugated boundary. Unfortunately the experimental results for attenuation observed by Bryant, 40-200 dB/m, showed a substantial degradation over that of a smooth wall square waveguide.

Bryant's explanations of the high attenuation were:

(i) Due to the presence of a large metal surface area in the waveguide.

(ii) Due to the method of construction of the waveguide.

However, he < 8 > claimed later that an antenna feed incorporating a corrugated waveguide section produced

losses that were not measurably greater than those in a smooth wall waveguide. Therefore, Bryant concluded that the losses of the first corrugated waveguide may have been due to the method of construction.

A rectangular waveguide with transverse periodic corrugations on two opposite sides, was theoretically investigated by Baldwin and McInnes < 9 >, <10 >. Their analysis is similar to that of Bryant, but the attenuation results they obtained showed an enormous advantage over those of a smooth wall rectangular waveguide of comparable dimensions. However, these results are shown to be in error <11 >, although the reduction in the field intensity at the corrugated surfaces does occur for this structure.

Yet another rectangular structure containing longitudinal corrugations on all sides was investigated by Dybdel et al <12>. The attenuation coefficient of this structure when calculated taking into account both the increased cross-sectional size and the reduced power-loss mechanism of the corrugated surface, was found to be lower than that of a comparable smooth wall rectangular waveguide. From the above examples, it is evident that a low-loss mechanism can be introduced in existing waveguides. The mechanism provides a means of lowering the field intensity near the metal surfaces and acts to confine the power carried by the particular mode, towards the axis of the waveguide. In fact, the effect of the new boundaries can be thought of as a beam waveguide,

thus providing the concentration of energy towards the centre of the waveguide.

In order to identify the nature of the new boundaries needed to achieve the above criterion, we must first form an understanding of the loss mechanism that takes place in commercially used waveguides, such as circular, rectangular and elliptical, and then search for a realistic means to minimise these losses. Power-loss occurs in waveguides due to the flow of currents in the metal wall of the boundaries, which possess finite conductivity. The ultimate objective is therefore to reduce the strength of the currents by either the introduction of new boundaries or by the modification of the original boundaries.

To reduce the power-loss components of a smooth wall elliptical waveguide, chapter two is devoted to the study of the attenuation and propagation characteristics of the waveguide. It is shown that a certain asymptotic expansion of the Mathieu function of the fourth kind <13> has been invalidly applied to previous elliptical waveguide calculations. The classical attenuation formula given by Chu <14> and the surface impedance results reported by Felciasecca et al <15>, are shown to be in error. An appropriate expansion of the fourth kind Mathieu function is discussed at some length and leads to a substantial modification of the published formulae. Numerical results of the attenuation coefficient are then compared with the results obtained by McLachlan <16>

and Kretzschmar <17>, who have used the usual perturbation technique employed in circular and rectangular waveguides. The effects of the ellipse eccentricity on the propagation characteristics of the even and odd modes are also illustrated.

The concept of surface impedance depending on position and exhibiting anisotropy for an isotropic wall material is discussed and an attempt is also made in chapter two to justify the reality of such substantial curvature effect. An anomalous property of the characteristic number of the Mathieu function insofar as it relates to the present problem is left for discussion in Appendix III.

The loss components of the elliptical waveguide are identified in chapter two, and a reduction in the major component is shown to be achieved when transverse periodic corrugations are introduced near the smooth metal boundary. In chapter three, the characteristic equation of the elliptical corrugated waveguide is formulated by ensuring field continuity across the boundary separating the slot and the central region of the waveguide. Classification of the elliptical corrugated waveguide modes is proposed and the attenuation and dispersion characteristics of different modes are also illustrated.

The circular corrugated waveguide which was investigated by Clarricoats et al <1> contains slots of rectangular profile. In chapter four, the analysis is

extended to circular corrugated waveguides with non-rectangular slots. The profile of a non-rectangular slot is represented by a staircase approximation profile employed by Clarricoats and Chan <19>, when investigating the properties of a selfoc fibre.

The dispersion, attenuation and radiation characteristics of the waveguide are then obtained, and experimental radiation patterns are compared favourably with the theoretical results. Circular corrugated waveguides with non-rectangular slots are easier to manufacture and possess higher flexibility merit than waveguides with rectangular slots. It could also be used for waveguides of elliptical cross-section.

The circumstance under which the corrugated circular waveguide exhibits low-attenuation is also one which permits more than one mode to propagate. Chapter five deals with the design of a mode filter to absorb the energy in the unwanted modes, and at the same time to have minimal effect on the attenuation of the desired mode. Because of the close resemblance of the field distribution of the desired mode to that of the dominant mode of the optical fibre, the monomode optical fibre features are employed in the mode filter design. The filter consists of two concentric dielectric cylinders and the absorbtion of the unwanted modes is achieved by placing a lossy dielectric layer near the slot region of the waveguide. The design of a matching section to the proposed mode filter is discussed at some length. The

suppression of the unwanted modes is observed experimentally, when mode filters are inserted in existing overmoded circular corrugated waveguides.

Another attempt is made in chapter six to modify the field components of the circular waveguide near the metal wall. This is done by coating the surface with a dielectric layer. The propagation characteristics of the circularly symmetric modes supported by the lined waveguide was first reported by Unger <18>, using perturbation techniques. The characteristic equation of the structure was later solved by Carlin and D'Agostino <5>, who have reported some interesting attenuation properties of the circularly symmetric modes. Brayer <20> reported some properties of the hybrid modes supported by the lined structure. The dispersion and attenuation characteristics of different hybrid modes are illustrated in this chapter and a discussion of the loss mechanism and the nature of the modes is also given. The study of circular waveguides is concluded in chapter seven by a parametric study of a microwave equivalent of the optical waveguide. Because of the well known characteristics of the optical waveguide <21>, the study is limited to obtaining parameters that would ensure low-attenuation characteristics of the dominant mode, and to present the unwanted modes with high attenuation. The group delay and excitation characteristics of the dominant mode are also taken into account in selecting the waveguide parameters. Practical use of the new

waveguide depends on future availability of low-loss dielectric materials <22>.

In chapter eight, the loss components of a smooth wall rectangular waveguide are identified and thus a structure with transverse periodic corrugations on two opposite sides is investigated. The dispersion and attenuation characteristics of the structure are illustrated and an error in earlier predictions of the attenuation coefficient by Baldwin and McInnes <9> is corrected. Circumstances under which the corrugated rectangular waveguide exhibits an attenuation advantage over a smooth wall rectangular waveguide are reported. The attenuation results are also compared with computed values obtained for a corrugated circular waveguide. Experimental results in favour of the predicted dispersion and attenuation results are shown, using resonance cavity techniques <23>.

The thesis is concluded by a brief list of the main contributions and suggestions for future research.

CHAPTER TWO

SMOOTH WALL ELLIPTICAL WAVEGUIDES

2.1 INTRODUCTION

In 1938 Chu <14> presented the theory of transmission of electromagnetic energy in hollow smooth wall waveguides of elliptical cross-section. In his analysis he identified the even and odd modes of propagation, relating them to Mathieu functions of even and odd types. In the formulation of the attenuation coefficient Chu assumed that the conductivity of the metal wall was finite but very large, and the field components in the metal region were represented by Mathieu function of the fourth kind <13>, whose large argument expansion <14> was essential in formulating the attenuation coefficient. Chu did not identify his reason for using the more exact perturbation technique in the formulation of the attenuation coefficient, rather than employing the usual power-loss perturbation method <24> normally used in circular and rectangular waveguides. Remembering the tedious numerical work involved in the calculations of the Mathieu functions <25>, we believe that his choice of the method was mainly due to computational difficulties that would have arisen if the usual perturbation method was to be employed.

The existence of the second even mode, TE_{c21}, was overlooked by Chu. For a certain range of eccentricities the presence of this mode will determine the upper frequency limit of the dominant unimode frequency range, and it is now suggested that its existence should be

taken into consideration by waveguide manufacturers <26>. In 1946 McLachlan <16> used the usual perturbation method to produce formulae for the attenuation coefficient in an elliptical waveguide. These formulae needed more computational efforts in evaluating integrals involving Mathieu functions and no numerical results were reported until 1972, when Kretzschmar <17> undertook the computational task. Kretzschmar's results were different from those obtained by Chu, and no physical reason was given to this discrepancy.

In 1973 Felciasecca, Someda and Valdoni <15>, applied the wall impedance theory to waveguides in general and drew attention to a curvature contribution to the attenuation coefficient of an elliptical waveguide. This curvature dependence was included automatically in the method of Chu, and on employing the usual perturbation method McLachlan had overlooked this curvature dependence. Furthermore Falciasecca <15> points out that in order to obtain agreement between the results, using their method and Chu's, it was necessary to specify both longitudinal and transverse surface impedances which depend on the azimuthal co-ordinate.

The concept of a surface impedance depending on position and exhibiting anisotropy for an isotropic wall material is a little surprising, and in the process of a thorough investigation of the formulae in <15>, it was discovered that they lead to an unacceptable form in the limiting case of an elongated ellipse. The cause of the

discrepancy was ultimately traced to the form of asymptotic expansion used for the radial Mathieu function of the fourth kind within the waveguide wall.

In this chapter the general theory of electromagnetic wave propagation in elliptical waveguides is presented, with special attention paid to the different types and kinds of Mathieu functions governing the wave solution in such a structure. The correct form of the fields in the metal wall is derived using the appropriate asymptotic expansions of the Mathieu functions. The correct formulae for the attenuation coefficient of different modes are derived, and the true form of the axial and transverse surface impedance is also shown.

The results obtained are then compared with those obtained in <14> and <17>, and all these previous results are shown to be in error due to the incorrect form of asymptotic expansion of Mathieu functions having been used. The characteristics of different modes supported by the waveguide are discussed and compared with corresponding modes in existing waveguides.

A general formulation of the curvature effect is presented, and a discussion is given of an unsuccessful attempt to create a generalised form that replaces the ellipse parameters by differentials of the local curvature of the surface. An attempt is also made to justify the reality of such a substantial curvature

effect. However, no effect occurs for flat surfaces or those of uniform curvature, confirming the validity of the usual perturbation technique of calculating waveguide attenuation in those cases.

The major loss components in the elliptical waveguide are also identified in this chapter in order to determine the nature of wall modifications needed to reduce these losses. As a result of this study, a transversely corrugated elliptical waveguide was found to be a promising structure. Chapter 3 will be devoted to the analysis and numerical results of this latter structure.

2.2 GENERAL THEORY OF ELLIPTICAL WAVEGUIDES

2.2.1 Introduction

The problem is formulated in terms of elliptical cylindrical co-ordinates, and by using large argument expansion of the radial Mathieu function the appropriate field equations in the metal region are deduced. The correct formulae for the attenuation coefficient and the surface impedance are then derived.

The elliptic cylinder co-ordinates system (ξ, η, z) is shown in Fig. (2.1) where the contour surfaces of constant ξ are confocal elliptic cylinders, and those of constant η are confocal hyperbolic cylinders. The constant h represents half the distance between the foci. The confocal cylinder $\xi = \xi_o$ coincides

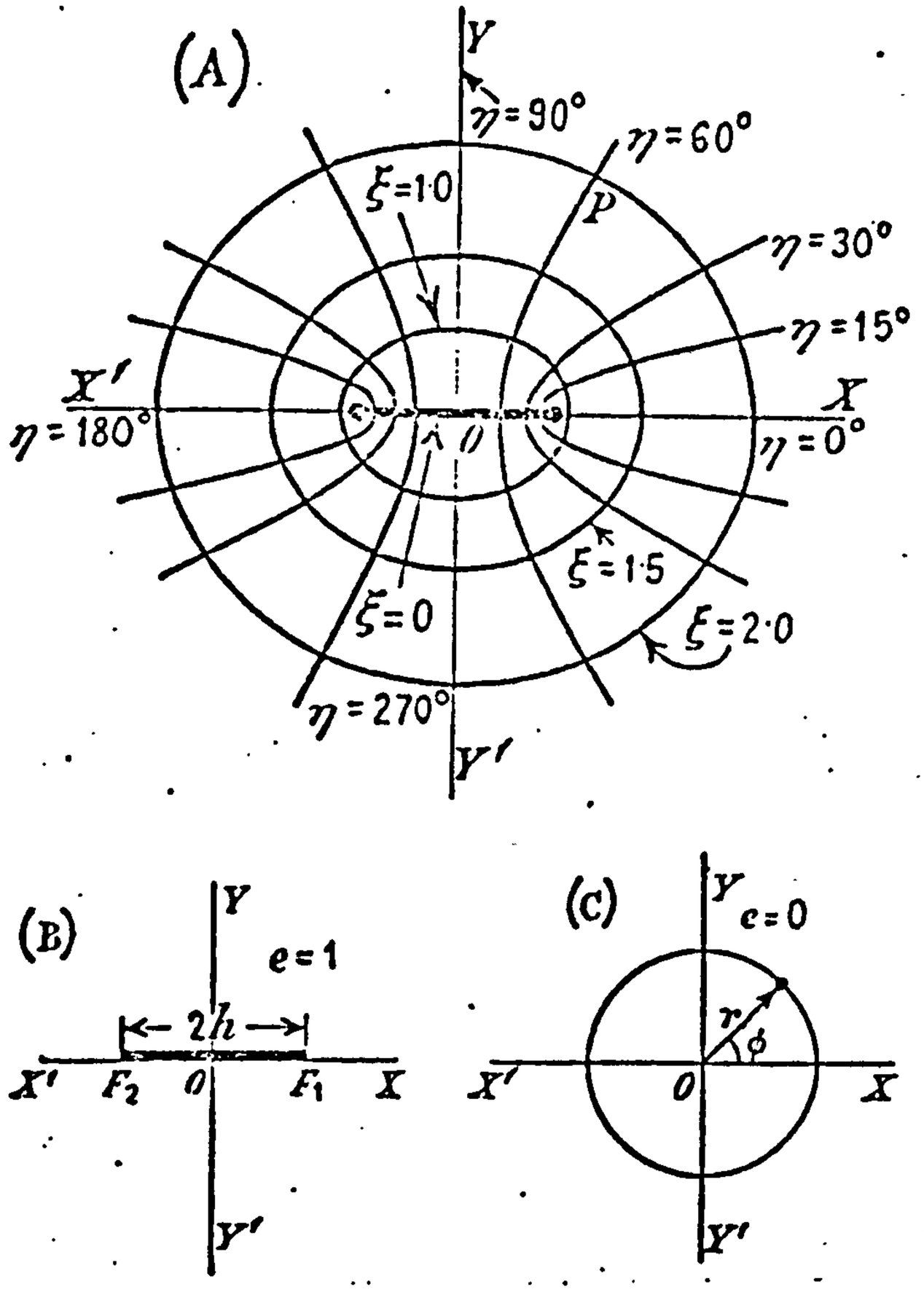

Figure (2.1)

(A) Orthogonally intersecting confocal ellipses and huperbolas for elliptical coordinates. P has elliptic coordinates $\xi=2$, $\eta= 1/3\pi(60^{o})$ and cartesian coordinate $x=h\cosh 2\cos 1/3\pi, y=h\sinh 2\sin 1/3\pi$

(B) Degenerate form of ellipse when e=1. As $e\to 1$, $a\to h$, $b\to 0$ and the ellipse → the interfocal line of length 2h.

(C) Degenerate form of ellipse, when eccentricity e=0. The foci coalesce at the centre of a circle radius r, equal to the semi-major axis. The original hyperbola through P (see A) is now radii making $\phi = \pm 1/3\pi$ with X'OX <16 >

with the inner boundary of the metal waveguide, and the z-axis coincides with the longitudinal axis of the elliptic waveguide. The eccentricity e of the cross-section is given by $1/\cosh \xi_0$. The major and minor axes are $2a = 2h \cosh \xi_0$ and $2b = 2h \sinh \xi_0$ respectively.

2.2.2 The Wave Equation

The general form of the wave equation in an orthogonal curvilinear system of co-ordinates enclosing an infinite source free medium of dielectric permittivity ε_0 and magnetic permeability μ_0 can be written in the form

$$\frac{1}{\ell_1^2}\frac{\partial^2\Lambda}{\partial\phi_1^2} + \frac{1}{\ell_2^2}\frac{\partial^2\Lambda}{\partial\phi_2^2} + \frac{1}{\ell_1\ell_2}\left[\frac{\partial(\ell_2/\ell_1)}{\partial\phi_1}\frac{\partial\Lambda}{\partial\phi_2} + \frac{\partial(\ell_1/\ell_2)}{\partial\phi_2}\frac{\partial\Lambda}{\partial\phi_1}\right] + K^2\Lambda = 0 \qquad \{2.1\}$$

where the axial variation $\partial/\partial z$ is assumed to have the form $-j\beta$, ℓ_1 and ℓ_2 are the first and second metric coefficients of the system, and in the elliptical system

$$\ell_1 = \ell_2 = h(\cosh^2\xi - \cos^2\eta)^{\frac{1}{2}} \qquad \{2.2\}$$

ϕ_1 and ϕ_2 are the transverse co-ordinates, equivalent to ξ, η in our system, and Λ is a scalar field function; which is equal to E_z for TM modes and H_z for TE modes.

Where

$$K = (\omega^2\varepsilon_0\mu_0 - \beta^2)^{\frac{1}{2}} \qquad \{2.3\}$$

and β is the phase-change coefficient.

Therefore the wave equation in the elliptic cylinder system has the form

$$\frac{\partial^2 \Lambda}{\partial \xi^2} + \frac{\partial^2 \Lambda}{\partial \eta^2} + 2q(\cosh 2\xi - \cos 2\eta)\Lambda = 0 \qquad \{2.4\}$$

where

$$4q = K^2 h^2 \qquad \{2.5\}$$

In order to obtain solutions of equation {2.4}, we set

$$\Lambda(\xi, \eta) = R(\xi)\ \theta(\eta),$$

substituting into {2.4} and applying the usual separation of variable procedure, two ordinary differential equations are obtained.

$$\frac{d^2\theta(\eta)}{d\eta^2} + (C - 2q\cos 2\eta)\ \theta(\eta) = 0 \qquad \{2.6\}$$

and

$$\frac{d^2R(\xi)}{d\xi^2} - (C - 2q\cosh 2\xi)\ R(\xi) = 0 \qquad \{2.7\}$$

where C is the separation constant.

Equation {2.6} is the angular Mathieu differential equation; equation {2.7}, which follows from {2.6} by the transformation $\eta = \pm j\xi$, is the modified Mathieu differential equation.

For a physically admissible single-valued electromagnetic field, $\Lambda(\xi, \eta)$ must be a periodic

function of η, of period π or 2π. The separation constant C, which in this case must be a function of q, is an infinite set of characteristic values for every q. When q is real the characteristic values are all real; when q is negatiye imaginary, as it is in one of the cases which is considered, the characteristic values can be either real or complex <16>.

Corresponding to q = 0 there are two independent periodic solutions, namely $\sin(n\eta)$ and $\cos(n\eta)$ with the separation constant $C = n^2$, where n is an integer. It can be shown that <27> when q differs from zero, a characteristic value C determines one and only one periodic solution which is either even or odd in η. The characteristic value C, giving rise to even and odd solutions are denoted by $a_n(q)$ and $b_n(q)$ respectively. The subscript n identifies those sets of characteristic values which approach n^2 as $q \to 0$.

For an arbitrary positive real q, the periodic solutions of Mathieu equation {2.6} are

$$\theta(\eta) = \begin{cases} ce_n(\eta, q) & \text{even} \quad a_n(q) \\ se_n(\eta, q) & \text{odd} \quad b_n(q) \end{cases} \qquad \{2.8\}$$

where $ce_n(\eta, q)$ and $se_n(\eta, q)$ are respectively the even and odd angular Mathieu functions. The corresponding solutions for the modified Mathieu equation {2.7} are

$$= L_1 \, Ce_n(\xi, q) + L_2 \, Fey_n(\xi, q) \quad - - - \text{even} \quad a_n(a)$$

$R(\xi)$

$$= L_3 \, Se_n(\xi, q) + L_4 \, Gey_n(\xi, q) \quad - - - \text{odd} \quad b_n(q)$$

{2.9}

where $Ce_n(\xi, q)$ and $Se_n(\xi, q)$ are radial even and odd Mathieu functions of the first kind, $Fey_n(\xi, q)$ and $Gey_n(\xi, q)$ are radial even and odd Mathieu functions of the second kind. L_1, L_2, L_3 and L_4 are constants.

2.3 PERFECTLY CONDUCTING ELLIPTICAL WAVEGUIDES

2.3.1 Cut-off Frequencies

The proper choice of the above solutions to represent the electromagnetic fields in an elliptical metal waveguide depends upon the boundary conditions. As all the field components must be finite or zero within the metal waveguide, then we must discard the functions $Fey_n(\xi, q)$ and $Gey_n(\xi, q)$, since they are infinite at the origin, i.e. at $\xi = 0$.

The solutions of the wave equation {2.4} are therefore

$$E_z = A_n Ce_n(\xi, q) ce_n(\eta, q) + A_n' \, Se_n(\xi, q) se_n(\eta, q) \quad \{2.10\}$$

and

$$H_z = B_n Ce_n(\xi, q) ce_n(\eta, q) + B_n' \, Se_n(\xi, q) se_n(\eta, q)$$

where A_n, A_n', B_n, B_n' are constants and the exponential dependence $j(\omega t - \beta z)$ is assumed.

As may be seen from {2.10} there are four types of propagation in an elliptical waveguide, namely, even and odd TE and TM modes. To distinguish between the different modes the first index of each mode designation will be c(cos-type) for even mode and s(sin-type) for an odd mode, while the second index n is related to the order of the Mathieu function. Furthermore, the following equations must hold in order that the boundary conditions be satisfied on the wall;

TM modes;

$$\begin{aligned} &\text{even} \quad Ce_n(\xi_o, q) = 0 \qquad n = 0, 1, 2, - - - \\ &\text{odd} \quad Se_n(\xi_o, q) = 0 \qquad n = 1, 2, 3, - - - \end{aligned} \tag{2.11}$$

TE modes;

$$\begin{aligned} &\text{even} \quad Ce'_n(\xi_o, q) = 0 \qquad n = 0, 1, 2, - - - \\ &\text{odd} \quad Se'_n(\xi_o, q) = 0 \qquad n = 1, 2, 3, - - - \end{aligned} \tag{2.12}$$

where the prime denotes derivative with respect to ξ.

As the parameter q is related to the wave number K by {2.5}, a different mode is obtained for each root of {2.11} and {2.12}. To resolve this ambiguity, a third subscript m, corresponding to the m-th parametric root, is required in the mode designation. With {2.5} the general formula for the cut-off wavelength of a TE or TM mode in an elliptical waveguide becomes

$$\lambda_c = \pi h/\sqrt{q} = \pi ae/\sqrt{q} \tag{2.13}$$

For a TM_{cnm} (TM_{snm}) mode $q = q_{cnm}(q_{snm})$ is the m-th parameter zero of the even (odd) modified first kind Mathieu function of order n with argument ξ_o. For a TE_{cnm} (TE_{snm}) mode $q = \bar{q}_{cnm}(\bar{q}_{snm})$ is the m-th parametric zero of the even (odd) derivative of the same function.

The Bessel function product series <16> were then used to find the values of q that satisfy {2.11} and {2.12} for a particular value of ξ_o. This procedure was repeated for different values of the eccentricity and the normalised cut-off frequency was then calculated using {2.13}. Figure (2.2) shows the normalised cut-off frequency for different even and odd type modes as the ellipse is deformed from circle (e=0) to a nearly flat plate ($e \to 1$). The split in the degeneracy which exists for circular waveguide modes is clearly shown, even for very small deformations.

The TE_s modes have their electric fields parallel to the major axis of the ellipse <14>, and so as the ellipse is deformed into an almost flat plate their cut-off wavelengths approach zero. This phenomenon is in accord with that obtained in a rectangular waveguide for a TE_{01} mode if the sides perpendicular to the electric field of the mode are reduced to zero, the cut-off wavelength will decrease to zero.

Similarly, cut-off behaviour of the even and odd TM type modes as the elliptical waveguide approaches the flat plate is in accord with the boundary condition on

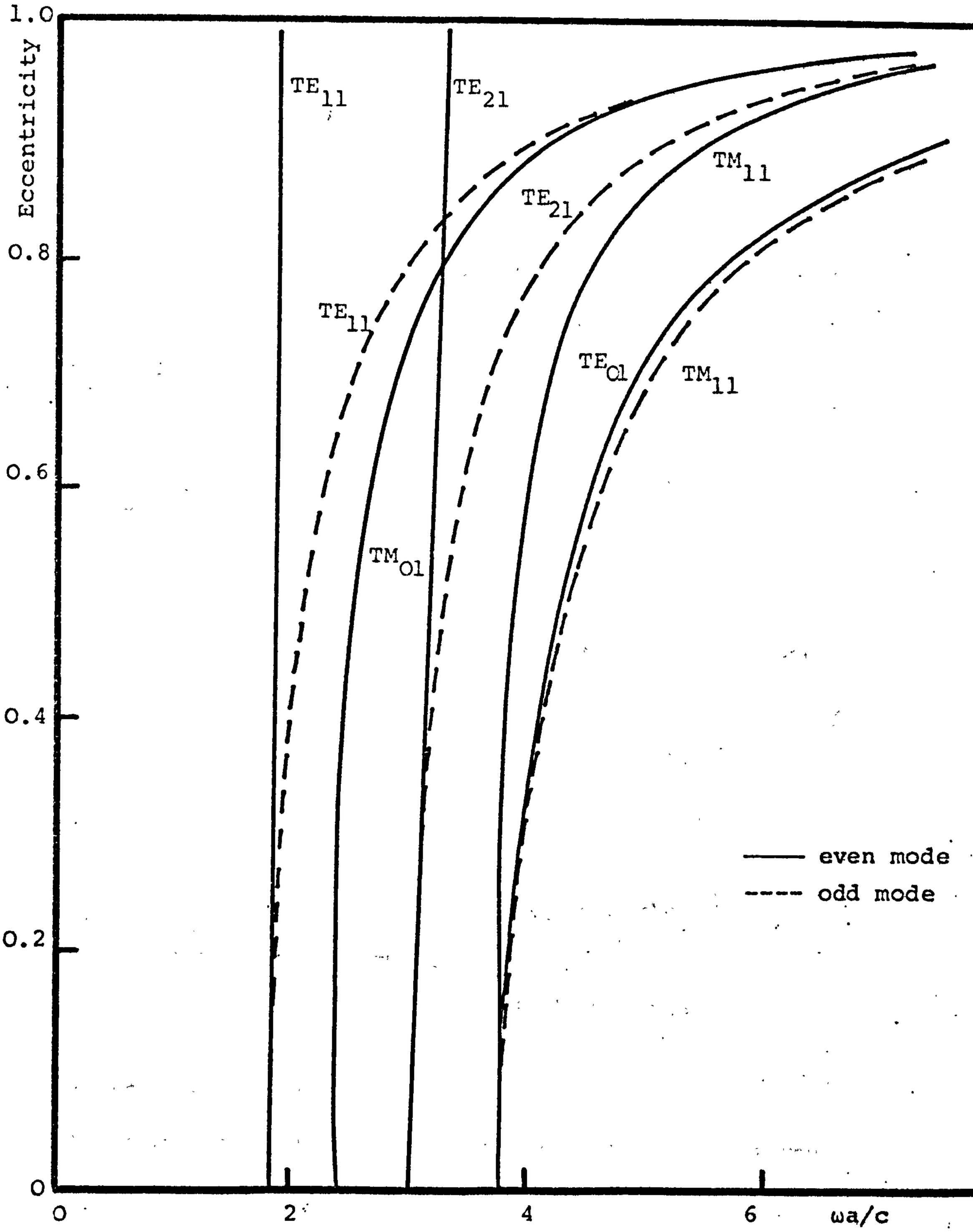

Figure (2.2) Normalised cut-off frequency of modes in an elliptical waveguide

the axial electric field. When the ellipse becomes very thin the modes exist only at a frequency which approaches infinity in the limit $e \to 1$.

2.3.2 Field Components

From the field equations {2.10} and Appendix 1, the following results are obtained.

TE modes:

$$H_z = A_n \begin{vmatrix} Ce_n(\xi, q) & ce_n(\eta, q) \\ \\ Se_n(\xi, q) & se_n(\eta, q) \end{vmatrix}$$

$$H_\xi = -\frac{\beta}{\omega\mu_o} E_\eta = -j\frac{\beta}{\ell_1 K^2} A_n \begin{vmatrix} Ce_n(\xi, q)ce_n'(\eta, q) \\ \\ Se_n(\xi, q)se_n'(\eta, q) \end{vmatrix} \quad \{2.14\}$$

and

$$H_\eta = \frac{\beta}{\omega\mu_o} E_\xi = -j\frac{\beta}{\ell_2 K^2} A_n \begin{vmatrix} Ce_n'(\xi, q)ce_n(\eta, q) \\ \\ Se_n'(\xi, q)se_n(\eta, q) \end{vmatrix}$$

The term expj($\omega t - \beta z$) is assumed.

The prime here denotes the first derivative with respect to either ξ or η.

TE waves in which the components E_ξ and H_η are zero cannot exist in elliptical waveguides.

By constrast, circular waveguides can support TE modes without E_r, H_θ components, corresponding to E_ξ, H_η. This can be explained from the wave equation {2.4}, when for the very nearly circular case the term cos 2η is negligible when compared with cosh 2ξ.

TM modes:

By setting $H_z = 0$, the remaining five components of the field are as follows

$$E_z = B_n \begin{vmatrix} Ce_n(\xi, q)ce_n(\eta, q) \\ \\ Se_n(\xi, q)se_n(\eta, q) \end{vmatrix}$$

$$E_\xi = \frac{\beta}{\omega\varepsilon_o} H_\eta = -j\frac{\beta}{\ell_1 K^2} B_n \begin{vmatrix} Ce_n'(\xi, q)ce_n(\eta, q) \\ \\ Se_n'(\xi, q)se_n(\eta, q) \end{vmatrix} \qquad \{2.15\}$$

$$E_\eta = -\frac{\beta}{\omega\varepsilon_o} H_\xi = -j\frac{\beta}{\ell_2 K^2} B_n \begin{vmatrix} Ce_n(\xi, q)ce_n'(\eta, q) \\ \\ Se_n(\xi, q)se_n'(\eta, q) \end{vmatrix}$$

The term expj$(\omega t-\beta z)$ is assumed.

None of the five field components may vanish in the TM mode, unless the ellipse degenerates into a circle, for reasons similar to that given in the TE mode case.

2.3.3 Attenuation Coefficient

The expressions for the attenuation coefficient using the power-loss perturbation technique can be formulated using the above field components. The technique assumes that the magnetic field at the inner metal surface of the waveguide is the same as it would be if the metal had zero resistivity.

For the TM_{cnm} modes, the tangential component of the magnetic field at the inner surface of the waveguide, where $\xi = \xi_o$ is

$$H_\eta = -j\frac{\omega\varepsilon_o}{\ell_1 K^2} B_n \, Ce_n'(\xi_o, q)\, ce_n(\eta, q)$$

The power loss P_ℓ due to this component is therefore

$$P_\ell = \frac{\omega^2\varepsilon_o^2 R_s}{2K^4} B_n^2 Ce_n'^2(\xi_o, q) \int_0^{2\pi} ce_n^2(\eta, q)\, ds_1/\ell_1^2$$

where ds_1 is an infinitesmal length along the contour ξ = constant, and is given by

$$ds_1 = \ell_1 d\eta$$

Thus,

$$P_\ell = \frac{\omega^2\varepsilon_o^2 R_s}{2aK^4} B_n^2 Ce_n'^2(\xi_o, q) \int_0^{2\pi} ce_n^2(\eta, q)\, d\eta/(1-e^2\cos^2\eta)^{\frac{1}{2}} \qquad \{2.15a\}$$

The mean power carried by the mode P_o, is given by

$$P_o = \tfrac{1}{2}\,\mathrm{Re}\int\int (\underset{\sim}{E}x\underset{\sim}{H}^*)\underset{\sim}{z}\,ds_1\,ds_2$$

$$=\frac{\omega\varepsilon_o\beta}{2K^4}B_n^2\int_0^{2\pi}\int_0^{\xi_o}\left[Ce_n'^2(\xi,q)ce_n^2(\eta,q)+Ce_n^2(\xi,q)ce_n'^2(\eta,q)\right]$$

$$ds_1\,ds_2/\ell_1\ell_2$$

where ds_2 is an infinitesimal length along the contour η = constant and is given by

$$ds_2 = \ell_2 d\xi$$

Thus,

$$P_o = \frac{\omega\varepsilon_o\beta}{2K^4}B_n^2\int_0^{2\pi}\int_0^{\xi_o}\left[Ce_n'^2(\xi,q)ce_n^2(\eta,q)+Ce_n^2(\xi,q)ce_n'^2(\eta,q)\right]d\xi d\eta$$

{2.15b}

The same procedure can be followed to obtain the power loss and the power flow in the TE modes and the attenuation coefficient for the two mode types can therefore be written in the form;

for TE_{cnm} modes,

$$\alpha_c = \frac{R_s}{aZ_o\sqrt{1-(f/f_c)^2}}\,Ce_n^2(\xi_o,\ q)$$

$$\frac{\frac{4q}{e}(\frac{f_c}{f})^2\cdot\int_0^{2\pi}ce_n^2(\eta,q)\,(1-e^2\cos^2\eta)^{\frac{1}{2}}d\eta+\left[1-(\frac{f_c}{f})^2\right]\cdot\int_0^{2\pi}\frac{ce_n'^2(\eta,q)}{(1-e^2\cos^2\eta)^{\frac{1}{2}}}d\eta}{2\int_0^{2\pi}\int_0^{\xi_o}\left[Ce_n'^2(\xi,q)ce_n^2(\eta,q)+Ce_n^2(\xi,q)ce_n'^2(\eta,a)\right]d\xi d\eta}$$

{2.16a}

and for TM_{cnm} modes,

$$\alpha_c' = \frac{R_s}{aZ_o\sqrt{1-(f/f_c)^2}} Ce_n'^2(\xi_o, q)$$

$$\times \frac{\int_0^{2\pi} \frac{ce_n^2(\eta, q)}{(1-e^2\cos^2\eta)^{\frac{1}{2}}} d\eta}{2\int_0^{2\pi}\int_0^{\xi_o} [Ce_n'^2(\xi,q)ce_n^2(\eta,q)+Ce_n^2(\xi,q)ce_n'^2(\eta,q)]d\xi d\eta} \qquad \{2.16b\}$$

By replacing the even Mathieu functions by odd Mathieu functions in the above expressions and using appropriate values of q, the attenuation coefficient for the odd type modes can be obtained.

The above expressions have been previously derived by McLachlan <16>. The integrals appearing in the numerator containing radial Mathieu functions of the first kind and have to be evaluated using numerical techniques, while terms containing the angular Mathieu function can be evaluated in a closed form in terms of their series coefficients (Appendix II). Integrals containing the term $\sqrt{1-e^2\cos^2\eta}$ can be integrated analytically be neglecting high power terms of the eccentricity $O(e^4)$, and using sufficient terms in the evaluation of the series for $ce_n(\eta, q)$ and $se_n(\eta, q)$. In 1972 Kretzchmar <17> evaluated the above integrals numerically on a computer and provided data for the attenuation coefficient for the eight lowest order modes

in the elliptical waveguide.

The validity of the formulae {2.16} and the results obtained in <17> will be discussed in the next section, where the more exact attenuation formulae will be derived.

2.4 IMPERFECTLY CONDUCTING ELLIPTICAL WAVEGUIDES

2.4.1 Introduction

In the previous section, the attenuation is evaluated using a perturbation solution in which the principal fields in the waveguide are assumed to be those which would be found, were the metal wall to possess infinite conductivity. In this section a more exact solution is sought in which the field in the metal is obtained as a solution of the Mathieu wave equation.

2.4.2 Mathieu Function Asymptotic Form

In the metal wall of an elliptical waveguide, the solution of the wave equation involves radial Mathieu functions of the fourth kind, <13>. These are analogous to the Hankel function $H_n^{(2)}$ required in cylindrical co-ordinates field representations. The complex wave-number K_2 in the metal wall has the form <28>

$$K_2 = (\omega/c)\ (\varepsilon'-j60\lambda\sigma)^{\frac{1}{2}} \qquad \{2.17\}$$

where ε' and σ are the usual metal constants, and $K_2^2h^2 = 4q_2$.

The solution will be stable provided that $\varepsilon' > 0$ and $\sigma > 0$ and unstable where $\varepsilon' < 0$ and $\sigma > 0$. If we let $(\varepsilon'-j60\lambda\sigma)^{\frac{1}{2}}$ have the form $\pm(\bar{\alpha}+j\bar{\beta})$ then the regions of stability and unstability governing the wavenumber are shown in Figure (2.3).

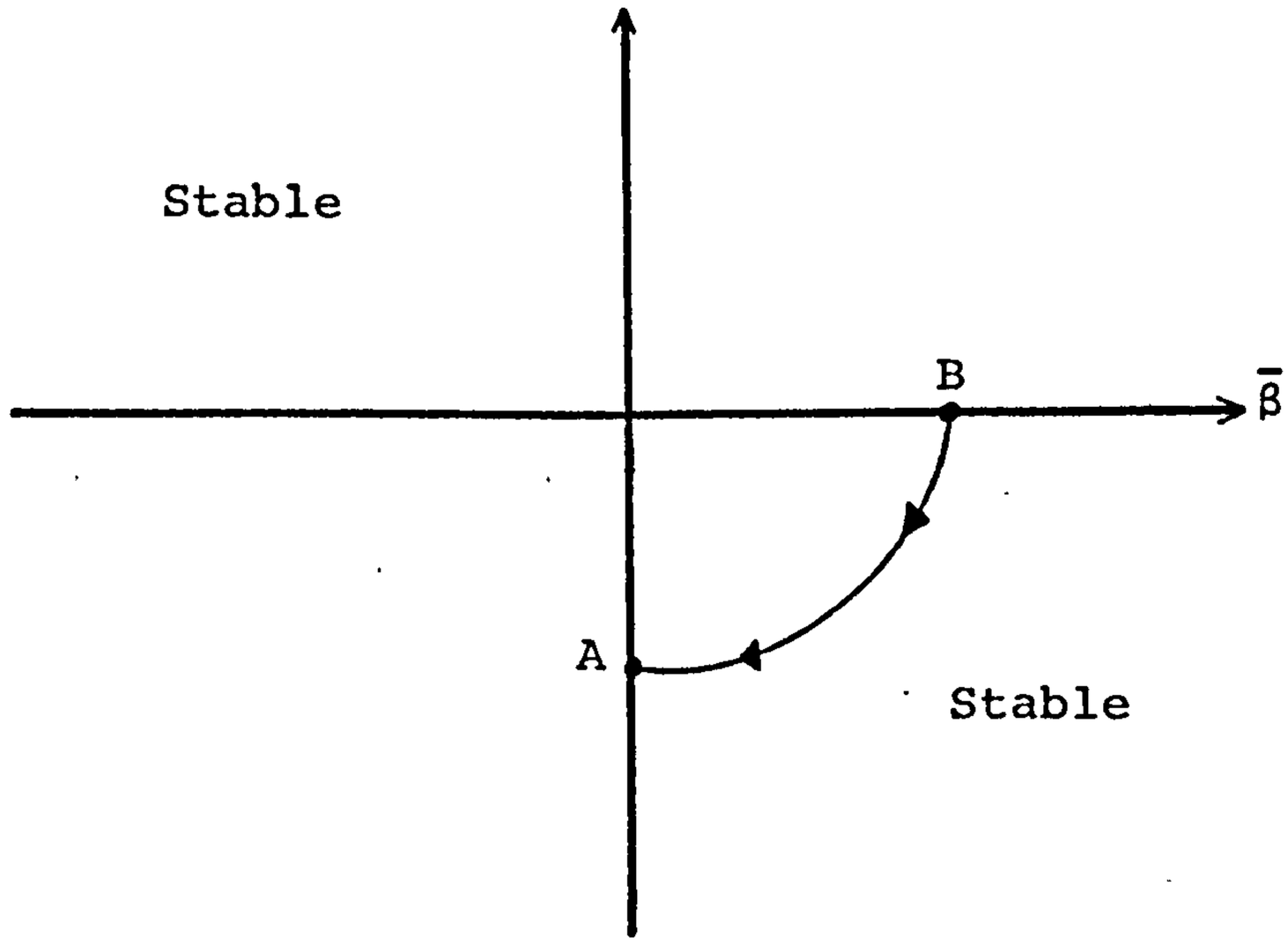

Figure (2.3)

Point B indicates a lossless material and as the material becomes lossy the contour of K_2 moves in the 4th quadrant towards the point A, where it is purely imaginary and the assumption $\sigma >> \omega\varepsilon'$ holds. The same contour will be traced out in the 2nd quadrant, due to the ±sign.

In the circular waveguide case the argument of the Hankel function has the form $(K_2 r)$; r being the radial transverse distance from the origin. When finding large argument asymptotic form of this function, with K_2 almost at A, the product (K_2 x r) always occurs as one quantity

and therefore if either of the variables is large, K_2 in this case, then the results obtained will be the same.

When dealing with the elliptical waveguide case, the function $M_c^{(4)}$ has the quantity $K_2h\cos\xi$ as its argument, both for even and odd functions. In contrast with the circular case, there are two types of asymptotic expansions of this function depending on whether K_2h is large or the radial distance ξ is large. It is clear that in this problem large argument expansions of K_2h must be sought, and not expansions for large ξ. Unfortunately many authors <14> and <15>, have used the incorrect expansion, and obtained incorrect results for the attenuation coefficient and for the surface impedance model. The expansion they used appears in <13>, which is derived from the expansion of the Mathieu function as a series of Bessel functions <16>. The dominant term comes from the asymptotic expansion of $J_{2r}(2q_2^{\frac{1}{2}}\cosh\xi)$ for large ξ, and since the argument is large whether it is ξ or q_2 that is large, it seems at first sight that the expansion based on large ξ will also hold for large q_2 whether or not ξ is large.

The asymptotic form of the fourth kind radial Mathieu function based on the large ξ assumption is given as <13>,

$$Mc_n^{(4)}(\xi, q_2) \approx (K_2h\cosh\xi)^{-\frac{1}{2}} \exp(-jK_2h\cosh\xi+\gamma_2) \quad \{2.18\}$$

where $\gamma_2 = j(2n+1)\pi/4$

Asymptotic expressions for large q exist <16>, and are referred to as Goldstein's expansions <13>. They have the exponent term dominated by $-jK_2h \sinh$, i.e.

$$Mc_n^{(4)}(\xi, q_2) \simeq (K_2h \cosh\xi)^{-\frac{1}{2}} \exp(-jK_2h \sinh\xi) \qquad \{2.19\}$$

It should be mentioned that in reference <13> the expansion is given for the case $q_2 > 0$ and real whereas we need q_2 complex and nearly imaginary Figure (2.3). The validity of the formula {2.19} is demonstrated in Appendix 2 to hold for the case when q_2 is large and imaginary.

The correct form of the radial Mathieu function that must be used to represent the field in the metal region of the elliptical waveguide is therefore given in {2.19} and we conclude that all previous publications based on the form appearing in {2.18} are incorrect.

2.4.3 Wall Impedance

The modal characteristics of waveguides with imperfectly conducting walls, which appear in <29>, is based on the assumption that the boundary conditions may be expressed by the surface impedance of the metal, calculated for an impinging uniform plane wave:

$$Z_o' = (1+j)R_s$$

Falciasecca <15> showed that the above condition of the surface impedance does not apply to any given geometry

and derived general equations for the axial and transverse surface impedance of the metal wall. These equations are independent of the mode in the structure, but take into account the geometry of the structure.

The axial and transverse surface impedance are given by

$$z_a = \frac{\ell_1 K_2^2}{j\omega\varepsilon'} \frac{\psi_n}{\psi_n'},$$

and {2.20}

$$z_t = \frac{j\omega\mu'}{\ell_1 K_2^2} \frac{\psi_n'}{\psi_n}$$

where ψ_n and ψ_n' are, respectively the wavefunction for the n^{th} mode of the radial line, and its derivative with respect to ϕ_1 (Appendix 1).

They used the asymptotic expansion for large ξ {2.18} to calculate the surface impedance derived above; with

$$\psi_n \simeq \tau_n(\eta)(K_2 h \cosh\xi)^{-\frac{1}{2}} \exp(-jK_2 h \cosh\xi) \qquad \{2.21\}$$

$$\psi_n' \simeq -jK_2 h \sinh\xi \, \tau_n(\eta)(K_2 h \cosh\xi)^{-\frac{1}{2}} \exp(-jK_2 h \cosh\xi) \qquad \{2.22\}$$

where $\tau_n(\eta)$ is function of angular Mathieu functions and is defined in {2.30}.

Substituting in equation {2.20} and simplifying we obtain

$$Z_a = Z_o' (1-e^2\cos^2\eta)^{\frac{1}{2}} \ (a/b) \qquad \{2.23\}$$

and

$$Z_t = Z_o' (1-e^2\cos^2\eta)^{-\frac{1}{2}} (b/a) \qquad \{2.24\}$$

Now, for a fixed b and $a \to \infty$, {2.23} gives $Z_a \to \infty$, which must be incorrect, since the region around $\eta = \pi/2$ clearly represents, under the above conditions, part of a parallel plate guide with $Z_a = Z_o'$.

This physical discrepancy was not pointed out in <15>, and it was the basis for finding the correct form of the asymptotic expansion. If the correct expansion {2.19} is used then;

$$\psi_n \approx \tau_n(\eta)(K_2h\ \cosh\xi)^{-\frac{1}{2}} \exp(-jK_2h\ \sinh\xi) \qquad \{2.25\}$$

and

$$\psi_n' \approx \tau_n(\eta)(-jK_2h\ \cosh\xi)(K_2h\ \cosh\xi)^{-\frac{1}{2}} \exp(-jK_2h\ \sinh\xi) \qquad \{2.26\}$$

Substituting in {2.20} and simplifying we get;

$$Z_a' = Z_o' (1-e^2\cos^2\eta)^{\frac{1}{2}} \qquad \{2.27\}$$

and

$$Z_t' = Z_o' (1-e^2\cos^2\eta)^{-\frac{1}{2}} \qquad \{2.28\}$$

Equation {2.27}, though still revealing an interesting position or curvature dependence effect, now correctly gives the expected value for the parallel plate limiting form.

A general formulation of the curvature effect on the attenuation will be given in section (2.6), with both quantitative and qualitative explanations.

2.4.4 Attenuation Coefficient

The attenuation coefficient of the imperfectly conducting elliptical waveguide is formulated by assuming that the field components inside the waveguide are not disturbed appreciably from those given in {2.14} and {2.15}. The attenuation coefficient for the TM_c modes will now be derived with the aid of the correct expansion of the fourth kind Mathieu function {2.19} needed to represent the field components in the metal region of the waveguide.

From {2.15} the value of H_η at the boundary wall is given by

$$H_\eta \simeq -j\frac{\omega\varepsilon_o}{\ell_1 K^2} B_n \, Ce_n'(\xi_o, q)\, ce_n(\eta, q)$$

The solution of the axial field E_z' in the metal region, obtained from equation {2.4}, is as follows:

$$E_z' = \sum_{p=0}^{\infty} A_p Mc_p(\xi, q_2)\, ce_p(\eta, q_2) \qquad \{2.29\}$$

Using equation {2.19} for the expansion of the radial fourth kind Mathieu functions leads to

$$E_z' = B_n' \tau_n(\eta)\,(K_2 h \cosh\xi)^{-\frac{1}{2}} \exp(-jK_2 h \sinh\xi)$$

where

$$B_n' \tau_n(\eta) = \sum_{p=0}^{\infty} A_p \, ce_p(\eta, q_2) \qquad \{2.30\}$$

The tangential magnetic field component is therefore given by

$$H_\eta' = B_n' \tau(\eta) \frac{\sigma}{\ell_1 K_2^2} (jK_2 h\cosh\xi)(K_2 h\cosh\xi)^{-\frac{1}{2}} \exp-(jK_2 h\sinh\xi)$$

The term exp j(ωt-βz) is assumed in the above expressions. The boundary conditions require that the two tangential fields H_η and H_η' must be the same. In the expressions for H_η and H_η', only $ce_n(\eta, q)/\ell_1$ and $\tau_n(\eta)/\ell_1$ are functions of η, hence the ratio $ce_n(\eta, q)/\tau_n(\eta)$ must be independent of η. This ratio can be set to unity, as we have not fixed the magnitude of $\tau_n(\eta)$ in the metal wall.

The necessity of the summation sign appearing in equation {2.30} is discussed in greater detail in the next chapter when analysing the corrugated elliptical waveguide.

The value of the constant B_n' is related to B_n by equating the two tangential magnetic field components at $\xi = \xi_o$;

$$B_n' = -B_n \frac{\omega\varepsilon_o K_2}{\sigma K} \left(\frac{1}{h\cosh\xi_o}\right) Ce_n'(\xi, q)(K_2 h\cosh\xi_o)^{\frac{1}{2}} \exp(jK_2 h\sinh\xi_o)$$

The two tangential field components E_z' and H_η' at the boundary are therefore;

$$E_z' = -B_n \frac{\omega\varepsilon_o K_2}{\sigma K^2} \cdot \left(\frac{1}{h\cosh\xi_o}\right) Ce_n'(\xi_o, q)\, ce_n(\eta, q)$$

and

$$H_\eta' = -B_n \frac{j\omega\varepsilon_o}{\ell_1 K^2} Ce_n'(\xi_o, q)\, ce_n(\eta, q)$$

The power loss, P_ℓ , into the metal wall is obtained by integrating the real part of the Poynting vector over the boundary;

for a unit length of the waveguide

$$P_\ell = -\tfrac{1}{2}\ \mathrm{Re}\int_0^{2\pi} (E_z' \cdot H_\eta'^{*})\ \ell_1\ell_2 d\eta$$

Using the above expressions;

$$\mathrm{Re}(E_z' \cdot H_\eta'^{*}) = -B_n^2\ \frac{\omega^2\varepsilon_o^{\,2}}{\ell_1^{\,2}K^4}\ \frac{Ce_n'^{\,2}(\xi_o,q)}{h\ \cosh\xi_o}\ ce_n^2(\eta,q)\cdot\mathrm{Re}(jK_2/\sigma)$$

But

$$K_2 = \sqrt{-j\omega\mu'\sigma} \qquad \mathrm{Re}(jK_2/\sigma) = \frac{1}{\sqrt{2}}\left[\frac{\omega\mu_o}{\sigma}\right]^{\frac{1}{2}} = \left[\frac{\pi f\mu_o}{\sigma}\right]^{\frac{1}{2}} = R_s$$

Thus

$$P_\ell = B_n^2\ \frac{R_s}{2}\ \frac{\omega^2\varepsilon_o^{\,2}}{K^4}\ \frac{Ce_n'^{\,2}(\xi_o,q)}{a}\int_0^{2\pi} ce_n^2(\xi_o,q)\,d\eta \qquad \{2.31\}$$

The power, P_o, transmitted in the waveguide, is obtained by using the field expressions for a perfectly conducting metal waveguide, and therefore takes the same form given in {2.15b}.

The attenuation coefficient of the TM_c modes can therefore be written in the form

$$\alpha_c' = \frac{R_s}{aZ_o\sqrt{1-(f_c/f)^2}}\ Ce_n^2(\xi_o,q)\ \frac{\frac{4q}{e}\left(\frac{f_c}{f}\right)^2\int_0^{2\pi} ce_n^2(\eta,q)\,d\eta + \left[1-\left(\frac{f_c}{f}\right)^2\right]\int_0^{2\pi} ce_n'^{\,2}(\eta,q)\,d\eta}{2\int_0^{2\pi}\int_0^{\xi_o}\left[Ce_n'^{\,2}(\xi,q)\,ce_n^2(\eta,q)+Ce_n^2(\xi,q)\,ce_n'^{\,2}(\eta,q)\right]d\xi\,d\eta}$$

$\{2.32\}$

The attenuation coefficient of the odd modes can be obtained by replacing the even Mathieu functions in {2.32} by the odd functions. The power loss expression, for the TM_{cnm} mode, derived by Chu <14>, was obtained using the form of the field in the metal region, based on the incorrect asymptotic form of the Mathieu function {2.18}.

The expression for the tangential electric field used by Chu had the form;

$$E_z' = -B_n \frac{\omega\varepsilon_o K_2}{\sigma K^2} \left(\frac{1}{h \sinh\xi_o}\right) Ce_n'(\xi_o,q)ce_n(\eta,q)$$

When formulating the power loss, P_ℓ, expression, the term $(\sinh\xi_o)$ will give the following result;

$$P_\ell = \frac{R_s}{2} B_n^2 \frac{\omega^2\varepsilon_o^2}{K^4} \frac{Ce_n'^2(\xi_o,q)}{a\sqrt{1-e^2}} \int_0^{2\pi} ce_n^2(\eta,q)d\eta \qquad \{2.33\}$$

The expression for the total power flowing in the waveguide derived by Chu had the correct form as in {2.15b}, because the correct expressions for the field in the air region of the waveguide were used in his analysis. The above two expressions for the power loss, P_ℓ, {2.31} and {2.33} and that obtained assuming a perfectly conducting metal wall {2.15a} will be compared in the next section.

2.4.5 Comparison of Results

The attenuation results most commonly used by those industries manufacturing elliptical waveguides <26>, are those obtained by Chu <14>. As pointed out in the previous section those results are in error, and this error is due to the formulation of the power loss in the waveguide.

In what follows we compare the expressions for the power loss, for the TM and TE modes, using the results obtained using perturbed fields based on the perfectly conducting metal case by McLachlan, and those obtained in the imperfectly conducting metal case.

For the TM modes, the three normalised power loss components, due to H_η, can be re-written, using equations {2.15a}, {2.31} and {2.33}, in the form

Mode	McLachlan	Chu	Correct
TM_{cnm}	$\int_0^{2\pi} \frac{ce_n^2(\eta,q)}{\sqrt{1-e^2\cos^2\eta}}\,d\eta$	$\frac{1}{\sqrt{1-e^2}}\int_0^{2\pi} ce_n^2(\eta,q)\,d\eta$	$\int_0^{2\pi} ce_n^2(\eta,q)\,d\eta$
TM_{snm}	$\int_0^{2\pi} \frac{se_n^2(\eta,q)}{\sqrt{1-e^2\cos^2\eta}}\,d\eta$	$\frac{1}{\sqrt{1-e^2}}\int_0^{2\pi} se_n^2(\eta,q)\,d\eta$	$\int_0^{2\pi} se_n^2(\eta,q)\,d\eta$

It can be deduced that for the TM modes;

(i) The attenuation coefficient obtained using McLachlan formula is always greater than that obtained using the

correct formula. This discrepancy between the two results will increase for increasing values of e.

(ii) The attenuation results obtained by Chu need to be reduced by a factor b/a. For the TE modes, the expressions for the power loss are a little more involved as there are two contributing terms, namely H_z and H_η. In order to compare the results obtained, the power losses are split into the two components and the respective terms compared choosing the appropriate ranges of frequency.

At frequencies near cut-off the dominant term will be that due to H_z, while at frequencies far from cut-off it will be due to H_η.

At $f \sim f_c$, the three normalised power loss components due to H_z, can be written in the form

Mode	McLachlan	Chu	Correct
TE_{cnm}	$\int_0^{2\pi} ce_n^2(\eta,q)\sqrt{1-e^2\cos^2\eta}\,d\eta$	$\sqrt{1-e^2}\int_0^{2\pi} ce_n^2(\eta,q)\,d\eta$	$\int_0^{2\pi} ce_n^2(\eta,q)\,d\eta$
TE_{snm}	$\int_0^{2\pi} se_n^2(\eta,q)\sqrt{1-e\cos^2\eta}\,d\eta$	$\sqrt{1-e^2}\int_0^{2\pi} se_n^2(\eta,q)\,d\eta$	$\int_0^{2\pi} se_n^2(\eta,q)\,d\eta$

It can be deduced that for the TE modes at $f \sim f_c$

(i) The attenuation results obtained using McLachlan formula are always smaller than those obtained using the correct formula. This discrepancy between the two results will decrease with increasing eccentricity.

(ii) The results obtained by Chu need to be increased by a factor a/b. At intermediate frequencies, the correct attenuation results cannot be obtained by simply multiplying Chu's attenuation results by the factor a/b. This is because the power-loss contribution of the azimuthal magnetic field component is comparable to that of the axial magnetic field component. However, the correction factor decreases with increasing frequency and reaches unity in value at some frequency, depending on the order of the TE mode and the eccentricity of the waveguide in consideration.

At $f >> f_c$, the three normalised power-loss components due to H , can be written in the form;

Mode	McLachlan	Chu	Correct
TE_{cnm}	$\int_0^{2\pi} \frac{ce_n'^2(\eta,q)}{\sqrt{1-e^2\cos^2\eta}}\,d\eta$	$\frac{1}{\sqrt{1-e^2}}\int_0^{2\pi} ce_n'^2(\eta,q)\,d\eta$	$\int_0^{2\pi} ce_n'^2(\eta,q)\,d\eta$
TE_{snm}	$\int_0^{2\pi} \frac{se_n'^2(\eta,q)}{\sqrt{1-e^2\cos^2\eta}}\,d\eta$	$\frac{1}{\sqrt{1-e^2}}\int_0^{2\pi} se_n'^2(\eta,q)\,d\eta$	$\int_0^{2\pi} se_n'^2(\eta,q)\,d\eta$

It can be deduced that for the TE modes at $f >> f_c$

(i) The attenuation results obtained using McLachlan's formula are always greater than those obtained using the correct formula, and the discrepancy between the two results will increase with increasing eccentricity.

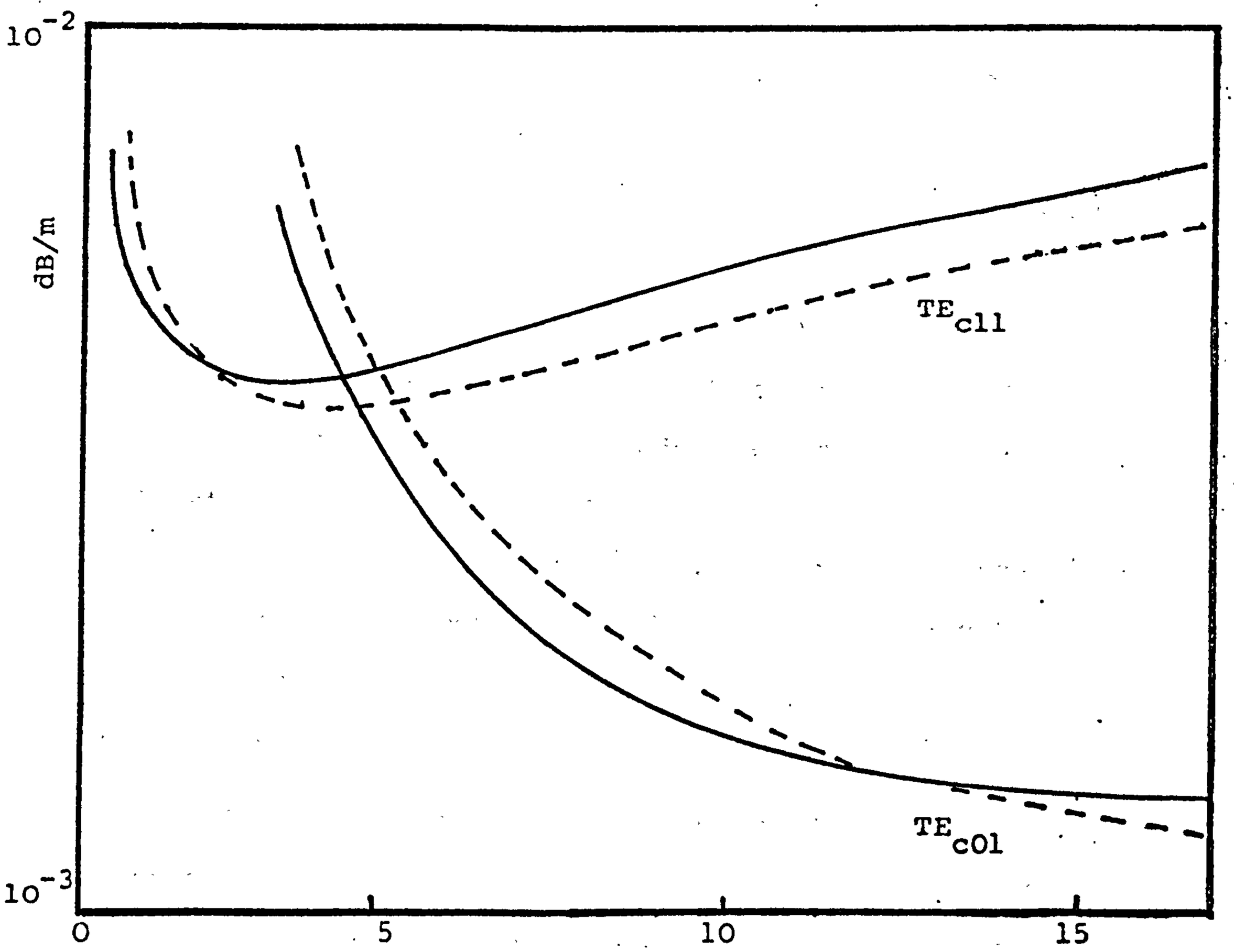

Figure (2.4) Attenuation characteristics of an elliptical waveguide.

TE_{c01} : e = 0.643, a = 7.719cm

TE_{c11} : e = 0.541, a = 6.903cm

$\sigma = 5.8 \times 10^{7}$ S/m

——— Chu's formulae <14>

----- correct formulae

(ii) The results obtained by Chu must be reduced by a factor b/a.

From the above deductions there appears to be a cross over point for the TE modes, at which the previous attenuation results will coincide with the correct results.

Figure (2.4) illustrates the comparison of the correct attenuation results with those obtained by Chu, for the TE_{c01} and TE_{c11} modes, for eccentricity in the neighbourhood of 0.6. The trend of the curves clearly demonstrates the behaviour described above.

The normalised attenuation coefficient is plotted for the TE_{c11} mode in Figure (2.5) using the correct formula and that derived by McLachlan. Different values of e are used to demonstrate the behaviour discussed above. The TE_{c11} mode is the mode used in commercial applications of the elliptical waveguide, with the waveguide's eccentricity being > 0.9. For this range of eccentricity the waveguide will be operated in the range of normalised frequency around $\omega a/c \sim 2.5$, as can be seen from Figure (2.2).

The percentage error in the attenuation coefficient, of this mode, obtained if the perturbation method (McLachlan) was to be used, is illustrated in Figure (2.6). The invalidity of the results obtained using McLachlan's formula, in the range of interest, is clearly demonstrated in the figure, where an error of nearly 40% is observed. We must emphasise that this

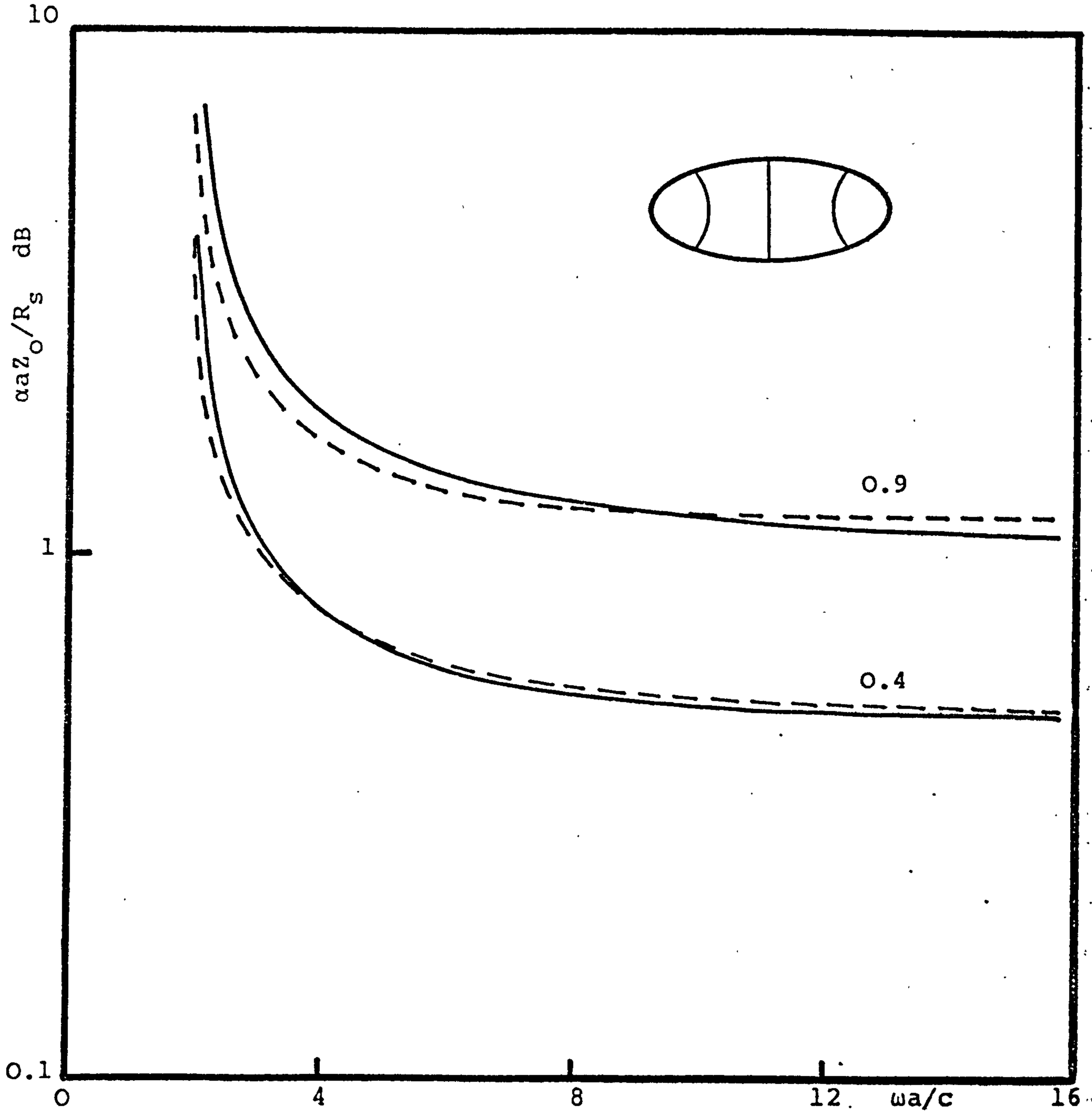

Figure (2.5) Attenuation characteristics of the TE_{c11} mode in an elliptical waveguide

Parameter (eccentricity)

----- McLachlan formula <16>

——— correct formulae

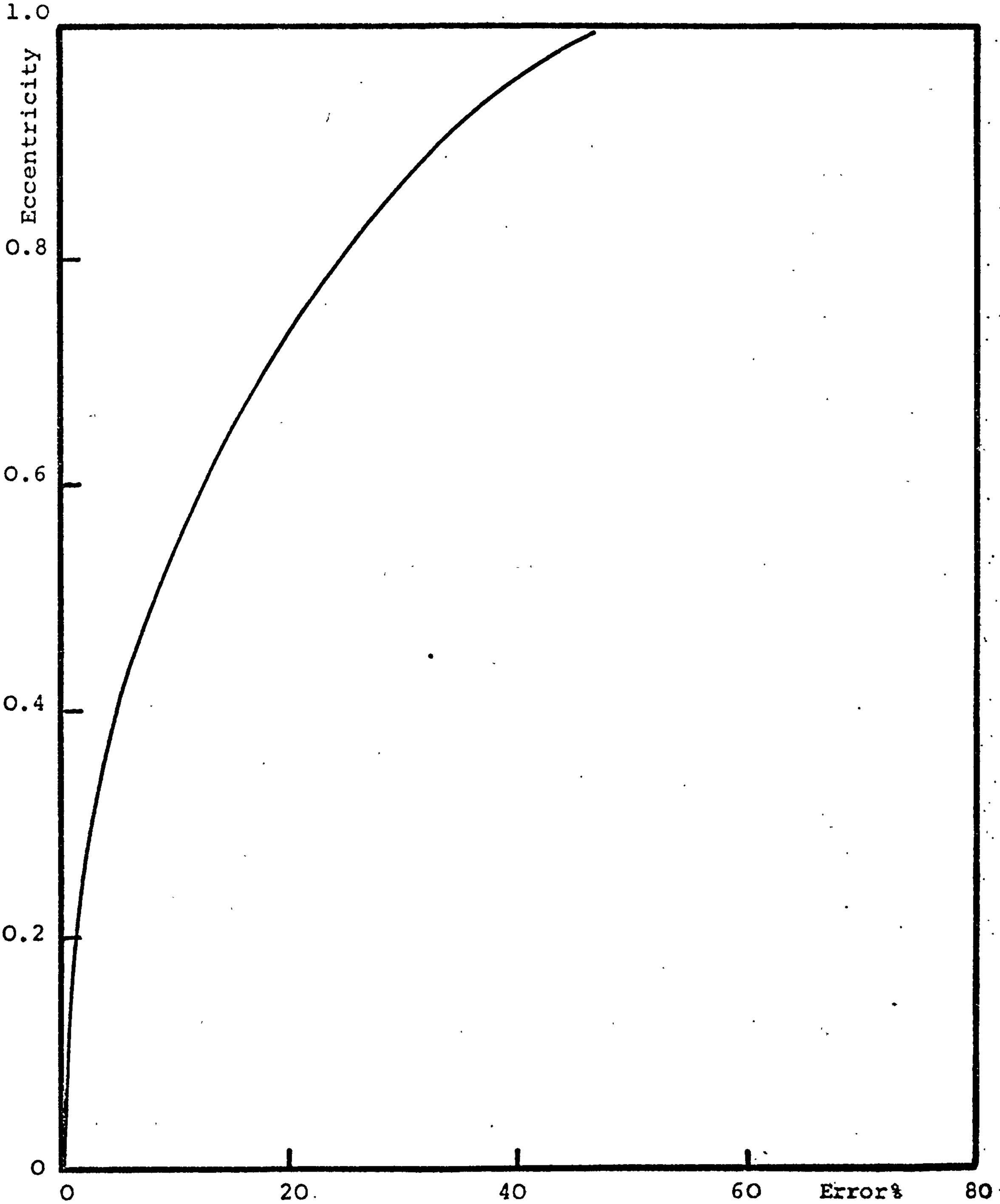

Figure (2.6) Error introduced by using the perturbation formulae in the attenuation of the TE_{c11} mode in an elliptical waveguide

error is mainly due to the non-uniform curvature of the ellipse surface, which has to be taken into account as will be shown in section (2.6).

For the circular or rectangular waveguides, if the attenuation coefficient was formulated using the method described in section (2.4) then the results obtained will be similar to those obtained using the usual perturbation method described in section (2.3). In the circular waveguide case, the factor $H_n^{(2)'}/H_n^{(2)}$, which occurs in formulating the metal wall field, is unity when large argument asymptotic expansion of the Hankel function <13> is used, thus causing the two results to be the same. This result is clearly demonstrated in Figure (2.6), where it is shown that when the ellipse is reformed into a circle (e=0) the percentage error reduces to zero, and $TE_{cll} \rightarrow TE_{ll}$

2.5 MODES CHARACTERISTICS

2.5.1 TE_{cll} mode

The TE_{cll} mode has an almost linearly polarised field, with its transverse electric field vector normal to the major axis of the elliptical waveguide <14>. In commercial elliptical waveguides, the dominant mode TE_{cll}, is used and eccentricities are in the range >0.9 and <0.98. The upper frequency limit for single mode operation is defined by the cut-off frequency of the higher order modes. These are TE_{sll} for e < 0.83 and TE_{c21} for e > 0.83, as shown in Figure (2.2).

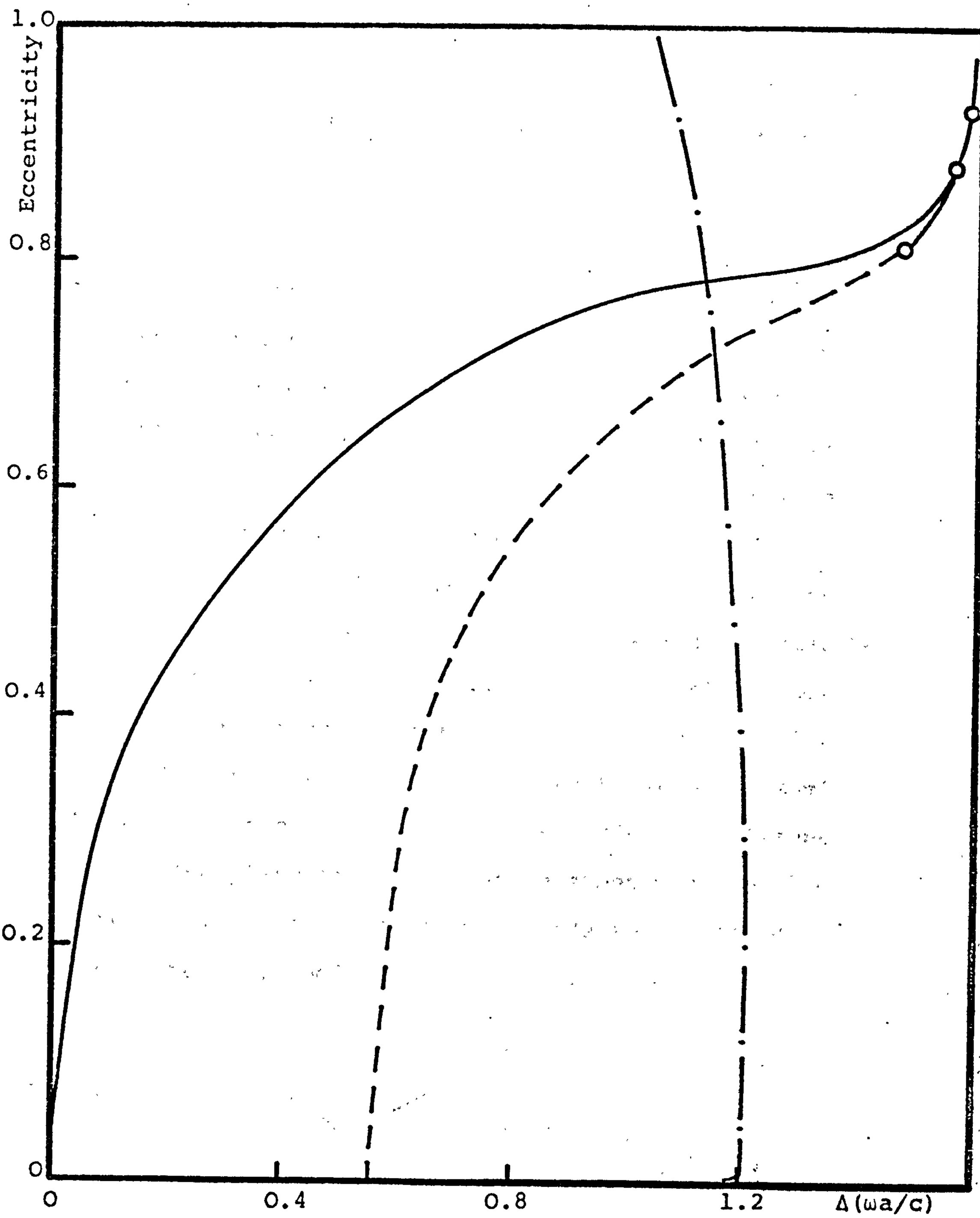

Figure (2.7) Difference in cut-off frequency of various modes in an elliptical waveguide

-.-.-.-. $(TE_{s21}-TE_{s11})$ ------- $(TM_{c01}-TE_{c11})$

———— $(TE_{s11}-TE_{c11})$ -o-o-o-o- $(TE_{c21}-TE_{c11})$

The variation of normalised single mode bandwidth with eccentricity is shown in Figure (2.7), where it can be seen that in the range of operation used commercially, maximum bandwidth is obtained.

For low eccentricities, the upper frequency limit could be substantially increased if a means could be devised to suppress the TE_{s11} mode, whose transverse electric field vector is normal to the minor axis of the elliptical waveguide. The upper frequency limit of the TE_{c11} mode will then be governed by the TM_{c01} mode, and this increase in normalised bandwidth is shown in Figure (2.7). If a long straight section of the waveguide was to be used then a simple mode filter could be employed to suppress the TE_{s11} mode. A possible mode filter might consist of a thin resistive sheet, appropriately shaped, and sandwiched between two semi-elliptical pieces of low density expanded polystyrene ($\tilde{\varepsilon}\simeq 1$). The plane of the resistive sheet must be placed along the major axis of the waveguide so as not to affect the TE_{c11} mode, Figure (2.8).

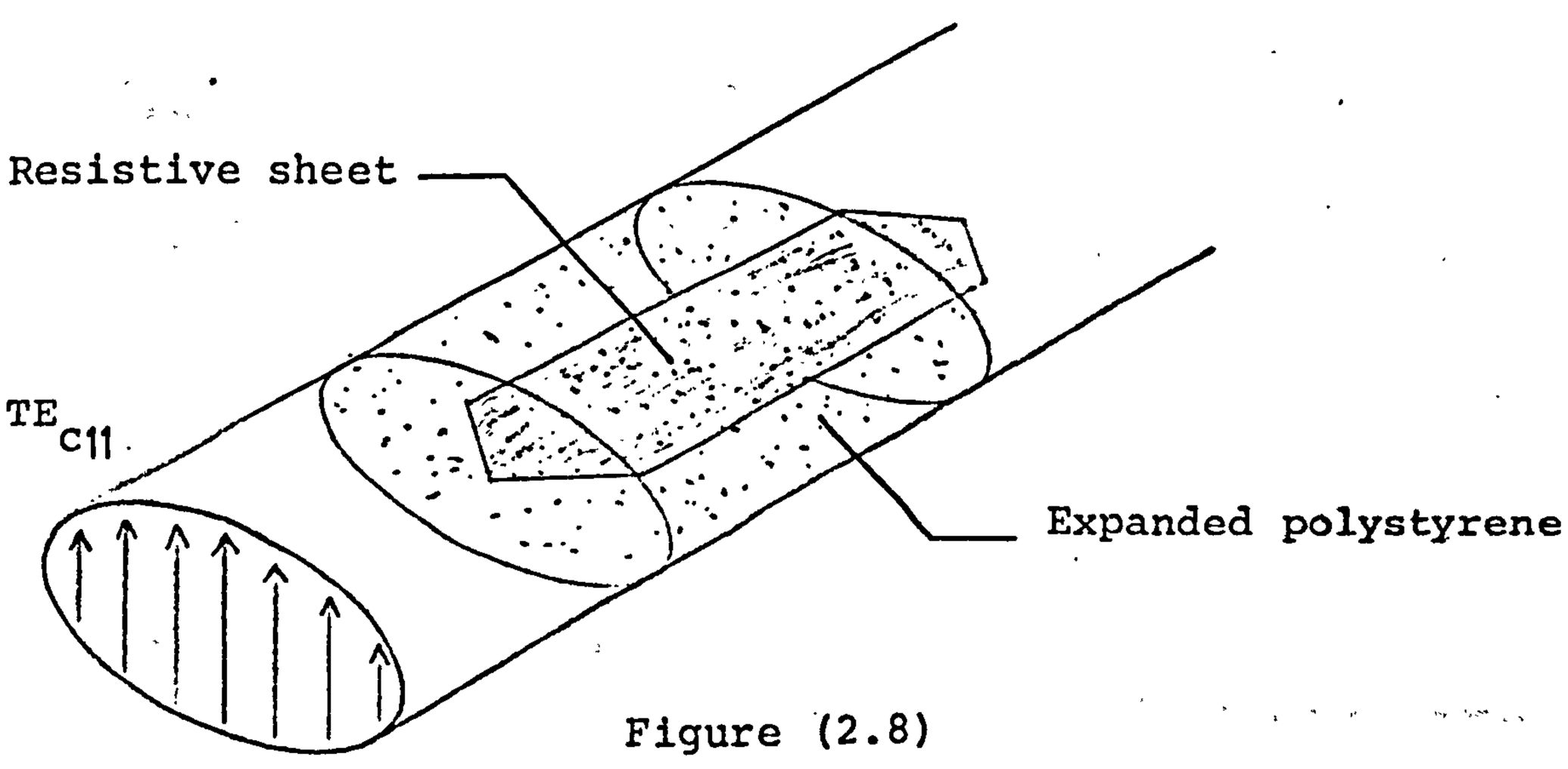

Figure (2.8)

Expanded polystyrene is used to fix the resistive material in the correct position without distorting the original field configuration in the waveguide. As the presence of the resistive material in the waveguide will not introduce new boundary conditions, we assume that the field configurations are unaltered. The power loss in the resistive material, P_ℓ', is given by the expression

$$P_\ell' = \frac{\omega\varepsilon''}{2} \int_s |\underline{E}|^2 ds$$

where $\underline{E}$ is the resultant electric field component in the material, s being the surface area of the lossy material (ε'') over which the field is acting.

For the TE modes

$$|\underline{E}|^2 = E_\xi E_\xi^* + E_\eta E_\eta^* = |E_\xi|^2 + |E_\eta|^2$$

Using the field expressions given in {2.14}, the following results are obtained;

in the plane $\eta = 0, \pi$

$$E_{e\eta} = \delta \qquad E_{e\xi} = 0$$

$$E_{s\eta} = 0 \qquad E_{s\xi} = \delta$$

and in the plane $\eta = \pi/2, 3\pi/2$

$$E_{e\eta} = 0 \qquad E_{e\xi} = \delta$$

$$E_{s\eta} = \delta \qquad E_{s\xi} = 0$$

δ being a finite quantity, s and e define the type of mode.

Therefore, if the thin sheet is placed in the plane $\eta = 0, \pi$, only the odd mode will be attenuated. The thickness of the sheet will determine the attenuation of the even mode.

A possible advantage in operating the waveguide with small eccentricities is shown in Figure (2.9) and Figure (2.10). Figure (2.9) shows the effect of changing the eccentricity on the attenuation coefficient of the TE_{c11} mode in a copper waveguide with a = 0.0114m, while Figure (2.10) shows the approximate increase in attenuation over a smooth wall circular waveguide. This is obtained from Figure (2.9) and is valid over a wide frequency range. A substantial increase in the attenuation is observed for waveguides with $e > 0.9$.

Commercially available elliptical waveguides with high eccentricities ensure single mode operation at the expense of high attenuation. The use of the mode filter described above in an elliptical waveguide of low eccentricity overcomes the attenuation penalty though bends and deformations might generate higher order modes.

Figure (2.9) also shows the attenuation coefficient of the TE_{10} mode in a copper rectangular waveguide of dimensions comparable to those of an elliptical waveguide of 0.97 eccentricity. It is observed that, at frequencies far from cut-off, the attenuation coefficient of the rectangular waveguide is very close to that of an elliptical waveguide operating in the TE_{c11} mode. At such high frequencies the power-

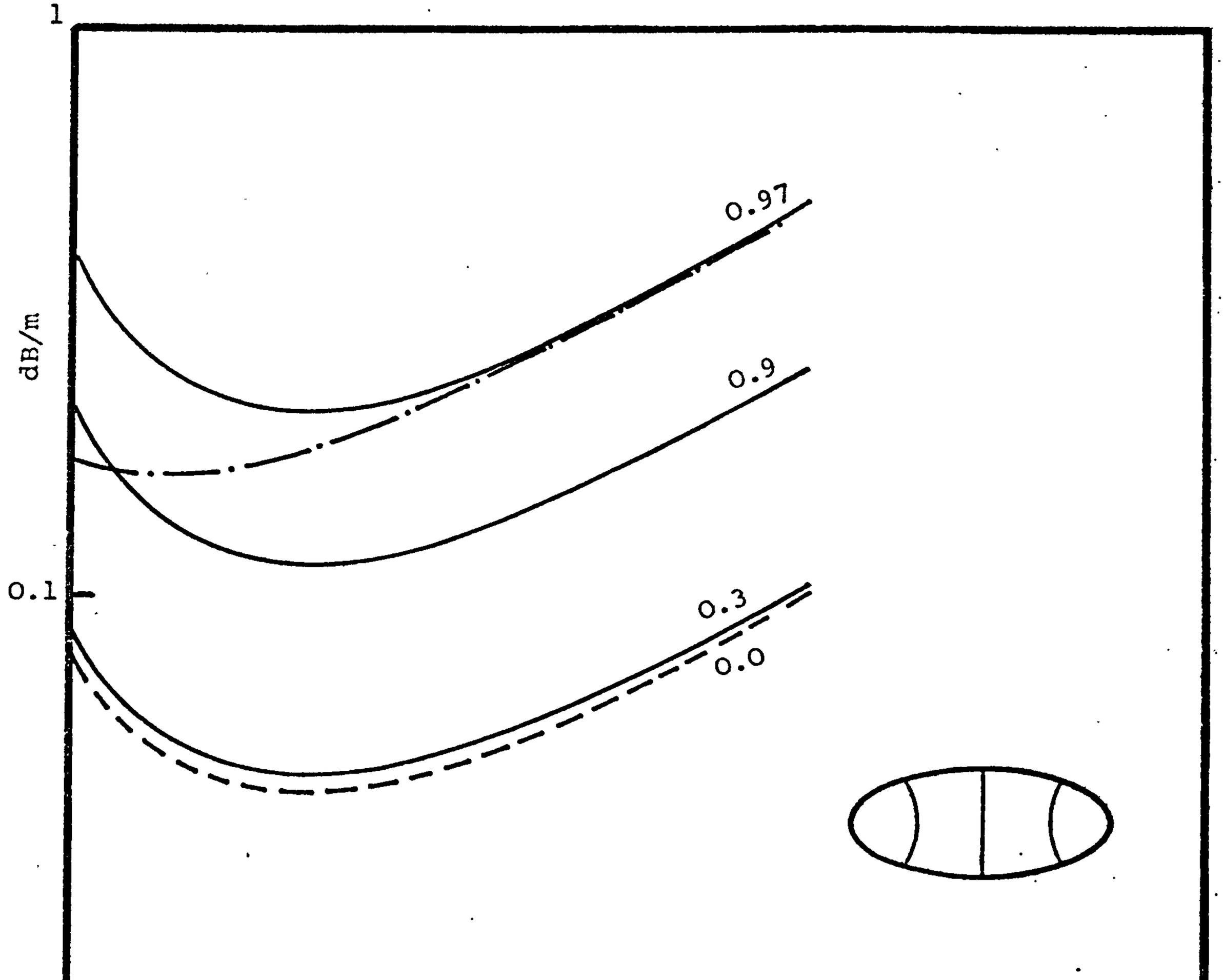

Figure (2.9) Attenuation characteristics of the TE_{c11} mode in an elliptical waveguide

$a = 1.14cm$ $\sigma = 5.8 \times 10^7$ S/m

Parameter (eccentricity)

-.-.-.- TE_{10} mode in a rectangular waveguide

$a = 2.28cm$ $b = .554cm$

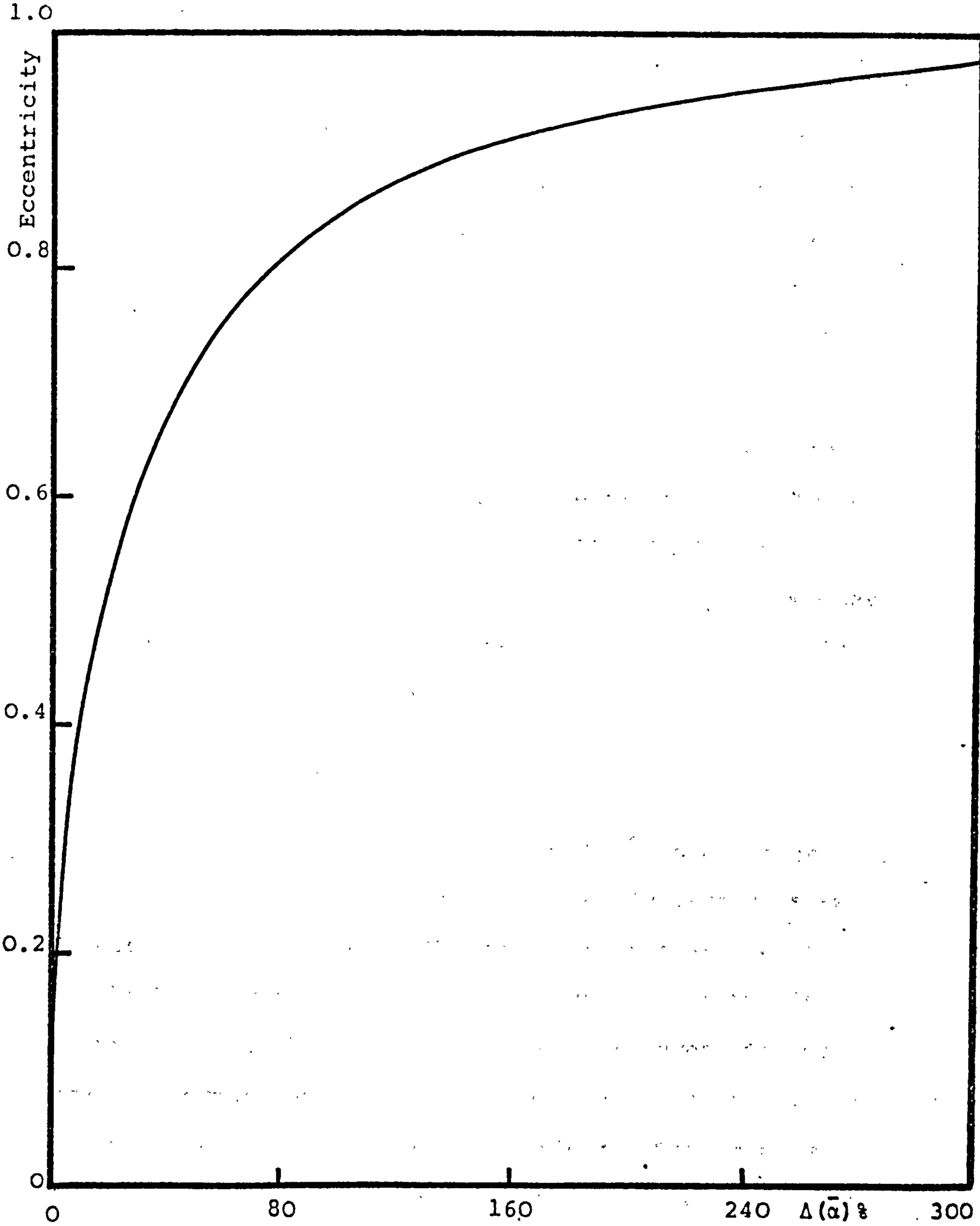

Figure (2.10) Increase in the attenuation coefficient of the TE_{c11} mode in an elliptical waveguide over the TE_{11} mode in a circular waveguide with r = a

$\bar{\alpha} = aZ_o/R_s$ dB

loss contribution of the wall perpendicular to the electric field vector is substantial when compared with the vertical wall losses. Then, because the former wall of the elliptical waveguide considered has a very large radius of curvature, the results obtained merely confirm the curvature effect contribution to the attenuation coefficient.

In section (2.5.3) the curvature effect is shown to be very significant when comparing the attenuation coefficient of the TE_{10} mode in a rectangular waveguide with that of the TE_{s11} mode in an elliptical waveguide, at high frequencies. This is because the TE_{s11} mode has its electric field vector perpendicular to the wall for small radius of curvature.

2.5.2 TE_{01} Even Mode

In a circular waveguide the $TE_{01}{}^{o}$ mode has an attenuation coefficient which continually decreases as frequency is increased. The attenuation characteristics of the TE_{01} even in elliptical waveguide is shown in Figure (2.11), where it can be seen that even for very small deformations from the circular cross-section, the attenuation will always have a minimum. This minimum occurs at very high frequencies for small eccentricities.

In the circular waveguide the attenuation of the TE_{01} mode is due to the power loss of the axial magnetic field component H_z, and is proportional to $f^{-3/2}$.

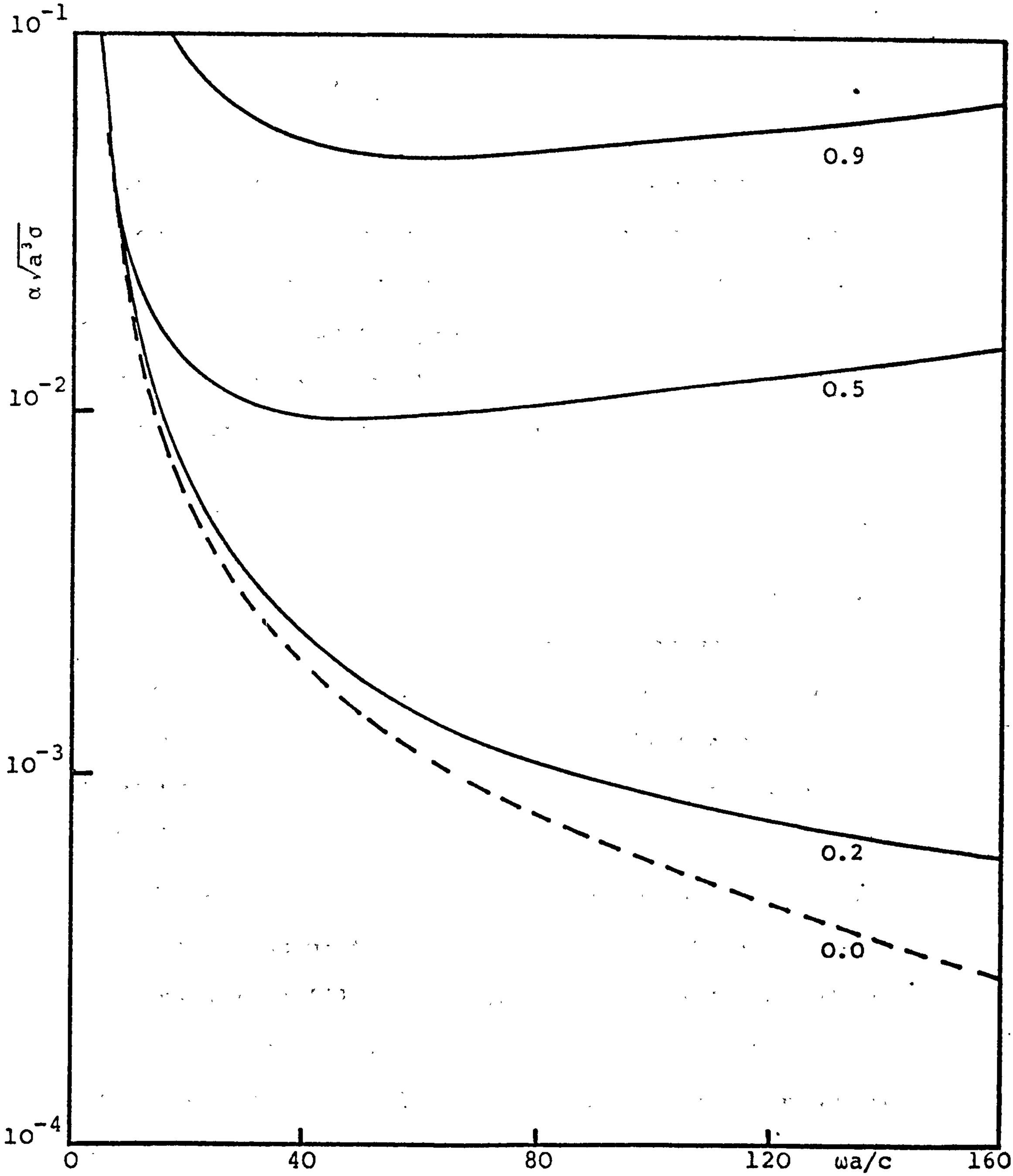

Figure (2.11) Attenuation characteristics of the TE_{c01} mode in an elliptical waveguide

Parameter (eccentricity)

However, for small values of e, an azimuthal magnetic field component will be present, in addition to the already existing axial component. The latter component maintains its decreasing property with increasing frequency, while the former component will have an increasing value with increasing frequency and becomes predominant for large eccentricities or higher frequencies. Thus the presence of the azimuthal magnetic component in the field of the TE_{c01} mode gives the mode its minimum attenuation property.

2.5.3 TE_{s11} Mode

The cut-off frequency for a number of odd modes is shown in Figure (2.2) by the dotted curves, where the non existence of zero order Mathieu function is clearly illustrated. This phenomenon reduces the number of odd modes present in the elliptical waveguide and opens up a possible use of odd modes.

In what follows the study of odd modes will be based on the assumption that the elliptical waveguide contains a mode filter, similar to the one described in the previous section, with its resistive sheet being along the minor axis of the waveguide, thus ensuring the suppression of the TE_{c11} mode.

Alternatively, the assumption that no cross coupling between the two modes will take place is implied. This is true for a perfectly made elliptical waveguide as the two modes will be stable <16>.

The normalised single mode bandwidth of the TE_{s11} mode is shown in Figure (2.7) by the dashed curve, where the upper frequency limit is set by the low frequency cut-off of the TE_{s21} mode for all the range of e. A substantial increase in the single mode bandwidth is observed as compared to the TE_{c11} mode, in particular for small values of e.

The attenuation characteristic of the TE_{s11} mode in copper waveguide with a = 0.0114m is shown in Figure (2.12) for different values of e. It is seen that as the circular waveguide is deformed into an elliptical waveguide, operating in the TE_{s11} mode, the point of minimum attenuation decreases in value and occurs at a higher frequency, until the eccentricity reaches a value of ∿0.5. Beyond this value of e the minimum attenuation point increases and reaches a maximum in the limit e → 1.

The invalidity of the conclusion reached by Kretzschmar <17>, when studying the TE_{s11} mode, that "at high frequencies the attenuation factor tends to be almost eccentricity independent and approximately equal to the attenuation factor of the TE_{11} mode", is clearly shown in Figure (2.12). Kretzschmar's results were terminated at a frequency where his conclusion applied. Figure (2.12) also shows the attenuation coefficient of the TE_{10} mode in a copper rectangular waveguide with dimensions comparable to those of an elliptical waveguide of 0.97 eccentricity. It is observed that at frequencies near cut-off the attenuation coefficient of the

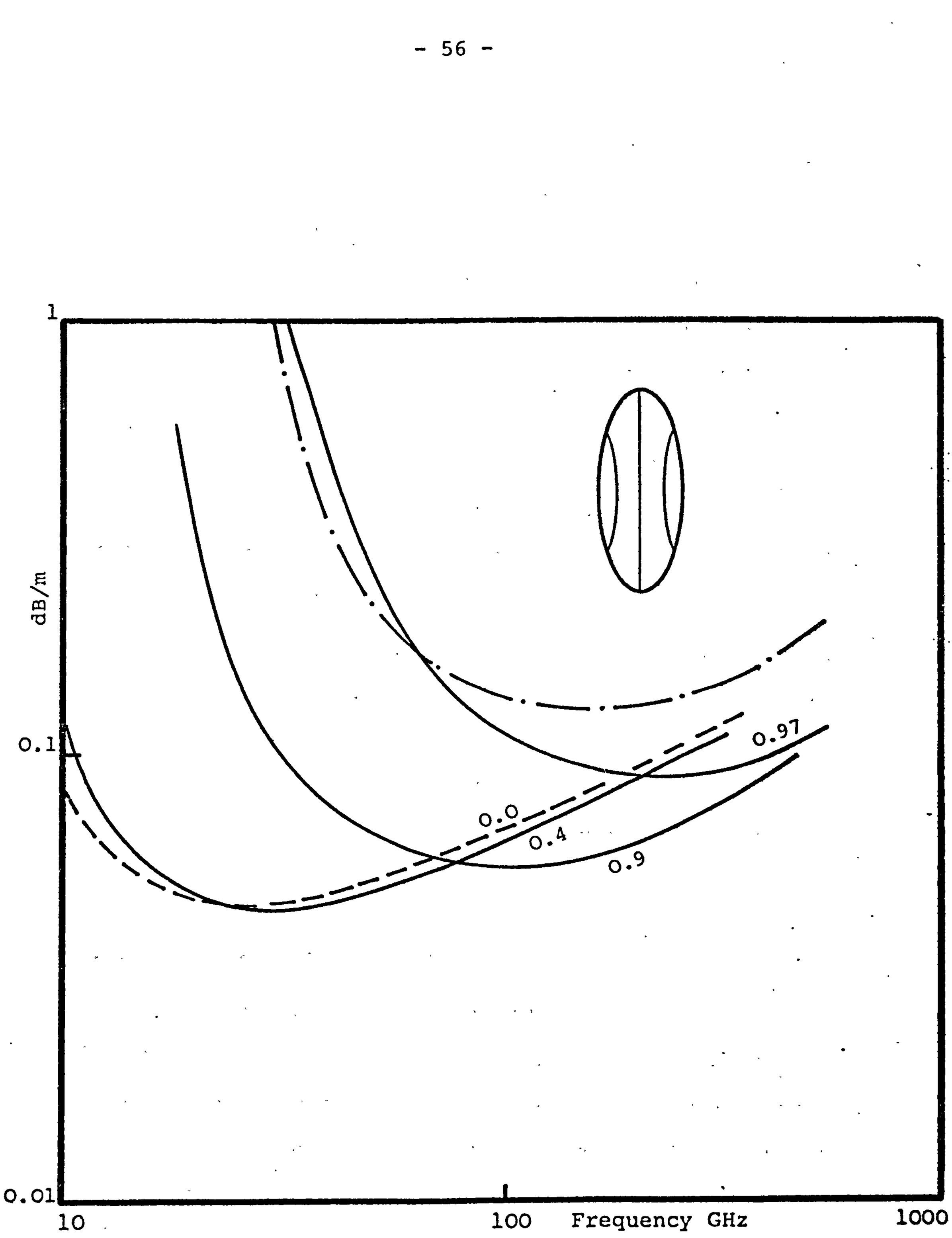

Figure (2.12) Attenuation characteristics of the TE_{s11} mode in an elliptical waveguide

a = 1.14cm $\sigma = 5.8 \times 10^7$ S/m

Parameter (eccentricity)

—.—.—.— TE_{10} mode in a rectangular waveguide

a = 0.554cm b = 2.28cm

rectangular waveguide is very close to that of an elliptical waveguide operating in the TE_{s11} mode, while at frequencies far from cut-off a significant difference is observed. At such high frequencies the power-loss contribution of the wall perpendicular to the electric field vector is substantial when compared with the vertical wall losses. Then, because the former wall of the elliptical waveguide considered in this example has a very small radius of curvature, the results obtained merely confirm the curvature-effect contribution to the attenuation coefficient.

On the other hand, at low frequencies the power-loss due to the wallparallel to the electric field vector is predominant and as this wall has a very large radius of curvature in the elliptical waveguide case, the two attenuation coefficients are seen to be very close.

2.5.4 Comparison of Modes

Neither physical nor mathematical explanations for the attenuation characteristics of the elliptical waveguide have appeared in the literature. An attempt will be made here to explain the characteristic when the elliptical waveguide is operated in dominant even or odd mode.

The power-loss components, in the TE_{c11} or TE_{s11} mode, are due to the axial and azimuthal magnetic field components. The normalised power-losses are

plotted in Figure (2.13) for the TE_{c11} mode, in a copper waveguide with a =0.0114m, for different values of e. It can be seen that as the circular waveguide is deformed the contributions due to both H_z and H_η components start to rise. The minimum attenuation point will occur at a frequency, f_m, when

$$\frac{\partial \hat{H}_z}{\partial f} = - \frac{\partial \hat{H}_\eta}{\partial f} \Bigg| \; f=f_m$$

where $\hat{H}_z$ and $\hat{H}_\eta$ are the normalised power-loss contributions due to H_z and H_η components respectively.

The derivative $\frac{\partial \hat{H}_z}{\partial f}$ is a negatively decreasing function of frequency, whereas $\frac{\partial \hat{H}_\eta}{\partial f}$ is a positively decreasing function. They have almost the same trend for different values of e as seen in Figure (2.13). Therefore the point of minimum attenuation is expected to appear at the same frequency for different values of e, and due to the increase in the values of $\hat{H}_z$ and $\hat{H}_\eta$, the attenuation coefficient must always be greater than that of the circular waveguide. This is illustrated in Figure (2.9).

The normalised power-losses for the TE_{s11} mode are plotted in Figure (2.14), for the same copper waveguide, with different values of e. It is observed that as the circular waveguide is deformed the contribution due to the $\hat{H}_z$ component starts to increase, while that due to the $\hat{H}_\eta$ component starts to DECREASE.

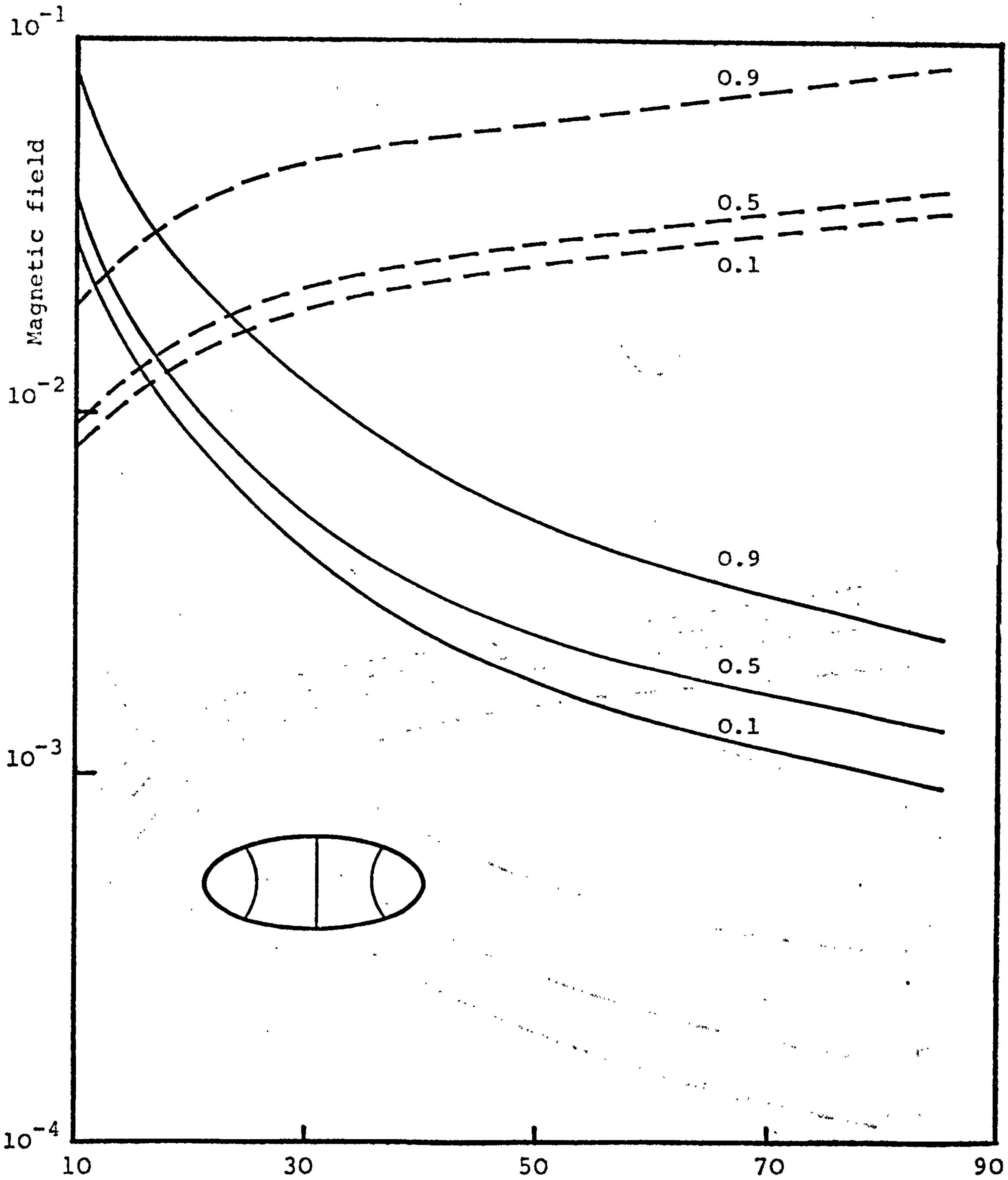

Figure (2.13) Magnetic field strength of the TE_{c11} mode against frequency

Parameter (eccentricity)

----- H_η ——— H_z

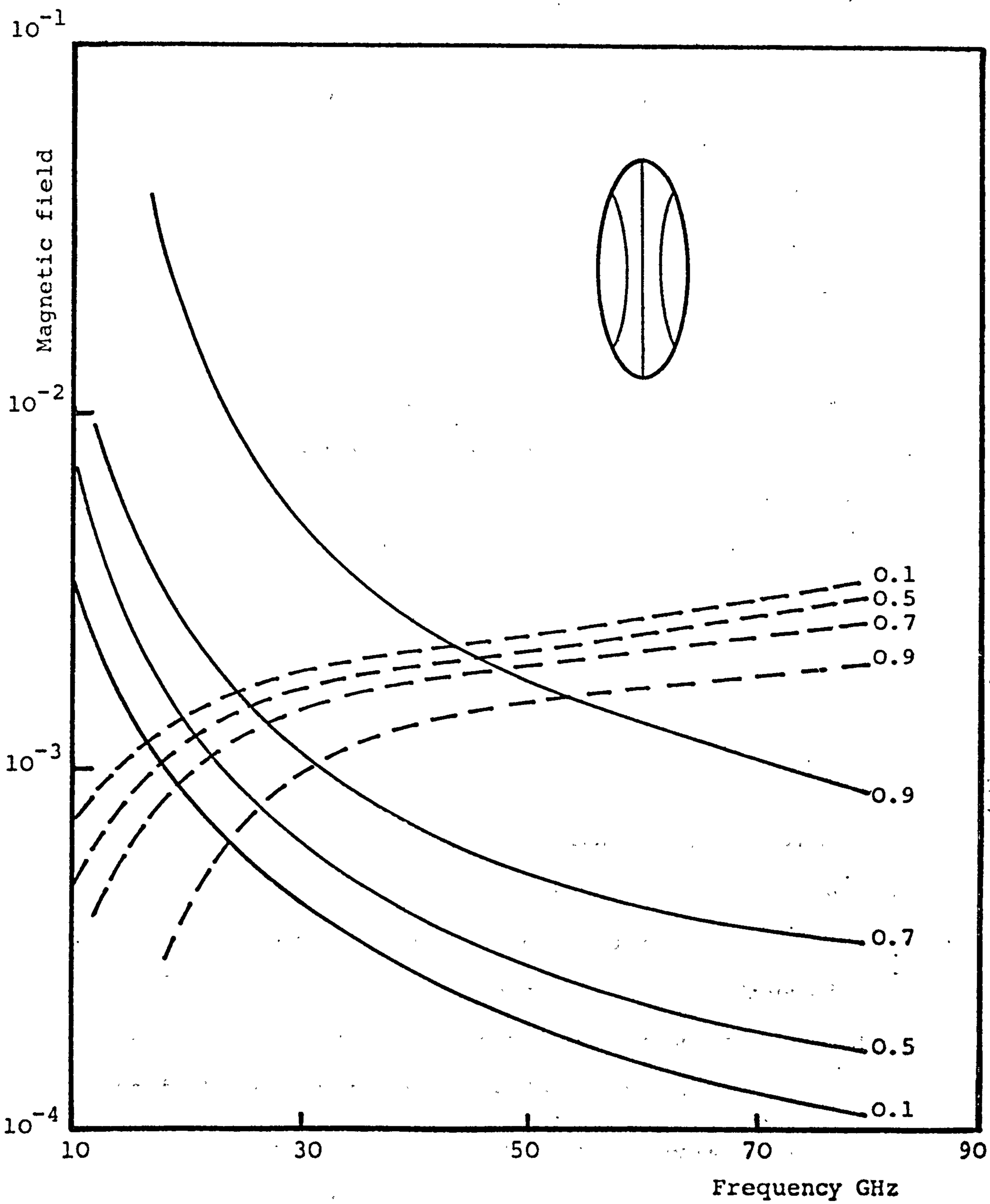

Figure (2.14) Magnetic field strength of the TE_{s11} mode against frequency

Parameter (eccentricity)

------ H_η ——— H_z

As the eccentricity is increased from ∿0.0, the value of the $\hat{H}_z$ component starts to increase at a slow rate until value of e ∿ 0.5. The change in the $\hat{H}_z$ component then becomes very sensitive to small changes in e, and this component becomes very pronounced for high eccentricities.

The decreasing minimum attenuation phenomenon of the TE_{s11} mode shown in Figure (2.12) can therefore be attributed to the decrease in the $\hat{H}_\eta$ component for small values of e. As the eccentricity rises the contribution of the $\hat{H}_z$ component becomes much more pronounced and thus an increase in the minimum attenuation point is expected.

The minimum attenuation point will occur at a frequency, f_m, when

$$\frac{\partial \hat{H}_z}{\partial f} = -\frac{\partial \hat{H}_\eta}{\partial f} \Bigg|_{f=f_m}$$

The two derivations will have the same nature as those of the even mode, but due to the substantial increase in the cut-off frequency of the odd mode, Figure (2.2), the trend of the curves is not the same for all values of e. Therefore, the point of minimum attenuation is expected to shift to higher frequencies for rising values of e.

Another interesting phenomenon appears when comparing the attenuation results for the TE_{c11} and TE_{s11} modes, Figures (2.9) and (2.12). Above certain frequencies, the attenuation coefficient of the TE_{s11} mode becomes smaller than the attenuation of the

TE_{c11} mode. The same phenomenon occurs in a rectangular waveguide when the attenuation of the TE_{01} mode becomes smaller than the attenuation of the dominant TE_{10} mode in the same waveguide for frequencies larger than a certain fixed frequency which depends on the ratio of the two sides.

*2.6 THE EFFECT OF SURFACE CURVATURE

2.6.1 Surface Curvature Formulas

The results of section (2.4.3) refer only to the elliptic cross-section. The reason why surface curvature - or, more accurately, variations in surface curvature, - might affect the surface impedance is discussed qualitatively in the next section. Here we shall attempt to express the curvature-dependent factor in terms independent of the ellipse parameters in the expectation that the result could be more general, and would apply to surfaces of other than elliptical cross-section.

Defining $M = (1-e^2\cos^2\eta)^{\frac{1}{2}}$, we note that the radius of curvature R at any point of the ellipse can be obtained from the well-known relation $R = \{1+(dy/dx)^2\}^{3/2}/(d^2y/dx^2)$.

For the ellipse this gives, after a little simplification,

$$R = a^2M^3/b \qquad \{2.34\}$$

This relation removes the explicit variation of M with η,

* Section 2.6 is essentially a transcript from a joint paper <30> involving Professor L. Lewin and the author.

expression it in terms of the local curvature. We choose the first and second gradient of radius of curvature to obtain two more relations to remove the parameters a and b. We have, on the contour,

$$\frac{\partial}{\partial s} = \frac{1}{(\partial s/\partial \eta)} \frac{\partial}{\partial \eta} = \frac{1}{aM} \frac{\partial}{\partial \eta}$$

whence the first gradient of radius of curvature can be written;

$$\partial R/\partial s = (3ae^2/2b)\sin 2\eta$$

Using this result it is readily verified that

$$M^2(1-M^2)a^2/b^2 = 1-M^2+(\partial R/\partial s)^2/9 \qquad \{2.35\}$$

The second gradient of radius of curvature gives

$$\partial^2 R/\partial s^2 = (3e^2/bM)\cos 2\eta$$

from which

$$R\partial^2 R/\partial s^2 = 3M^2[1+(1-2M^2)a^2/b^2] \qquad \{2.36\}$$

Eliminating a/b from {2.35} and {2.36} gives a quadratic in M. Choosing the sign of the square root so that $M^2 \leq 1$ for the ellipse gives, finally,

$$M=\sqrt{1+\frac{1}{9}\left(\frac{\partial R}{\partial s}\right)-\frac{R}{6}\frac{\partial^2 R}{\partial s^2}-\left(\frac{1}{9}\left(\frac{\partial R}{\partial s}\right)^2+\left[\frac{1}{9}\left(\frac{\partial R}{\partial s}\right)^2-\frac{R}{6}\frac{\partial^2 R}{\partial s^2}\right]^2\right)^{\frac{1}{2}}} \qquad \{2.37\}$$

In this form, only the local properties of the surface are involved. For both the circular cross-section and for flat plates, $\partial R/\partial s = 0$ and $M = 1$, the familiar case. However, {2.37} cannot represent a unique relationship because use could also have been made of higher order derivatives, leading to an unlimited number of possible forms. Although {2.37} seems to be the simplest of these, unfortunately it has the sole merit of giving the correct form for the flat plate, circle and elliptic shapes. For a parabolic shape $y = Ax^2$, {2.37} gives identically zero, so it cannot be the sought-for generalisation. Changing the sign of the inner square root does not help matters either, and it has to be concluded that a generalisation of {2.27} to other than elliptic shapes, and based solely on local properties has yet to be found. But if there is a genuine curvature effect it will necessarily involve higher order differentiations than the second.

2.6.2 A Qualitative Examination of the Curvature Effect

It is unlikely that a straightforward explanation of any such formulas as {2.27} or {2.37} will be readily forthcoming. What is interesting is that the curvature variations can apparently give a substantial, zero-order, correction to the flat-surface impedance formula, a result that microwave engineers, accustomed to working with the perturbation method of attenuation calculation, may find rather surprising, and not in accord with their

intuitive understanding of the process. After all, the wave only penetrates a minute distance, of the order of a few skin-depths, into the metal. How can the curvature of the surface, unless it is correspondingly large, as at a sharp corner, enter into the calculations? This section attempts a qualitative approach to this question, at least to the point of indicating that a zero-order correction might be reasonably expected.

Figure (2.15) shows the orthogonal contours, η = constant, to the ellipse, and we can assume that the propagation in the metal occurs along the direction of these flow lines. Far away from the contour the propagation is radial, but close in it is along curved paths which diverge non-uniformly from each other. Both the curvature and the divergence seem relevant, though uniform divergence, as with the radii of a circle, does not contribute to the effect under study. We shall try and indicate here how a uniform curvature of the flow lines, without divergence, may be expected to have a substantial effect. Although the contours in Figure (2.15) are not of this character, the demonstration of a zero-order effect should give some confidence in the reality of the curvature effects in the ellipse.

Suppose a curved contour to be subdivided, as in Figure (2.16), with a segment of length d, from which propagation into the metal wall takes place along a curved path of constant curvature radius R_o. Such a propagation

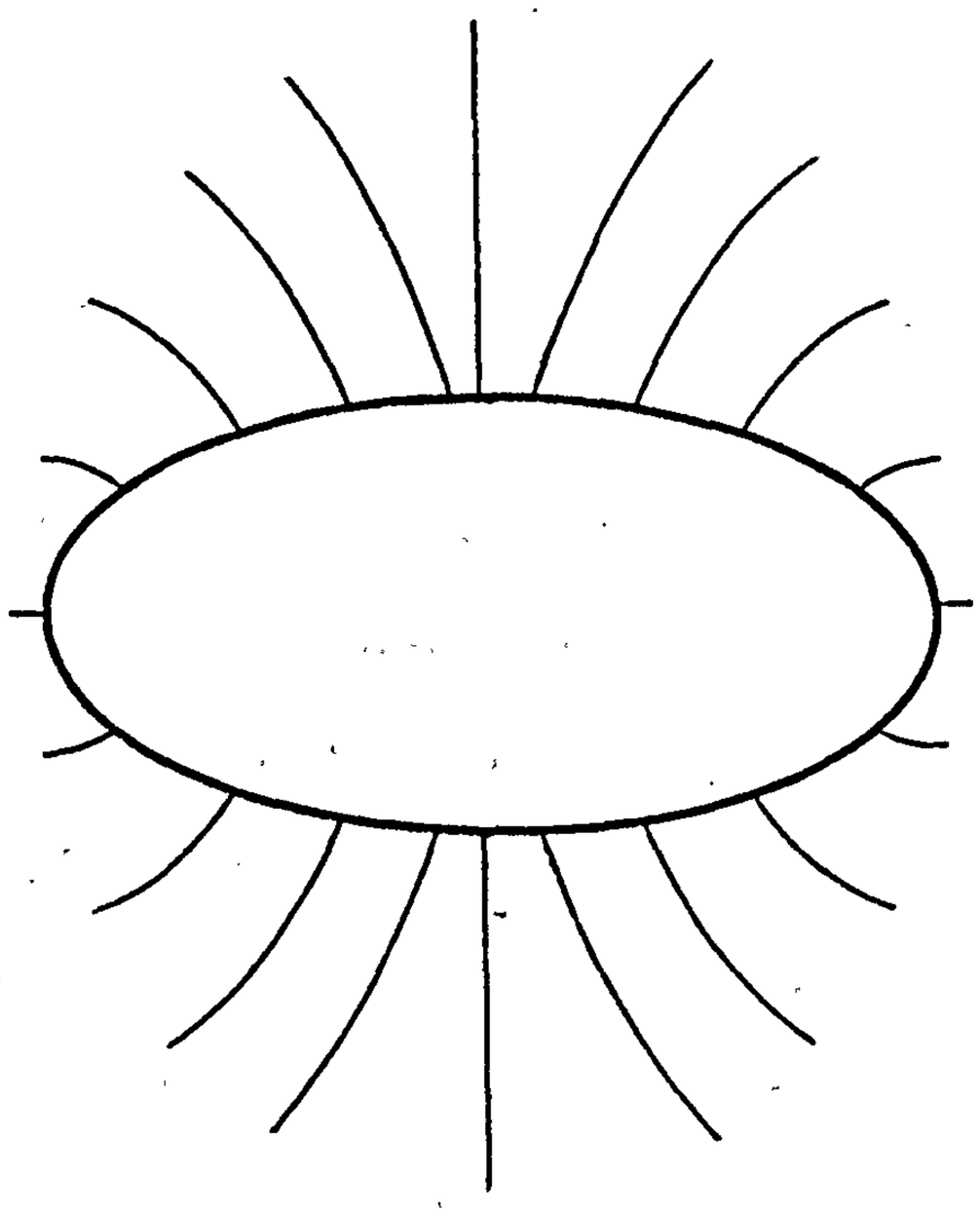

Figure (2.15) Flow contours in the waveguide wall

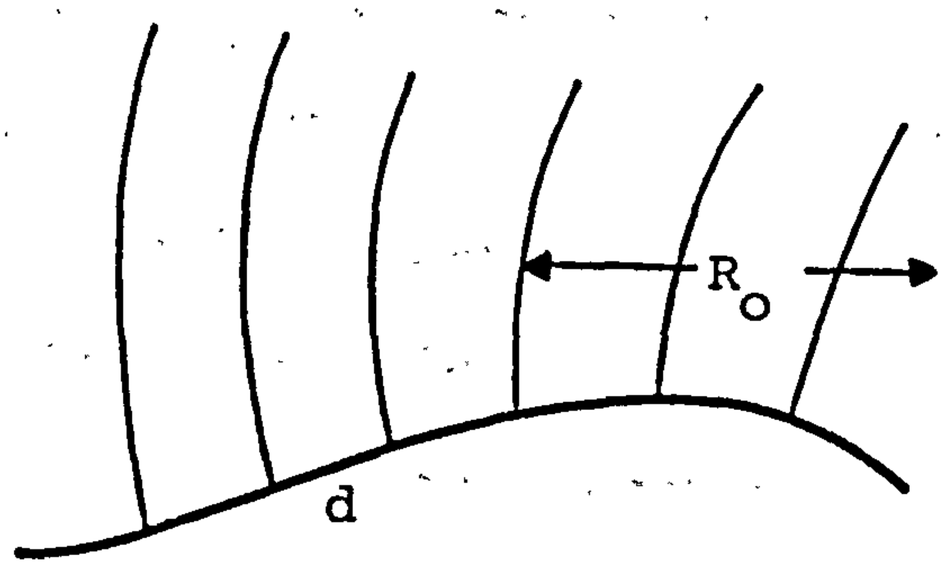

Figure (2.16) Flow from contour segment

would be closely similar to propagation of a dominant TE mode in a curved waveguide of breadth d. The analysis of this configuration <31> indicates a first-order correction (in d/R_o) to the dominant mode form, via the appearance of an axial electric field component of order of magnitude $k_2^2 d^2/\bar{\varepsilon}_2 k R_o$, where $\bar{\varepsilon}_2 = -j60\lambda\sigma$, and $k_2 = k\bar{\varepsilon}_2^{\frac{1}{2}}$ is inversely proportional to the skin depth δ. Continuity of the normal component of the electric displacement therefore requires a corresponding normal component of electric field in the hollow guide of order of magnitude $k_2^2 d^2/k R_o$ due to this cause. If we assume that the wave in the metal is effectively extinguished in a distance of a few skin depths and that d should be large enough to substantially support a plane wave over this distance, then we need $d = n\delta$ where n is at least unity, and may be of the order of, say, 5 or more. Since R_o will be of the order of the guide dimensions, and therefore comparable to λ_o, it is clear that the induced normal component of field into the guide is far from negligible. Perhaps another way of putting this conclusion is to say that the path curvature in the metal introduces an effect as from a slight tilt in the wave direction there, and because of the high permittivity in the metal, the laws of refraction at a boundary require a zero-order change in the direction of an incoming wave to correspond to this small effective tilt.

Although far from rigorous, this approach does indicate the possibility of substantial curvature effects, via the emergence of a non-negligible component of normal electrical displacement.

2.6.3 Discussion

The unfamiliar and rather recondite properties of the Mathieu functions clearly add to the difficulties of correctly analysing the elliptic configuration. The requirement that the axial surface impedance at the broad wall of an elongated ellipse approach the known value for the parallel plate case must be considered over-riding for use as a check point for any formulas derived. The corrected formulas of this section do satisfy this criterion, though the ensuing discussion on the properties of Mathieu functions of complex argument does leave something to be desired.

An effect which is here interpreted as a curvature-dependent effect survives the present corrections, and must be assumed to be a genuine phenomenon, surprising though its presence may seem. It would be desirable to produce an independent and at least semi-quantitative support for the basic formulas {2.27} and {2.28}. A generalisation to achieve what {2.37} failed to achieve is highly desirable if, indeed, it is possible. Presumably an analysis of an ellipsoidal resonator could introduce yet a further curvature factor, arising from the curvature in the perpendicular plane. Clearly the

standard perturbation method rests on rather shaky ground and engineers using it for other than the simplest shapes have presumably been oblivious of the need for the entry of these curvature factors into their calculations.

CHAPTER THREE

CORRUGATED ELLIPTICAL WAVEGUIDES

3.1 INTRODUCTION

In the previous chapter it is shown that, for the even and odd TE_{11} modes, the power-loss contribution due to the azimuthal (η) magnetic field component is much more significant than that due to the axial magnetic field component. Clearly, if the H_η term could be removed near the wall or made proportional to the longitudinal component of the field at the metal boundary, then lower power-losses are expected. Since an H_η field component requires a longitudinal wall current, we seek to annul this component without disturbing the peripheral current required to support the longitudinal magnetic field component. Evidence in favour of this surmise was demonstrated by Clarricoats and Saha <1>, when investigating the characteristics of a circular waveguide containing corrugations transverse to the direction of propagation, Figure (4.1). The circular structure satisfies the above condition when the slot depth is such that the electric length transfers the short-circuit termination at the outer slot boundary to an open-circuit (magnetic wall) at the boundary of the propagation region. This condition implies a slot depth of one quarter wavelength.

In this chapter, the concept is extended to waveguides with non-circular cross-sections. The principle can most easily be investigated for elliptical and rectangular waveguides. The elliptical

waveguide with modified wall will be first considered in this chapter and in the latter part of the thesis the concept is extended to the rectangular structure. Formulation of the characteristics equation of the corrugated elliptical waveguide leads to mathematical and computational difficulties, arising from the nature of the Mathieu functions required to represent the field components. It is believed that for these reasons no attempt has been made to analyse the elliptical waveguide with modified boundaries. Krank<32> analysed the helical elliptical waveguide, by assuming that the field perturbation in the waveguide grooves is sufficiently small so that the results differ only slightly from those obtained for the smooth wall elliptical waveguide.

In this chapter, solutions of the wave equation are obtained in the two regions ($0 < \xi_1 < \xi$) and ($\xi_1 < \xi < \xi_2$) shown in Figure (3.1). The form of the characteristic equation obtained using a space-harmonic representation of the field is rather complicated and, when the computer time-factor is considered, is unsuitable for present day computers. The form of the characteristic equation employed in obtaining the results presented in this chapter, is derived using only the fundamental harmonic of the modes supported by the structure. The dispersion and attenuation characteristics of different modes are illustrated in this chapter, and excellent agreement is obtained between the circular corrugated waveguide results and those obtained when the

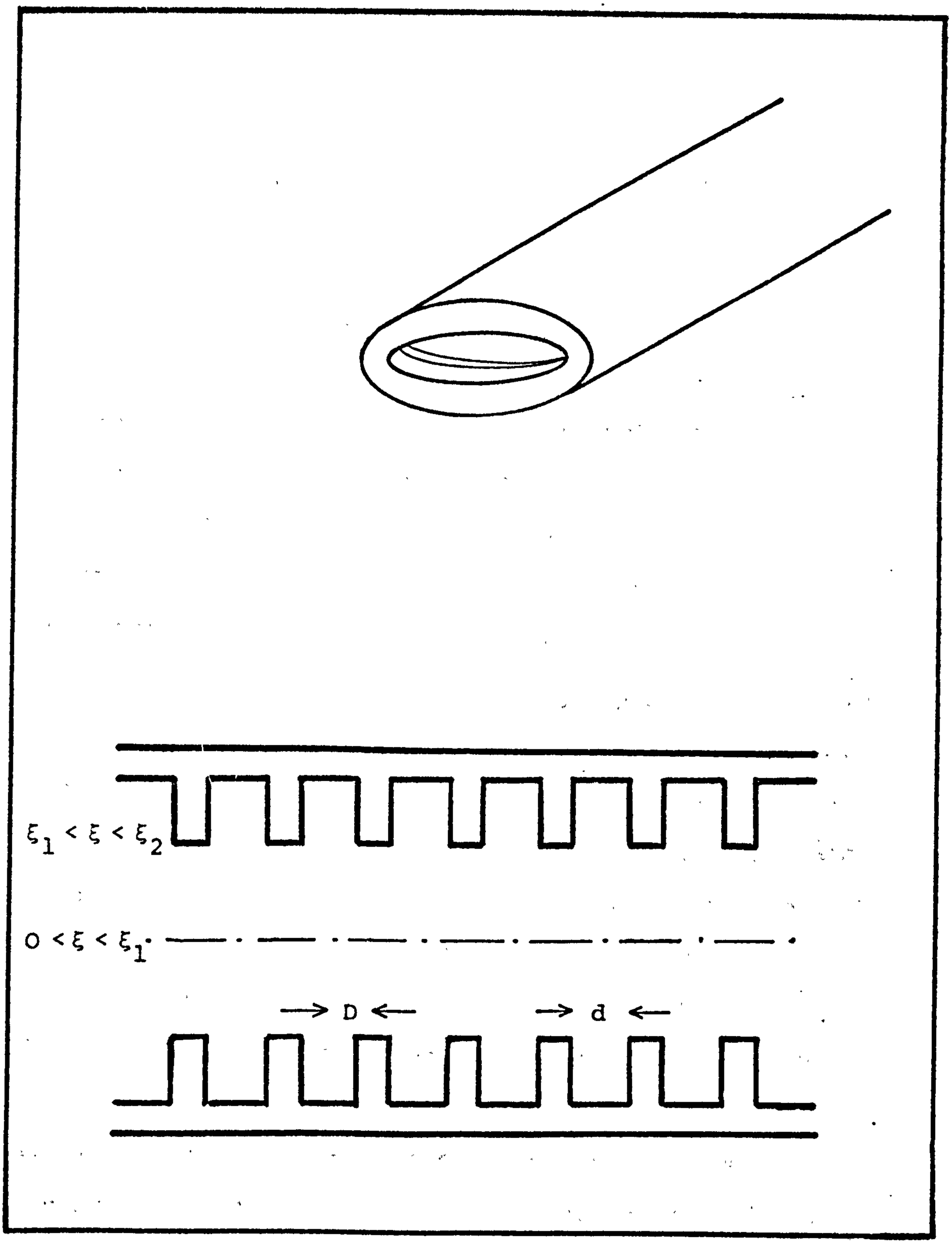

Figure (3.1) Elliptical corrugated waveguide

Region $0 < \xi < \xi_1$ major axis $2a_1$, minor axis $2b_1$, eccentricity e_1

Region $\xi_1 < \xi < \xi_2$ major axis $2a_2$, minor axis $2b_2$, eccentricity e_2

elliptical corrugated waveguide is re-formed into a circular shape. Mode classifications are proposed to follow the classifications employed in the circular corrugated waveguide.

3.2 FIELD COMPONENTS

To obtain the propagation and attenuation characteristics of the elliptical corrugated waveguide, the structure is divided into two regions;

(i) a central region ($0 < \xi < \xi_1$) and

(ii) an outer slot region ($\xi_1 < \xi < \xi_2$), where standing waves are assumed to exist, Figure (3.1).

Solutions of the wave equation {2.4} are obtained independently in the two regions in terms of either even or odd Mathieu function. Appropriate boundary conditions are then applied to ensure the continuation of the field across the boundary between the two regions. In the previous chapter it is shown that there are two independent solutions to the wave equation in the elliptical co-ordinate system, giving rise to even and odd TE modes or TM modes. In the corrugated structure studied in this chapter, the existence of the two independent solutions of the wave equation is implied. However, the presence of the second region, which introduces an anisotropic boundary, will always couple the pure TE mode and TM mode supported by the smooth wall structure. Notations and classifications of the hybrid modes in the corrugated structure are given in

section (3.6). Modes whose axial magnetic field component is represented by even Mathieu functions are considered in this section, and the theory is extended to the second type of modes at the end of the section. The axial field components of the hybrid modes considered have the form;

$$
\begin{aligned}
{}_1E_z &= \sum_{v} \sum_{m=-\infty}^{\infty} B_{vm}\, Se_v(q_{1m},\xi)\, se_v(q_{1m},\eta)\, e^{-j\beta_m z} \quad \dagger \\
{}_1H_z &= Y_o \sum_{v} \sum_{m=-\infty}^{\infty} A_{vm}\, Ce_v(q_{1m},\xi)\, ce_v(q_{1m},\eta)\, e^{-j\beta_m z}
\end{aligned}
\qquad \{3.1\}
$$

in the inner region, $0 < \xi < \xi_o$, $2\pi \geq \eta \geq 0$ and $-\infty > z > +\infty$. In the slot region, the axial field components have the form;

$$
\begin{aligned}
{}_2E_z &= \sum_{r} \sum_{\mu=0}^{\infty} L_{r\mu}\, \P_r(q_{2\mu},\xi_2,\xi)\, se_r(q_{2\mu},\eta)\cos\Gamma_\mu z \\
&\quad + \sum_{r} \sum_{\mu=1}^{\infty} L'_{r\mu}\, \P_r(q'_{2\mu},\xi_2,\xi)\, se_r(q'_{2\mu},\eta)\sin\Gamma'_\mu z \\
{}_2H_z &= Y_o \sum_{r} \sum_{\mu=1}^{\infty} P_{r\mu}\, \Xi_r(q_{2\mu},\xi_2,\xi)\, ce_r(q_{2\mu},\eta)\sin\Gamma_\mu z \\
&\quad + Y_o \sum_{r} \sum_{\mu=1}^{\infty} P_{r\mu'}\, \Xi_r(q_{2\mu'},\xi_2,\xi)\, ce_r(q_{2\mu'},\eta)\cos\Gamma_\mu' z
\end{aligned}
\qquad \{3.2\}
$$

for $0 \leq |z-iD| \leq d/2$

and for $d/2 \leq |z-iD| \leq D/2$ $\quad {}_2E_z = 0 = {}_2H_z$

$i = 0, 1, 2, \text{---}.$

† Throughout this chapter the notation MF(q,η or ξ) is used instead of the notation MF(η or ξ,q) employed in chapter two, where MF denotes the Mathieu function.

The following notations have been used in the above expressions.

$$4q_{1m} = h^2(\omega^2\varepsilon_o\mu_o - \beta_m^2) \qquad 4q_{2\mu} = h^2(\omega^2\varepsilon_o\mu_o - \Gamma_\mu^2)$$

$$4q_{2\mu}' = h^2(\omega^2\varepsilon_o\mu_o - \Gamma_\mu'^2)$$

where

$$\Gamma_\mu = \frac{2\pi\mu}{d} \qquad (\mu = 0, 1, 2, - - -)$$

$$\Gamma_\mu' = \frac{\pi}{d}(2\mu - 1) \quad (\mu = 1, 2, 3, - - -)$$

β_m is the phase-change coefficient of the (m+1)th spatial harmonic and is related to the phase-change coefficient of the fundamental harmonic , by the relationship

$$\beta_m = \beta + \frac{m\pi}{D}$$

B, A, L, L', P and P' are amplitude coefficients and the factors ¶ and Ξ are defined below;

$$¶_i(q,\xi_2,\xi) = \frac{Se_i(q,\xi)GeY_i(q,\xi_2) - Se_i(q,\xi_2)GeY_i(q,\xi)}{GeY_i(q,\xi_2)} \qquad \{3.4\}$$

$$\Xi_i(q,\xi_2,\xi) = \frac{Ce_i(q,\xi)Fe'\,Y_i(q,\xi_2) - Ce_i'(q,\xi_2)FeY_i(q,\xi)}{FeY_i(q,\xi_2)} \qquad \{3.5\}$$

The prime means first derivative of the function with respect to ξ, and the factor expj(ωt) is assumed throughout.

In {3.1} and {3.2} the summation is carried out over the eigenfunctions (v, r are the number of the eigenfunctions). The solutions of the wave equation written in the form {3.1}, {3.2}, satisfy the boundary conditions at the lateral sides of the slots;

$$E_\xi = 0 = E_\eta$$

where E_ξ and E_η are derived using Appendix 1. Applying the boundary conditions;

$$\begin{aligned} {}_1E_z &= {}_2E_z', & {}_1H_z &= {}_2H_z', \\ {}_1E_\eta &= {}_2E_\eta', & {}_1H_\eta &= {}_2H_\eta \end{aligned} \qquad \{3.6\}$$

for $\xi = \xi_1$, $2\pi \geq \eta \geq 0$ and $+\infty > z > -\infty$,

the characteristic equation of the elliptical corrugated waveguide is then obtained.

The form of the characteristic equation will be similar to that of the corrugated circular waveguide <4>, but of a more complicated nature. The complexity arises due to the presence of the angular Mathieu functions, which are not only functions of η, the angular co-ordinate, but also of the electrical properties of the medium in which they apply. In order to simplify the form of the characteristic equation and for practical computations, the first spatial harmonic will only be used to represent the field components in the inner region of the waveguide. This assumption implies that the field is

constant within the slots along the axis of the waveguide. This assumption has a real physical basis, since the condition $\lambda >> d(\lambda=2\pi/\beta)$ is satisfied fairly well in the waveguide.

Under this approximation the field components in the inner region have the form;

$$_1E_z = \sum_{v=0} B_v Se_v(q_1,\xi)se_v(q_1,\eta)$$

$$_1H_z = Y_o \sum_{v=1} A_v Ce_v(q_1,\xi)ce_v(q_1,\eta)$$

$$_1E_\eta = -j\frac{\beta}{\ell K^2} \sum_v B_v Se_v(q_1,\xi)se_v'(q_1,\eta)$$

$$+j\frac{k}{\ell K^2} \sum_v A_v Ce_v'(q_1,\xi)ce_v(q_1,\eta)$$

$$_1H_\eta = -j\frac{\omega\varepsilon_o}{\ell K^2} \sum_v B_v Se_v'(q_1,\xi)se_v(q_1,\eta)$$

$$-j\frac{\beta Y_o}{\ell K^2} \sum_v A_v Ce_v(q_1,\xi)ce_v'(q_1,\eta)$$

$$_1E_\xi = -j\frac{\beta}{\ell K^2} \sum_v B_v Se_v'(q_1,\xi)se_v(q_1,\eta)$$

$$-j\frac{k}{K^2} \sum_v A_v Ce_v(q_1,\xi)ce_v'(q_1,\eta)$$

$$_1H_\xi = j\frac{\omega\varepsilon_o}{\ell K^2} \sum_v B_v Se_v(q_1,\xi)se_v'(q_1,\eta)$$

$$-j\frac{\beta Y_o}{\ell K^2} \sum_v A_v Ce_v'(q_1,\xi)ce_v(q_1,\eta) \qquad \{3.7\}$$

The factor $\exp j(\omega t-\beta z)$ is assumed throughout.

The field components ${}_2H_z$, ${}_2E_\xi$ and ${}_2E_\eta$ are zero at the lateral metal sides of the slots, and therefore the assumption made above does not permit their existence in the slot region. An analogy can be drawn between the above null components and the null field components in the slots of a circular corrugated waveguide <33>, viz. ${}_2H_z$, ${}_2E_\theta$ and ${}_2E_r$.

The remaining field components are therefore;

$$
\begin{aligned}
{}_2E_z &= \sum_{r=1} L_r \P_r(q_2,\xi_2,\xi)se_r(q_2,\eta) \\
{}_2H_\eta &= j\frac{\omega\varepsilon_o}{\ell k^2} \sum_r L_r \P_r'(q_2,\xi_2,\xi)se_r'(q_2,\eta) \\
{}_2H_\xi &= j\frac{\omega\varepsilon_o}{\ell k^2} \sum_r L_r \P_r(q_2,\xi_2,\xi)se_r'(q_2,\eta) \qquad \{3.8\}
\end{aligned}
$$

where $4q_1 = h^2(k^2-\beta^2)$, $4q_2 = h^2k^2$, $k^2 = \omega^2\varepsilon_o\mu_o$ and ℓ is the first or second metric coefficient defined in {2.2}. The factor expj(ωt) is assumed, and the prime here denotes the first derivative with respect to either ξ or η.

3.3 BOUNDARY CONDITIONS

The boundary condition {3.6} that the tangential components of the electric and magnetic field must be continuous across the boundary $\xi = \xi_1$ will be utilised to obtain the characteristic equation under the above assumption. In order to illustrate the difficulties encountered in satisfying the above boundary conditions for the elliptical corrugated waveguide, the case of the

circular corrugated waveguide will be illustrated first.

The axial electric field component in the inner region has the form

$$_1E_z = \sum_{n=0}^{\infty} B_n J_n(K_1 r)\cos(n\theta)\, e^{-j\beta z}$$

and in the slot region

$$_2E_z = \sum_{n=0}^{\infty} L_n \Phi_n(kr_2, kr)\cos(n\theta)$$

where the function ϕ_n is a combination of the ordinary and modified Bessel functions of the n-th order. Making use of the assumption that the field is invariant with respect to the z-direction at the corrugation edge $r = r_1$, Figure (4.1), then the boundary conditions {3.6} yield

$$\sum_n B_n J_n(K_1 r_1)\cos(n\theta) = \sum_n L_n \Phi_n(kr_2, kr_1)\cos(n\theta) \qquad \{3.9\}$$

for $2\pi \geq \theta \geq 0$ and $-\infty \leq z \leq \infty$

Multiplying both sides of {3.9} by $\cos(m\theta)$ and integrating with respect to θ from 0 to 2π, and making use of the orthogonality of the trigonometric functions, {3.9} yields

$$B_m J_m(K_1 r_1) = L_m \Phi_m(kr_2, kr_1) \qquad \{3.10\}$$

It should be noted that for each mode (in this case for each m) there should be only one propagation coefficient, for a particular root of the characteristic equation. Equation {3.10} shows that the boundary conditions may be

satisfied for each m separately, due to the orthogonality in θ of the fundamental solutions and the fact that the angular functions $\cos(n\theta)$ or $\sin(n\theta)$ are independent of the characteristics of the medium. When representing the fields in the corrugated elliptical waveguide, the summation sign over the eigen-numbers (v and r) must not be deleted, otherwise a corresponding equation to {3.10} containing the η dependance will be obtained, i.e.

$$B_m Ce_m(q_1,\xi)ce_m(q_1,\eta) = L_m \P_m(q_2,\xi_1,\xi_2)ce_m(q_2,\eta) \quad \{3.11\}$$

where $ce_m(q_1,\eta)$ and $ce_m(q_2,\eta)$ are functions of η. The only way that equation {3.11} can be satisfied is by assuming that

$$ce_m(q_1,\eta) = ce_m(q_2,\eta)$$

which is not true except when the eccentricity is zero.

3.4 THE CHARACTERISTIC EQUATION

In order to obtain the dispersion characteristics of the elliptical corrugated waveguide, it is necessary to solve the characteristic equation relating ω and β. The non-existence of the field components H_z, E_ξ and E_η in the slot region of the waveguide implies the following boundary conditions; at $\xi = \xi_1$

$$ {}_1E_z = {}_2E_z $$

$$ {}_1H_\eta = {}_2H_\eta \qquad \{3.12\} $$

and

$$ {}_1E_\eta = 0 $$

for $2\pi \geq \eta \geq 0$ and $+\infty > z > -\infty$.

Substituting the appropriate field components from {3.7} and {3.8} in the boundary conditions {3.12} the following relationships are obtained;

$$ E_\eta \rightarrow $$

$$ \bar{\beta} \sum_{v=1} B_v Se_v(q_1,\xi_1) se_v'(q_1,\eta) = \sum_{v=1} A_v Ce_v'(q_1,\xi_1) ce_v(q_1,\eta) $$

$$ \{3.13\} $$

In order to eliminate the η dependence, the expansion

$$ se_v'(q_1,\eta) = \sum_{\mu=0}^{\infty} \alpha_{v,\mu} ce_\mu(q_1,\eta) $$

where

$$ \alpha_{v,\mu} = \int_0^{2\pi} se_v'(q_1,\eta) ce_\mu(q_1,\eta) d\eta / \int_0^{2\pi} ce_\mu^2(q_1,\eta) d\eta $$

is used in {3.13} to obtain

$$ \bar{\beta} \sum_{v=1} \sum_{\mu=0} B_v Se_v(q_1,\xi_1) ce_\mu(q_1,\eta) \alpha_{v,\mu} = \sum_{v=1} A_v Ce_v'(q_1,\xi_1) ce_v(q_1,\eta) \qquad \{3.14\} $$

Multiplying both sides of {3.14} by $ce_n(q_1,)$ and integrating with respect to η between 0 and 2π, leads to

$$\bar{\beta} \sum_{v=1} B_v Se_v(q_1,\xi_1)\alpha_{v,n} = A_n Ce_n'(q_1,\xi_1) \qquad \{3.15\}$$

where $\bar{\beta} = \beta/k$.

$E_z \rightarrow$

$$\sum_{v=1} B_v Se_v(q_1,\xi_1)se_v(q_1,\eta) = \sum_{v=1} L_v \P_v(q_2,\xi_1,\xi_2)se_v(q_2,\eta) \qquad \{3.16\}$$

using the expansion

$$se_v(q_1,\eta) = \sum_{\mu=1}^{\infty} \theta_{v,\mu} se_\mu(q_2,\eta)$$

where

$$\theta_{v,\mu} = \int_0^{2\pi} se_v(q_1,\eta)se_\mu(q_2,\eta)d\eta \Big/ \int_0^{2\pi} se_\mu^2(q_2,\eta)d\eta \qquad \{3.17\}$$

and following the same procedure above, {3.16} leads to

$$\sum_{v=1} B_v Se_v(q_1,\xi_1)\theta_{v,n} = L_n \P_n(q_2,\xi_1,\xi_2) \qquad \{3.18\}$$

$H_\eta \rightarrow$

$$\sum_{v=1} B_v Se_v'(q_1,\xi_1)se_v(q_1,\eta) + \bar{\beta} \sum_{v=1} A_v Ce_v(q_1,\xi_1)ce_v'(q_1,\eta)$$

$$= \left(\frac{K}{k}\right)^2 \sum_{v=1} L_v \P_v'(q_2,\xi_1,\xi_2)se_v(q_2,\eta) \qquad \{3.19\}$$

The expansion

$$ce_v'(q_1,\eta) = \sum_{\mu=1}^{\infty} \delta_{v,\mu} se_\mu(q_2,\eta)$$

where

$$\delta_{v,\mu} = \int_0^{2\pi} ce_v'(q_1,\eta) se_\mu(q_2,\eta)\,d\eta \Big/ \int_0^{2\pi} se_\mu^2(q_2,\eta)\,d\eta$$

and {3.17} are used in {3.19} to give

$$\sum_{v=1} B_v \left[Se_v'(q_1,\xi_1) - \left(\frac{K}{k}\right)^2 \frac{\P_n'(q_2,\xi_1,\xi_2)}{\P_n(q_2,\xi_1,\xi_2)} Se_v(q_1,\xi_1) \right] \theta_{v,n}$$

$$+ \bar{\beta} \sum_{v=1} A_v Ce_v(q_1,\xi_1)\delta_{v,n} = 0 \qquad \{3.20\}$$

where the coefficient L_n has been eliminated using {3.18}. Substituting in {3.20} for the coefficient A_v from {3.15} leads to

$$\sum_{v} B_v \left[Se_v'(q_1,\xi_1) - \left(\frac{K}{k}\right)^2 \frac{\P_n(q_2,\xi_1,\xi_2)}{\P_n(q_2,\xi_1,{}_2)} Se_v(q_1,\xi_1) \right] \theta_{v,n}$$

$$+ \bar{\beta}^2 \sum_{v} \sum_{r} B_v Se_v(q_1,\xi_1) \frac{Ce_r(q_1,\xi_1)}{Ce_r'(q_1,\xi_1)} \alpha_{v,r}\delta_{r,n} = 0 \qquad \{3.21\}$$

Equation {3.21} can be written in the form

$$\sum_{v}' B_v \nabla_{n,v} = 0 \qquad \{3.22\}$$

for n = 2, 4, 6, - - -

or n = 1, 3, 5, - - -

where $\nabla_{n,v}$ is given in {3.21}.

It is noted that in equations {3.15} through {3.22} when n is odd, the series are summed over all odd values of v, and when n is even, the series are summed over all even values of v. This is due to properties of the Mathieu functions. Equations {3.22} form a set of infinite homogeneous linear algebraic equations in the coefficients B_v. For a non-trivial solution, the determinant of these equations must vanish. The roots of this infinite determinant provide the values from which the phase-change coefficient, β, can be determined. The infinite determinant for the modes considered, summing over odd values of v, is

$$\begin{vmatrix} \nabla_{11} & \nabla_{13} & \nabla_{15} & \cdot & \cdot & \cdot \\ \nabla_{31} & \nabla_{33} & \nabla_{35} & \cdot & \cdot & \cdot \\ \nabla_{51} & \nabla_{53} & \nabla_{55} & \cdot & \cdot & \cdot \\ \cdot & \cdot & \cdot & \cdot & \cdot & \cdot \\ \cdot & \cdot & \cdot & \cdot & \cdot & \cdot \end{vmatrix} = 0 \qquad \{3.23\}$$

Another equation similar to {3.23} can be obtained when the summation is carried over the even values of v. Applying similar mathematical techniques to the modes whose axial magnetic field component is represented by odd type Mathieu functions, one can write their characteristic equation in the form;

$$\begin{vmatrix} \Delta_{11} & \Delta_{13} & \Delta_{15} & \cdot & \cdot & \cdot \\ \Delta_{31} & \Delta_{33} & \Delta_{35} & \cdot & \cdot & \cdot \\ \Delta_{51} & \Delta_{53} & \Delta_{55} & \cdot & \cdot & \cdot \\ \cdot & \cdot & \cdot & \cdot & \cdot & \cdot \\ \cdot & \cdot & \cdot & \cdot & \cdot & \cdot \end{vmatrix} = 0 \qquad \{3.24\}$$

for n = 0, 2, 4, - - -

or n = 1, 3, 5, - - -

where

$$\Delta_{n,v} = Ce_v'(q_1,\xi_1)\theta'_{v,n} - \left(\frac{K}{k}\right)^2 \frac{\tau_n'(q_2,\xi_1,\xi_2)}{\tau_n(q_2,\xi_1,\xi_2)} Ce_v(q_1,\xi_1)\theta'_{v,n}$$

$$+ \bar{\beta}^2 Ce_v(q_1,\xi_1) \sum_r \frac{Se_r(q_1,\xi_1)}{Se_r'(q_1,\xi_1)} \delta'_{r,n}\ \alpha'_{v,n} \qquad \{3.25\}$$

where

$$\tau_n(q_2,\xi,\xi_2) = \frac{Ce_n(q_2,\xi)Fey_n(q_2,\xi_2) - Ce_n(q_2,\xi_2)Fey_n(q_2,\xi)}{Fey_n(q_2,\xi_2)}$$

$$\theta'_{v,r} = \int_0^{2\pi} ce_v(q_1,\eta)ce_r(q_2,\eta)d\eta \Big/ \int_0^{2\pi} ce_r^2(q_2,\eta)d\eta$$

$$\alpha'_{v,r} = \int_0^{\pi} ce_v'(q_1,\eta)se_r(q_1,\eta)d\eta \Big/ \int_0^{2\pi} se_r^2(q_1,\eta)d\eta$$

and

$$\delta'_{v,r} = \int_0^{2\pi} se_v'(q_1,\eta)ce_r(q_2,\eta)d\eta \Big/ \int_0^{2\pi} ce_r^2(q_2,\eta)d\eta$$

Another equation similar to {3.24} can be obtained when even values of v are used. It must be noted here that if the characteristic impedance of the slot region, ${}_2E_z/{}_2H_\eta$, was equated to the characteristic impedance of the inner region, ${}_1E_z/{}_1H_\eta$, at the boundary $\xi = \xi_1$, then the same characteristic equations {3.23} and {3.24} would have been obtained provided that the summation signs appearing in the field expressions were not omitted. If the field is represented by a single term of the series {3.7} and {3.8}, then the characteristic equation derived using the boundary conditions {3.12}, has the form;

$$Se_v'(q_1,\xi_1) - \left(\frac{K}{k}\right)^2 \frac{\P_v'(q_2,\xi_1,\xi_2)}{\P_v(q_2,\xi_1,\xi_2)} Se_v(q_1,\xi_1)$$

$$= \bar{\beta}^2 Se_v(q_1,\xi_1) \frac{Ce_v(q_1,\xi_1)}{Ce_v'(q_1,\xi_1)} \alpha_{v,v}^2 \qquad \{3.26\}$$

which is not the form given in {3.23}. Under this assumption the characteristic impedance of the slot region, ${}_2E_z/{}_2H_\eta$, is independent of the azimuthal position (η) around the waveguide. This condition is not necessarily true in general except for a circular waveguide i.e. when the eccentricity is zero.

3.5 TRANSITION TO CIRCULAR CROSS-SECTION

An elliptical corrugated waveguide is reformed into a circular corrugated waveguide when its focal length, h, tends to zero while ξ_1 and ξ_2 approach infinity. The products $h\cosh\xi_1$ or $h\sinh\xi_1$ then tend to r_1, the inner

radius of the circular waveguide, and $h\cosh\xi_2$ or $h\sinh\xi_2$ tend to r_2, the outer radius. The degenerate forms of the angular and radial Mathieu functions are given in <16>. Using the degenerate expressions one obtains the following degenerate forms for the factors appearing in the characteristic equation;

$$Ce_n(q_1,\xi) \sim Se_n(q_1,\xi) \sim J_n(x_1)$$

$$Ce_n'(q_1,\xi) \sim Se_n'(q_1,\xi) \sim x_1 J_n'(x_1)$$

$$Ce_n(q_2,\xi) \sim Se_n(q_2,\xi) \sim J_n(x_2)$$

$$Ce_n'(q_2,\xi) \sim Se_n'(q_2,\xi) \sim x_2 J_n'(x_2)$$

$$Fey_n(q_1,\xi) \sim Gey_n(q_1,\xi) \sim Y_n(x_1)$$

$$Fey_n'(q_1,\xi) \sim Gey_n'(q_1,\xi) \sim x_1 Y_n'(x_1)$$

$$\theta_{v,r} \sim \begin{cases} 1 & \text{when } v = r \\ 0 & \text{when } v \neq r \end{cases}$$

$$\alpha_{v,r} \sim -\delta_{v,r} \sim \begin{cases} v & \text{when } v = r \\ 0 & \text{when } v \neq r \end{cases}$$

where $x_1^2 = r_1^2(k^2-\beta^2)$, $x_2^2 = r_2^2 k^2$

All terms in the infinite determinant {3.23} vanish except those along the main diagonal of the determinant. It is also noted that the degenerate forms of {3.23} and {3.24} are identical, hence, the even and odd modes are degenerate in the circular corrugated waveguide.

The degenerate infinite determinant then becomes

$$\prod_{n} \nabla_{n,n} = 0$$

with n = 1, 2, 3, - - - representing all possible hybrid modes of order n = 1, 2, 3, - - - respectively in the circular corrugated waveguide. Substituting the degenerate expansions for different Mathieu functions in $\nabla_{n,n}$ or $\Delta_{n,n}$, leads to the expression

$$x_1 \frac{J_n'(x_1)}{J_n(x_1)} - n^2\bar{\beta}^2 \frac{J_n(x_1)}{x_1 J_n'(x_1)} = \left(\frac{K}{k}\right)^2 x_1' \frac{J_n'(x_1')Y_n(x_2) - J_n(x_2)Y_n'(x_1)}{J_n(x_1')Y_n(x_2) - J_n(x_2)Y_n(x_1)} \qquad \{3.27\}$$

which is the characteristic equation of the corrugated circular waveguide given in <1>, with $x_1'^2 = r_1^2 k^2$. Therefore, it is concluded that, for the corrugated circular waveguide the terms in the infinite series {3.7} and {3.8} are uncoupled and the summation sign may be omitted.

3.6 CUT-OFF CONDITIONS AND CLASSIFICATIONS OF MODES

In a corrugated circular waveguide, it is known that <33>, the co-existence of E and H modes gives rise to hybrid modes. For reasons explained by Clarricoats and Saha <34> these modes are designated by HE if the cut-off frequency of the modes is that of an E-type mode in a smooth wall circular waveguide and by EH if the cut-off frequency of the modes corresponds to that of an H-type

mode in the smooth wall structure. With this notation the fields away from cut-off, of modes used in practice, resemble H-type and E-type modes respectively.

This classification of the modes is illustrated when finding the roots of equation {3.27} in the limit $\beta \to 0$, i.e.

$$J_n'(kr_1) \quad \to \quad EH_{nm} \text{ modes}$$

and

$$J_n(kr_2) \quad \to \quad HE_{nm} \text{ modes}$$

The subscripts n and m denote respectively the number of azimuthal variations with θ and the m-th root of the characteristic equation {3.27} for either EH or HE mode. These hybrid modes are doubly degenerate since an equally valid solution results if $\sin(n\theta)$ is replaced by $\cos(n\theta)$, and $\cos(n\theta)$ by $-\sin(n\theta)$. However, in the elliptical corrugated waveguide it is possible to have two orientations {2.8} for the field configurations. Thus a hybrid mode in this waveguide will be designated by a prescript e or o, indicating an even or an odd mode.

In order to distinguish between the even and odd HE or EH modes, the following field dependence will be utilised, for reasons given below. The axial magnetic and electric field components of an even EH mode or an odd HE mode are represented by odd and even Mathieu functions respectively. The reasons are as follows;

in the next section it is shown that the main diagonal terms of equation {3.23} dominate in the calculations of the dispersion characteristics of different modes. Thus, in order to establish a reasonable means of mode classification, the roots of the main diagonal terms are found when $\beta \to 0$. The roots of the equation

$$\lim_{\beta \to 0} \nabla_{n,n} = 0 \qquad \{3.28\}$$

are

$Se_n(q_2,\xi_2)$ and $Ce_n'(q_2,\xi_1)$ while those of the equation

$$\lim_{\beta \to 0} \Delta_{n,n} = 0 \qquad \{3.29\}$$

are

$Ce_n(q_2,\xi_2)$ and $Se_n'(q_2,\xi_1)$

Therefore, following the mode classifications used in the previous chapter, the roots of {3.28} are those of the odd TE modes and even TM modes, while the roots of {3.29} are those of the even TE modes and odd TM modes. Thus, to follow the mode classification used in the corrugated circular waveguide <34>, the solutions of equation {3.23} will give rise to the

$_oHE_{nm}$ modes and $_eEH_{nm}$ modes

and of equation {3.24} will give rise to the

$_eHE_{nm}$ modes and $_oEH_{nm}$ modes

The double subscript (n,m) employed here denotes the order of a mode which corresponds to the order (n,m) for an HE_{nm} mode or an EH_{nm} mode in the circular corrugated waveguide when the eccentricities e_1 and e_2 become zero. With this notation the field of the ${}_oHE_{11}$ mode and ${}_eHE_{11}$ mode, away from cut-off, resemble that of the TE_{c11} mode and TE_{s11} mode respectively.

3.7 DISPERSION CHARACTERISTICS

It is known that the angular Mathieu functions may be expanded in terms of an infinite series of trigonometric functions, and that the corresponding modified Mathieu functions can be expanded in terms of an infinite series of products of Bessel functions (Appendix II). As has been pointed out in the previous chapter, in order that the solutions of the Mathieu differential equation be periodic, the characteristic number C or the separation constant of the wave equation must satisfy a certain transcendental equation which is a function of q. Furthermore, the coefficients of these infinite series are functions of q and C.

Supposing one is interested in obtaining the numerical value of a certain modified Mathieu function of order m, one must first determine the value of the characteristic number which is the root of an infinite continued-fraction transcendental equation <35> and then find the coefficients from the three-term recurrence relations <25> which are functions of q and C.

Substituting these coefficients into the infinite Bessel function product series and carrying out the computations one finally obtains the result. According to the above description, it is quite evident that the task of computing the numerical values for a great number of angular Mathieu functions and modified Mathieu functions is very time consuming, even on a fast computer. Thus, for practical computations, the infinite determinants {3.23} and {3.24} must be reduced to contain the minimum number of terms that will produce sufficiently accurate results.

In section (3.5) it is shown that, for small eccentricities, the term $\nabla_{n,n}$ when equated to zero, gives a good indication of the dispersion characteristics for the mode (n,n). Therefore, for a first approximation of the roots of the (1,1) mode, the determinant {3.23} is reduced to the form;

$$\nabla_{11} = 0 \qquad \{3.30\}$$

The roots of {3.30} were calculated for different values of e_1 and e_2. The series summation over r in {3.21} was found to be very rapidly converging and only the first three terms were used in the calculations. The roots obtained for the case $e_1 \sim e_2 \sim 0$, were in very good agreement with those obtained for the circular corrugated waveguide equation {3.27}. In order to obtain a better approximation of the roots, the equation

$$\begin{vmatrix} \nabla_{11} & \nabla_{13} \\ \nabla_{31} & \nabla_{33} \end{vmatrix} = 0 \qquad \{3.31\}$$

is solved for different values of e_1 and e_2, and the roots obtained were then compared with computed values using {3.30}.

It was found that, for a particular value of the normalised phase-change coefficient, the values of the normalised frequency obtained from {3.30} and {3.31} were almost identical for small eccentricities. This difference was found to be of the order of 1% even at high eccentricities.

Table (3.1) shows computed results for the $_oHE_{11}$ mode, obtained using the above two approximations, for different values of e_1, with $e_2 = 0.8e_1$.

e_1	βa_1	$(\omega a_1/c)$ {3.30}	$(\omega a_1/c)$ {3.31}
.1	1.8	3.407	3.422
.5	1.8	3.577	3.592
.7	1.8	3.813	3.826
.9	3.6	5.098	5.063

Table (3.1)

The values of the phase-change coefficient obtained using equation {3.30}, would only produce an error of the order of 5 MHz, which is a very small error at an operation frequency of the order of 5 GHz, and would be within the limits of experimental observations. Computed results for the normalised phase-change coefficient of the $_{o}HE_{11}$ mode are shown in Figure (3.2) as a function of normalised frequency. The figure clearly illustrates the proximity of the roots of equations {3.30} and {3.31}, for a wide range of frequencies. Because of the long computational time involved in calculating the roots of equation {3.31}, the roots of the slightly less complicated equations

$$\Delta_{11} = 0 \qquad \text{and} \qquad \nabla_{11} = 0 \qquad \{3.32\}$$

were used to obtain the dispersion characteristics of the even and odd modes shown in Figure (3.3).

At a particular frequency, the even and odd HE_{11} modes in an elliptical corrugated waveguide are observed to have the same phase-change coefficient. This implies very high coupling between the two modes, and thus this frequency must be avoided when the waveguide is to be used in a practical system. No attempt has been made to compute the dispersion characteristic for values of $\beta > k$. This is because of the extreme mathematical complexity of the Mathieu functions needed to perform the computations <16>. In any case, a low-

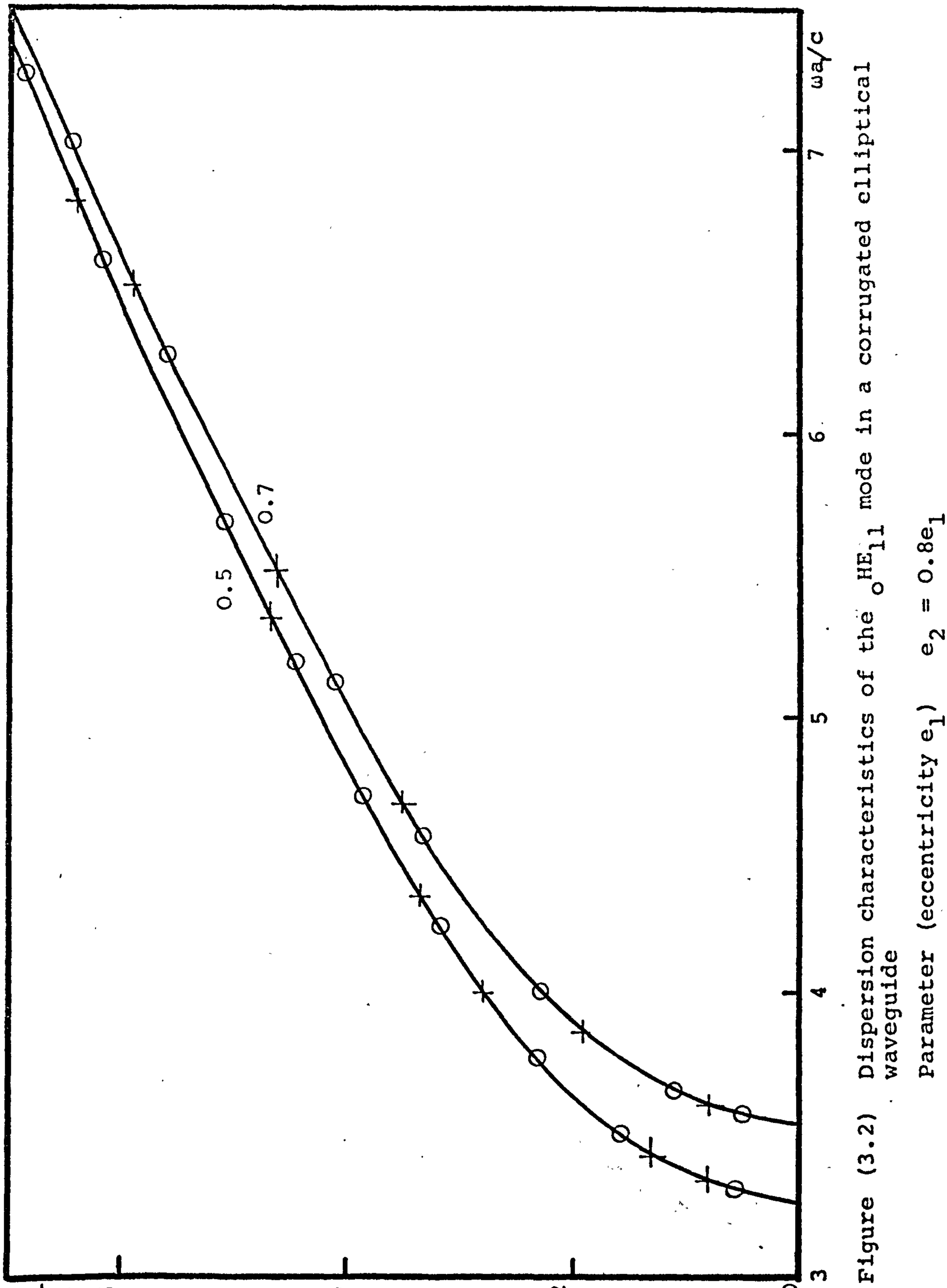

Figure (3.2) Dispersion characteristics of the $_oHE_{11}$ mode in a corrugated elliptical waveguide

Parameter (eccentricity e_1) $e_2 = 0.8e_1$

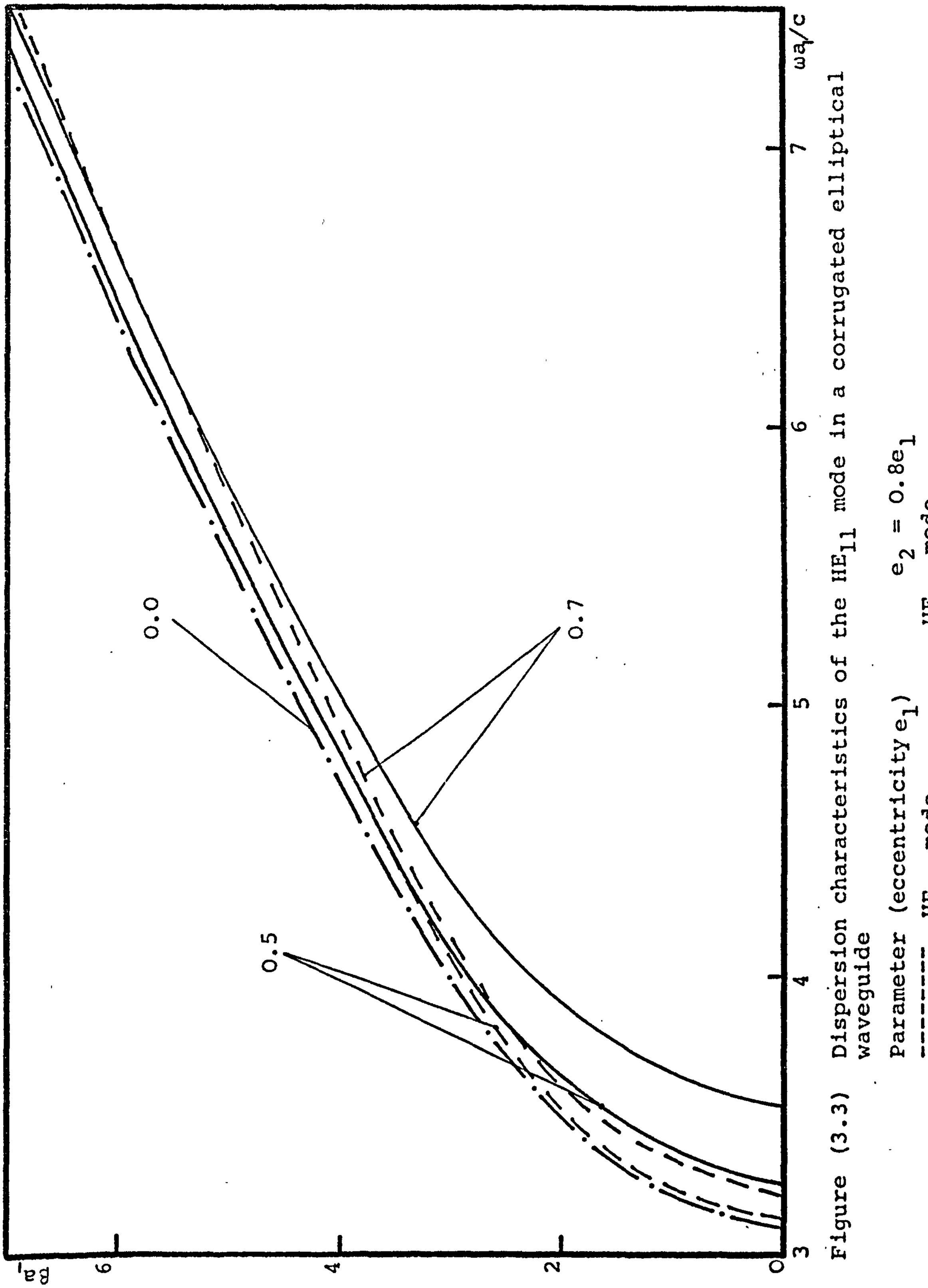

Figure (3.3) Dispersion characteristics of the HE_{11} mode in a corrugated elliptical waveguide

Parameter (eccentricity e_1) $e_2 = 0.8e_1$

--------- HE_{11} mode

attenuation waveguide will not be operated in the range $\beta > k$, as high attenuation figures are expected in this range.

3.8 ATTENUATION CHARACTERISTICS

In previous sections, field expressions in different regions of the waveguide are presented and the dispersion characteristics of the corrugated waveguide are shown.

In order to formulate the attenuation coefficient of the waveguide, it is necessary to calculate the power carried by different modes. Furthermore, the power-losses due to the imperfectly conducting metal slots must also be calculated.

3.8.1 POWER FLOW

The time average power flow over an area S is given by the integral of the complex Poynting vector,

$$P_o = \tfrac{1}{2}\,\mathrm{Re}\int (\underset{\sim}{E} \times \underset{\sim}{H}^*).\underset{\sim}{z}\,dS,$$

in cylindrical elliptical co-ordinates this simplifies to

$$P_o = \tfrac{1}{2}\,\mathrm{Re}\int (E_\xi H_\eta^* - E_\eta H_\xi^*)\,\ell_1\ell_2\,d\xi d\eta$$

For the corrugated elliptical waveguide, P_o is formulated in terms of the inner region field expressions given in {3.7}. Following the argument used in the computations of the dispersion characteristics, only the appropriate

terms of the series given in {3.7} are used to formulate the average power flow of different modes. Therefore, for the modes ${}_{o}HE_{nm}$ or ${}_{e}EH_{nm}$, the average power flow, P_o, is given by;

$$2K^4P_o = B_n^2\omega\varepsilon_o\beta\int_0^{\xi_1}\int_0^{2\pi}(Se_n'^2(q_1,\xi)se_n^2(q_1,\eta)+Se_n^2(q_1,\eta)se_n'^2(q_1,\eta))d\eta$$

$$+A_n^2kY_o\beta\int_0^{\xi}\int_0^{2\pi}(Ce_n'^2(q_1,\xi)ce_n^2(q_1,\eta)+Ce_n^2(q_1,\xi)ce_n'^2(q_1,\eta))\,d\eta d\xi$$

$$+A_nB_nY_o(k^2+\beta^2)I\int_0^{\xi_1}(Se_n'(q_1,\xi)Ce_n(q_1,\xi)+Ce_n'(q_1,\xi)Se_n(q_1,\xi))d$$

where $I = \int_0^{2\pi} se_n(q_1,\eta)ce_n'(q_1,\eta)d\eta$.

For the ${}_{e}HE_{nm}$ or ${}_{o}EH_{nm}$ modes, the average power flow, P_o, has exactly the same form given above, except the term I is now replaced by -I. This can easily be shown using the identity of the angular Mathieu functions;

$$\int_0^{2\pi} se_n(q_1,\eta)ce_n'(q_1,\eta)d\eta = -\int_0^{2\pi} se_n'(q_1,\eta)ce_n(q_1,\eta)d\eta,$$

it is noted here that I is a negative quantity.

Terms involving the integrals of the angular Mathieu functions or their derivatives, can be evaluated using some combinations of the coefficients of the trigonometric series generating the angular Mathieu functions. On the other hand, terms involving the integrals of the radial Mathieu functions or their derivatives, cannot be

integrated in a closed form, and therefore numerical integration techniques are used to evaluate them.

3.8.2 Power losses

The usual perturbation techniques <24> are used to formulate the power losses in the slot region of the waveguide. The technique assumes that, the magnetic field component near the slot metal surface is not influenced by the finite conductivity of the metal.

The techniques employed in section (2.4) when formulating the attenuation coefficient of the smooth wall elliptical waveguide, will not be employed here. The reason is merely due to the extreme mathematical complexity of the Mathieu functions required to represent the field components inside the metal region of the slots. However, the results obtained for the smooth wall waveguide can always be used as a guide to attaining a better estimate of the attenuation coefficient of the corrugated waveguide. The power loss of each slot can be divided into two components;

P_1 = Power loss on the two lateral sides of the slot,

and P_2 = Power loss on the base of the slot.

The contribution to the attenuation coefficient, of the power loss at the top of the ridges is neglected. This does not mean that the ridges have an infinitesimal thickness, where high current concentration occurs, but it merely implies that this component of the loss is very small when compared with P_1 or P_2. In fact, in

the circular waveguide, the ratios of P_1 or P_2 to the ridge power loss is of the order of 10^4, in the frequency range of interest.

For the ${}_oHE_{nm}$ or ${}_eEH_{nm}$ modes, the power loss expressions are;

$$P_1 = R_s \int_S (|{}_2H_\eta|^2+|{}_2H_\xi|^2)\ell_1\ell_2 d\eta d\xi$$

$$= \frac{R_s\omega^2\varepsilon_o{}^2}{k^4} L_n{}^2 \int_{\xi_1}^{\xi_2}\int_0^{2\pi} [\P_n{}'^2(q_2,\xi_2,\xi)se_n^2(q_2,\eta)$$

$$+ \P_n{}^2(q_2,\xi_2,\xi)se_n{}'^2(q_2,\eta)]d\xi d\eta$$

and

$$P_2 = \frac{R_s}{2} d \int_0^{2\pi} |{}_2H_\eta|^2_{\xi=\xi_2} \ell d\eta$$

$$=\frac{R_s\omega^2\varepsilon_o{}^2 d}{2a_2k^4} L_n{}^2 \P'^2(q_2,\xi_2,\xi_2)\int_0^{2\pi} se_n^2(q_2,\eta)/(1-e_2^2\cos^2\eta)^{\frac{1}{2}}d\eta$$

Since $e_2 < 1$, the denominator of the integrand, in the expression for P_2, may be expanded binominally, i.e.

$$\int_0^{2\pi} se_n^2(q_2,\eta)x\left[1+\tfrac{1}{2}e_2^2\cos^2\eta+\frac{1.3}{2^2.2!}\, e_2^4\cos^4\eta+ - - - -\right]\ d\eta,$$

which can be integrated in a closed form in terms of the coefficients of the trigonometric series generating the angular Mathieu function.

For the ${}_eHE_{nm}$ or ${}_oEH_{nm}$ modes, the odd Mathieu

functions are replaced by even Mathieu functions in the expressions for P_1 and P_2.

The attenuation coefficient is finally calculated using the formula;

$$\alpha = \frac{P_1+P_2}{2DP_o}$$

Computed results of the attenuation coefficient for the even and odd HE_{11} modes are illustrated in Figures (3.4) and (3.5), as a function of frequency. The internal and external major axes of the waveguide, $2a_1$ and $2a_2$, are fixed at 8 and 10 cm. respectively and the inner region eccentricity, e_1, is varied in the computations with $e_2 = 0.8e_1$. An increase in the minimum attenuation value is observed for the $_oHE_{11}$ mode as the eccentricity is raised from zero value. On the other hand, for the $_eHE_{11}$ mode a decrease in both the minimum attenuation value and the frequency at which the point occurs is observed, for increasing values of the eccentricity. However, the decrease in the minimum attenuation value reaches a minimum when the value of $e_1 \simeq 0.55$, and then starts rising again. This value of the eccentricity is rather interesting as it was found to provide the TE_{s11} mode, propagating in a smooth wall elliptical waveguide, with its minimum attenuation value.

A similar phenomenon was observed by Yeh <36>, when studying electromagnetic wave propagation along a dielectric cylinder of elliptical cross-section.

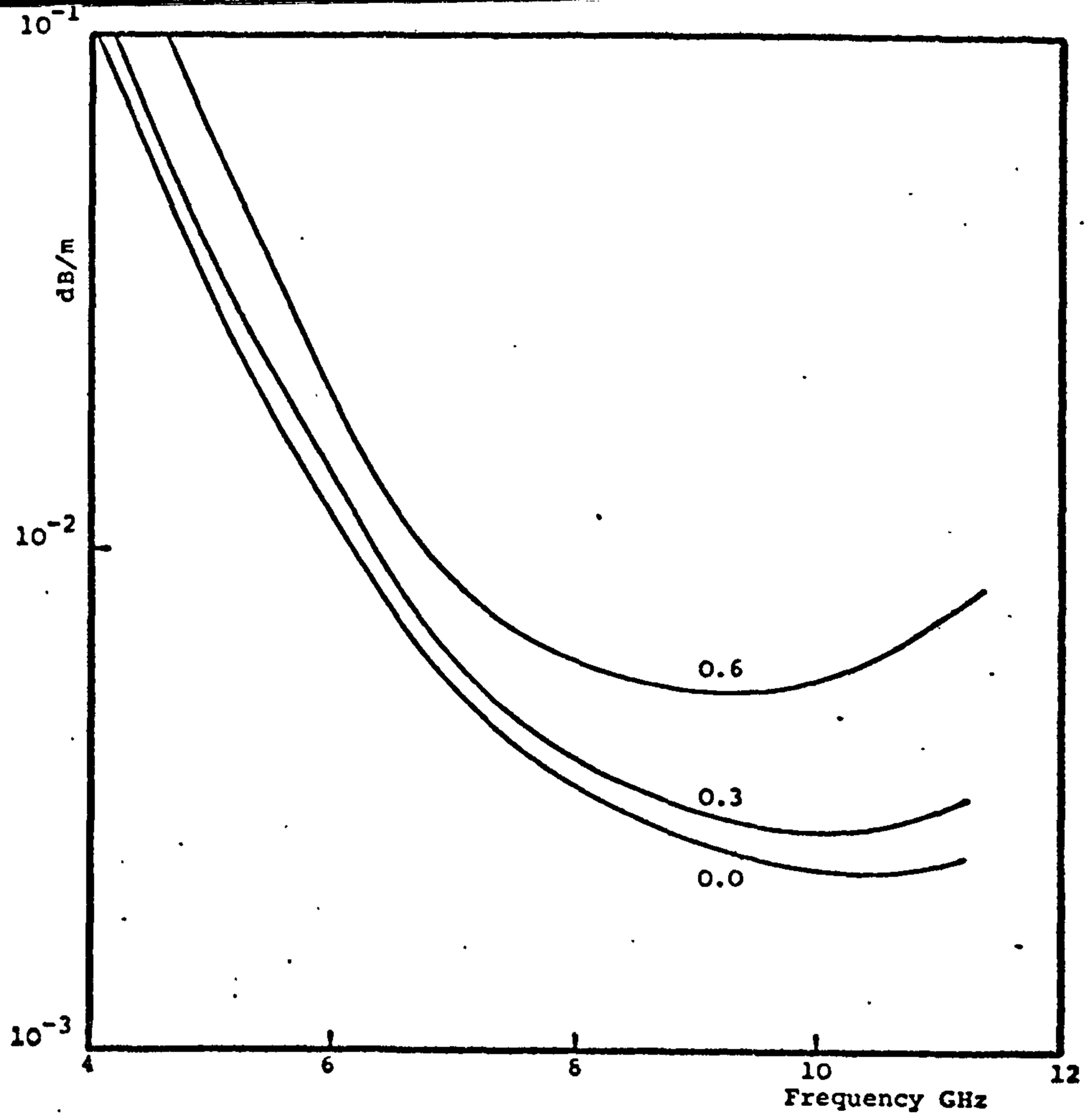

Figure (3.4) Attenuation characteristics of the $_{o}HE_{11}$ mode in a corrugated elliptical waveguide.

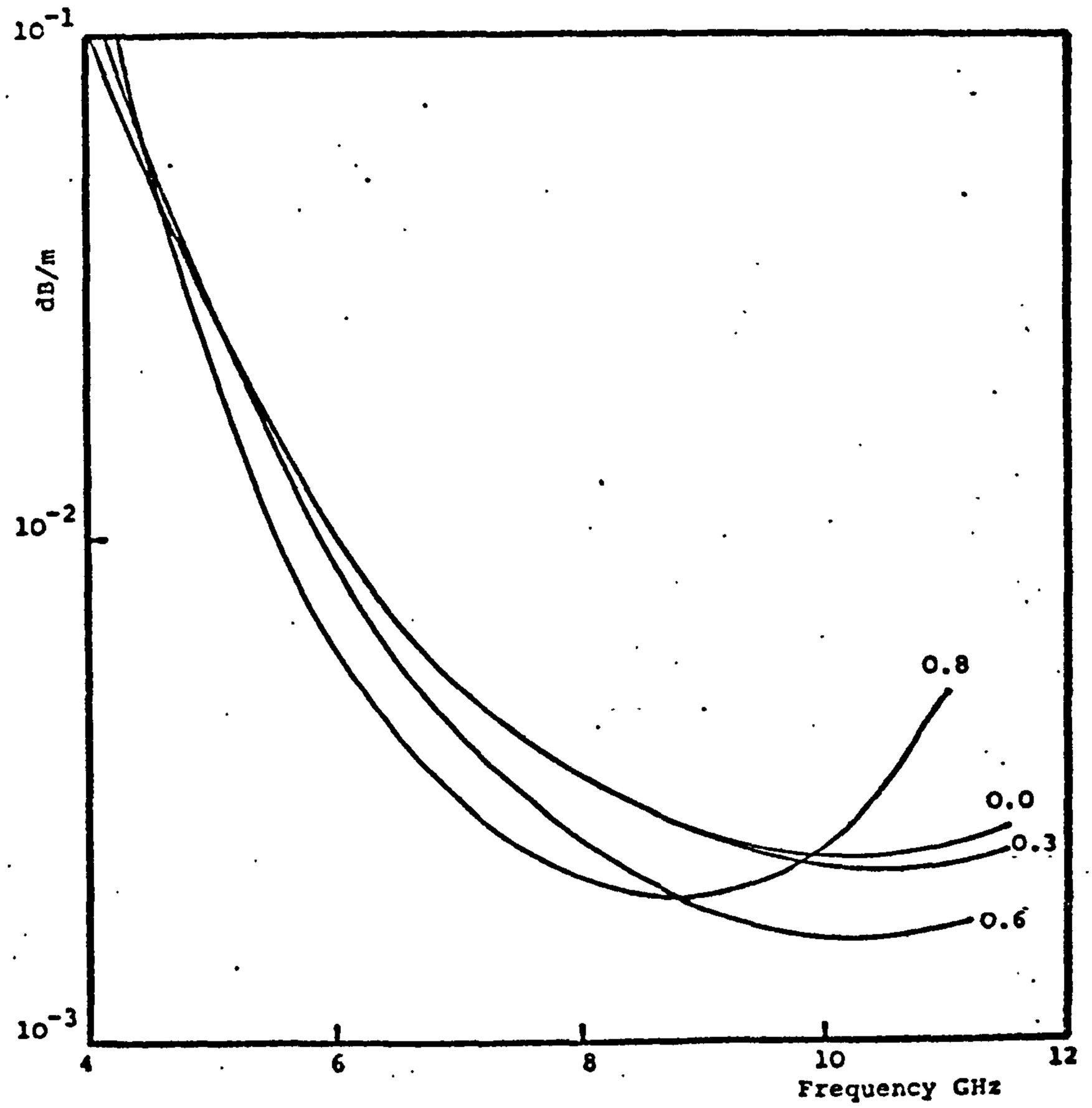

Figure (3.5) Attenuation characteristics of the $_{e}HE_{11}$ mode

CHAPTER FOUR

INFLUENCE OF SLOT SHAPE ON THE PERFORMANCE OF A CORRUGATED CIRCULAR WAVEGUIDE

4.1 INTRODUCTION

Recent investigations of the circular corrugated waveguide by Clarricoats and Olver <2> indicate the presence of low-attenuation properties of linearly polarised hybrid modes, of which the HE_{11} mode has practical importance. The structure supporting such a low-attenuation mode has been analysed with rectangular transverse slots, Figure (4.1). Commercial use of the circular corrugated waveguide has been impeded because of manufacturing difficulties. It is hard to conceive a simple means for manufacturing a flexible waveguide with rectangular slots. However, since the presence of the slots forms the very basis of the low-attenuation property of the waveguide, the effect on the attenuation coefficient of modifying the shape of the slot to aid manufacture purposes must be well understood.

When studying the circular waveguide structure with non-rectangular slots, the difficulty arises in obtaining solutions to the wave equation in the slot region of the waveguide. The method employed in synthesising the field is, to replace the non-rectangular continuous profile of a slot by a staircase approximation consisting of a series of rectangular slots. The field solution in each individual rectangular step of the staircase approximation is then obtained and field continuity at the interface of consecutive steps is ensured. A surface-impedance model boundary is then

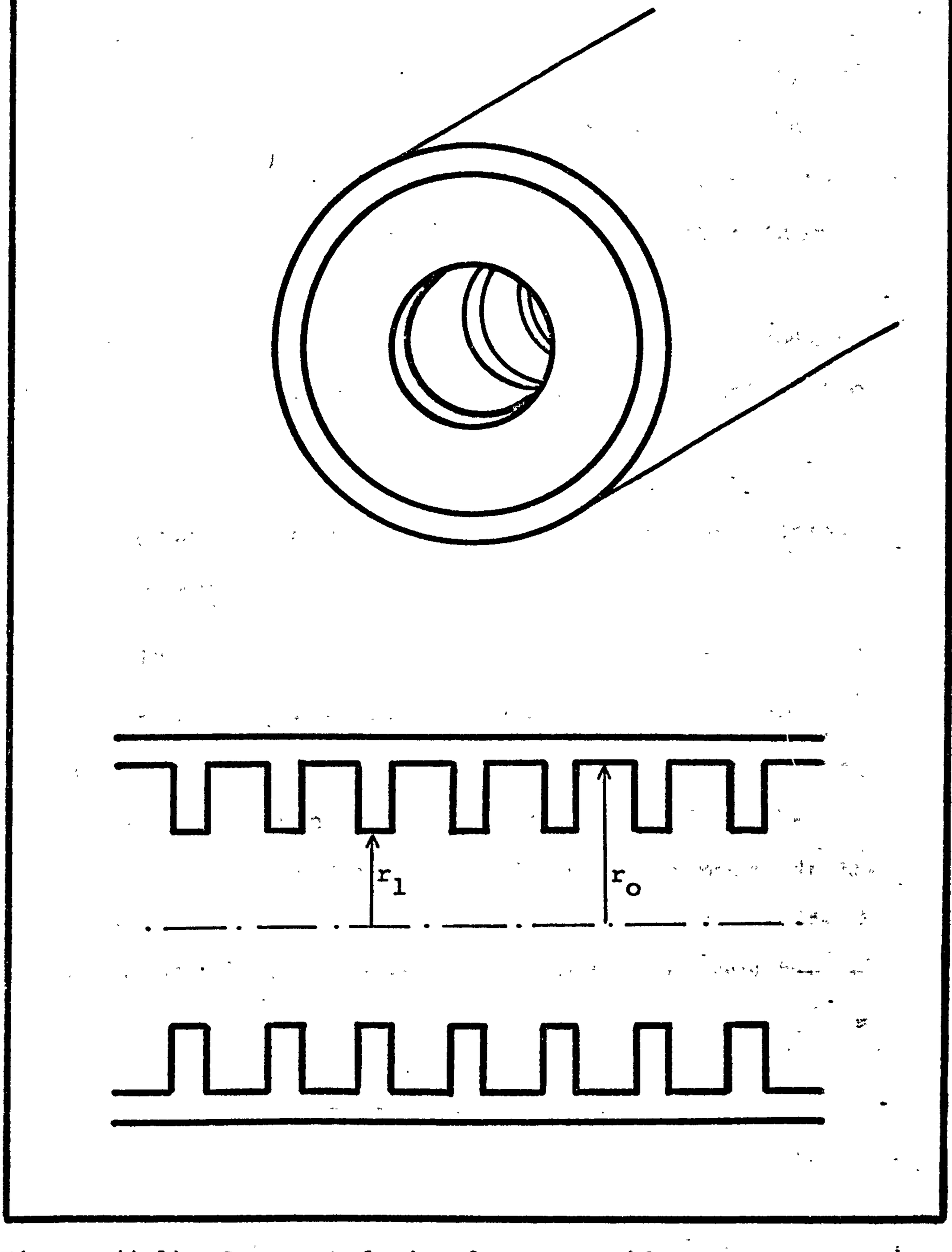

Figure (4.1) Corrugated circular waveguide

used to represent the slot-region of the waveguide, and the characteristic equation of the structure is thus obtained. The effects of non-rectangular slots on the dispersion, attenuation and radiation characteristics of the waveguide are illustrated in this chapter. Experimental verification of this effect on the radiation characteristics is presented in the latter part of the chapter.

4.2 CIRCULAR CORRUGATED WAVEGUIDE WITH RECTANGULAR SLOTS

4.2.1 Introduction

Recently, the corrugated circular waveguide shown in Figure (4.1) has been studied by Clarricoats and Olver < 2 > using a space-harmonic field in the inner region ($0 < r < r_1$), and higher order modes in the slot region ($r_1 < r < r_o$). In their analysis the field solution of the wave equation in the two regions has the form;

$$ {}_1E_z = \sum_v \sum_{m=-\infty}^{\infty} B_{vm}\, J_v(K_{1m} r)\cos(v\theta)\; e^{-j\beta_m z} $$

$$ {}_1H_z = Y_o \sum_v \sum_{m=-\infty}^{\infty} A_{vm}\, J_v(K_{1m} r)\sin(v\theta)\; e^{-j\beta_m z} $$

and for $r_1 < r < r_o$

$$ {}_oE_z = \sum_n \sum_{\mu=0}^{\infty} [L_{n\mu} \P_n(K_{2\mu} r_o, K_{2\mu} r) \cos\Gamma_\mu z + L'_{n\mu} \P'_n(K'_{2\mu} r_o, K'_{2\mu} r) $$

$$ \sin\Gamma'_\mu z] \cos(n\theta) $$

$$ {}_oH_z = Y_o \sum_n \sum_{\mu=1}^{\infty} [P_{n\mu} \Xi_n(K_2\ r_o, K_{2\mu} r) \sin\Gamma_\mu z + P'_{n\mu} \Xi'_n(K'_{2\mu} r_o, K'_{2\mu} r) $$

$$ \cos\Gamma' z] \sin(n\theta) $$

where the different notations used are similar to those used in the analysis of the elliptical corrugated waveguide, equations {3.1} and {3.2}, except for the angular and radial Mathieu functions, which are replaced by trigonometric and Bessel functions.

On making use of the boundary conditions at $r = r_1$, for $2\pi \geq \theta \geq 0$,

$$ {}_1E_z = {}_oE_z \qquad {}_1H_z = {}_oH_z $$

$$ {}_1E_\theta = {}_oE_\theta \qquad {}_1H_\theta = {}_oH_\theta \ , $$

and after some very cumbersome algebra one obtains a homogeneous system of equations for the coefficients B_{vm}, A_{vm}, L_n, L'_n, P_n and P'_n. By using the condition of non-triviality, the characteristic equation is then obtained in the form of a (4m+2) determinant, which is solved for a finite number of μ and m. From a knowledge of the phase-change coefficient the attenuation coefficient is calculated, taking into account the higher order modes in the slot region.

The same structure was previously analysed by Clarricoats and Saha <34>, using a surface impedance model to represent the boundary at $r = r_1$. A much simpler representation of the field in the central region is used and the slots assumed to support a cut-off TM mode only. This is equivalent to taking first terms of the space harmonic formulation. The ratios (E_z/H_θ), which are assumed to be independent of the propagation direction, are then equated at the boundary $r = r_1$, Figure (4.1), to obtain the characteristic equation of the structure. The above approximation is valid when the numbers of slots per wavelength is large. The attenuation coefficient can then be formulated using the field components in the slot region.

Table (4.1) shows numerical results obtained for the HE_{11} mode in a corrugated waveguide, with $r_1 = 4$ cm and $r_o = 5$ cm, when using the simple and exact formulations mentioned above. The exact formulation results shown are obtained with m(=2) pairs of space-harmonics and μ(=2) higher order slot modes.

βr_1	$\omega r_1/c$			α dB/m		
	Simple	Exact	Error %	Simple	Exact	Error %
0.6	2.86	2.90	1.4	0.479	0.457	4.6
1.6	3.10	3.14	1.1	0.139	0.153	9.0
2.6	3.60	3.59	0.1	0.081	0.058	28.3

Table (4.1)

The values of the phase-change coefficient obtained using the simple theory have been found to lie within the limits of experimental observations obtained by Olver et al < 3 > using resonant cavity techniques. In fact, in the frequency range in which low-attenuation occurs, the difference between the values of frequency obtained using exact and simple theories is only of the order of 5 MHz, which is very small when compared with the operating frequency of 9 GHz. Therefore, the application of the simple theory to circular corrugated waveguides with different transverse surface impedances, at the boundary $r = r_1$, should give quite accurate propagation curves. Although the differences in the attenuation results are of the order of 35% in the range of operation, the surface impedance theory should still provide a useful indication of the attenuation coefficient. A detailed comparison of the above theories appears in < 4 >.

In what follows, various practical structures will be analysed using the simple surface-impedance model. The analysis for a circular corrugated waveguide with rectangular slots will first be presented, and the method then extended to structures with non-rectangular slots such as are used in practical flexible corrugated waveguides, Figure (4.2a).

4.2.2 Surface-Impedance Theory

The transverse surface-admittance presented to the central region by a rectangular slot at the surface $r = r_1$,

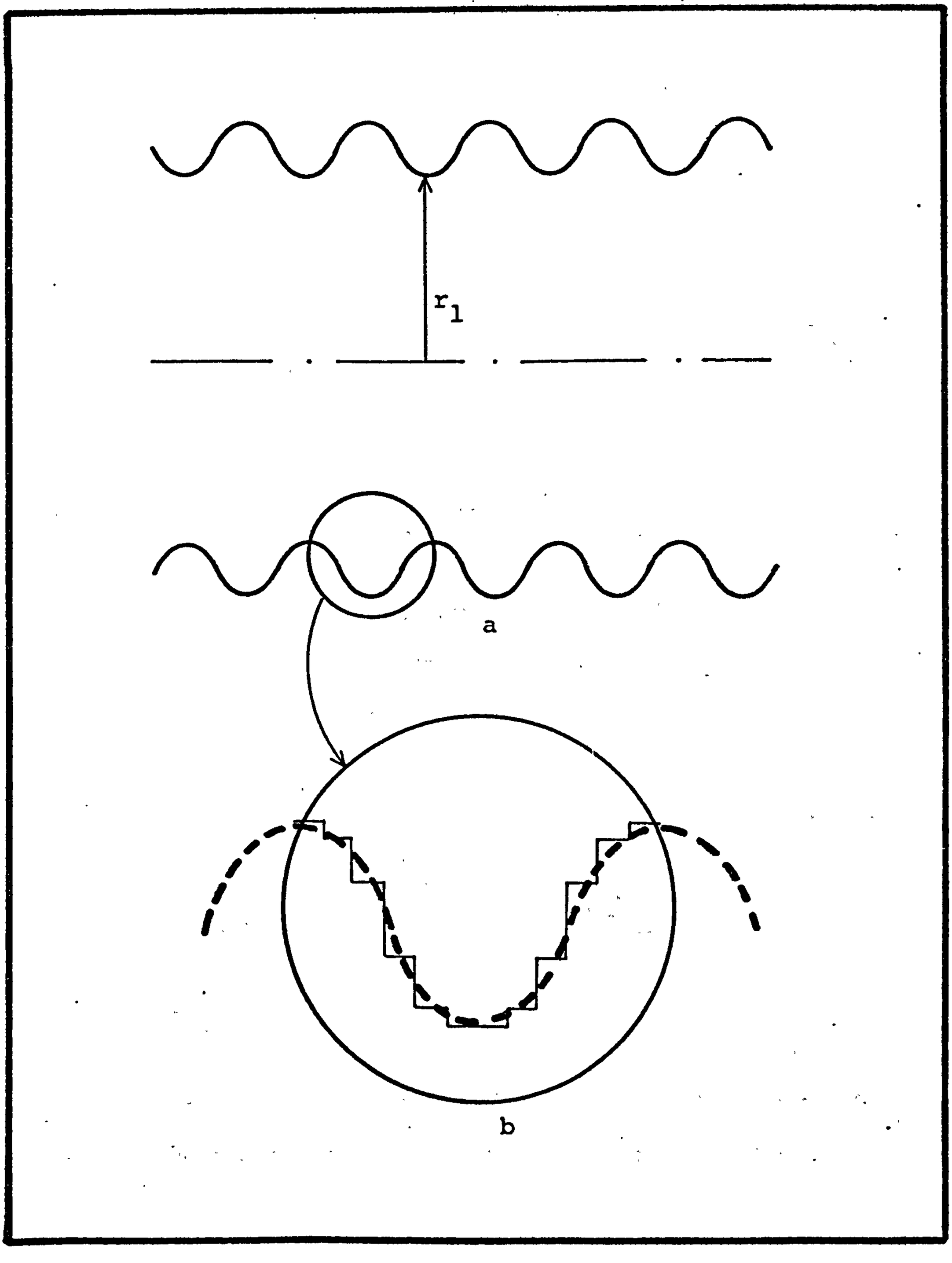

Figure (4.2) Corrugated circular waveguide

a : practical slot profile

b : staircase representation of an arbitrary slot

is given by the ratio of the azimuthal magnetic field component to the axial electric field component in the slot, evaluated at $r = r_1$, i.e.

$$-jY_o S_n'(\bar{r}_1, \bar{r}_o) \equiv -jY_o Y \qquad \{4.1\}$$

where Y is the normalised surface-admittance of the slot, $Y_o = \sqrt{\varepsilon_o/\mu_o}$, $\bar{r}_1 = kr_1$, $\bar{r}_o = kr_o$, $k = \omega\sqrt{\mu_o\ \varepsilon_o}$ and

$$S_n'(x,y) = \frac{J_n'(x)Y_n(y) - J_n(y)Y_n'(x)}{J_n(x)Y_n(y) - J_n(y)Y_n(x)}$$

The transverse surface-admittance presented by the inner region at $r = r_1$, is given by the same ratio of the field components in the inner region, i.e.

$$-jY_o \bar{r}_1 \frac{F_n^2(Kr_1) - (n\bar{\beta})^2}{(Kr_1)^2 F_n(Kr_1)} \qquad \{4.2\}$$

where $(Kr_1)^2 = \bar{r}_1^2 - (\beta r_1)^2$, $F_n(x) = x\frac{J_n'(x)}{J_n(x)}$,

$\bar{\beta} = \beta r_1/\bar{r}_1$.

The characteristic equation is then obtained by equating the admittances given in {4.1} and {4.2} and leads to

$$\bar{r}_1 \frac{F_n^2(Kr_1) - (n\bar{\beta})^2}{(Kr_1)^2 F_n(Kr_1)} = Y \qquad \{4.3\}$$

The transverse surface admittance {4.2} is derived by assuming that the azimuthal electric field component vanishes on the slot edge, this is due to the presence

of the transverse impedance boundary at $r = r_1$. This assumption will not be affected by the shape of the slots provided that there is a large number of slots per wavelength. Changing the slot shape will not affect the field expressions in the central region of the waveguide, and equation {4.2} will still be valid. The characteristic equation of the corrugated structure with non-rectangular slots will therefore have the same form as {4.3}, with the appropriate value of Y obtained for the new slot shape. The first step is therefore to obtain the value of Y for different slot shapes.

4.3 CIRCULAR CORRUGATED WAVEGUIDE WITH NON-RECTANGULAR SLOTS

4.3.1 Introduction

Figure (4.2a) shows a possible profile for slots in a corrugated circular waveguide. The continuous profile of each slot is replaced by a staircase approximation of equal widths as shown in Figure (4.2b). Each step is then considered to support a cut-off TM mode, and field continuity at the interface of two neighbouring steps must be ensured. The transverse admittance of each individual step is then calculated using the appropriate field components and this admittance is then related to the admittance of the neighbouring step. A re-occurrence procedure is then developed to transfer the admittance of successive steps until the transverse slot admittance at $r = r_1$ is

obtained. The staircase procedure has been previously used in synthesising a continuous radial variation in the refractive index of an optical waveguide. The results obtained by Clarricoats and Chan <19> in synthesising a parabolic profile of a Selfoc fibre were found to be in very good agreement with the results obtained by Kirchhoff <37>, who formulated an exact characteristic equation of the fibre taking into account the parabolic refractive index profile.

4.3.2 Formulation of the Problem

Figure (4.3) shows a profile that has been replaced by an (m-1) step-staircase approximation. The quantity $Y_{s,q}$ defines the normalised transverse admittance of the q-th region at radius $r = r_s$, looking radially outwards. The axial width of the q-th region is d_q. The normalised surface admittance of the m-th region at radius r_{m-1} is therefore given by;

$$Y_{m-1,m} = S_n'(\bar{r}_{m-1}, \bar{r}_m) \qquad \{4.4\}$$

For an intermediate region q, the field components are given by;

$$ {}_qE_z = A_q J_n(\bar{r}) + B_q Y_n(\bar{r}), \qquad {}_qH_z = 0,$$

$$ {}_qH_\theta = -jY_o[A_q J_n'(\bar{r}) + B_q Y_n'(\bar{r})], \quad {}_qE_\theta = 0,$$

$$ {}_qH_r = j\frac{Y_o}{\bar{r}}\, {}_qE_z, \qquad {}_qE_r = 0. \qquad \{4.5\}$$

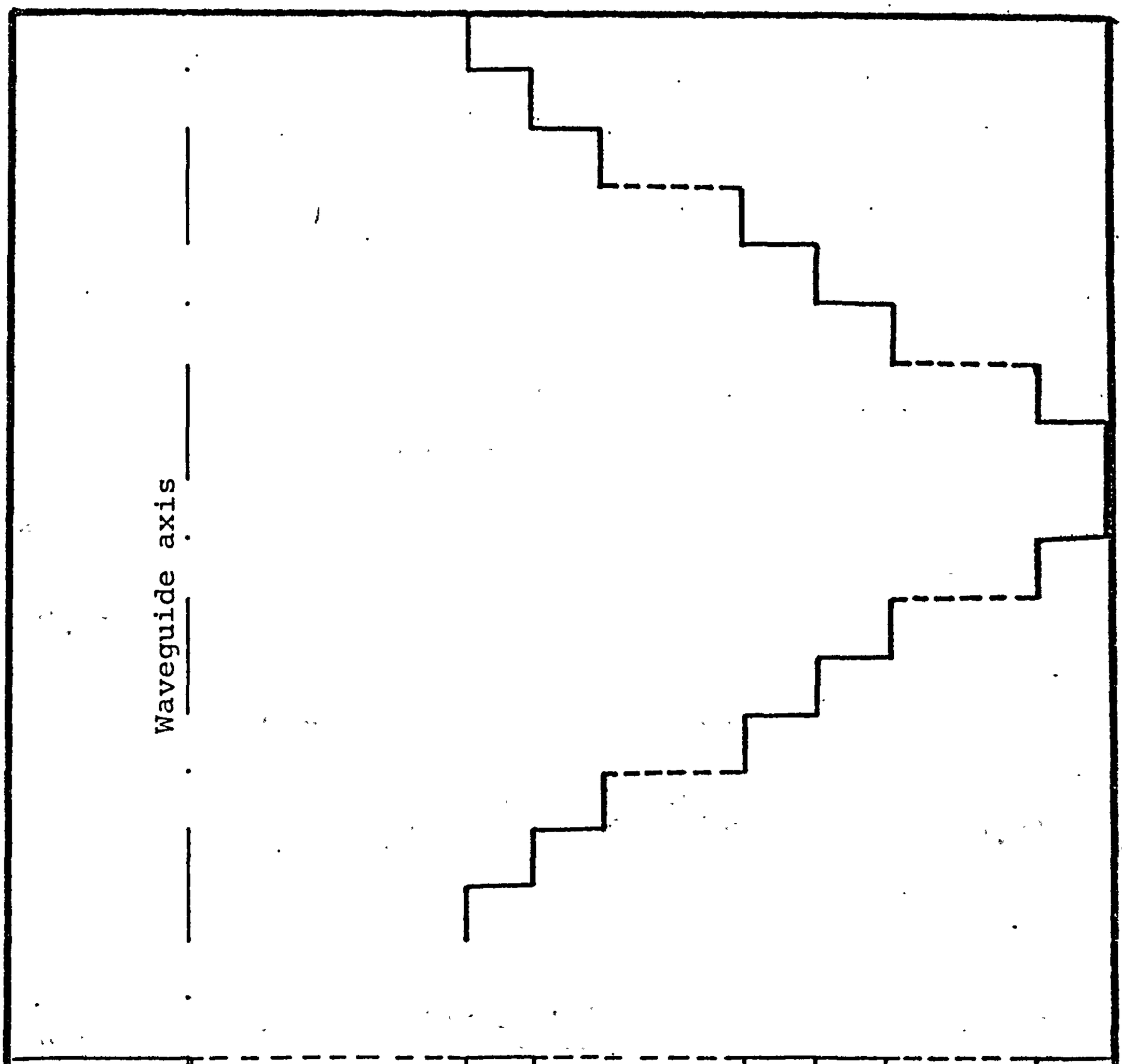

RADIUS	r_1	r_2		r_q	r_{q+1}		$r_m = r_o$
REGION	1	2		q	q+1		m
LONGI-TUDINAL WIDTH	d_1	d_2		d_q	d_{q+1}		d_m

Figure (4.3) Step representation of an arbitrary profile

Therefore,

$$Y_{q,q} = \frac{J_n'(\bar{r}_q)+C_qY_n'(\bar{r}_q)}{J_n(\bar{r}_q)+C_qY_n(\bar{r}_q)} \qquad \{4.6\}$$

and

$$Y_{q-1,q} = \frac{J_n'(\bar{r}_{q-1})+C_qY_n'(\bar{r}_{q-1})}{J_n(\bar{r}_{q-1})+C_qY_n(\bar{r}_{q-1})} \qquad \{4.7\}$$

where

$$C_q = B_q/A_q$$

Eliminating C_q from {4.6} and {4.7} leads to

$$Y_{q-1,q} = S_n'(r_{q-1},r_q)\ \frac{R_n'(\bar{r}_q,\bar{r}_{q-1})-Y_{q,q}}{S_n'(\bar{r}_q,\bar{r}_{q-1})-Y_{q,q}} \qquad \{4.8\}$$

where

$$R_n'(x,y) = \frac{J_n'(x)Y_n'(y)-J_n'(y)Y_n'(x)}{J_n(x)Y_n'(y)-J_n'(y)Y_n(x)} \quad .$$

So far we have obtained the relationship between the surface admittances of a single step when observed at the two inner boundaries of the step. The next stage is to obtain the relationship between the surface admittances of two consecutive steps, when observed at the interface of the two steps.

The admittance presented by the q-th step to the boundary at $r = r_q$ can be written in the form <39>

$$Y_{q,q} = \frac{\int_0^{d_q}\int_0^{2\pi} |{}_qE_z \cdot {}_qH_\theta|_{r=r_q}\ d\theta dz}{\left[\int_0^{d_q} {}_qE_z\ dz\right]^2_{r=r_q}} = r_q\ \frac{Y_{q,q}}{d_q}$$

The admittance represented in this way can be thought of as the ratio of the reactive power flowing into the slot to the square of the voltage across the slot.

Similarly

$$\bar{Y}_{q,q+1} = \frac{r_q \int_0^{d_{q+1}} \int_0^{2\pi} \left| {}_{q+1}E_z \cdot {}_{q+1}H_\theta \right|_{r=r_q} d\theta dz}{\left(\int_0^{d_{q+1}} {}_{q+1}E_z{}^2 dz \right)_{r=r_q}^2} = r_q \frac{Y_{q,q+1}}{d_{q+1}}$$

But $\bar{Y}_{q,q}$ must be equal to $\bar{Y}_{q,q+1}$, using power conservation thus

$$\frac{Y_{q,q}}{Y_{q,q+1}} = \frac{d_q}{d_{q+1}} \qquad \{4.9\}$$

Substituting the relationship {4.9} in equation {4.8} leads to

$$Y_{q-1,q} = S_n'(\bar{r}_{q-1}, \bar{r}_q) \frac{d_{q+1} R_n'(\bar{r}_q, \bar{r}_{q-1}) - d_q Y_{q,q+1}}{d_{q+1} S_n'(\bar{r}_q, \bar{r}_{q-1}) - d_q Y_{q,q+1}} \qquad \{4.10\}$$

Physically, equation {4.10} transfers the surface admittance from the upper part of region q+1 through the lower part of region q, to the upper part admittance of region q as shown in Figure (4.4).

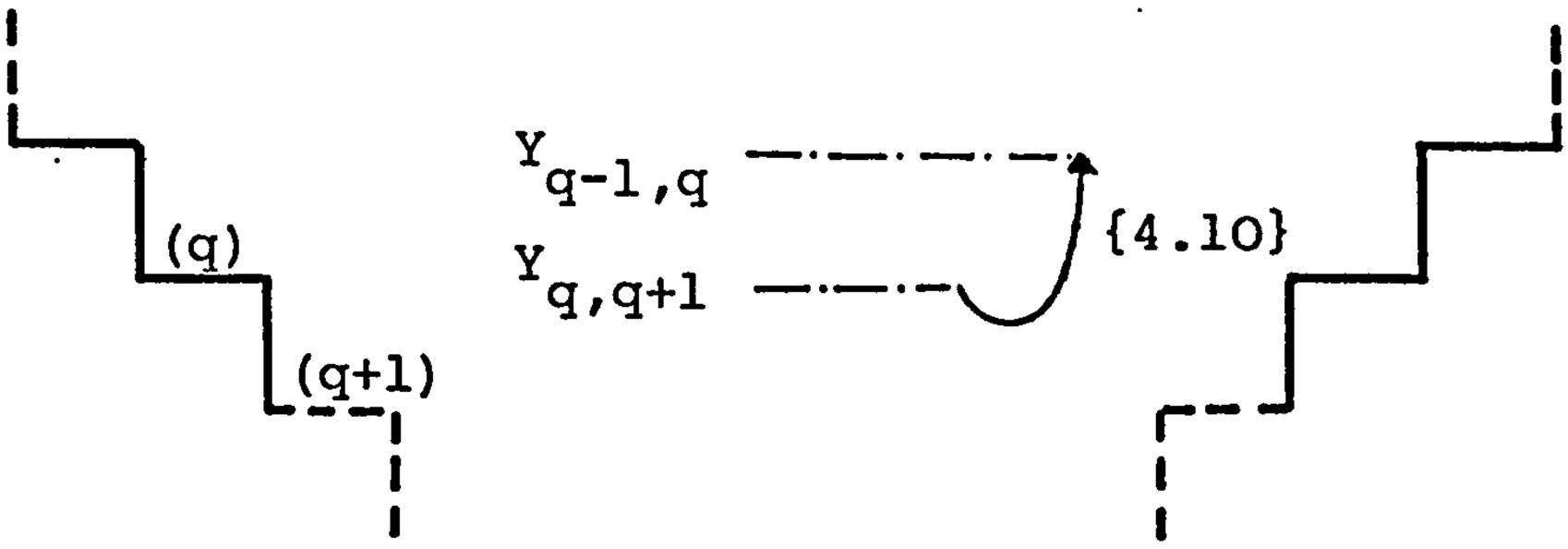

Figure (4.4)
Physical representation of {4.10} relationship

4.3.3 Influence of Number of Steps

The overall transverse surface admittance Y of the slot can be calculated using the following procedure;

(a) the transverse admittance of the m-th step is obtained using equation {4.4},

(b) the recurrence relationship given in {4.10} is then used (m-2) times to find the admittance $Y_{1,2}$, and

(c) finally the relation {4.9} is used to find the surface admittance of the slot $Y = Y_{1,1}$.

A computer program was developed to calculate the surface admittance of different profiles, by subdividing the given profile into equal (m-1) horizontal intervals, and then finding a suitable height for each step, to fit the smooth profile as closely as possible. Alternatively, the co-ordinate points of the profile are inserted into the program. The influence of the number of steps required to approximate a smooth profile was first

studied using different profiles. Figure (4.5) shows this influence when approximating a cosine profile, shown in Figure (4.6). The results converge as the number of steps are increased, and for m > 21 the results show negligible change with further increase.

4.3.4 Influence of Slot Shape

The profile of the different slot shapes shown in the insert of Figure (4.6) were replaced by a 20 step staircase approximation, and the normalised surface admittance was then calculated using the procedure developed. Figure (4.6) shows the normalised admittance as a function of normalised slot depth. It is evident that for non-rectangular slots, a deeper slot depth is required to produce the open-circuit condition, with the triangular slots being the deepest. We observe that the corrugated surface is capacitive at low frequencies, and that as the frequency is increased it acts as an open circuit boundary. Further increase in frequency causes the surface to become inductive. Figure (4.6) also shows that, as the frequency is increased, the rectangular slots have the fastest rate of change of admittance.

In passing, we note that for a hybrid mode in a circular corrugated waveguide, the condition that the surface is inductive is not a sufficient condition for a surface wave as it is in the plane case. When the wave phase velocity is less than the velocity of light, the condition becomes sufficient and the surface supports a

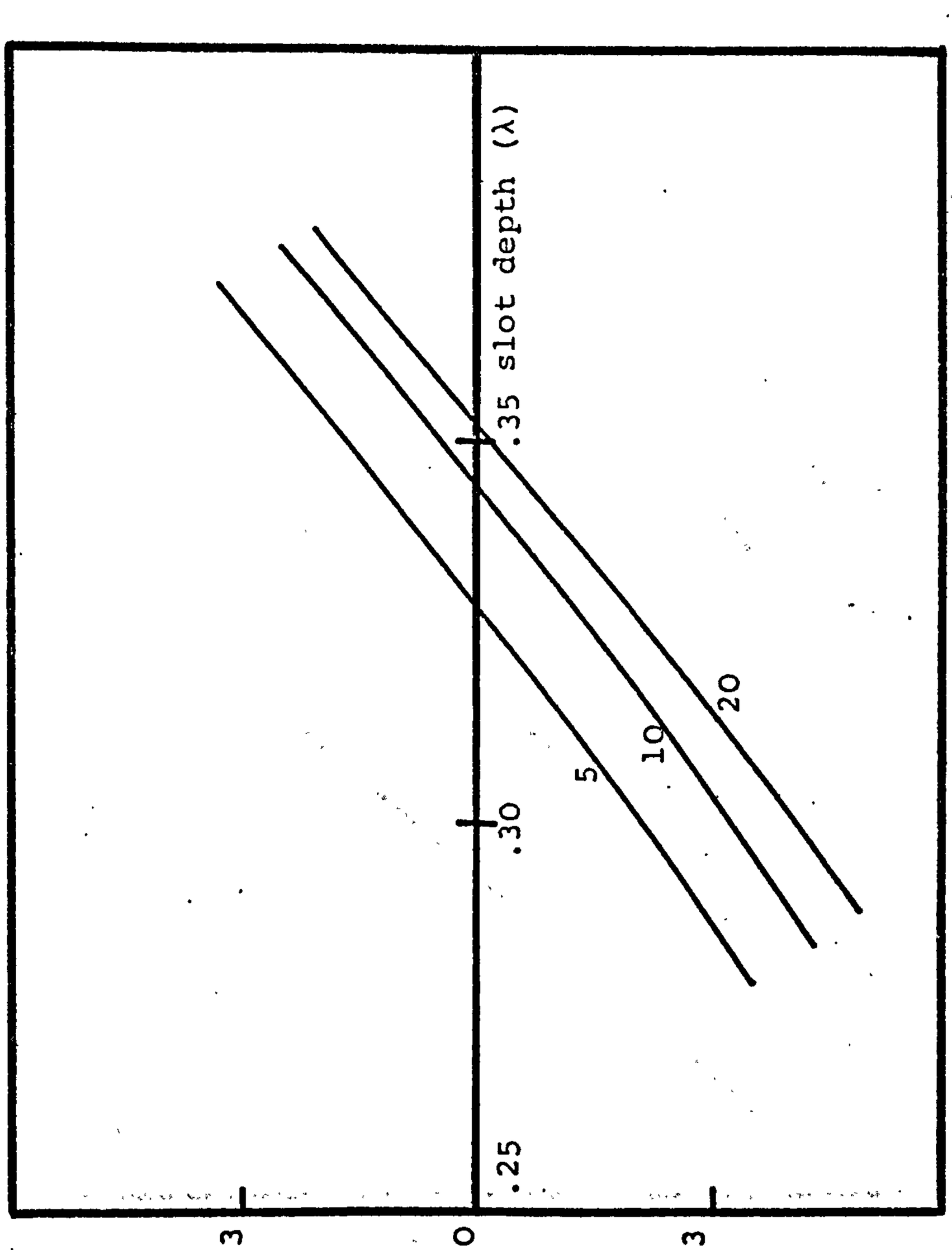

Figure (4.5) Normalised admittance of a cosine profile slot against normalised slot depth

Parameter (number of steps employed to approximate the profile)

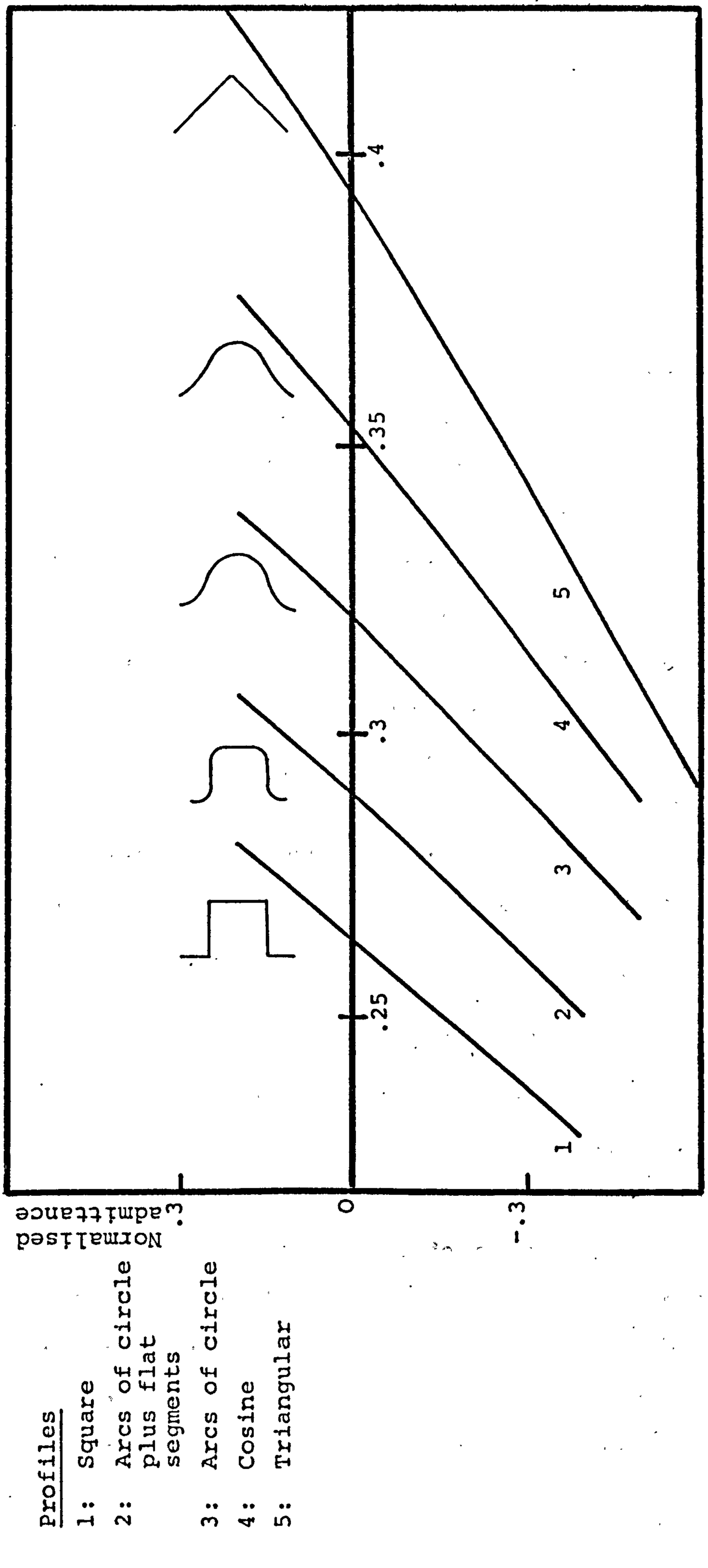

Figure (4.6) Normalised admittance of various profile slots against normalised slot depth.
20-steps approximation.

Profiles

1: Square
2: Arcs of circle plus flat segments
3: Arcs of circle
4: Cosine
5: Triangular

surface wave with its field localised near the surface. This phenomenon will therefore take place in the corrugated waveguide when $\bar{\beta} > 1$, as both conditions are satisfied.

In order to overcome the difficulties in producing rectangular slots, which give the shortest slot depth to provide the open circuit condition, slots with shapes that produce the same condition with the least increase in slot depth are sought. For large scale production of a flexible waveguide, slots with rounded edges are easier to manufacture. The effect of rounding the top and bottom edges of a square slot is shown in Figure (4.7), where the edges are considered to form an arc of a circle of radius (h-d)/2. A twenty step approximation was used to synthesise the slot profile and it is seen that, rounding of the edges will not increase the depth required to produce the open circuit condition by a great amount.

4.3.5 Influence of Central Region Radius

As the slot surface admittance is a function of the central region radius of the waveguide, then the influence of this radius on the open-circuit condition is studied. If a larger waveguide radius r_1, was chosen, then a smaller slot-depth would have been necessary to cause the open-circuit condition for all the profiles shown in Figure (4.6). Figure (4.8) shows the dependence of the normalised slot depth needed to produce

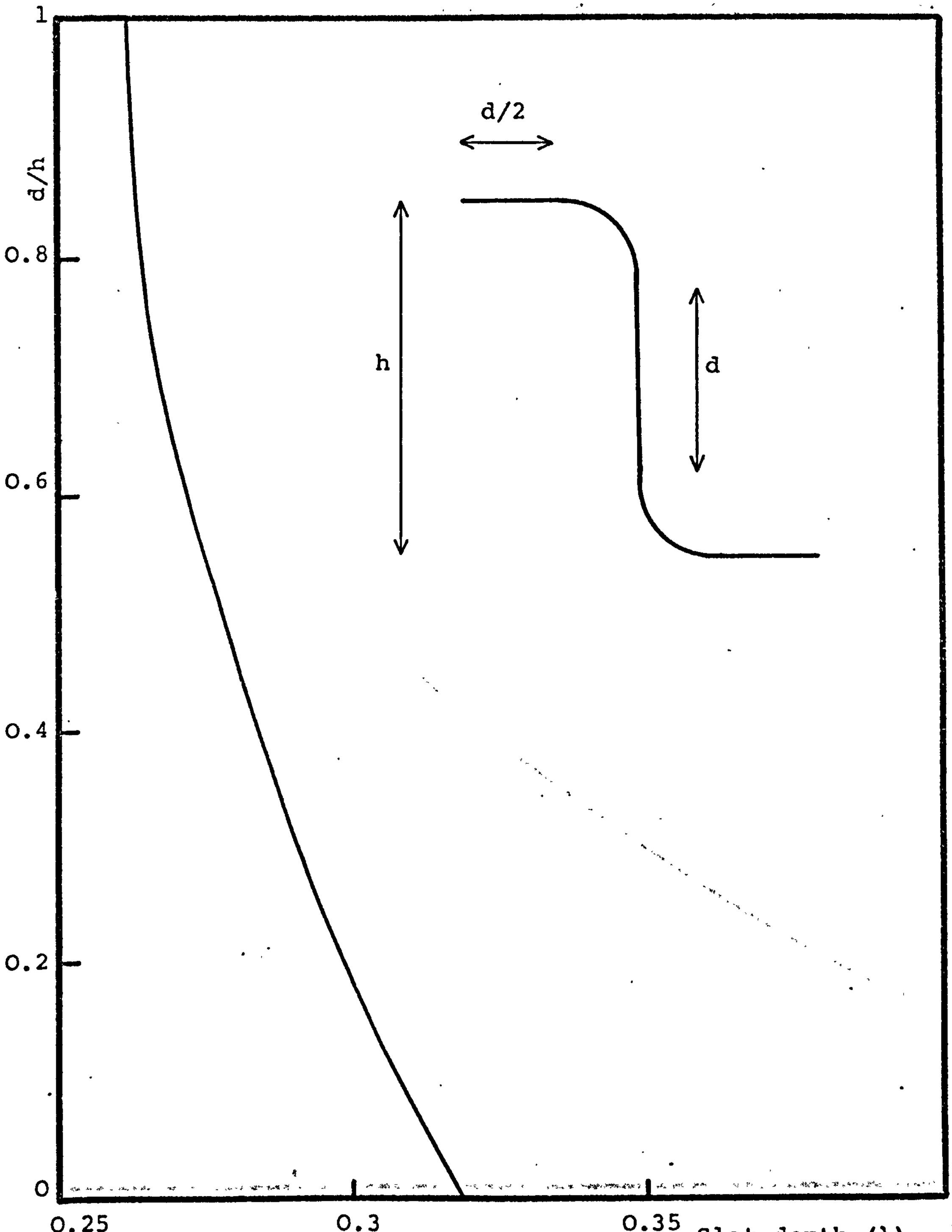

Figure (4.7) Flat segment length required to produce open-circuit condition at $r = r_1$ against normalised slot depth.

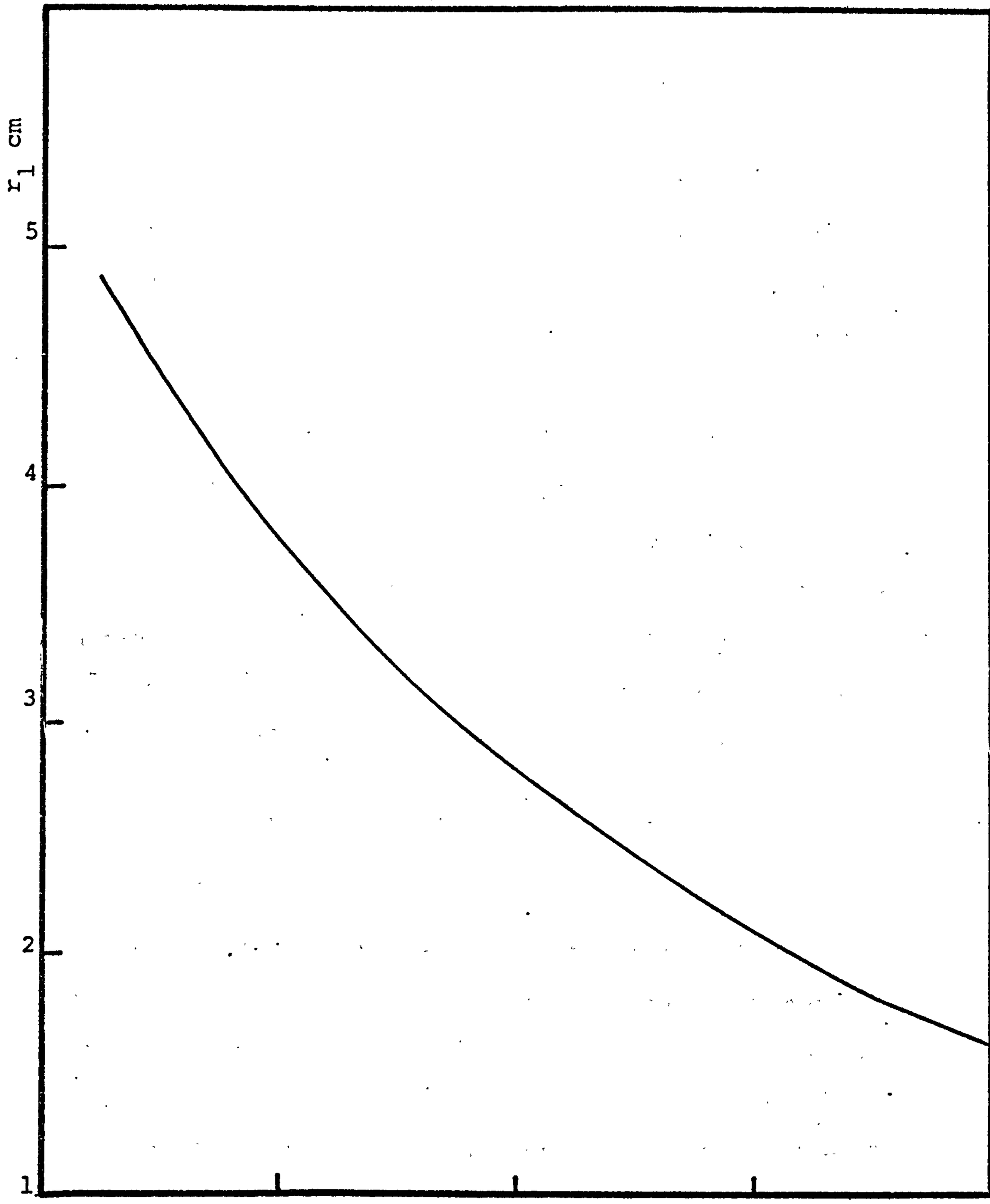

Figure (4.8) Inner region radius required to produce the open circuit condition for a rectangular slot against slot depth.

the open-circuit condition for a variable central region radius of a circular corrugated waveguide with rectangular slots, where it can be seen that as the central region radius of the waveguide increases, the slot-depth required approaches one quarter-wavelength in depth. This characteristic is also revealed by considering the large argument expansion of the $J_n(\bar{r}_1)$ and $Y_n(\bar{r}_1)$ functions appearing in the expression of $S_n'(\bar{r}_1,\bar{r}_o)$. When $\bar{r}_o$ and $\bar{r}_1$ are large, $S_n'(\bar{r}_1,\bar{r}_o)$ reducesto a trigonometric cotangent function. This condition is expected physically, as the transverse surface admittance of a plane corrugated surface ($r_1=\infty$) is given by $jY_o \cot(\bar{d})$, where $\bar{d}$ is the normalised corrugation depth. $\bar{d}$ is equal to $\pi/2$ for the open circuit condition.

4.4 DISPERSION CHARACTERISTIC

4.4.1 Introduction

The characteristic equation of the circular corrugated waveguide, using the surface impedance model theory is given in equation {4.3}, where the variable Y is the only term influenced by changing the slot shape of the waveguide. For an arbitrary slot shape, the value of Y is first calculated at a particular frequency, using the procedure described above, with a knowledge of the physical dimensions of the waveguide. This value of Y is then substituted in equation {4.3} and an iteration process is then used to solve the dispersion equation of the waveguide. The dispersion characteristic of a

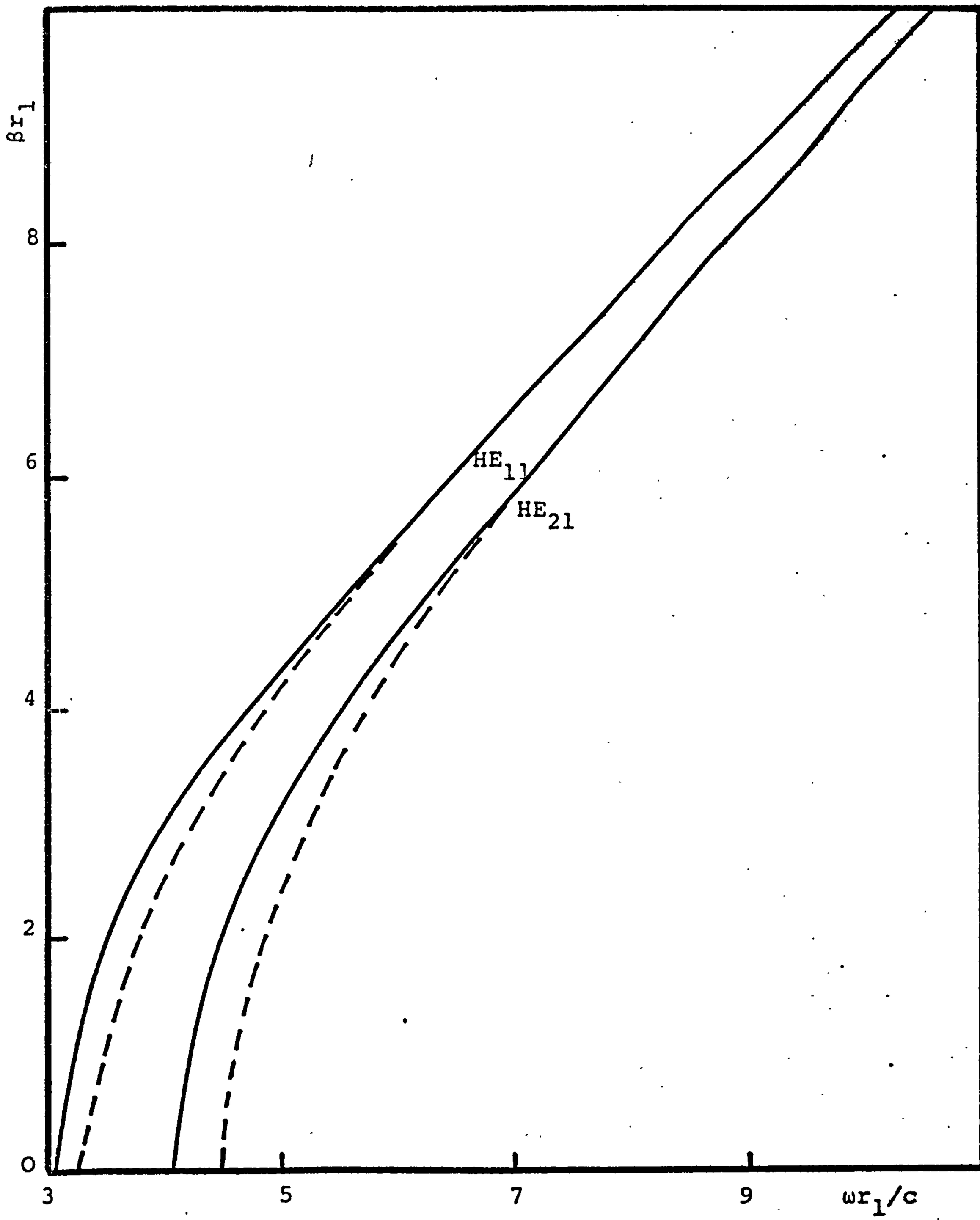

Figure (4.9) Dispersion characteristics of a corrugated circular waveguide.

$r_1/r_o = 0.8$

——— square slots ------ cosine slots

corrugated waveguide, with $r_1 = 4$ cm, $r_o = 5$ cm, containing eithersquare or cosine profile slots is shown in Figure (4.9), for the modes HE_{11} and HE_{21}, with the latter profile being approximated using 20 steps.

4.4.2 Cut-off Conditions

The low frequency cut-off condition of the modes is obtained by setting the value of the phase-change coefficient, β to zero in equation {4.3}. The resultant expression is therefore:

$$\frac{F_n(\bar{r}_1)}{(\bar{r}_1)} = Y \qquad \{4.11\}$$

In the region of $\bar{r}_1$ we are interested in, the function $F_n(\bar{r}_1)/(\bar{r}_1)$ is sketched in Figure (4.10) by the dotted curve, for n = 1.

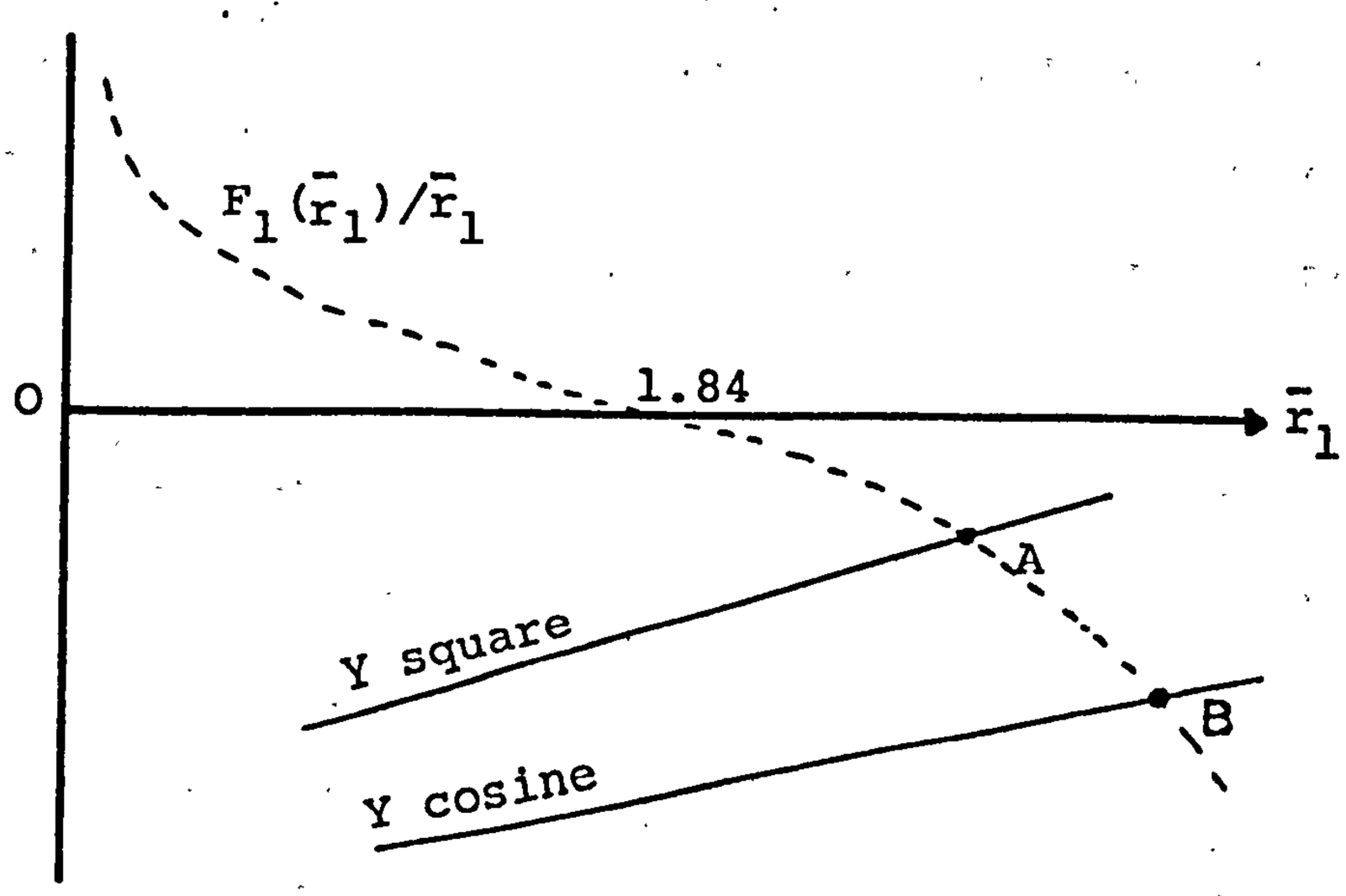

Figure (4.10)

The approximate variation of the surface admittance with respect to $\bar{r}_1$ is also shown by the continuous curves, for the case of a square and a cosine profile slot. From the trend of the curves, it can be seen that the solution of equation {4.11} for non-rectangular slots will always yield a value of r_1 greater than that obtained for a rectangular slot. Therefore, an increase in the low frequency cut-off is expected for modes propagating in a circular corrugated waveguide with non-rectangular slots. As the left hand side of equation {4.11} is not influenced by the outer radius of the waveguide, it is therefore possible to construct a circular corrugated waveguide with outer radius r_o' and with non-rectangular slots, so as to possess the same low frequency cut-off as that corresponding to a waveguide with rectangular slots and a radius r_o. From Figure (4.6) it can be seen that, if the two waveguides had the same inner radius than the ratio r_o/r_o' is < 1. In the cosine slot case, the effect of increasing r_o will merely shift the solution point B towards the point A, in Figure (4.10), where the two corresponding modes will have the same low frequency cut-off.

The high frequency cut-off of different modes occurs when the boundary at $r = r_1$ presents an open circuit condition. As the frequency is increased, from below the dominant mode cut-off, the first open circuit condition will cause the EH_{11} mode to be at cut-off, while the second condition will correspond to the high

frequency cut-off of the HE_{11} mode. Table (4.2) shows the normalised high frequency cut-off in different waveguides.

Slot Shape	Square			Cosine			Triangle		
Mode	EH_{11}	HE_{11}	EH_{12}	EH_{11}	HE_{11}	EH_{12}	EH_{11}	HE_{11}	HE_{12}
$\omega r_1/c$	6.6	8.8	9.7	19.0	20.8	21.7	31.6	33.0	33.8

Table (4.2)

4.4.3 Influence of Slot Shape

The effect, on the dispersion characteristic, of choosing different slot shapes is very pronounced at and near the low frequency cut-off. But as the frequency is increased, the effect becomes less pronounced, as shown in Figure (4.9). This phenomenon is not surprising as at such frequencies the left hand side of equation {4.3} becomes dominant and small changes in the Y value, due to the choice of different slot shapes, will not affect the overall solution of the characteristic equation.

Figure (4.11) shows the effect of changing the normalised slot admittance value, Y, on the phase-change coefficient, β, when the corrugated waveguide is operated at different normalised frequencies in the HE_{11} mode. At high values of $\bar{r}_1$, the solution will be almost independent of the slot shape. Physically, this phenomenon occurs due to the nature of the HE_{11} mode field in the central region of the waveguide. At these values of $\bar{r}_1$, the presence of the corrugated surface can be thought of as a series of convex lenses placed along the z-axis of the waveguide. These lenses act to focus the

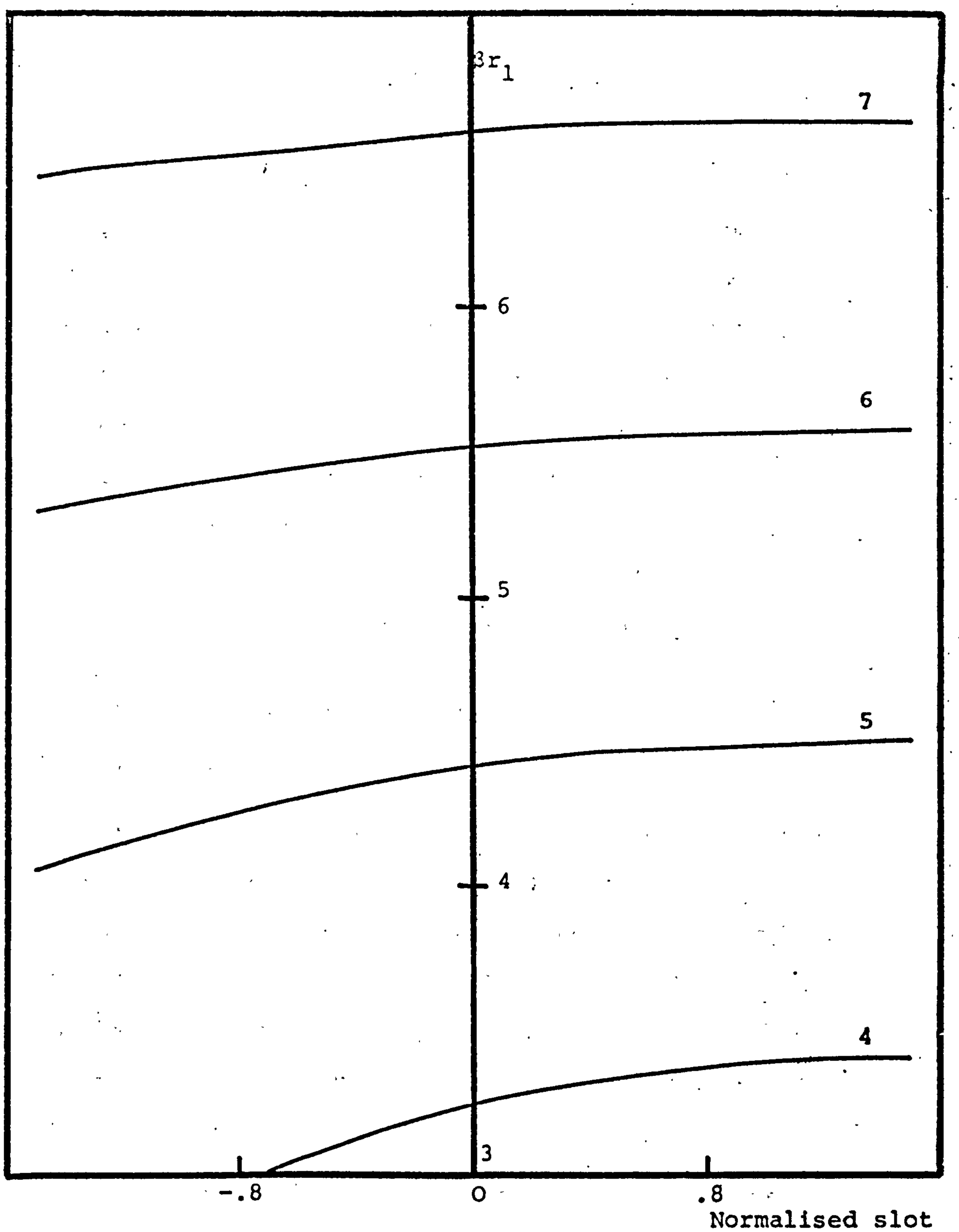

Figure (4.11) Variation of phase-change coefficient against slot admittance. HE_{11} mode in corrugated circular waveguide $r_1/r_o = 0.8$ Parameter $(\omega r_1/c)$

power, carried by the mode, towards the centre of the inner region and the field has an almost gaussian like decay towards the boundary $r = r_1$. This phenomenon, of the HE_{11} mode, also accounts for the low-loss property of the mode, as will be discussed in the next section.

However, as the frequency is further increased, the corrugated surface becomes highly inductive and the field becomes stronger near the corrugation edges. The influence on the dispersion characteristic, of the surface admittance value is again significant thus causing the different high frequency cut-off for different slot shapes, as shown in Table (4.2).

4.5 ATTENUATION CHARACTERISTIC

4.5.1 Introduction

In order to obtain the attenuation coefficient of the corrugated structure, the overall power-loss of each slot must first be calculated. The total power-loss on the sides of a single rectangular slot has been formulated <33>, and the attenuation coefficient is then calculated knowing the power flow in the central region of the waveguide.

As a result of the staircase approximation used to represent the smooth slot profile, the power-loss contribution of each individual step must first be calculated and the overall slot loss is then calculated by numerically summing up the contributions of each individual step. The increase in the surface area of

the slots, due to the stepping effect is taken into account by introducing a correction factor in the power-loss expression. The influence of the slot shapes on the overall attenuation is also discussed, and an equivalent waveguide inner radius, with non-rectangular slots, is found to give the same attenuation coefficient for waveguides with rectangular slots.

4.5.2 Slots Power-Loss

The power-loss of each individual step is divided into components associated with horizontal and vertical parts of the step, and for the q-th region, the symbols ${}_qP_h$ and ${}_qP_v$ are used respectively. Then using the field components in the q-th region given in equation {4.5 } the horizontal loss component is due to the ${}_qH_\theta$ component evaluated on the axial surface at $r = r_q$, while the vertical component ${}_qP_v$ is due to ${}_qH_\theta$ and ${}_qH_r$ components evaluated on the transverse slot surface enclosed by the radii r_q and r_{q-1}, as shown in Figure (4.12).

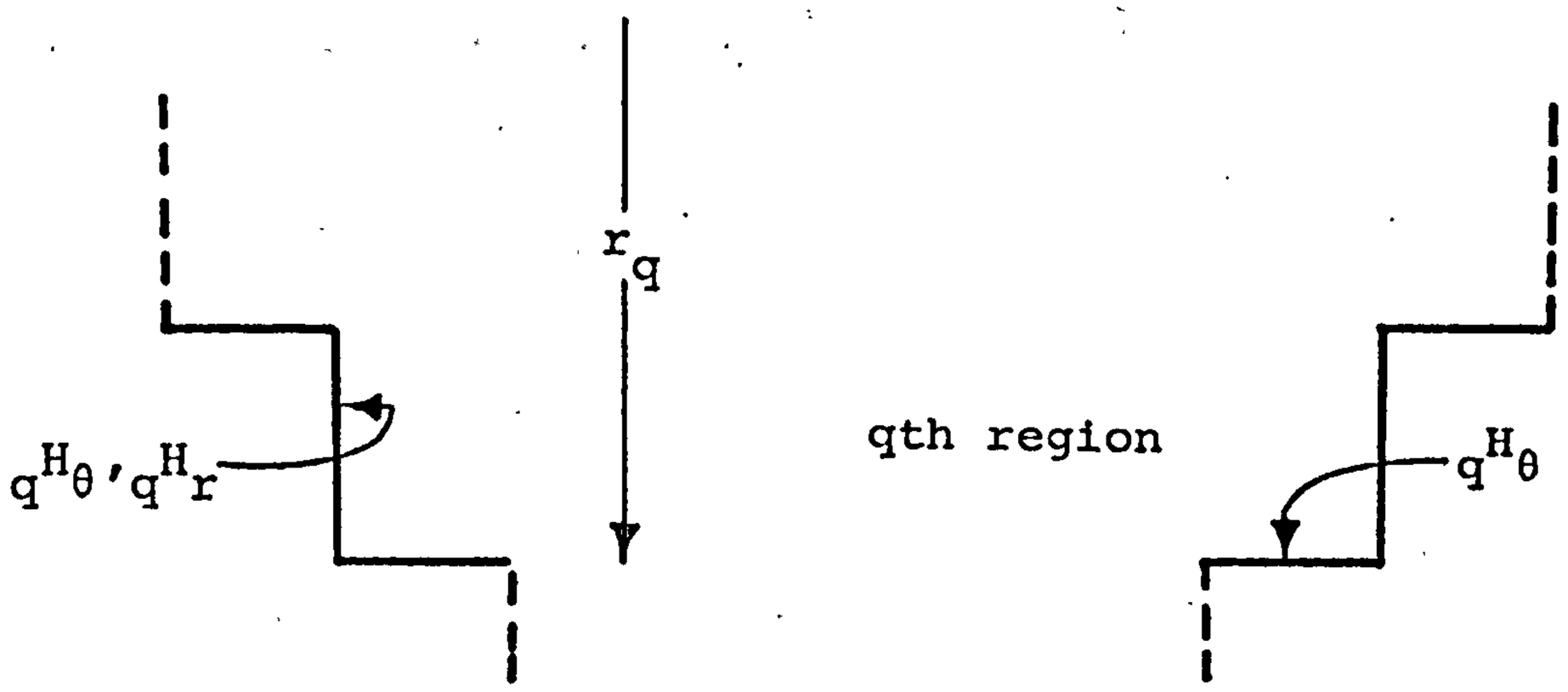

Figure (4.12)

The total power loss due to the q-th step is therefore given by;

$$ {}_qP_v + {}_qP_h = \tfrac{1}{2}R_s\left[4\pi\int_{r_{q-1}}^{r_q}(|{}_qH_\theta|^2+|{}_qH_r|^2)\,r\,dr+2\pi r_q(d_q-d_{q+1})\,|{}_qH_\theta|^2_{r=r_q}\right] $$

after simplification the vertical power-loss component can be written in the form,

$$ {}_qP_v = \frac{2\pi R_s}{\bar{r}_q^{\,2}Z_o^{\,2}}\,r_q^2\Big[\tfrac{1}{2}(\bar{r}_q^2-n^2)\{A_qJ_n(\bar{r}_q)+B_qY_n(\bar{r}_q)\}^2 $$

$$ -\tfrac{1}{2}(\bar{r}_{q-1}^2-n^2)\{A_qJ_n(\bar{r}_{q-1})+B_qY_n(\bar{r}_{q-1})\}^2 $$

$$ +\bar{r}_qA_qJ_n(\bar{r}_q)\{A_qJ_n'(\bar{r}_q)+B_qY_n(\bar{r}_q)\} $$

$$ -\bar{r}_{q-1}A_qJ_n(\bar{r}_{q-1})\{A_qJ_n'(\bar{r}_{q-1})+B_qY_n(\bar{r}_{q-1})\} $$

$$ +\bar{r}_qB_qY_n(\bar{r}_q)\{B_qY_n'(\bar{r}_q)+A_qJ_n'(\bar{r}_q)\} $$

$$ -\bar{r}_{q-1}B_qY_n(\bar{r}_{q-1})\{B_qY_n'(\bar{r}_{q-1})+A_qJ_n'(\bar{r}_{q-1})\} $$

$$ +\frac{\bar{r}_q^{\,2}}{2}\{A_qJ_n'(\bar{r}_q)+B_qY_n'(\bar{r}_q)\} $$

$$ -\frac{\bar{r}_{q-1}^{\,2}}{2}\{A_qJ_n'(\bar{r}_{q-1})+B_qY_n'(\bar{r}_{q-1})\}\Big] $$

The horizontal power-loss component have the form,

$$ {}_qP_r = \frac{\pi r_qR_s}{Z_o^{\,2}}\{A_qJ_n'(\bar{r}_q)+B_qY_n'(\bar{r}_q)\}^2(d_q-d_{q+1}) $$

The constant $C_q(=B_q/A_q)$ is computed using equation {4.7}, and the coefficient A_q is related to the central region coefficient A_1 via the relationship {4.12} derived assuming the continuity of the H_θ components at the interface of two neighbouring steps, viz

$$A_q = A_1 \bar{r}_1 \frac{J_n(Kr_1)}{(Kr_1)} \{F_n(Kr_1) - \frac{(n\bar{\beta})^2}{F_n(Kr_1)}\} \frac{\prod_{i=2}^{q} [J_n'(\bar{r}_i) + C_i Y_n'(\bar{r}_i)]}{\prod_{i=1}^{q} [J_n'(\bar{r}_i) + C_{i+1} Y_n'(\bar{r}_i)]} \quad \{4.12\}$$

The overall power-loss of the (m-1) steps profile, P_ℓ, can therefore be calculated using the relationship;

$$P_\ell = \sum_{q=2}^{m} ({}_qP_v + {}_qP_h) + 2\pi r_1 (d_1 - d_2) \cdot (|{}_1H_\theta|^2 + |{}_1H_z|^2)_{r=r_1}$$

where $d_{m+1} = 0$

The power flow in the central region, P_o, is found using the relation

$$P_o = \tfrac{1}{2} Re \int_S ({}_1\underline{E} X {}_1\underline{H}) \cdot d\underline{s}$$

The attenuation coefficient of the structure is formulated using the above expressions and is given by;

$$\alpha = \frac{P_\ell}{2d_1 P_o}$$

The staircase approximation used in synthesising the smooth profile of the slot, introduces an increase in the overall surface area of the profile. In order to account for this increase, when calculating the total

slot power-loss, an approximate correction factor must therefore be introduced to account for this increase in surface area. The attenuation coefficient α, is therefore given by;

$$\alpha = \xi \frac{P_\ell}{2d_1 P_o}$$

where the correction factor ξ is the ratio of the original smooth profile length to the overall length of the steps.

4.5.3 Influence of Slot Shapes

The attenuation characteristic of a corrugated waveguide, with r_1 = 4 cm, r_o = 5 cm, containing different slot profiles is shown in Figure (4.13) for the HE_{11} mode. The square slot profile is seen to have the lowest attenuation coefficient. By rounding the bottom corners of the slot, the attenuation is slightly increased, and further increase in the attenuation is observed if the square slots were replaced by cosine profile slots.

From Figure (4.9), it is seen that, at frequencies below the open-circuit condition frequency, it is possible to find an equivalent central region radius for waveguides with non-rectangular slots, so as to have the same attenuation coefficient as a waveguide with rectangular slots, when both waveguides are operated at the same frequency. Table (4.3) shows the equivalent inner radius needed for a corrugated circular waveguide, when different slot shapes are being used.

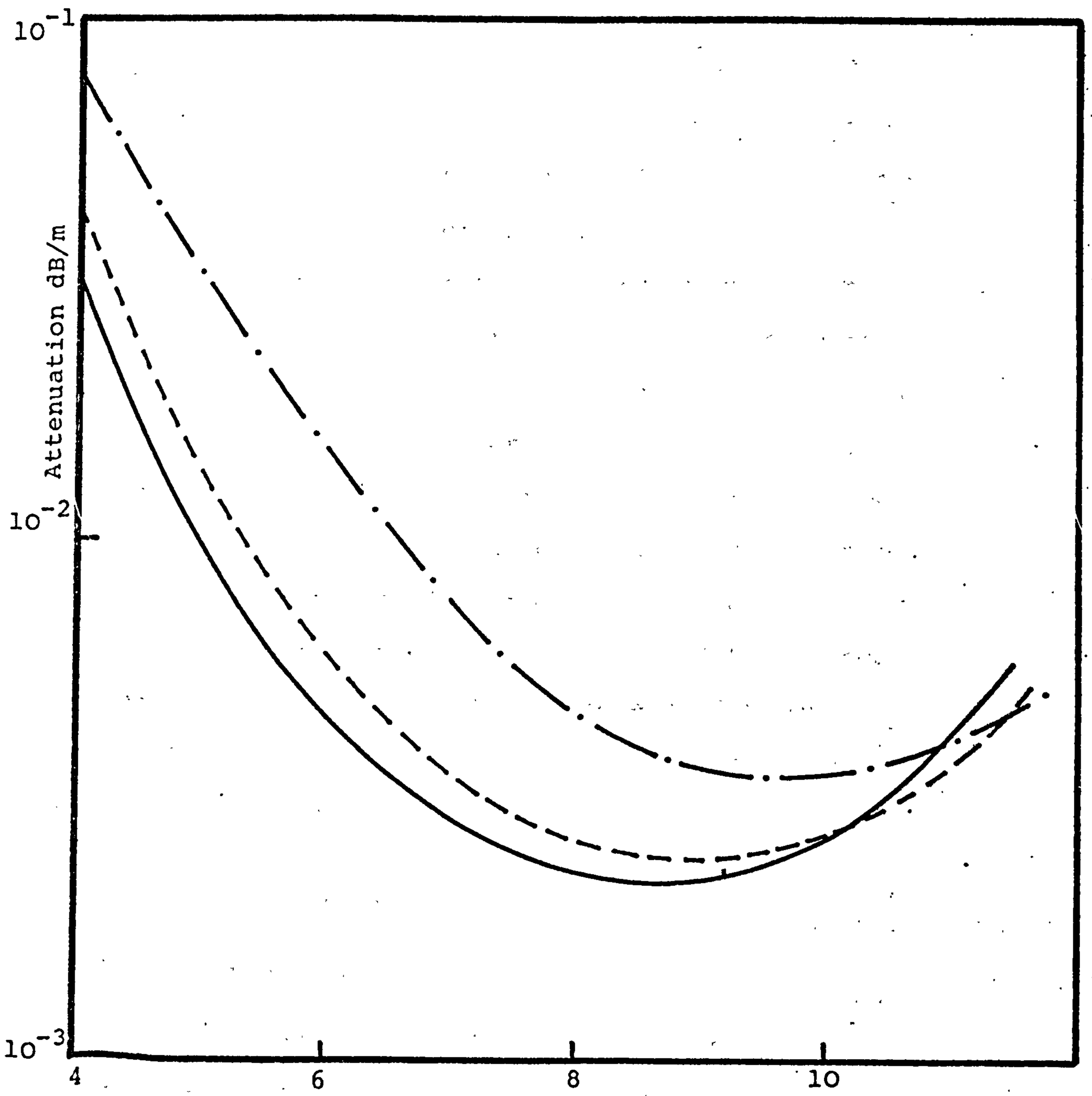

Figure (4.13) Attenuation characteristics of the HE_{11} mode in a corrugated circular waveguide.

r_1 = 4cm, r_o = 5cm, σ= 1.57 x 10^7 S/m.

-.-.-. cosine slots ----- arcs of circle plus flat base

——— square slots

SLOTS SHAPE	RECTANGULAR	COSINE	TRIANGULAR
CENTRAL REGION RADIUS	r_1	$r_1/0.75$	$r_1/0.63$

Table (4.3)

Physically, increasing the central region radius of the waveguide will merely lower the open-circuit condition frequency of the slots, as shown in Figure (4.6). This effect will cause the waveguide to have lower attenuation at a given frequency, as the open-circuit condition frequency is reached much more rapidly. At frequencies above the open-circuit condition frequency, finding an equivalent radius is no longer possible, as the slots will begin to act as an open-circuit boundary for the square profile but not for the other profiles. Minimum power-losses are expected to occur at frequencies slightly higher than the open-circuit condition frequency and due to the increase in this frequency for non-rectangular slots the shift of the minimum attenuation point is also expected.

4.6 Radiation Characteristics

4.6.1 Introduction

The boundary condition ${}_1E_\theta = 0$ at $r = r_1$ discussed in section (4.2.2), due to the presence of the surface-impedance model, yields the equation

$$n\bar{\beta} = -\bar{\Lambda}F_n(Kr_1) \qquad \{4.13\}$$

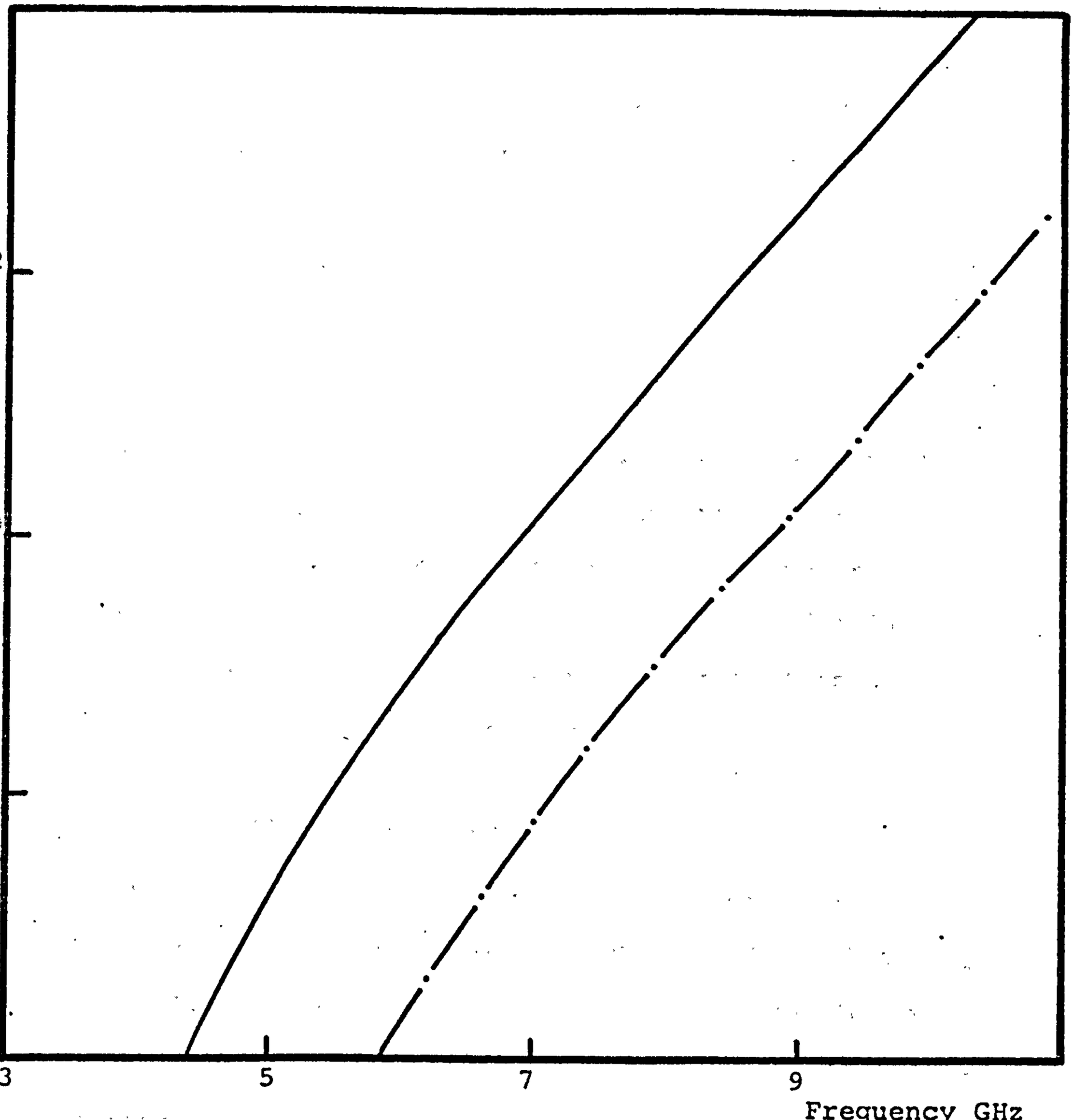

Figure (4.14) Normalised hybrid factor against frequency.
HE_{11} mode. Parameters as Figure (4.13)

——— square slots —.—.—.—. cosine slots

where $\bar{\Lambda}$ is a scalar factor, known as the hybrid coefficient, and is defined by the expression

$$-jY_o\bar{\Lambda} = {}_1H_z/{}_1E_z$$

Its modulus, $|\bar{\Lambda}|$, is therefore defined as the ratio of the longitudinal admittance of the wave to the free space wave admittance. When the slots act as an open-circuit boundary, the characteristic equation {4.3}, reduces to the form;

$$n\bar{\beta} = \pm F_n(Kr_1) \qquad \{4.14\}$$

Comparing equations {4.13} and {4.14}, it can be deduced that under this condition $\bar{\Lambda} = \mp 1$, this is known as the balanced hybrid condition. Physically, this condition means that if the waveguide is terminated and radiation from its open end is allowed, the radiation pattern in both E and H planes will be identical.

4.6.2 Influence of Slot Shapes

As the open-circuit boundary condition is affected by the slots shape in the waveguide, Figure (4.6), then a change in the frequency where balanced hybrid condition occurs is also expected. This change must be towards higher frequencies for circular waveguides with non-rectangular slots in order to follow the open-circuit frequency condition. Figure (4.14) shows the theoretical variation in $\bar{\Lambda}$ against normalised frequency when a corrugated waveguide is operated in the HE_{11} mode, with either square

or cosine slots. The shift in the frequency where balanced hybrid condition occurs is clearly illustrated.

4.6.3 Experimental Results

The frequency at which balanced hybrid condition occurs for a flexible corrugated waveguide was at 8.0 GHz, when calculated using the space-harmonic theory, which assumes rectangular slots profile. The exact profile slot of the flexible waveguide was then used to obtain the true balanced hybrid condition frequency, using the step approximation theory developed above, and it was found to occur at 9.6 GHz. Due to the large difference between the two frequencies, an experiment was carried out to locate the frequency at which the balanced hybrid condition occurs. The radiation pattern of the waveguide was measured at different frequencies in both E and H planes, and the results were then compared at corresponding frequencies. Figures (4.15) and (4.16) show the measured radiation pattern at 8.0 and 9.6 GHz respectively, where the narrow beam of the E plane pattern is illustrated, and also the increased rate of change of the E plane pattern with respect to frequency, over the H plane pattern is also shown.

At each particular frequency the difference between the E and H planes beam widths is measured at different power points below the OdB point. The differences were found to be very pronounced at frequencies below and above 9.3 GHz. This confirms

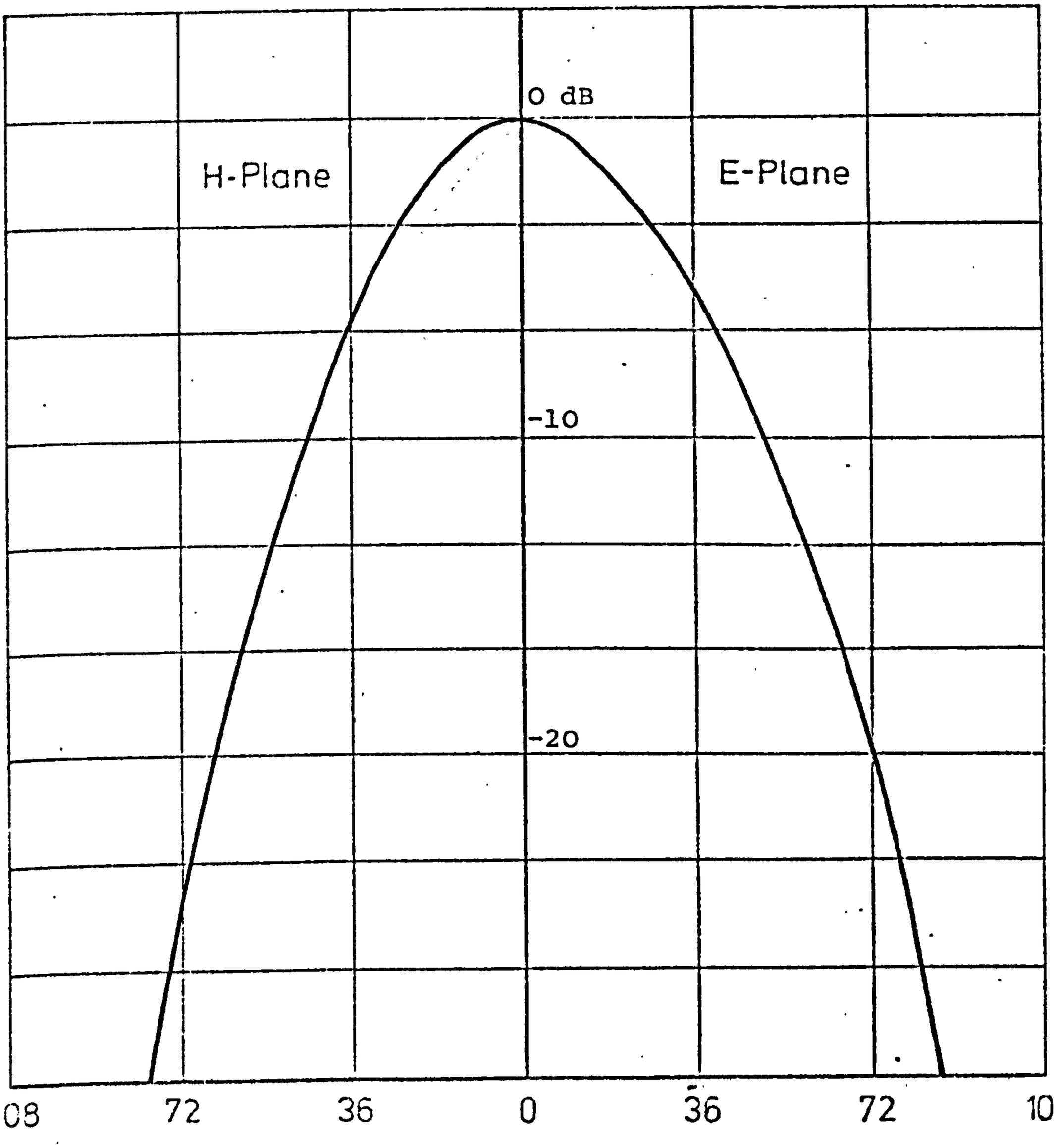

Figure (4.15) Measured radiation patterns of a corrugated circular waveguide.
HE_{11} mode

r_1 = 2.54cm. f = 8.0 GHz

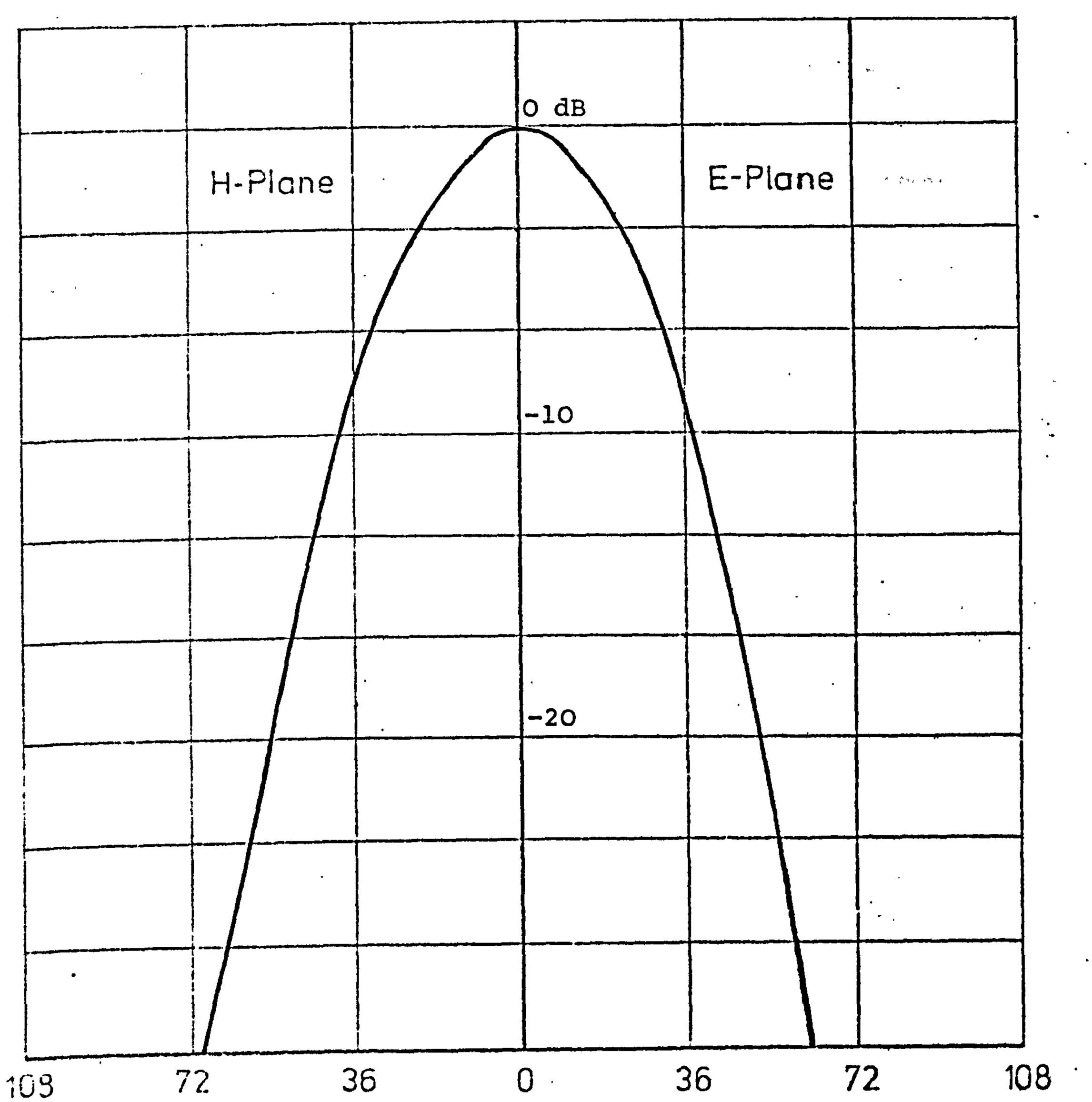

Figure (4.16) Measured radiation patterns of a corrugated circular waveguide.
HE_{11} mode.

r_1 = 2.54 cm, f = 9.6 GHz

the theoretical results within 3% error, this error is expected in measuring techniques used to determine radiation patterns. For waveguides with rectangular slots Saha, <33 >, found a very good agreement between the theoretical and experimental values of balanced hybrid condition frequency. The difference of 14% in this case clearly demonstrates the effect of using non-rectangular slots on the open circuit condition frequency and thus confirms the shift in the balanced hybrid condition frequency.

CHAPTER FIVE

A NEW MODE FILTER FOR USE IN CORRUGATED CIRCULAR WAVEGUIDES

5.1 INTRODUCTION

The circumstance under which the corrugated waveguide exhibits low-attenuation is also one which permits more than one mode to propagate. If the input and output waveguides support only a single mode then the higher order modes in the connecting waveguide cause trapped mode resonance, see for example the typical transmission characteristics as a function of frequency, shown in Figure (5.1). In most microwave communication systems stringent requirements exist for a flat transmission characteristic as non-linearities cause co-channel interference in a broadband multi-channel system. A characteristic such as in Figure (5.1) is unacceptable, thus in a practical system, higher modes must be severely attenuated without appreciably increasing the attenuation of the dominant mode. This chapter is concerned with the design of a filter to accomplish this objective.

One type of mode filter consists of a suitable metallic screen placed in the transverse plane of the waveguide <40>. The screen is so designed that the undesirable mode or modes are reflected without affecting the transmission of the desired mode. For example, a screen can be designed with thin wires along the direction of the transverse electric fields for the undesirable modes provided the desired mode has no transverse electric field along the same direction.

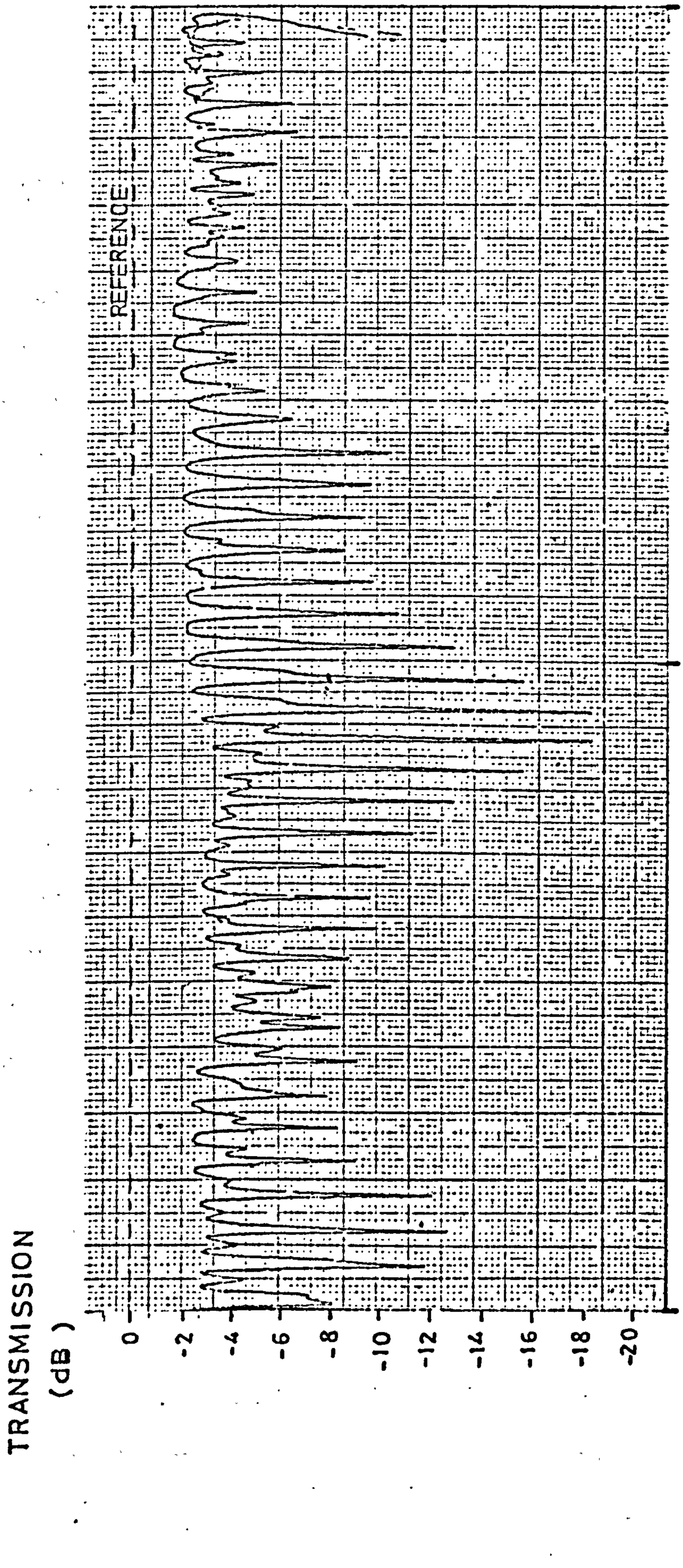

Transmission characteristics of a flexible corrugated waveguide <4>

Figure (5.1)

Sometimes, it may be undesirable to reflect the unwanted modes back into the waveguide <41 >, instead it may be preferable that they are absorbed by some means. The means adopted should be one that will absorb the unwanted modes without materially reflecting the desired mode. As a practical matter it is impossible to achieve perfect reflection or absorption for all undesirable modes without influencing the desired mode. Therefore, in multimode waveguides, mode filters are introduced to provide sufficient differential transmission loss between the unwanted modes and the desired mode.

The corrugated circular structure shown in Figure (4.1) is a multimode waveguide, supporting the desired low-attenuation HE_{11} mode and other unwanted modes. The HE_{11} mode comprises an almost linearly polarised field <33>, and bears a close resemblance to the dominant HE_{11} mode of the optical waveguide <21>. Because of this similarity between the modes in the two structures, the unimode optical waveguide features will be utilized in proposing a mode filter for the corrugated circular waveguide.

A study of the field distribution of the unwanted modes in the empty corrugated waveguide gave rise to the mode filter structure shown in Figure (5.2), which provides sufficient differential attenuation between the unwanted modes and the desired HE_{11} mode in the corrugated waveguide. By arranging that the central core has a permittivity greater than that of the surrounding cladding,

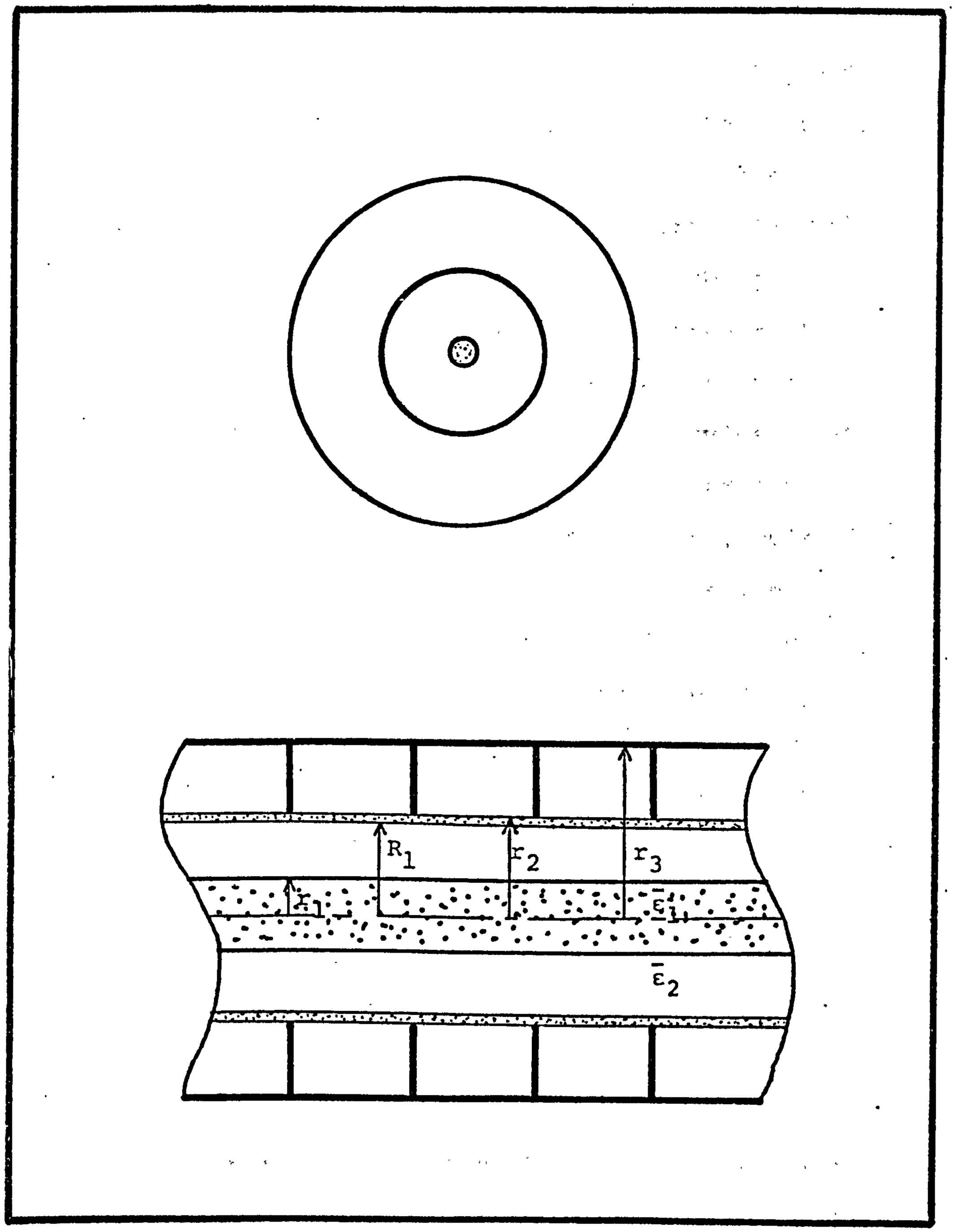

Figure (5.2) Corrugated circular waveguide containing a mode filter

it is possible to arrange that only the desired HE_{11} mode propagates with most of its field confined to the core region of the mode filter. The unwanted modes have fields extending radially well beyond the core. Then if a lossy layer is provided it will act to absorb the energy carried by these modes, and thus a substantial differential attenuation can be achieved between the desired HE_{11} mode and the unwanted modes. Provided that the core region has a very low-loss tangent, and its diameter is arranged to confine most of the HE_{11} mode power, then the influence of the lossy layer on the desired mode can be rendered almost negligible. When small sections of the proposed mode filter are inserted in the empty corrugated waveguide, it is immediately recognised that a means must be devised to provide the desired HE_{11} mode with minimum reflection at the junction between the empty section of the corrugated waveguide and the section containing the mode filter.

This chapter aims to identify suitable parameters for the proposed concentric mode filter for use, in existing circular corrugated waveguides, at the frequency of minimum attenuation of the HE_{11} mode. The general principles can also be applied at other frequencies. The dispersion and attenuation characteristics of the corrugated waveguide, containing the mode filter, for the desired mode and two of the unwanted modes are illustrated. The design of a matching device for the mode filter is explained in detail in the

latter sections of this chapter.

Finally, experimental results obtained with a corrugated circular waveguide containing the proposed mode filter clearly illustrate the suppression of the unwanted modes and also the effectiveness of the matching device at the design frequency.

5.2 FORMULATION OF THE PROBLEM

5.2.1 Introduction

The structure proposed which will least affect the lowest attenuating HE_{11} mode and at the same time set to absorb the unwanted propagating modes in the corrugated circular waveguide is shown in Figure (5.2).

The core region, $0 < r < r_1$ consists of a dielectric material of relative permittivity $\bar{\varepsilon}_1$ and very low loss angle δ_1. The cladding region, $r_1 < r < R_1$ of relative permittivity $\bar{\varepsilon}_2 (< \bar{\varepsilon}_1)$ and loss angle δ_2, acts as a low-loss support for the core region. The absorption of the unwanted modes is achieved by placing a thin lossy layer $R_1 < r < r_2$, of relative permittivity $\bar{\varepsilon}_2$ and loss angle δ_3 near the corrugation edge.

A solution of the wave equation is obtained assuming a loss-free structure and perturbation techniques are then used to obtain the dielectric power-loss in different regions of the waveguide and the metal power-loss of the corrugation region. The influence of the different parameters on the attenuation coefficient

of different modes is studied in order to achieve the highest possible differential attenuation between the HE_{11} mode and the unwanted modes. The TE_{01} mode and the HE_{21} mode are chosen as a basis of comparison for the unwanted modes. This is because the HE_{11} mode couples easily into these modes when bends are negotiated <4>, and secondly due to their low attenuation characteristic when compared with other higher order modes <1>. Field expressions obtained in the next section are based on the assumption that the structure shown in Figure (5.2) extends to infinity at either end.

5.2.2 Field Components

In the core region, $0 < r < r_1$, solutions of the wave equation have the form

$$
\begin{aligned}
{}_1E_z &= A_1 J_n(K_1 r)\cos n\theta \\
{}_1H_z &= C_1 Y_o J_n(K_1 r)\sin n\theta
\end{aligned}
\qquad \{5.1\}
$$

Field expressions written in this form satisfy the boundary condition for finite field at the origin r = 0, where A_1, C_1 are amplitude coefficients, $Y_o = \sqrt{\varepsilon_o/\mu_o}$ $K_1^2 = \omega^2 \bar{\varepsilon}_1 \varepsilon_o \mu_o - \beta^2$, and β being the phase-change coefficient. The transverse field components are obtained using Appendix I;

$$_1E_\theta = \left[j \frac{n\beta}{K_1^2 r} A_1 J_n(K_1 r) + j\frac{k}{K_1} C_1 J_n'(K_1 r) \right] \sin n\theta$$

$$_1H_\theta = Y_o \left[-j \frac{n\beta}{K_1^2 r} C_1 J_n(K_1 r) - j \frac{k\varepsilon_1}{K_1} A_1 J_n'(K_1 r) \right] \cos n\theta$$

$$_1E_r = \left[-j \frac{\beta}{K_1} A_1 J_n'(K_1 r) - j \frac{nk}{K_1^2 r} C_1 J_n(K_1 r) \right] \cos n\theta$$

$$_1H_\theta = Y_o \left[-j \frac{\beta}{K_1} C_1 J_n'(K_1 r) - j \frac{nk\varepsilon_1}{K_1^2 r} A_1 J_n(K_1 r) \right] \sin n\theta$$

where $k^2 = \omega^2 \varepsilon_o \mu_o$ and ω = angular frequency.

In the second dielectric region $r_1 < r < r_2$, the field components have the following form;

$$_2E_z = \left[A_2 J_n(K_2 r) + B_2 Y_n(K_2 r) \right] \cos n\theta$$

$$_2H_z = Y_o \left[C_2 J_n(K_2 r) + D_2 Y_n(K_2 r) \right] \sin n\theta$$

$$_2E_\theta = \left(j \frac{n\beta}{K_2^2 r} \left[A_2 J_n(K_2 r) + B_2 Y_n(K_2 r) \right] + j\frac{k}{K_2} \left[C_2 J_n'(K_2 r) + D_2 Y_n'(K_2 r) \right] \right) \sin n\theta$$

$$_2H_\theta = Y_o \left(-j \frac{n\beta}{K_2^2 r} \left[C_2 J_n(K_2 r) + D_2 Y_n(K_2 r) \right] - j \frac{k\varepsilon_2}{K_2} \left[A_2 J_n'(K_2 r) + B_2 Y_n'(K_2 r) \right] \right) \cos n\theta$$

$$_2E_r = \left(-j \frac{\beta}{K_2} \left[A_2 J_n'(K_2 r) + B_2 Y_n'(K_2 r) \right] - j \frac{nk}{K_2^2 r} \left[C_2 J_n(K_2 r) + D_2 Y_n(K_2 r) \right] \right) \cos n\theta$$

$$2H_r = Y_o\left[-j\,\frac{\beta}{K_2}\left[C_2J_n'(K_2r)+D_2Y_n'(K_2r)\right]\right.$$
$$\left.-j\,\frac{nk\bar{\varepsilon}_2}{K_2^2r}\left[A_2J_n(K_2r)+B_2Y_n(K_2r)\right]\right]\sin n\theta \qquad \{5.3\}$$

where A_2, B_2, C_2 and D_2 are amplitude coefficients and $K_2^2 = \omega^2\varepsilon_o\bar{\varepsilon}_2\mu_o - \beta^2$.

In the above field expressions, a factor $\exp j(\omega t-\beta z)$ is assumed.

The slots, $r_2 < r < r_3$ are assumed to support a TM cut-off mode; an account of this assumption is given in chapter (4) and in <4> and <33>. Field components satisfying the boundary conditions at the metal wall $r = r_3$, are given by;

$$3E_z = \frac{A_3}{Y_n(kr_3)}\left[J_n(kr)Y_n(kr_3)-Y_n(kr)J_n(kr_3)\right]\cos n\theta$$

$$3H_\theta = -j\,Y_o\,\frac{A_3}{Y_n(kr_3)}\left[J_n'(kr)Y_n(kr_3)-Y_n'(kr)J_n(kr_3)\right]\cos n\theta$$

$$3H_r = -j\,Y_o\,\frac{nk}{k^2r}\,\frac{A_3}{Y_n(kr_3)}\left[J_n(kr)Y_n(kr_3)-Y_n(kr)J_n(kr_3)\right]\sin n\theta$$

$\{5.4\}$

where A_3 is an amplitude coefficient, and the primed Bessel functions means first derivatives with respect to their arguments.

5.2.3 Boundary Conditions

At the boundary $r = r_1$, the boundary conditions; equal tangential electric and magnetic field components are applied to relate the amplitude coefficients in the two regions; i.e.

$$A_1 J_n(K_1 r_1) - A_2 J_n(K_2 r_1) - B_2 Y_n(K_2 r_1) = 0$$

$$C_1 J_n(K_1 r_1) - C_2 J_n(K_2 r_1) - D_2 Y_n(K_2 r_1) = 0$$

$$\frac{n}{r_1} A_1 J_n(K_1 r_1) + kK_1 C_1 J_n'(K_1 r_1) - \frac{n\beta}{r_1} K^2 \left[A_2 J_n(K_2 r_1) + B_2 Y_n(K_2 r_1)\right]$$

$$- kK_2 K^2 \left[C_2 J_n'(K_2 r_1) + D_2 Y_n'(K_2 r_1)\right] = 0$$

$$kK_1 \bar{\varepsilon}_1 A_1 J_n'(K_1 r_1) + \frac{n\beta}{r_1} C_1 J_n(K_1 r_1) - kK_2 K^2 \bar{\varepsilon}_2 \left[A_2 J_n'(K_2 r_1) + B_2 Y_n'(K_2 r_1)\right]$$

$$- \frac{n\beta}{r_1} K^2 \left[C_2 J_n(K_2 r_1) + D_2 Y_n(K_2 r_1)\right] = 0$$

where $K^2 = (K_1/K_2)^2$

A surface impedance model is used to represent the boundary at $r = r_2$ of Figure (5.2), i.e. the ratio E_z/H_θ is assumed to be invariant with respect to the propagation z-direction. This impedance model also implies a vanishing azimuthal electric field component at this boundary. The above conditions yield;

$$\frac{n\beta}{r_2} \left[A_2 J_n(K_2 r_2) + B_2 Y_n(K_2 r_2)\right] + kK_2 \left[C_2 J_n'(K_2 r_2) + D_2 Y_n'(K_2 r_2)\right]$$

$$= 0$$

and equating ${}_2H_\theta/{}_2E_z$ to ${}_3H_\theta/{}_3E_z$ yields

$$\frac{\frac{n\beta}{K_2^2 r_2}\left[C_2 J_n(K_2 r_2)+D_2 Y_n(K_2 r_2)\right]+\frac{k\bar{\varepsilon}_2}{K_2}\left[A_2 J_n'(K_2 r_2)+B_2 Y_n'(K_2 r_2)\right]}{A_2 J_n(K_2 r_2) + B_2 Y_n(K_2 r_2)}$$

$$= \frac{S_n(Kr_2, kr_3)}{kr_2}$$

where

$$S_n(x,y) = x\,\frac{J_n'(x)Y_n(y) - J_n(y)Y_n(x)}{J_n(x)Y_n(y) - J_n(y)Y_n(x)}$$

The validity of the above approximation is justified provided that the number of slots per wavelength is large, a detailed account of this approximation appears in <4>.

5.2.4 Characteristic Equation

In order to obtain the dispersion characteristics of the loaded corrugated waveguide, it is necessary to solve the characteristic equation relating ω and β. The set of equations derived in the previous section completely describes the propagation of the hybrid modes in the structure and this set is homogeneous in the arbitrary amplitude coefficients A_1, C_1, A_2, B_2, C_2 and D_2.

The set of equations when written in a matrix form is

$$\underline{D}.\underline{X} = 0 \qquad \{5.5\}$$

where $\underline{D}$ is a square matrix of order 6 x 6 and its elements are the field component functions, and $\underline{X}$ is a 6 column vector consisting of the amplitude coefficients. For non-trival solution of equation {5.5} the determinant of $\underline{D}$ must vanish, i.e.

$$\det \underline{D} = 0 \qquad \{5.6\}$$

Equation {5.6} is the characteristic equation of the structure since det $\underline{D}$ can be expanded into a single equation. On solving {5.6} for ω and β, the dispersion characteristics are obtained. This operation is performed numerically on a digital computer. In the process of solving the characteristic equation, it is also necessary to evaluate the associated arbitrary constants which are required in the computation of power, attenuation, and field components. For a general matrix equation with non-trival solution, i.e.

$$\underline{D}.\underline{X} = O$$

where $\underline{D}$ is a singular matrix of order m x m with det $\underline{D}$ = O and $\underline{X}$ is a column vector with m elements

$$\underline{X} = (X_1, X_2, - - - X_m)$$

the value of the elements are given by

$$X_j = L_{1j} \quad (j = 1, 2, - - - m)$$

where L_{1j} is the co-factor of the j-th element in the

i-th row of det $\underline{D}$. The row number is immaterial because the value of the co-factor is independent of the row, which means

$$L_{1j} = L_{2j} = - - - = L_{mj}$$

The value of $\underline{X}$ so evaluated is not, however, absolute since it can be multiplied by any arbitrary constant without affecting the validity of the equation $\underline{D}.\underline{X} = 0$. $\underline{X}$ is normalised with respect to the element with maximum modulus.

5.2.5 Dispersion Characteristics

Computed dispersion characteristics of the circular corrugated waveguide is illustrated in Figure (5.3), for the two cases of an empty and loaded waveguide. Expanded foam of relative permittivity 1.02 is used to support the core region of relative permittivity 2.25 and 1 cm. radius.

The effect of the core region on the dispersion curves of different modes is clearly illustrated in Figure (5.3), where its effect is seen to be most significant on the HE_{11} mode. This is due to the field concentration of this mode in the central region of the waveguide.

The value of the normalised phase-change coefficient $\bar{\beta}(=\beta/k)$ falls in three ranges for all the modes;

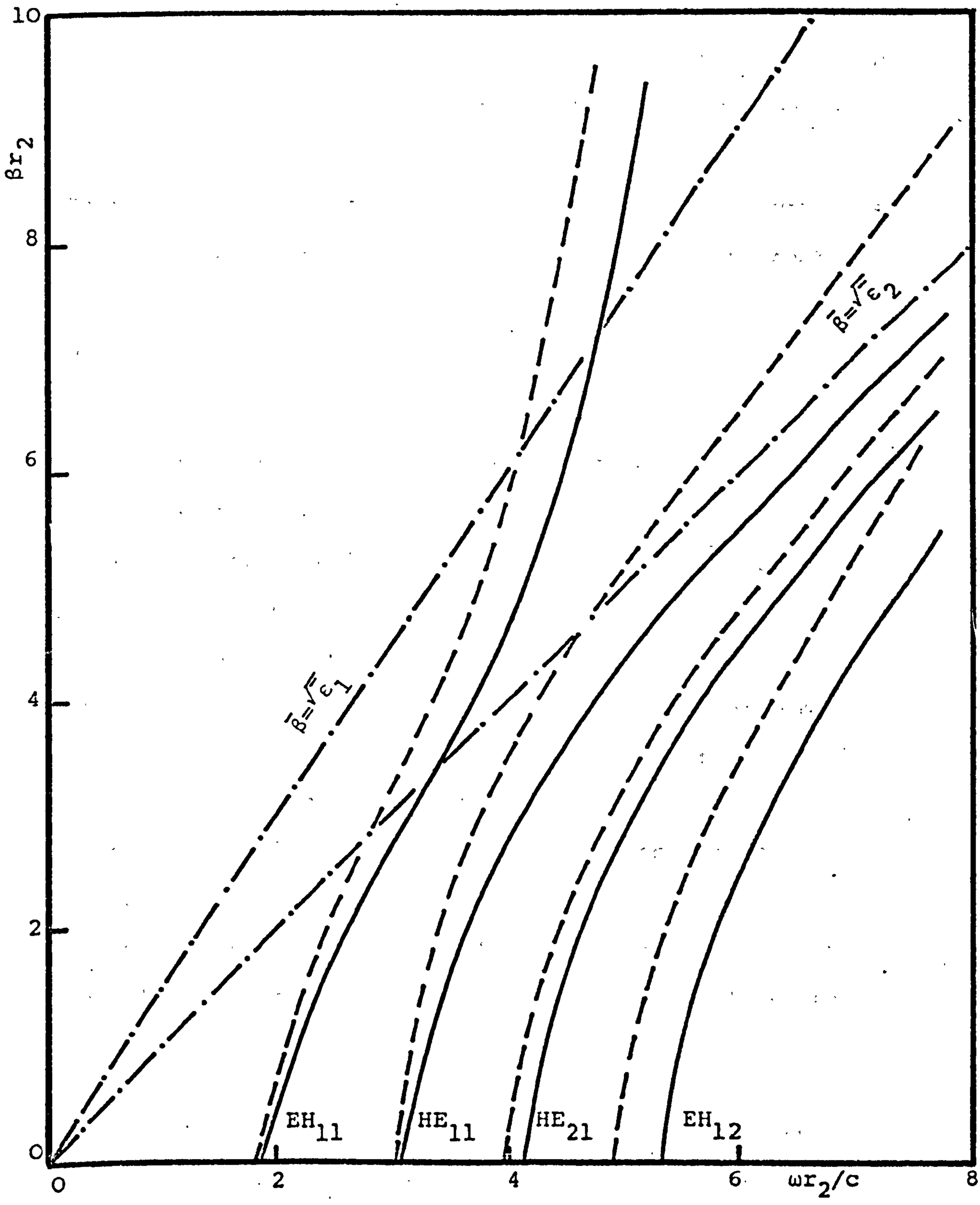

Figure (5.3) Dispersion characteristics in corrugated circular waveguide

——— without dielectric rod $r_2 = 4cm$ $r_3 = 5cm$

----- with dielectric rod $r_1 = 1cm$ $\bar{\epsilon}_1 = 2.25$

$\bar{\epsilon}_2 = 1.02$

(a) $0 < \bar{\beta} < \sqrt{\bar{\varepsilon}_2}$

The cut-off frequency of different modes supported by an empty corrugated circular waveguide decreases when an axial dielectric region is present in the waveguide. Figure (5.4) shows as a function of r_2/r_1, the normalised cut-off frequency for different modes which approaches that of the empty corrugated waveguide for large values of r_2/r_1.

The influence of the core region on the modes with power distribution not concentrated in the central region of the waveguide, is not significant, and their characteristics in this part of the range of $\bar{\beta}$ are similar to modes supported by a corrugated waveguide filled with a dielectric material of relative permittivity $\bar{\varepsilon}_2$. On the other hand, the influence of the core region on the HE_{11} mode, whose power distribution is mainly in the central region of the waveguide is significant and its field concentration in the central region rises with increasing frequency. For this part of the range of $\bar{\beta}$, the arguments of the Bessel functions in all field expressions will be real.

(b) $\sqrt{\bar{\varepsilon}_2} < \bar{\beta} < \sqrt{\bar{\varepsilon}_1}$

when $\bar{\beta}$ is greater than $\sqrt{\bar{\varepsilon}_2}$, the mode becomes a slow wave whose energy is mainly concentrated in the core region of the waveguide. The influence of the core region on the HE_{11} mode is very significant and weak power distribution outside the core region is expected

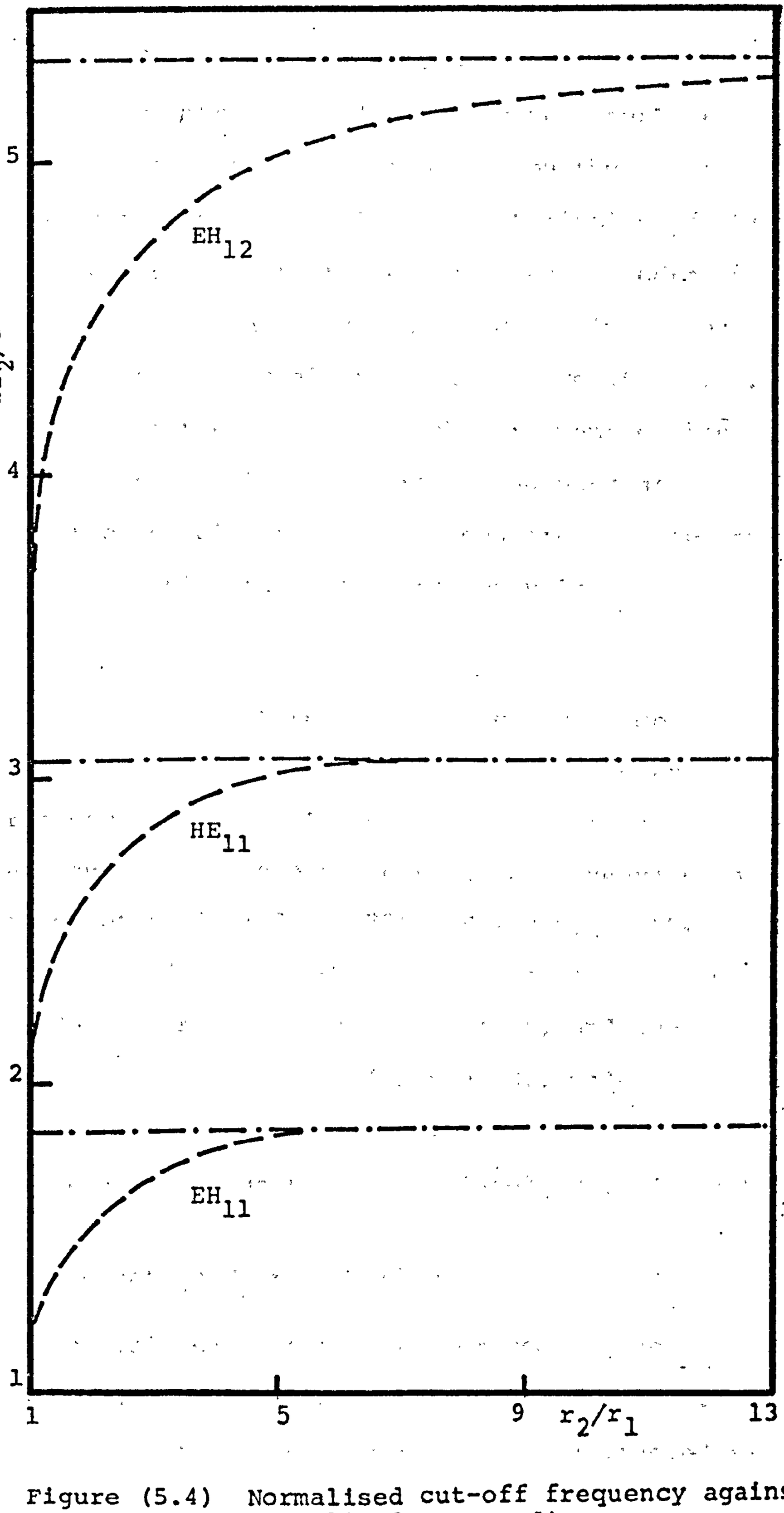

Figure (5.4) Normalised cut-off frequency against normalised core radius

$\bar{\varepsilon}_1 = 2.25 \quad r_2/r_3 = 0.8$

for this mode. This form of power distribution for the HE_{11} mode formsthe very basis of the mode filter design, and thus the mode filter parameters must be chosen so that in the region of operation the value of $\bar{\beta}$ falls within this range. The characteristics of the modes are very similar to those exhibited by modes in a corrugated circular waveguide when completely filled with a dielectric material of relative permittivity ε_1. For this part of the range of $\bar{\beta}$, the argument of the Bessel functions in {5.3} is purely imaginary and therefore the Bessel J and Y functions are replaced by the modified I and K functions respectively.

(c) $\sqrt{\varepsilon_1} < \bar{\beta} \rightarrow \infty$

Due to the periodic nature of the waveguide under investigation, different modes will have different high-frequency cut-off. An account of the high-frequency cut-off in an empty corrugated waveguide is given in chapter (4) and in <33>. However, in the loaded corrugated waveguide the high-frequency cut-off of the modes occurs at lower frequencies, and the decrease is very significant for the HE_{11} mode. The Bessel functions arguments in {5.1}, {5.2} are purely imaginary and the J function is replaced by an I function.

5.2.6 Attenuation Characteristics

The field expressions are derived in the previous section assuming a loss-free structure, i.e. the imaginary part of the permittivity is neglected and

one assumes perfectly conducting metal slots. It is possible to formulate and solve the characteristic equation in complex mathematical form to obtain an exact solution. This method is, however, lengthy and involved. The attenuation coefficient can be more conveniently found by the perturbation method <24> which is accurate for small dielectric loss and sufficient for the present purpose.

The attenuation coefficient α per unit length of the loaded corrugated waveguide consists of two components

$$\alpha = \tfrac{1}{2}(\alpha_d + \alpha_m)$$

where α_d is the normalised dielectric power-loss and α_m is the normalised metal power-loss. Applying the first order perturbation formula, the normalised dielectric power-loss can be written in the form;

$$\alpha_d = \frac{\omega[\bar{\varepsilon}_1 \tan\delta_1 P_1 + \bar{\varepsilon}_2 \tan\delta_2 P_2 + \bar{\varepsilon}_2 \tan\delta_3 P_2']}{2P_o}$$

The three terms are due to the power-loss in the core, cladding and lossy layers respectively, with

$$P_1 = \int_0^{2\pi} \int_0^{r_1} {}_1\underline{E}\ r\,dr\,d\theta,$$

$$P_2 = \int_0^{2\pi} \int_{r_1}^{R_1} {}_2\underline{E}\ r\,dr\,d\theta + \int_0^{2\pi} \int_{R_2}^{r_2} {}_2\underline{E}\ r\,dr\,d\theta,$$

$$P_2' = \int_0^{2\pi} \int_{R_1}^{r_2} {}_2\underline{E}\, r dr d\theta, \qquad \{5.7\}$$

P_o = average power flow in the waveguide

where ${}_q\underline{E} = {}_qE_z{}^2 + {}_qE_r{}^2 + {}_qE_\theta{}^2$. The lossy layer of relative permittivity $\bar{\varepsilon}_2$ and loss angle δ_3 is assumed to lie within the radial co-ordinate R_1 and R_2. In Figure (5.2) the lossy layer is situated such that $R_2 = r_2$. The normalised metal power-loss is obtained by calculating the power-loss in metal surfaces of a single unit cell of the corrugations, i.e.

$$\alpha_m = \frac{R_s (P_4+P_5+P_6)}{2P_o D}$$

where P_4 due to the top of a ridge at $r = r_2$,

P_5 due to the two side walls of a slot and

P_6 due to the base of a slot

R_s = surface resistivity of the metal.

Therefore,

$$P_4 = (D-d) r_2 \int_0^{2\pi} |{}_2H_\theta|^2_{r=r_2}\, d\theta,$$

$$P_5 = 2 \int_0^{2\pi} \int_{r_2}^{r_3} ({}_3H_\theta{}^2 + {}_3H_r{}^2) r dr d\theta$$

and

$$P_6 = dr_3 \int_0^{2\pi} |{}_3H_\theta{}^2|_{r=r_3}\, d\theta,$$

where d is the slot width and (D-d) is the ridge width.

$$P_o = \tfrac{1}{2}\int_0^{2\pi}\int_0^{r_1}({}_1E_{r1}H_\theta^* - {}_1E_{\theta 1}H_r^*)\,r\,dr\,d\theta + \tfrac{1}{2}\int_0^{2\pi}\int_{r_1}^{r_2}({}_2E_{r2}H_\theta^* - {}_2E_{\theta 2}H_r^*)\,r\,dr\,d\theta$$

Analytical techniques were first used to obtain closed form expressions for the above integrals. These techniques appear in <21> for the dielectric power losses and in <33> for the metal power losses. The total electric field distribution ${}_q\underline{E}$ is clearly a major factor influencing the dielectric loss component, thus a study of the electric field distribution of the HE_{11} mode should prove useful in positioning the lossy layer in the waveguide.

5.3 PROPERTIES OF HE_{11} MODE

5.3.1 Field Distribution

The magnitude of the normalised total electric field in a loaded corrugated circular waveguide is plotted in Figure (5.5) as a function of waveguide radius. The discontinuity at the core-cladding interface, $r = r_1$, is due to the discontinuity in the E_r component at this boundary. The curve shows a decrease in the magnitude towards the slot edge, $r = r_2$, where it has a minimum value. Therefore, in order to minimise the attenuation of the HE_{11} mode caused by the presence of a lossy layer, this layer must be positioned near the corrugation edge, as shown in Figure (5.2). The presence of the core region concentrates the HE_{11} mode power into the central region of the waveguide and

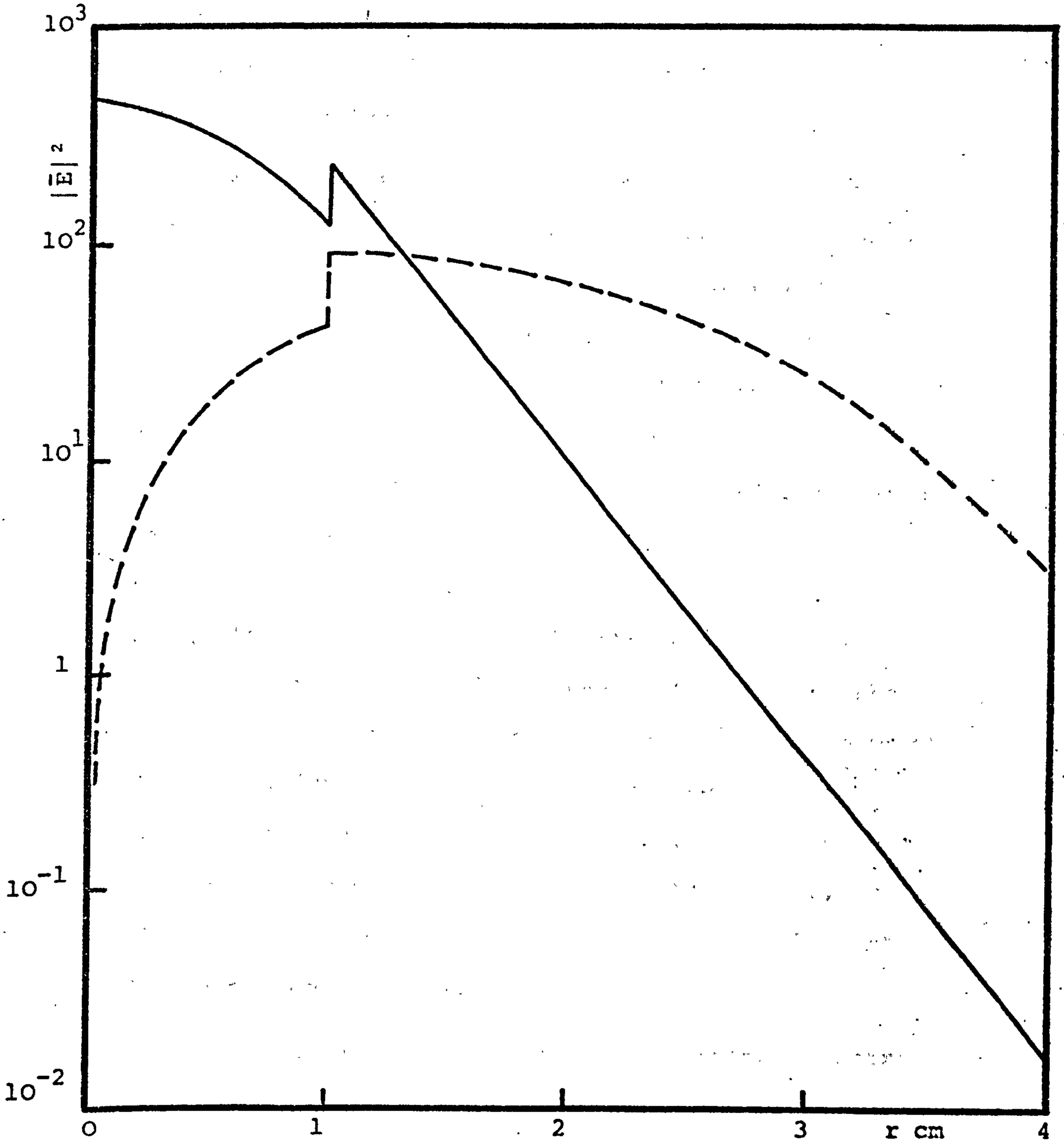

Figure (5.5) Total electric field against waveguide radius

r_1 = 1cm r_2 = 4cm $\bar{\varepsilon}_1$ = 2.25 $\bar{\varepsilon}_2$ = 1.02

f = 9.1 GHz

——— HE_{11} mode ----- HE_{21} mode

thus, the effect of $\bar{\varepsilon}_1$ and r_1 on the electric field strength of the HE_{11} mode near the corrugation edge must be investigated, enabling the correct choice of the core parameters resulting in minimum electric field strength in the lossy layer.

Figure (5.6) shows computed total electric field strength at the boundary $r = r_2$ as a function of normalised core radius. The core relative permittivity $\bar{\varepsilon}_1$ is set to 2.25 in the computations, which were carried out at a fixed frequency of 9 GHz. The effect of the cladding region was omitted by setting the value of $\bar{\varepsilon}_2$ to unity and the corrugation depth was fixed. It can be seen that as the core radius increases the power concentration of the HE_{11} mode increases in the core region, thus weakening the field strength near the boundary $r = r_2$. The field strength at $r = r_2$ reaches a minimum for a particular value of core radius, a point beyond which further increase in the core region size increases the field strength at $r = r_2$. This phenomena is expected to occur beyond certain values of r_1, as the field outside the core will no longer have sufficient radial distance to decay.

The value of r_1 giving rise to minimum electric field strength at $r = r_2$ is, however, not necessarily an optimum value for the mode filter design, but it is the maximum value of r_1 that can be chosen, and therefore will be designated the symbol r_{1max}. This is because, when selecting the value of r_1, the core loss that would

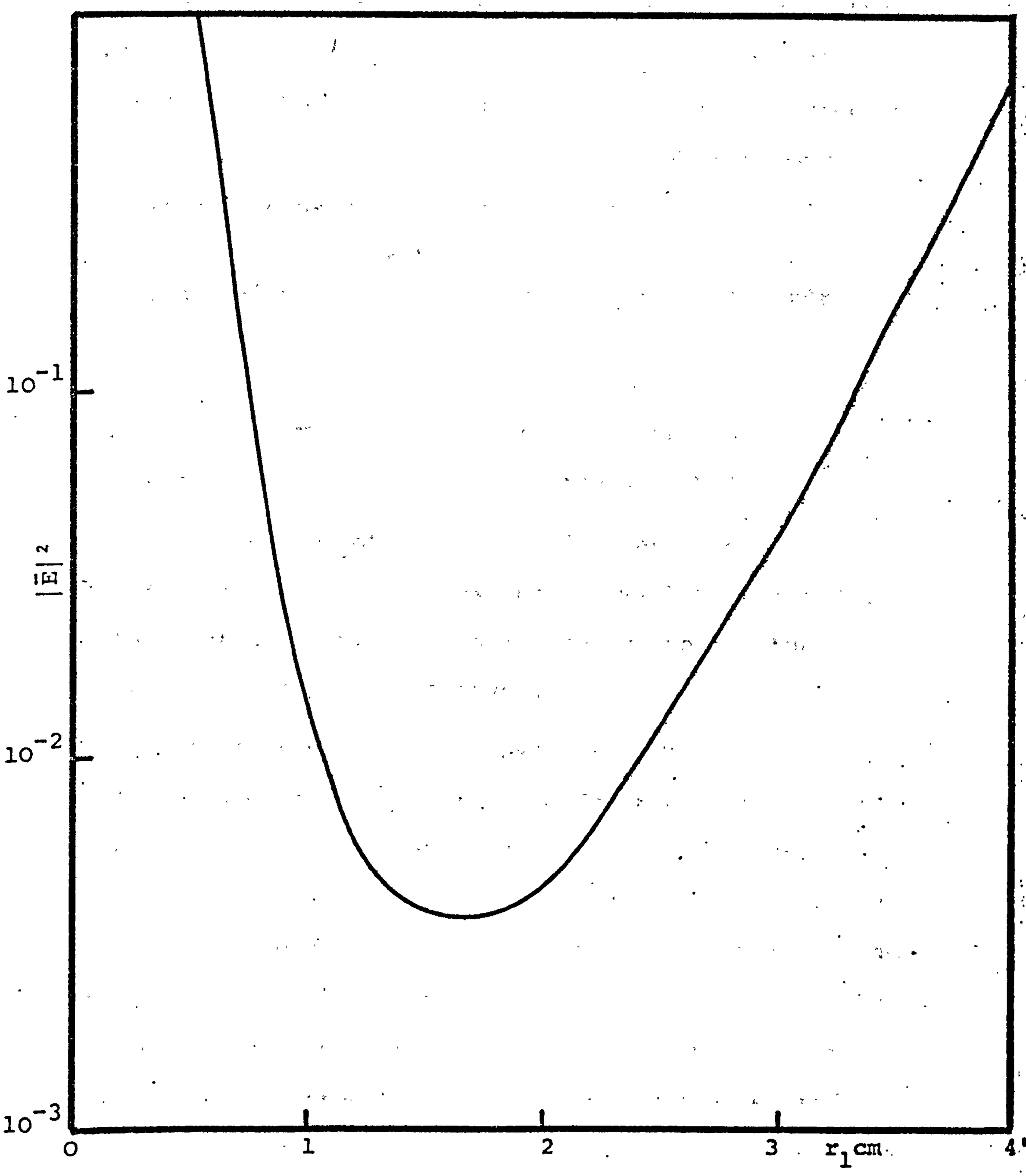

Figure (5.6) Total electric field strength of the HE_{11} mode at $r = r_2$ against core radius

$r_2 = 4$cm $\quad \bar{\varepsilon}_1 = 2.25 \quad \bar{\varepsilon}_2 = 1.0 \quad f = 9.0$ GHz

be introduced due to the increase in the core size must be weighed against the advantage gained in lowering the field strength at $r = r_2$. For example, by increasing the value of the core radius by Δr_1 $(=r_1' - r_1'')$, a drop in the total electric field at $r = r_2$ by $\Delta_2\underline{E}$ is produced. The difference between the quantities

$$(\bar{\varepsilon}_1 \tan\delta_1 - \bar{\varepsilon}_2 \tan\delta_2) \int_{r_1'}^{r_1''} {}_1\underline{E}\, r\,dr - \bar{\varepsilon}_2 \tan\delta_3 \int_{R_1}^{r_2} \Delta_2\underline{E}\, r\,dr \quad \{5.8\}$$

when evaluated must be made zero by altering Δr_1 so that at the optimum value of the core radius r_1' is obtained.

The choice of the core radius and the significance of the above expression will be illustrated in the next section, where numerical values of the dielectric power-loss are given.

Evaluating the above expression is rather tedious and cannot be generalised for the design of mode filters, as the lossy layer thickness, loss angle, relative permittivity, and the corrugation depth will all influence the evaluation of the fields. However, in the design of mode filters, the core radius is chosen to be very slightly less than r_{1max}, thus ensuring minimum electric field strength at the corrugation edge, and negligible increase in core loss.

The influence of increasing the core radius on the dispersion characteristics of the HE_{11} mode is shown in Figure (5.7). It can be seen that, the point $\bar{\beta} = \sqrt{\bar{\varepsilon}_2}$, at

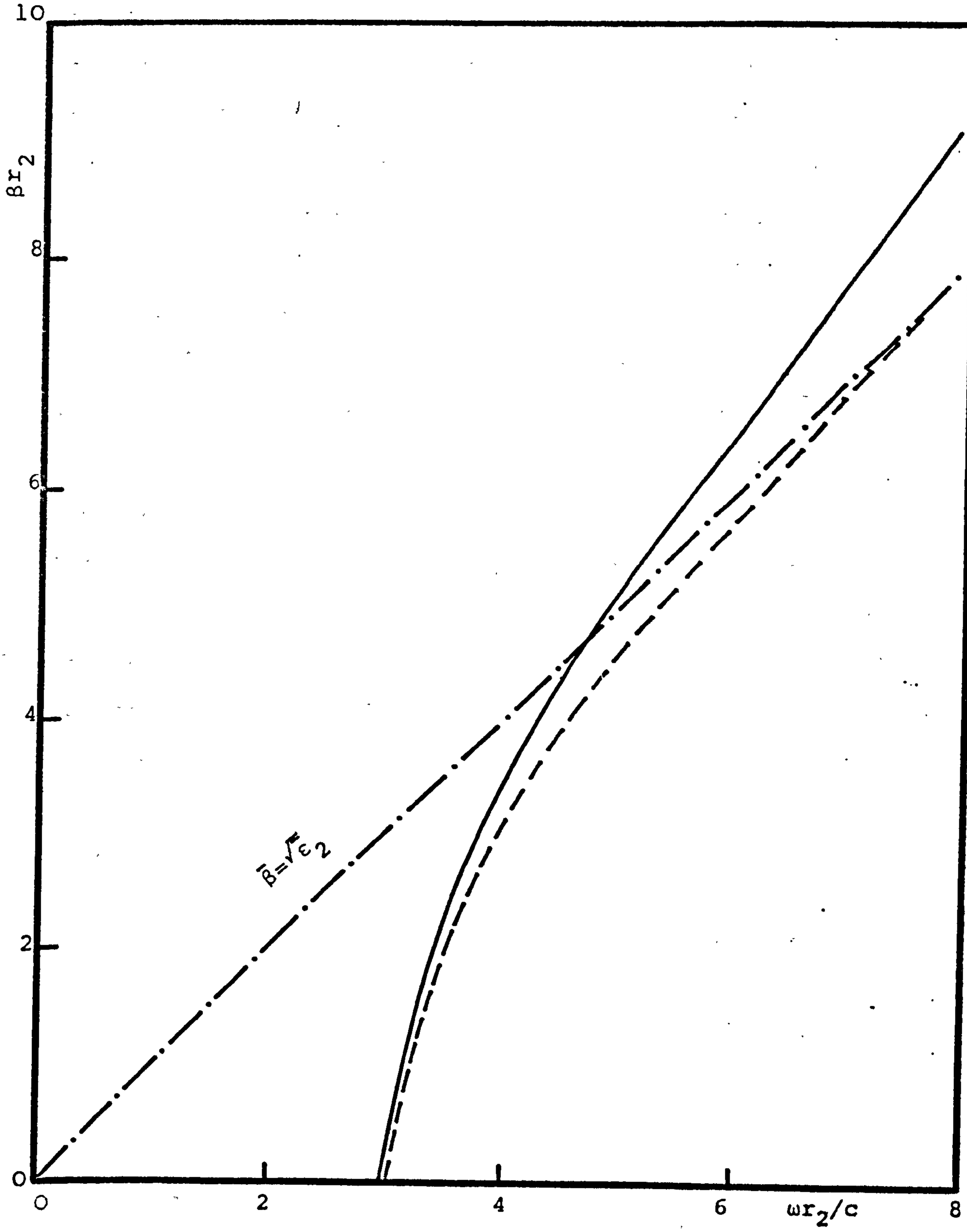

Figure (5.7) Dispersion characteristics of the HE_{11} mode in a corrugated circular waveguide containing a dielectric rod

$r_2 = 4cm \quad r_3 = 5cm \quad \bar{\epsilon}_1 = 2.25 \quad \bar{\epsilon}_2 = 1.02$

——— $r_1/r_2 = .25$ ------ $r_1/r_2 = .125$

which the fields begin to be confined to the core region, occurs at lower frequencies as the core radius is increased. The effect of the core radius on the cut-off frequency of the mode is also shown. The influence of the core relative permittivity $\bar{\varepsilon}_1$, on the field concentration of the HE_{11} mode in a fixed radius core region is illustrated in table (5.1). It is seen that the point $\bar{\beta} = \sqrt{\bar{\varepsilon}_2}$, moves to lower frequencies as the value of the core permittivity is increased, thus confirming the effect of the core region on the HE_{11} mode power distribution in the waveguide. The similar effects of r_1 and $\bar{\varepsilon}_1$ on the HE_{11} mode characteristics introduce another dimension in selecting the core radius, but due to the limitation in available low-loss dielectric materials, the influence of different values of $\bar{\varepsilon}_1$ on the attenuation characteristics of different modes is not studied. It is evident that very low-loss dielectric materials must be employed in the fabrication of the core region.

$\bar{\varepsilon}_1$	$(\omega r_2/c)$ at $\bar{\beta} = \sqrt{\bar{\varepsilon}_2}$
1	9.6
1.5	7.0
2.0	4.96
2.5	4.55
3.0	4.14

Table (5.1)

Influence of $\bar{\varepsilon}_1$ on core field concentration of the HE_{11} mode $r_1 = 1$ cm., $r_2 = 4$ cm., $r_3 = 5$ cm.

5.3.2 Effects of the Lossy Layer

The metal and dielectric losses of the loaded corrugated waveguide are studied separately, using appropriate expressions derived above. In order to visualise the effect of the lossy layer on the overall dielectric power-loss of different modes, parameters of the core and cladding regions are maintained. For such a set of parameters the influence of the thickness and the loss angle of the lossy layer on the overall dielectric loss is shown in Figure (5.8) for the HE_{11} mode as a function of frequency. The dimensions of the empty corrugated waveguide chosen in this example will cause the HE_{11} mode to have minimum attenuation at a frequency of nearly 9 GHz.

The effect of increasing the lossy layer thickness is clearly shown, but at the frequency of operation it is seen to be almost negligible. On the other hand, the effect of increasing the value of the loss tangent, $\tan\delta_3$, is more pronounced. For a lossy layer of 3 mm thickness, the attenuation nearly doubles when the loss tangent is increased by 10 times. The above two phenomena merely illustrate that the total electric field component of the HE_{11} mode is small at the boundary $r = r_2$, as predicted previously. The choice of the loss tangent and the thickness of the lossy layer will be made not only so as to provide the HE_{11} mode with the least possible loss, but also to present the unwanted modes with the highest possible

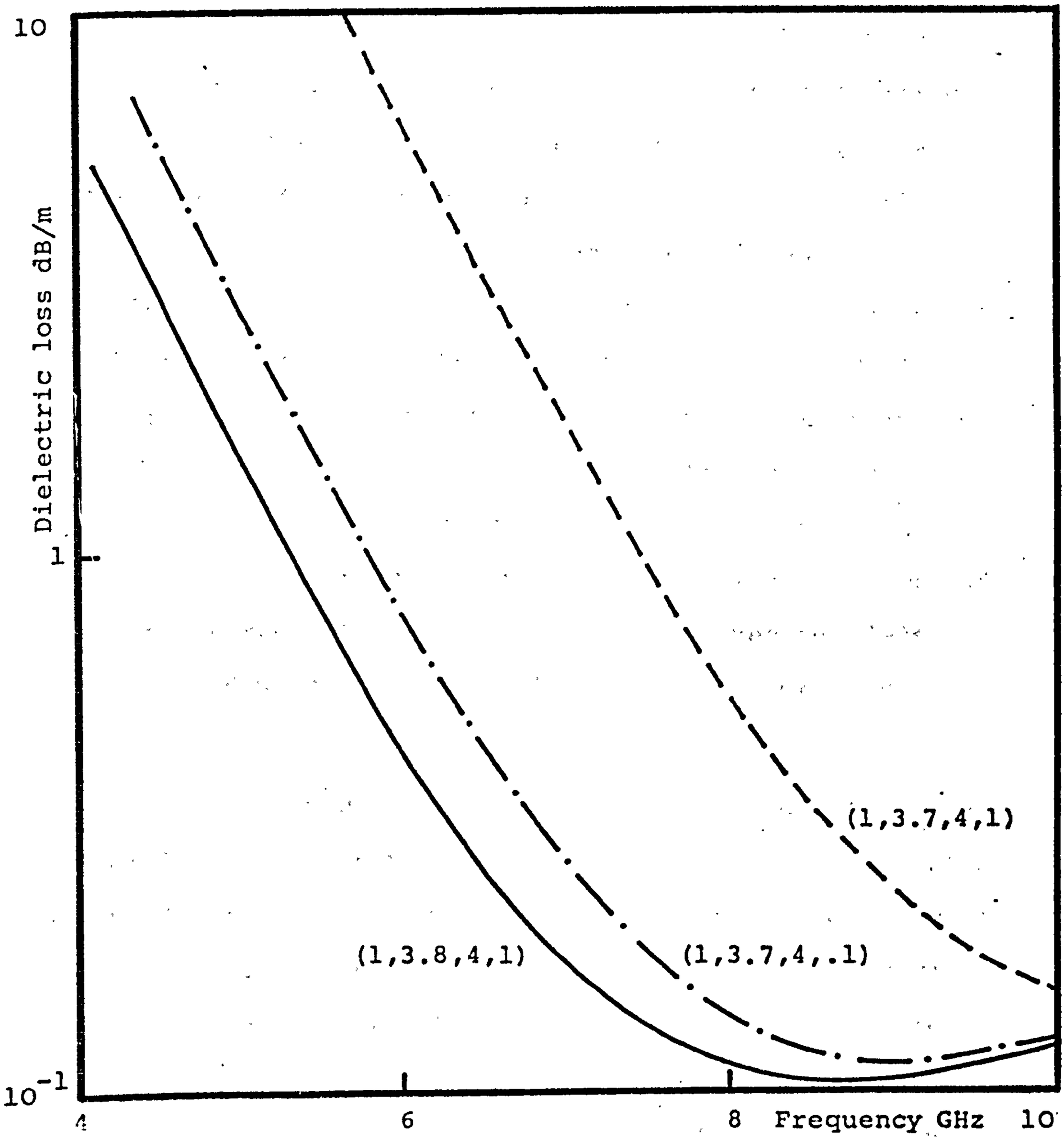

Figure (5.8) Attenuation due to loss in dielectric for the HE_{11} mode against frequency

$\bar{\varepsilon}_1 = 2.25 \quad \bar{\varepsilon}_2 = 1.02 \quad \tan\delta_1 = 10^{-4} \quad \tan\delta_2 = 10^{-5}$

Parameter $(r_1, R_1, r_2, \tan\delta_3)$

attenuation coefficient. The effects of the lossy layer on the unwanted modes will be discussed in the coming sections.

5.3.3 Influence of Core Radius

Results showing computed normalised dielectric power-loss for different values of core radius, as a function of frequency are presented in Figure (5.9), with all other parameters of the waveguide and the dielectric layers being fixed. At frequencies near cut-off, the increase in the dielectric power-loss with increasing core radius is attributed to a change in the cut-off frequency of the HE_{11} mode. As frequency increases, the power concentration in the core region rises at a faster rate when the core radius is large and therefore the effect of the lossy layer becomes less pronounced when compared with the smaller core size configuration.

At a frequency of 9 GHz, it is noticed that the overall dielectric power loss for the 1.5 cm core radius configuration is higher than that of the 1.0 cm structure, which is contradictory to the results shown in Figure (5.6). There it was shown that, when r_1 = 1.0 cm the value of the total electric field component near the corrugation edge is nearly 4 times that obtained when r_1 = 1.5 cm. The inconsistency of the results is attributed to the significant core power-loss introduced by increasing the core radius. The results clearly

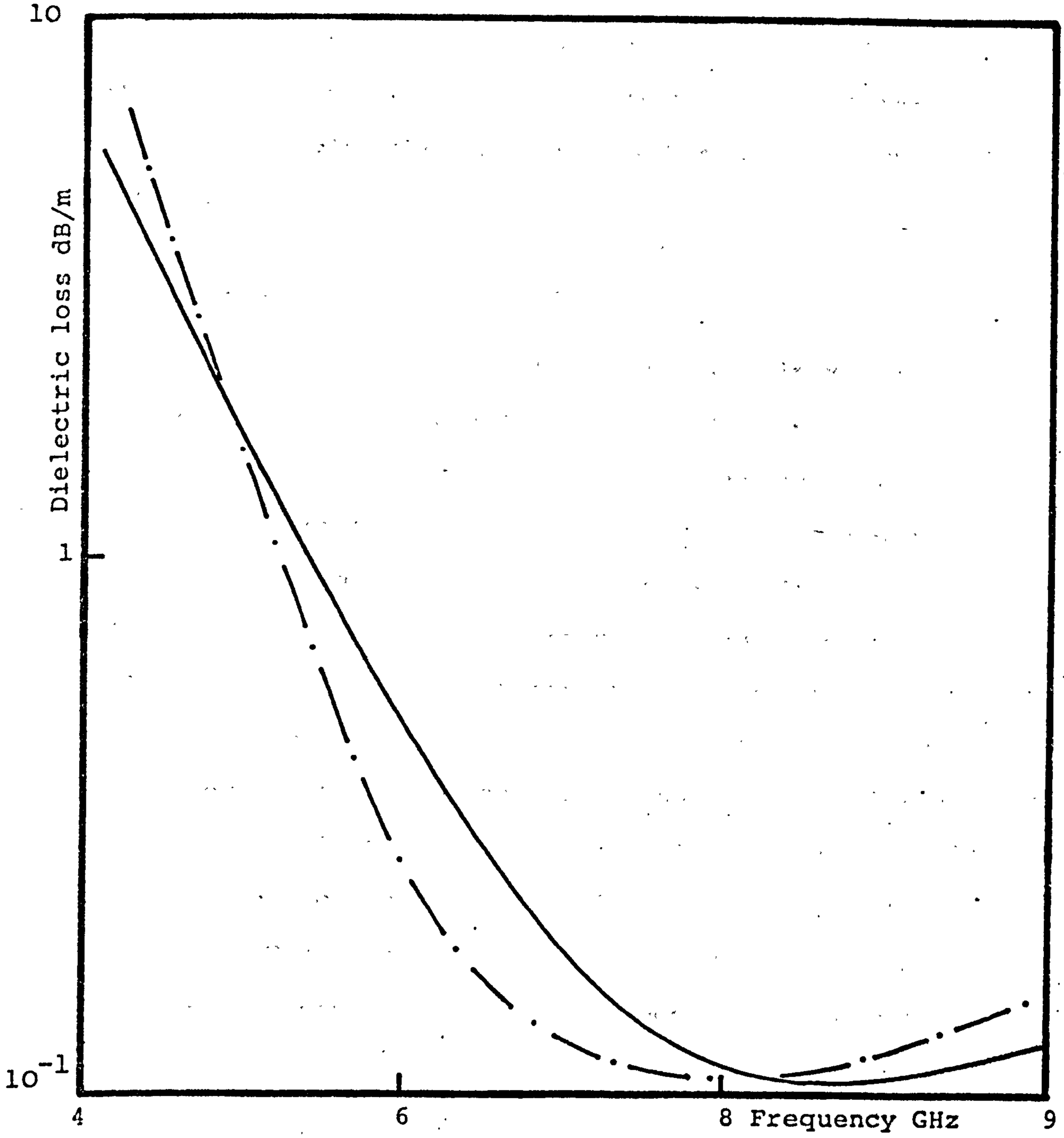

Figure (5.9) Attenuation due to loss in dielectric for the HE_{11} mode

$\bar{\varepsilon}_1 = 2.25$ $\bar{\varepsilon}_2 = 1.02$ $R_1 = 3.8cm$ $r_2 = 4cm$

$\tan\delta_1 = 10^{-4}$ $\tan\delta_2 = 10^{-5}$ $\tan\delta_3 = 10^{-1}$

——— $r_1 = 1cm$ -.-.-.- $r_1 = 1.5cm$

demonstrate the importance of the expression {5.8} in obtaining an optimum core radius for a particular configuration.

Due to the small influence of the core radius on the overall dielectric power-loss of the HE_{11} mode, the choice of the core radius will be made to provide the unwanted modes with the maximum possible attenuation coefficient.

5.3.4 Power-Losses in Metal Surfaces

Computed results for the power-loss in metal surfaces for the HE_{11} mode are shown in Figure (5.10), with the core radius fixed at 1.0 cm and using different values for the core permittivity. The cladding region is assumed to be air for all values of $\bar{\varepsilon}_1$. The influence of increasing the core permittivity on the metal power-loss clearly demonstrates the increase in the concentration of the power carried by the HE_{11} mode in the central region of the waveguide. It was found that even for very high values of $\tan\delta_3$, the power-loss contribution of the dielectric regions always dominates that of the metal part. Therefore, when searching for high differential attenuation values between the HE_{11} mode and the unwanted modes, only the dielectric power-loss contribution of different modes will be taken into account. From the results shown in Figure (5.10), the existence of a very low-loss loaded corrugated circular waveguide may be envisaged although its achievement will

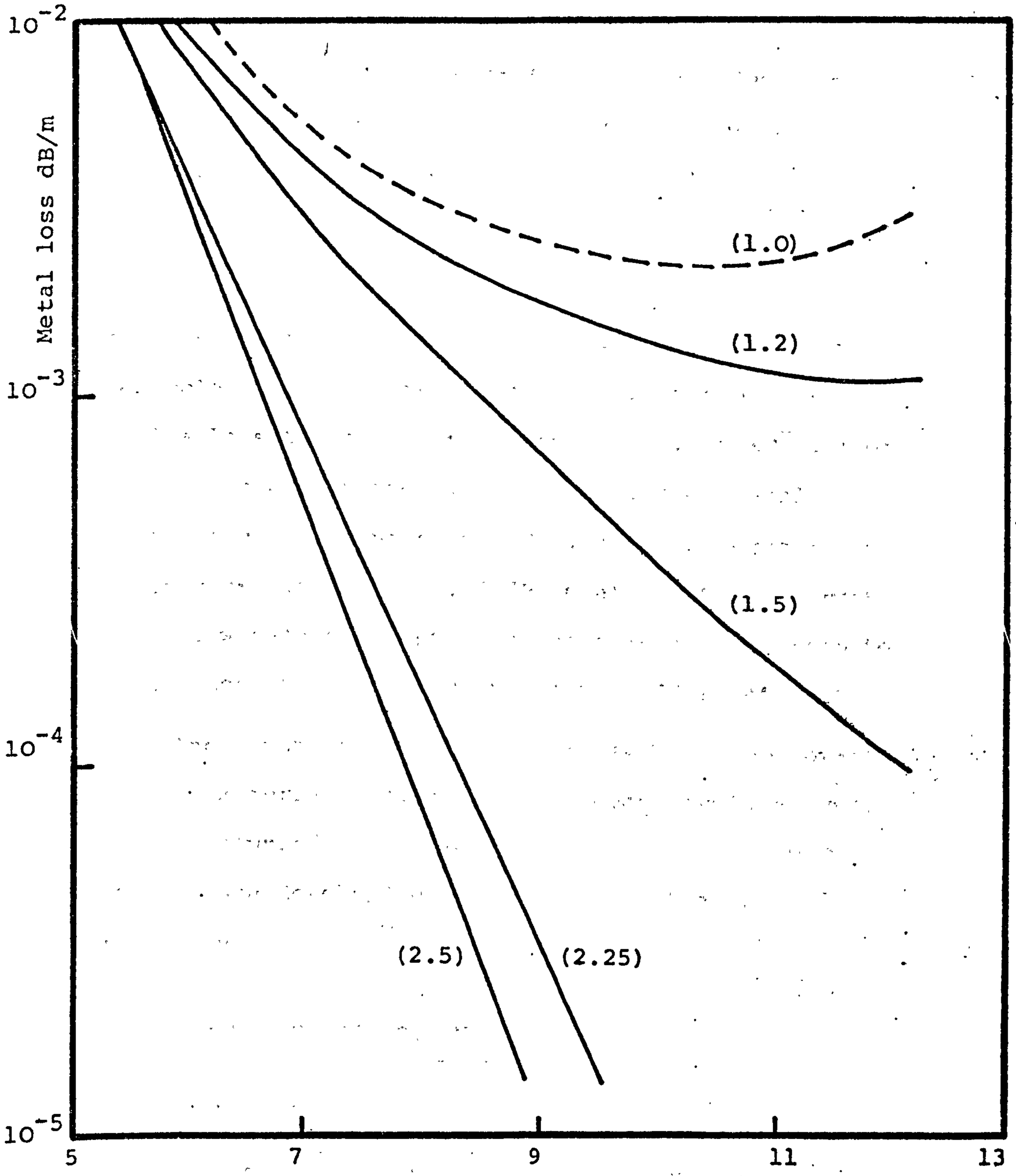

Figure (5.10) Attenuation due to loss in metal for the HE_{11} mode

$r_1 = 1cm \quad r_2 = 4cm \quad r_3 = 5cm$

$\sigma = 1.57 \times 10^7$ S/m $\quad \bar{\varepsilon} = 1.02$

Parameter ($\bar{\varepsilon}_1$)

depend on ensuring a low dielectric loss contribution in the core region.

An approximate formula for the dielectric power-loss of the core region can be derived <21> assuming a plane wave incident in the core region; then,

$$\alpha = \frac{\pi \bar{\varepsilon}_1}{\lambda} \tan\delta_1 \qquad \text{neper/m.}$$

where λ is the free-space wavelength.

For example, if a core region of relative permittivity 1.5 had a loss tangent, $\tan\delta_1$, equal to 8.0×10^{-7}, then using the expression and Figure (5.10), the overall attenuation coefficient of the HE_{11} mode propagating in this structure would be ∿0.46 dB/Km at 10 GHz. An empty corrugated waveguide supporting the same mode is seen to have an attenuation coefficient of ∿2.2 dB/Km at 10 GHz.

The advantage in attenuation is based on low-loss dielectric materials which have not been developed yet, but it is known, <22> and <42>, that Imperial Chemical Industries are developing an ultra low attenuation polypropylene.

5.4 PROPERTIES OF HE_{21} MODE

5.4.1 Introduction

In Figure (5.3) the dispersion characteristics of an empty circular corrugated waveguide are shown. At the operating frequency of 9 GHz several other modes can be excited apart from the low attenuation HE_{11} mode.

Some of these modes have high attenuation coefficients <34> when compared with the attenuation of the HE_{11} mode, and therefore will decay very rapidly. The remaining modes, such as HE_{21}, TE_{01}, have slightly higher attenuation coefficients than that of the HE_{11} mode and can cause signal distortion if excited. The influence of the mode filter on two of these modes will be investigated; these are the hybrid HE_{21} mode and the circularly symmetric TE_{01} mode. These modes are chosen, as they could be easily excited by the HE_{11} mode when bends are negotiated <4>.

5.4.2 Field Distribution

The magnitude of the total normalised electric field of the HE_{21} mode in a loaded corrugated circular waveguide is plotted in Figure (5.5) as a function of waveguide radius. The discontinuity at the core-cladding boundary, $r = r_1$, is due to the discontinuity in the radial electric field component at this boundary. The curve shows an initial rapid increase in the electric field distribution towards the boundary $r = r_1$, which is then followed by a slow decrease towards the boundary $r = r_2$. At this boundary it is found that the value of the normalised electric field of the HE_{21} mode is nearly two orders of magnitude higher than that of the HE_{11} mode. This clearly confirms the effectiveness of positioning the lossy layer near the corrugation edge. The overall differential attenuation between the HE_{11}

mode and the HE_{21} mode will not necessarily be of this order of magnitude, because of the core and cladding losses being different for these modes.

5.4.3 Effects of the Core Radius and the Lossy Layer

The influence of the core radius r_1 on the overall dielectric power-loss of the HE_{21} mode is illustrated in Figure (5.11), for a particular thickness and loss angle of the lossy layer. For frequencies near cut-off, the increase in the loss for higher values of r_1, is merely due to the change in the cut-off frequency of the mode. The decrease in the dielectric power-loss with increasing core radius, at frequencies far from cut-off, is attributed to the higher field concentration of the HE_{21} mode in the core region of the waveguide, and thus giving rise to weaker field near the corrugation edge. The effect of decreasing the core radius on the dielectric power-loss of the HE_{11} mode Figure (5.9), is seen to be almost negligible when compared with the increase obtained for the HE_{21} mode, Figure (5.11), at 9 GHz. The influence of the thickness and the loss angle of the lossy layer on the overall dielectric power-loss of the HE_{21} mode is shown in Figure (5.12), with all other parameters being fixed.

At the frequency of operation, 9 GHz, it is seen that an order of magnitude increase inthe loss tangent of the lossy layer is followed by a similar increase in the overall dielectric power-loss of the mode. This

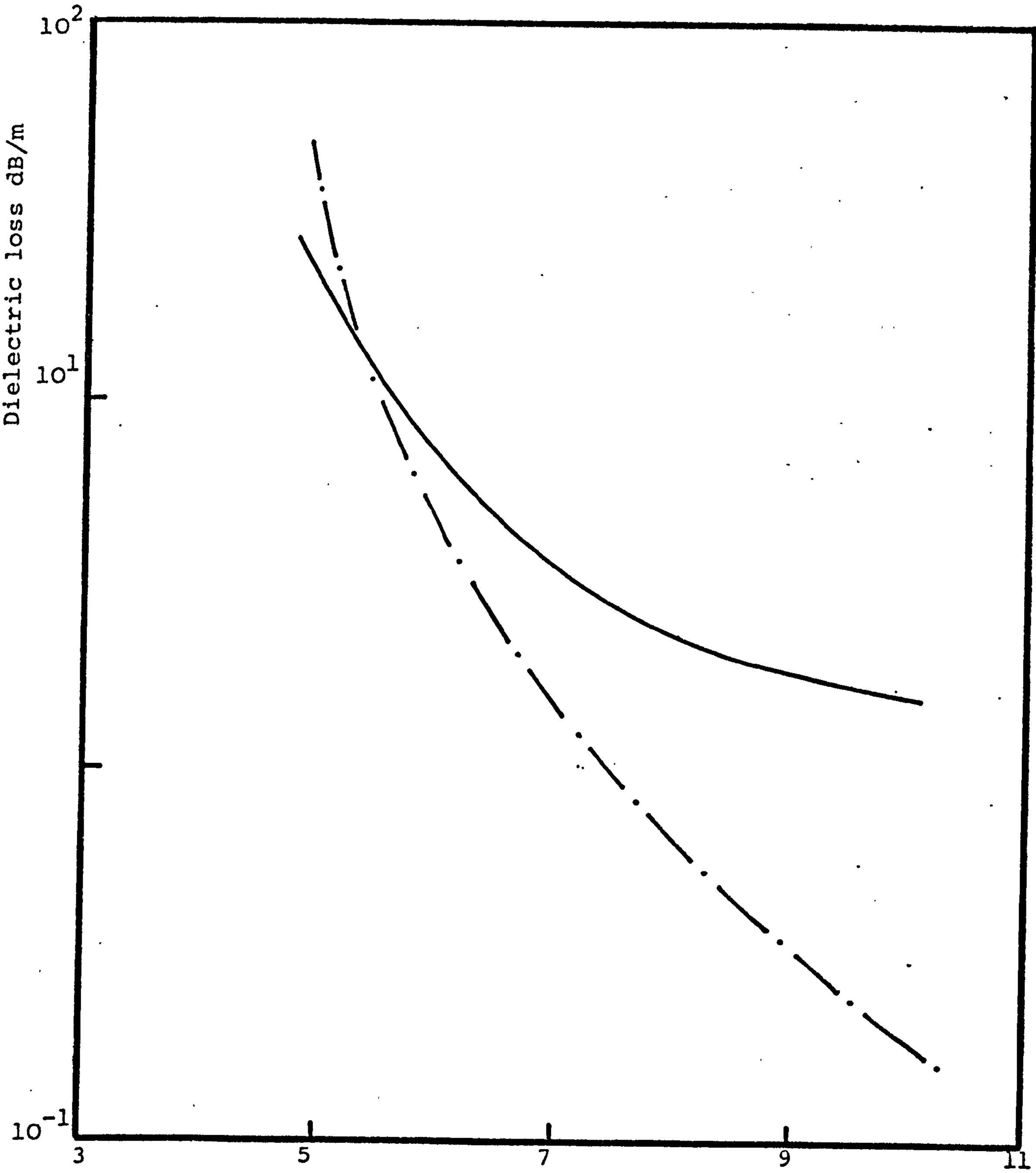

Figure (5.11) Attenuation due to loss in dielectric for the HE_{21} mode

$\bar{\varepsilon}_1 = 2.25$ $\bar{\varepsilon}_2 = 1.02$ $R_1 = 3.7cm$ $r_2 = 4cm$

$\tan\delta_1 = 10^{-4}$ $\tan\delta_2 = 10^{-5}$ $\tan\delta_3 = 10^{-1}$

——— $r_1 = 1cm$ -.-.- $r_1 = 1.5cm$

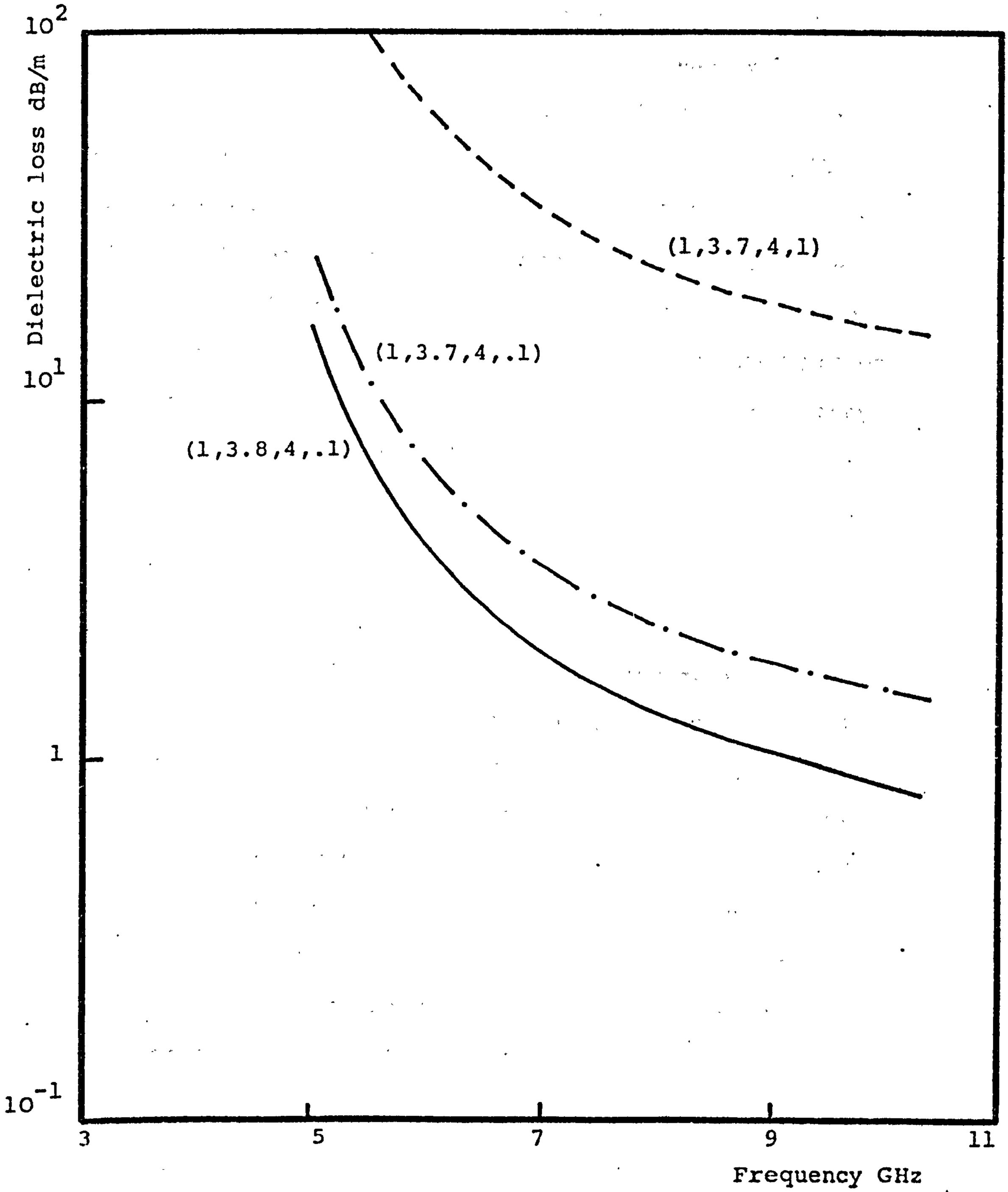

Figure (5.12) Attenuation due to loss in dielectric for the HE_{21} mode

$\bar{\varepsilon}_1 = 2.25 \quad \bar{\varepsilon}_2 = 1.02 \quad \tan\delta_1 = 10^{-4} \quad \tan\delta_2 = 10^{-5}$

Parameter $(r_1, R_1, r_2, \tan\delta_3)$

compared with nearly two-fold increase in the dielectric power-loss of the HE_{11} mode for the same configuration, Figure (5.8). On the other hand, by increasing the lossy layer thickness by 1 mm, a two-fold increase in the dielectric power-loss is observed, compared with a negligible effect on the HE_{11} mode power-loss, Figure (5.8). Therefore, in order to present the HE_{21} mode propagating in an empty corrugated circular waveguide with a maximum absorbing device, the mode filter proposed must consist of a small core diameter and a very lossy layer of reasonable thickness.

5.5 PROPERTIES OF TE_{01} MODE

5.5.1 Theory

The surface impedance model used to represent the boundary at $r = r_2$, Figure (5.2), was found to give very satisfactory results for the hybrid modes in an empty corrugated waveguide when compared with the space-harmonic formulation of those modes given in <4 >. This boundary representation provides an open circuit condition for the E-radial line, but for the H-mode line it is assumed to be short circuited and therefore does not permit an H-radial mode to propagate.

In order to avoid the use of the space-harmonic formulation for the TE modes, it is clear that the surface impedance model representation of the boundary at $r = r_2$ must be modified. Since the aim of the study is to evaluate the effects of introducing the dielectric

core region and the lossy layer on the TE_{01} mode propagating in the empty corrugated waveguide, and as the dielectric power loss is mainly dependent on the azimuthal electric field component of this mode, the distribution of this component will be evaluated first.

Computed values of the normalised E_θ component in an empty corrugated circular waveguide are shown in Figure (5.13) as a function of waveguide radius. When using the space-harmonic formulation which takes into account the field distribution in the slot region, the results clearly illustrate the extension of this component in the slot region, which vanishes at the base boundary of the slots, $r = r_3$. On the other hand, the simple surface impedance approach shows a vanishing azimuthal electric field component at the boundary $r = r_2$. Therefore, if the surface impedance approach is used to calculate the loss introduced by the lossy layer placed near the boundary $r = r_2$, the results obtained will be much smaller than those obtained using the correct field representation. As the field distribution in the slot region is of no importance in this analysis, the search is directed towards finding a function which will give rise to the same field distribution in the region $0 < r \leq r_2$ as that obtained using the exact formulation. Remembering the favourite position of the lossy layer reached when investigating the HE_{11} mode field distribution, the new function representing the TE_{01} mode field distribution must therefore be very close to

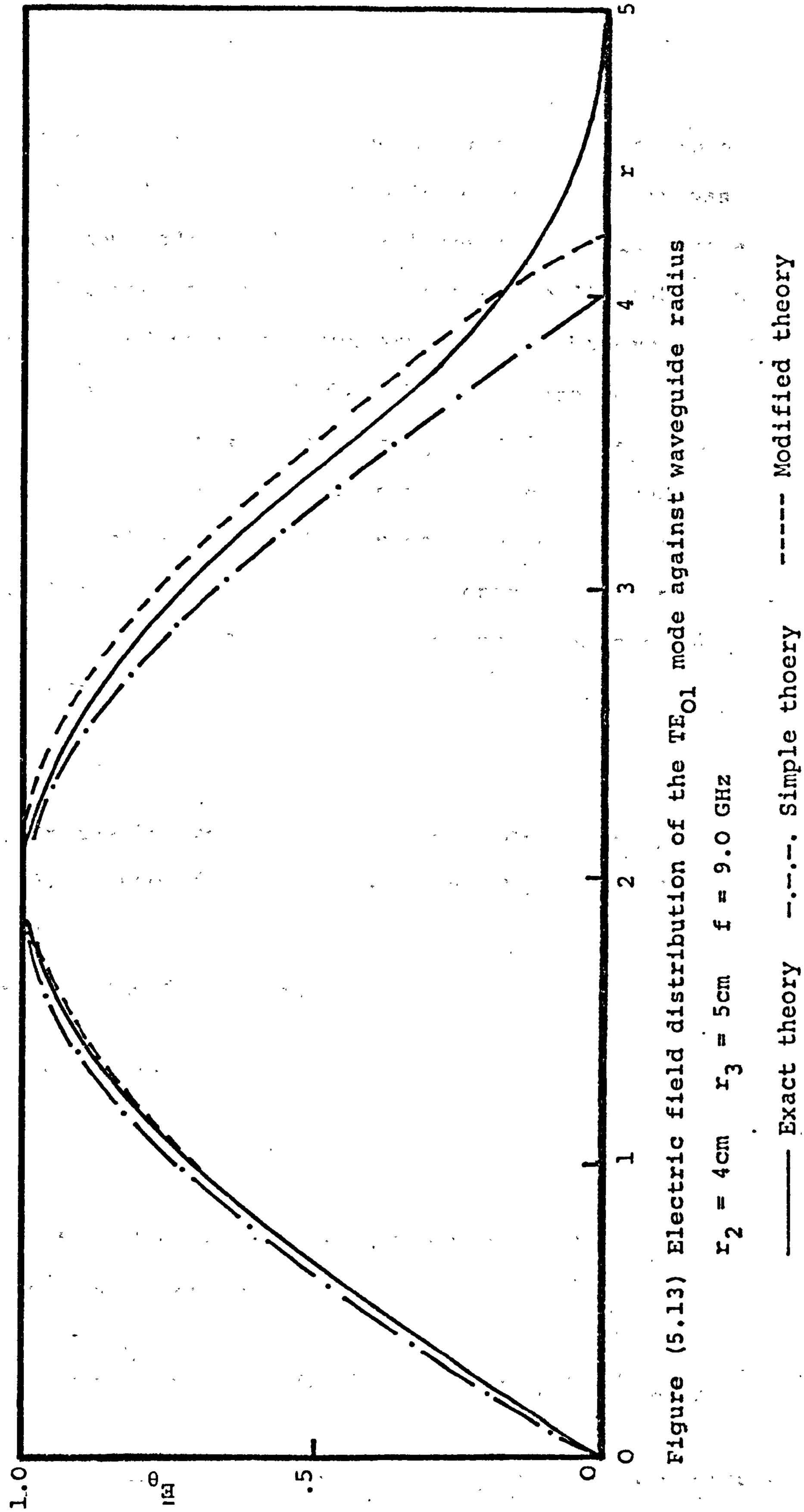
E_θ
1.0
.5
0
1
2
3
4
5
r
Electric field distribution of the TE_{01} mode against waveguide radius
r_2 = 4cm r_3 = 5cm f = 9.0 GHz
——— Exact theory -.-.- Simple theory ----- Modified theory

Figure (5.13)

the exact theory field distribution in the region close to r_2. It was found that if the impedance boundary was moved to a new radius r_2' ($=r_2+\Delta r_2$) instead of r_2, then a value of Δr_2 can be found for which the two distributions coincided at and near the boundary $r = r_2$. Figure (5.13) shows the results obtained when the impedance boundary is placed at the new radius $r_2' = r_2 \times 21/20$. It is seen that very good agreement between the two normalised fields is obtained in particular near the slot edge $r = r_2$. For values $r > r_2$, the discrepancy is of no importance as no attempt will be made to calculate the metal power-loss of the TE_{01} mode.

5.5.2 Field Components

In the loaded corrugated waveguide shown in Figure (5.2), some field components of the TE_{01} mode are given by:

in the region $0 < r < r_1$

$$_1H_z = Y_o C_1 J_o(K_1 r)$$

$$_1E_\theta = j\left(\frac{k}{K_1}\right) C_1 J_o'(K_1 r)$$

and in the cladding region $r_1 < r < r_2'$, the components are given by

$$_2H_z = Y_o \frac{C_2}{Y_o(K_2 r_2')}\left[J_o(K_2 r) Y_o'(K_2 r_2') - J_o(K_2 r_2') Y_o(K_2 r)\right]$$

$$_2E_\theta = j\left(\frac{k}{K_2}\right) \frac{C_2}{Y_o'(K_2 r_2')}\left[J_o'(K_2 r) Y_o'(K_2 r_2') - J_o(K_2 r_2') Y_o'(K_2 r)\right]$$

The field components written in the above form satisfy the boundary conditions, namely, finite field at the origin and vanishing tangential electric field component at the impedance boundary $r = r_2'$.

C_1 and C_2 are amplitude coefficients, and the factor $\exp j(\omega t-\beta z)$ is assumed throughout, other symbols are defined in section (5.2).

At the boundary $r = r_1$ the boundary conditions, equal tangential electric and magnetic field components are applied to obtain the characteristic equation for the TE_{01} mode in the structure, i.e.

$$K\frac{J_o'(K_1r_1)}{J_o(K_1r_1)} = \left[\frac{J_o'(K_2r_2')Y_o'(K_2r_2')-J_o'(K_2r_2')Y_o'(K_2r_1)}{J_o(K_2r_1)Y_o'(K_2r_2')-J_o'(K_2r_2')Y_o(K_2r_1)}\right]$$

5.5.3 Effects of Core Radius

The TE_{01} mode power-loss at different regions of the mode filter are formulated using the same perturbation techniques used in the formulation of the hybrid modes power-loss, with the integrands containing E_θ component only. When obtaining the dielectric power-loss of the lossy layer the integration given in {5.7}, was carried out between the limits R_1 and r_2 and not between R_1 and r_2'. This is because of the actual physical position of the lossy layer in the waveguide.

The influence of the core radius r_1 on the overall dielectric power-loss of the TE_{01} mode is illustrated in Figure (5.14) for a particular thickness

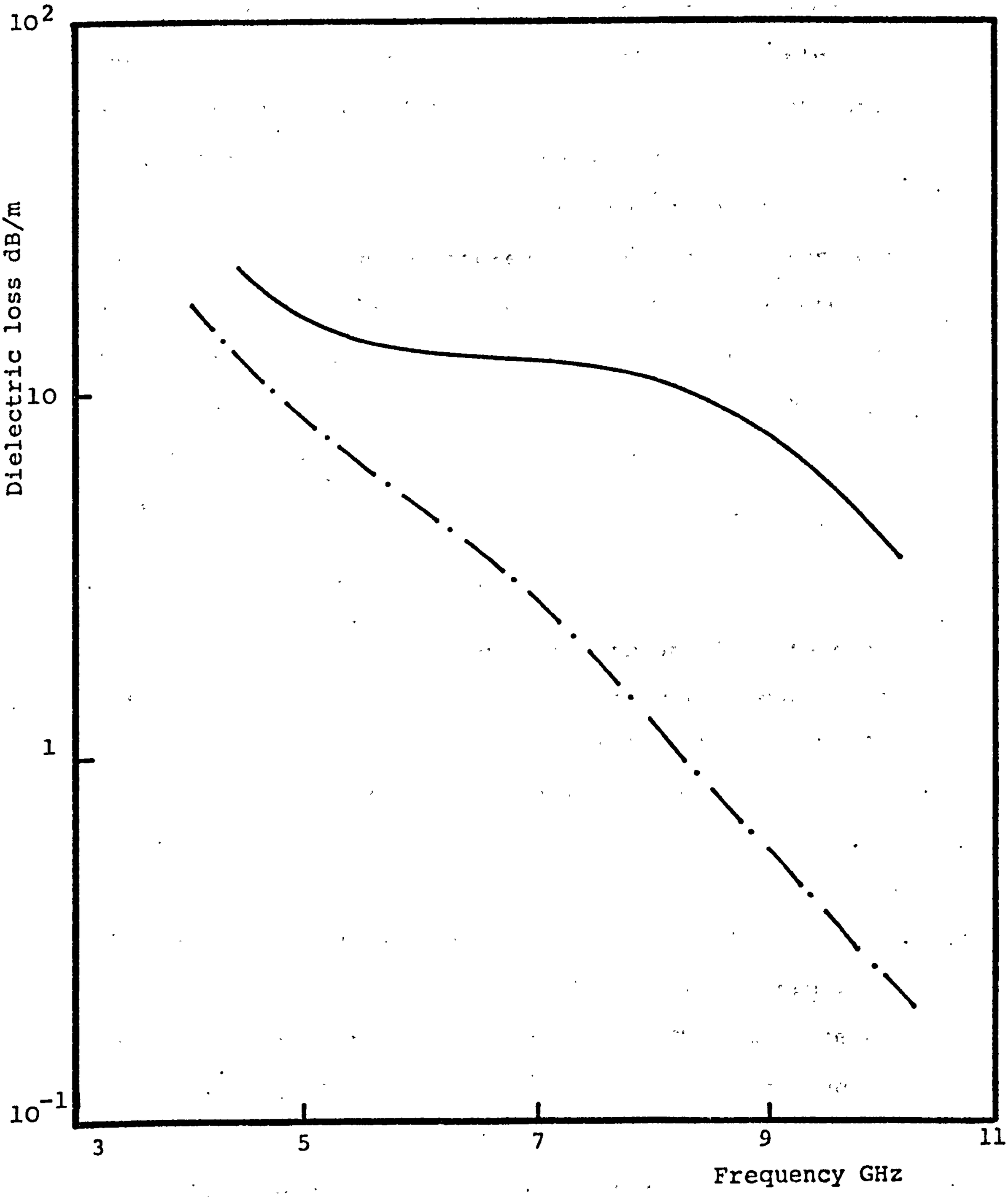

Figure (5.14) Attenuation due to loss in dielectric for the TE_{01} mode against frequency

$\bar{\varepsilon}_1 = 2.25$ $\bar{\varepsilon}_2 = 1.02$ $R_1 = .037m$ $r_2 = .04m$

$\tan\delta_1 = 10^{-4}$ $\tan\delta_2 = 10^{-5}$ $\tan\delta_3 = 1.0$

——— $r_1 = 1cm$ —.—.—.— $r_1 = 1.5cm$

and loss angle of the lossy layer. It is seen that as the core size is increased, the dielectric power-loss decreases with increasing frequency, this is mainly due to the concentration of the TE_{01} mode field in the core region of the waveguide. As the electric field component of the TE_{01} mode has zero value on the waveguide axis, then the increase in the core power-loss is not expected to be very significant when the core size is increased. It is clear that in order to obtain high values for the attenuation coefficient of the TE_{01} mode, a small core radius would be appropriate to choose.

5.5.4 Effects of the Lossy Layer

The influence of the thickness and loss tangent of the lossy layer on the overall dielectric power-loss of the TE_{01} mode are studied separately. Figure (5.15) shows this influence when all other parameters are maintained. At the frequency of operation, 9 GHz, it is seen that for an order of magnitude increase in the loss angle of the lossy layer, the overall dielectric power-loss rises by the same order. This phenomena merely confirms the high field strength of the TE_{01} mode near the slot edge. On the other hand, by increasing the lossy layer thickness by 1 mm, the overall loss rises two-fold. Therefore, in order to absorb the TE_{01} mode propagating in the empty circular corrugated waveguide, a mode filter consisting of a small core diameter, and a lossy layer of a very high loss tangent is needed.

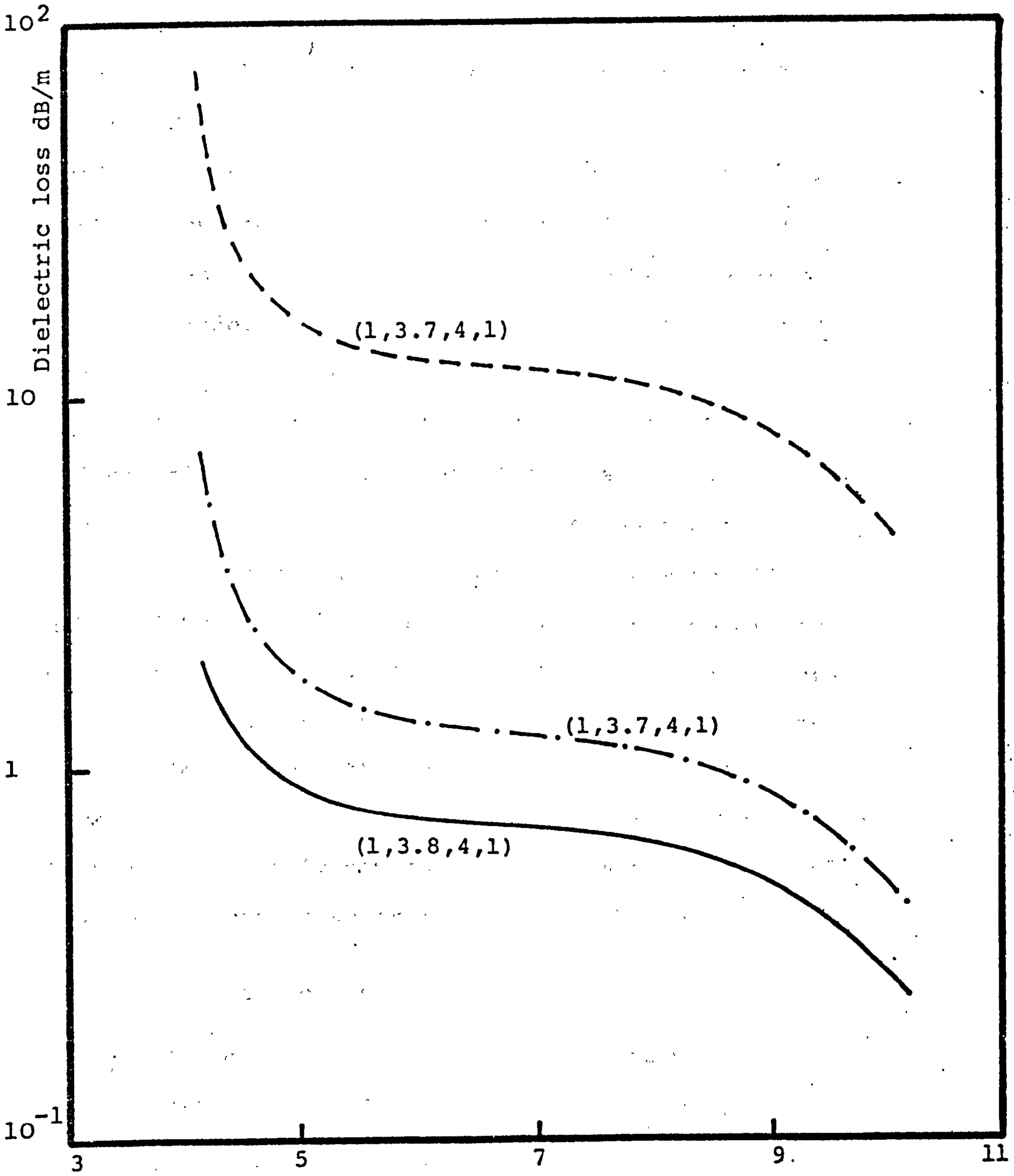

Figure (5.15) Attenuation due to loss in dielectric for the TE_{01} mode against frequency

$\bar{\varepsilon}_1 = 2.25 \quad \bar{\varepsilon}_2 = 1.02 \quad \tan\delta_1 = 10^{-4} \quad \tan\delta_2 = 10^{-}$

Parameter $(r_1, R_1, r_2, \tan\delta_3)$

5.6 MODE FILTER DESIGN

From the above results, the possibility of obtaining high differential attenuation between the desired HE_{11} mode and the unwanted modes is quite evident. The choice of the mode filter parameters is dictated by the amount of differential attenuation required and the attenuation which can be tolerated by the HE_{11} mode. Very low loss dielectric materials will obviously improve the mode filter performance, in particular the losses of the desired mode. The differential attenuation can always be achieved by increasing the thickness or the loss angle of the lossy layer. The theoretical performance of a mode filter achieved by proper choice of different parameters is shown in Table (5.2). Theoretical attenuation figures obtained using a space harmonic <4> approach in the formulation of the attenuation coefficient is also shown. The differential attenuation ratio shown in the last column clearly demonstrates the effectiveness of the mode filter in absorbing the unwanted modes energy.

Mode Filter Parameters

$r_1 = 1.0$ cm	$R_1 = 3.7$ cm	$r_2 = 4.0$ cm
$\bar{\varepsilon}_1 = 2.25$	$\bar{\varepsilon}_2 = 1.02$	$r_3 = 5.0$ cm
$\tan\delta_1 = 10^{-4}$	$\tan\delta_2 = 10^{-5}$	$\tan\delta_3 = 1.0$

$f = 9.0$ GHz $\qquad R_s = .0474\Omega$

MODE	$\frac{\alpha_m}{2}$ dB/m	Differential Ratio	$\frac{\alpha_d}{2}$ dB/m	Differential Ratio
HE_{11}	0.0034		0.23	
HE_{21}	0.0095	$\sim$ 3	19	$\sim$ 83
H_{01}	0.0034	1	8	$\sim$ 35

Table (5.2)

The presence of the lossy layer near the corrugation edge will absorb most of the energy carried by the modes within this region and therefore the metal power-loss of different modes will be almost negligible. However, the metal power-loss of the unwanted modes will merely improve the overall performance of the mode filter.

5.7 MATCHING SECTION DESIGN

5.7.1 Introduction

In previous sections the mode filter design was based on studying the characteristics of an infinitely long corrugated waveguide containing the concentric dielectric structure. In practice, small sections of the mode filter will be inserted in the long empty corrugated waveguide to provide the required differential attenuation. The length of the mode filter sections will depend on the amount of attenuation tolerated by the HE_{11} mode and the

loss angle of the lossy layer for a particular core size.

It is immediately recognised that a matching section must be used between the empty section of the corrugated waveguide and the section containing the mode filter in order to avoid serious losses by reflection and the setting up of standing waves at the junction. One method of providing good matching into the mode filter is by tapering the core region to very small core radius. The theory of designing an optimum arrangement is described by Klopfenstein <43>. This method is based on solving a first order non-linear differential equation involving the reflection coefficient at any position along the taper. Exact mathematical solutions to the differential equation are only possible when the reflection coefficient varies along the longitudinal direction of propagation in some specific manner. Examples of possible reflection coefficient variations are given in <40>, giving rise to the design of Bessel, hyperbolic and exponential tapers. Collin and Brown <44> describe the use of a quarter-wave transformer to match the junction between an empty and a filled smooth wall waveguide.

Application of the quarter-wave transformer theory requires the evaluation of the reflection coefficient for the two configurations,

(i) the junction between an empty corrugated waveguide and one containing a core dielectric of variable size and permittivity and

(ii) the junction between two similar corrugated waveguides containing axial core regions of different size, Figure (5.18) junctions a and b respectively. The second method will be used in designing the matching section of the mode filter, as the first method requires the knowledge of the reflection coefficient for a continuous range of the core radius and in general very long sections of the taper are needed to produce low reflection coefficient.

In the following sections an account of the theory of the matching section is given and the junction reflection coefficient in a corrugated circular waveguide is formulated in terms of known field components, using a modified form of the variational method employed by Farmer <45>. The overall V.S.W.R. of the matching transformer is computed using transmission line theory <40>.

5.7.2 Transformer Prototype Theory

Figure (5.16) shows the junction between an empty corrugated waveguide and one containing an axial dielectric rod of radius r_1 and relative permittivity $\bar{\varepsilon}_1$. For the values of r_1 and $\bar{\varepsilon}_1$ chosen in the mode filter design, the reflection coefficient of the junction will be very high and cannot be tolerated in practice. A matching section to minimise the reflection of the desired HE_{11} mode at the junction may be designed on the same principle as a transmission line quarter-wave

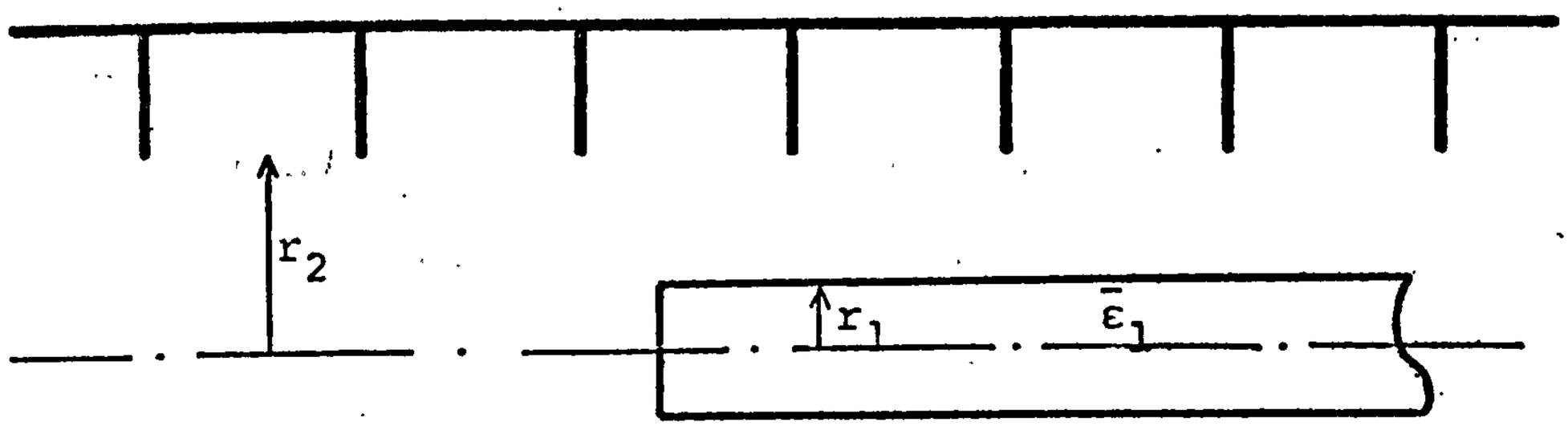

Figure (5.16) Dielectric rod in a corrugated circular waveguide

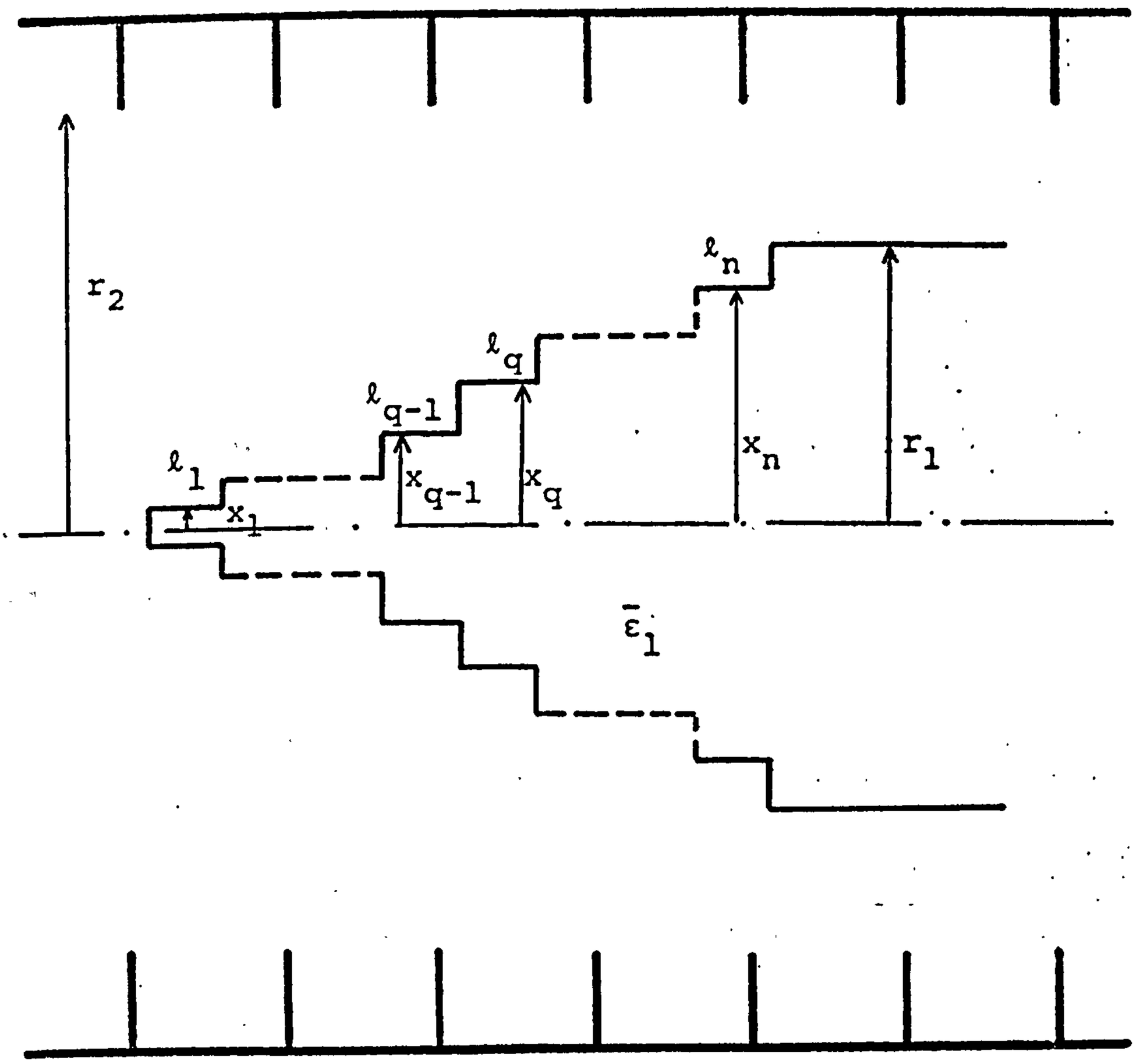

Figure (5.17) n-section matching transformer

transformer. A matching transformer consisting of n-sections is shown in Figure (5.17), where the ratio (R/Z_o) being the V.S.W.R. of the junction shown in Figure (5.16). For n-sections of transmission lines in cascade, each having the same electric length but different characteristic impedance, the overall transfer or wave matrix <46>, have the form

$$T = \frac{1}{2^{n+1}} \left[\prod_{i=1}^{n} \left(\underset{\sim}{A} + \frac{Z_{i-1}}{Z_i} \underset{\sim}{B} \right) \right] \left(\underset{\sim}{A}_o + \frac{Z_n}{R} \underset{\sim}{B}_o \right) \qquad \{5.9\}$$

where

$$\underset{\sim}{A} = \begin{bmatrix} e^{j\theta} & e^{-j\theta} \\ e^{j\theta} & e^{-j\theta} \end{bmatrix} \qquad \underset{\sim}{B} = \begin{bmatrix} e^{j\theta} & -e^{-j\theta} \\ -e^{j\theta} & e^{-j\theta} \end{bmatrix}$$

$$\underset{\sim}{A}_o = \begin{bmatrix} 1 & 1 \\ 1 & 1 \end{bmatrix} \qquad \underset{\sim}{B}_o = \begin{bmatrix} 1 & -1 \\ -1 & 1 \end{bmatrix}$$

θ being the electric length of each section.

The overall transfer matrix T is a 2 x 2 matrix and can be replaced by

$$\begin{bmatrix} T_{11} & T_{12} \\ T_{21} & T_{22} \end{bmatrix}$$

The matrix element T_{11} represents the reciprocal of the amplitude of the transmission coefficient <40>.

Therefore the power absorbed by the load through the n-section transmission line is

$$(T_{11}T_{11}^{*}\ R)^{-1}$$

where T_{11}^{*} is the complex conjugate of T_{11} and R is the normalised load impedance of the end of the line, i.e. the core region of the mode filter. If a unit amplitude of incident wave is assumed, then the power loss ratio is defined as P_t, then

$$P_t = T_{11}T_{11}^{*}\ R$$

From {5.9} it is seen that the polynomial representing P_t is an even function of $\cos\theta$ and is symmetrical about the point $\theta = 0$. But P_t is related to the input reflection coefficient Γ, viz.

$$P_t = [1-|\Gamma|^2]^{-1} \simeq 1 + |\Gamma|^2 \qquad |\Gamma|^2 << 1.$$

Since the performance of an n-section transformer is determined by the input reflection coefficient , then P_t is synthesised so that the desired bandwidth and passband tolerance needed for the transformer can be achieved. After P_t has been synthesised to obtain the predetermined frequency response, the appropriate characteristic impedance Z_i of each section can be determined.

As might be expected, there are many possible combinations of the characteristic impedances. Three special cases are described in <41 >;

(i) where all impedance steps are equal (linear),

(ii) where the percentage change at each step is a constant (exponential); and

(iii) where the steps are proportional in accordance with the so called "binomial distribution". A Chebysher polynomial of various degrees can also be used to synthesise the reflection coefficient behaviour in the passband <40>.

5.7.3 Characteristic Impedance

The V.S.W.R. of different junctions form the basis of formulating the input reflection coefficient Γ of the transformer. Therefore, the V.S.W.R. at two types of junctions in the loaded corrugated circular waveguide must first be investigated.

Consider a single step quarter-wave transformer section to match the core region of the filter in a corrugated waveguide, Figure (5.18). It is required to formulate the V.S.W.R. at the junctions (a) and (b) shown in Figure (5.18). The radii x_1, r_1 of the first and core regions are assumed arbitrary with $\bar{\varepsilon}_1$ being the relative permittivity of both regions. The cladding relative permittivity $\bar{\varepsilon}_2$ is assumed unity, thus permitting the use of the results obtained at junction (b), when a multi-section transformer is considered.

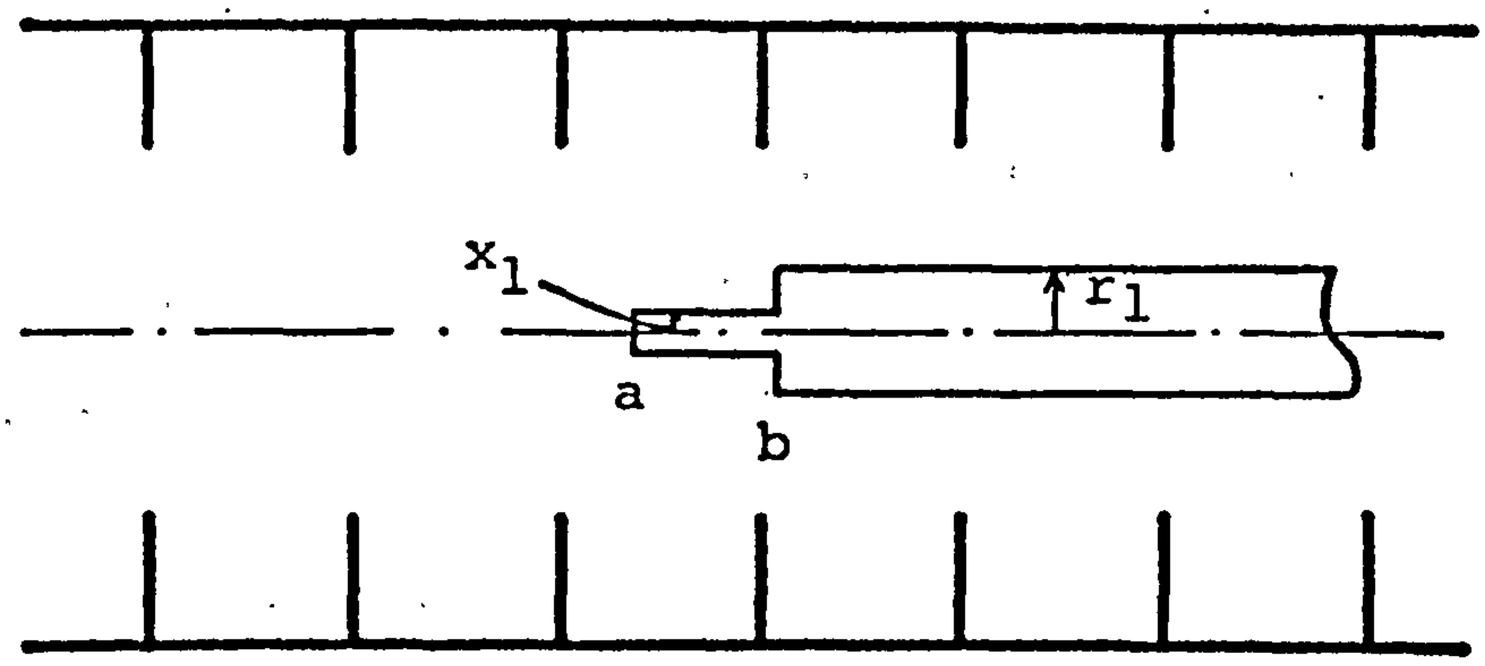

Figure (5.18) Single step transformer in a corrugated circular waveguide

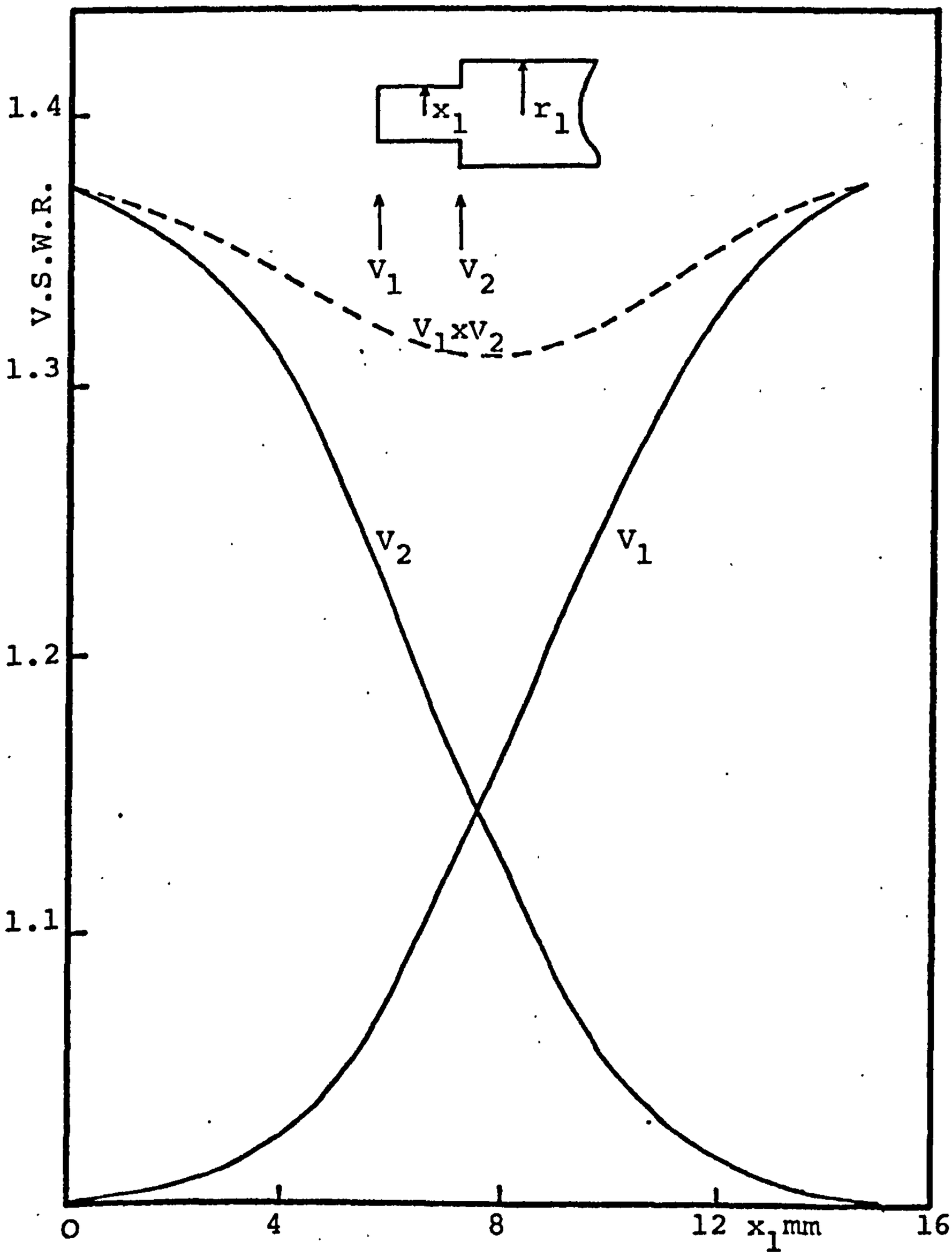

Figure (5.19) Theoretical V.S.W.R. of a single section transformer against section radius

$r_1 = 1.5cm \quad r_2 = 4cm \quad \bar{\varepsilon}_1 = 2.25$

By using a modified form of the variational method employed by Farmer <45>, it is shown by Clarricoats <47> that

$$Z_1/Z_o = \frac{\int_o^{x_1} \underset{\sim}{E}_a \times \underset{\sim}{H}_b^* r dr + \int_{x_1}^{r_1} \underset{\sim}{E}_c \times \underset{\sim}{H}_b^* r dr}{\int_o^{x_1} \underset{\sim}{E}_b \times \underset{\sim}{H}_a^* r dr + \int_{x_1}^{r_1} \underset{\sim}{E}_b \times \underset{\sim}{H}_c^* r dr} \qquad \{5.10\}$$

and

$$Z_2/Z_1 = \frac{\int_o^{x_1} \underset{\sim}{E}_d \times \underset{\sim}{H}_a^* r dr + \int_{x_1}^{r_1} \underset{\sim}{E}_d \times \underset{\sim}{H}_c^* r dr + \int_{r_1}^{r_2} \underset{\sim}{E}_e \times \underset{\sim}{H}_c^* r dr}{\int_o^{x_1} \underset{\sim}{E}_a \times \underset{\sim}{H}_d^* r dr + \int_{x_1}^{r_1} \underset{\sim}{E}_c \times \underset{\sim}{H}_d^* r dr + \int_{r_1}^{r_2} \underset{\sim}{E}_c \times \underset{\sim}{H}_e^* r dr} \qquad \{5.11\}$$

where the transverse field components are given in table (5.3).

Region	Radius	Transverse Field		Relative Permittivity
0	$0 - r_2$	$\underset{\sim}{E}_a$	$\underset{\sim}{H}_a$	1
1	$0 - x_1$	$\underset{\sim}{E}_b$	$\underset{\sim}{H}_b$	$\bar{\varepsilon}_1$
1	$x_1 - r_2$	$\underset{\sim}{E}_c$	$\underset{\sim}{H}_c$	1
2	$0 - r_1$	$\underset{\sim}{E}_d$	$\underset{\sim}{H}_d$	$\bar{\varepsilon}_1$
2	$r_1 - r_2$	$\underset{\sim}{E}_e$	$\underset{\sim}{H}_e$	1

Table (5.3)

where $\underset{\sim}{E}_a$, $\underset{\sim}{H}_a$ are the transverse electric and magnetic field components of the empty corrugated waveguide.

The above junction V.S.W.R.'s are calculated using transverse field components of a particular mode at a given frequency and therefore, the following assumptions are implied;

(i) the phase-change coefficient of the given mode is frequency independent in any given section of the waveguide, and

(ii) the characteristic impedance of various sections are also frequency independent.

The transformer design is based on providing the HE_{11} mode with the least possible reflection coefficient and as the object of the mode filter is to attenuate the unwanted modes, then the reflection coefficients of the unwanted modes are not significant.

Transverse field components of the HE_{11} mode in appropriate sections of the corrugated waveguide are substituted in {5.10} and {5.11} to calculate the V.S.W.R. at the two junctions. The transverse field components are obtained by first solving the characteristic equation {5.5} for given values of ω and r_1, and then values of β and the amplitude coefficients are inserted in the appropriate expressions.

For a core radius of 1.5 cm the V.S.W.R. at the junctions (a) and (b) of Figure (5.18) is shown in Figure (5.19), as a function of transformer radius x_1. If V_1 and V_2 denotes the V.S.W.R. at the junctions (a) and (b) then

$$V_1 = Z_1/Z_o \qquad V_2 = Z_2/Z_1$$

When the transformer radius x_1 is equal to zero or to the core radius 1.5 cm, the junction V.S.W.R. will be the same and is given by Z_2/Z_o(=1.372). The product (V_1 x V_2) must be constant for all values of x_1 and equal to 1.372. But this is shown to be not the case in Figure (5.19), where a maximum departure of nearly 4% is observed. This error can be attributed to the neglect of the junction reactance in the transmission line equivalent circuit <48>. Due to the neglect of the junction reactance there is a small non-reciprocity of the formula used {5.10} and{5.11} to obtain V_1 and V_2,

$$\text{i.e.} \quad \frac{Z_1}{Z_o} \cdot \frac{Z_2}{Z_1} \neq \frac{Z_2}{Z_o} \qquad \forall(x_1)$$

This implies slightly incorrect results for the two-junction problem. However, the small error introduced in the calculations of the junction V.S.W.R. will be neglected as the transverse field components used in the calculations are also approximate. This is because they were derived assuming an impedance boundary model at $r = r_2$.

5.7.4 Junction V.S.W.R.

The V.S.W.R. at a junction between an empty corrugated waveguide and one containing an axial dielectric region is shown in Figure (5.20) as a function of the core radius r_1. The field components of the HE_{11} mode were used in the computation of {5.10} for two values of corrugation radius r_2, at a fixed frequency of 9 GHz. The relative permittivity of the core region used in calculating the field component was 2.25. It is seen that for a particular value of core radius r_1, the junction V.S.W.R. decreases with increasing value of corrugation radius r_2. This phenomena occurs due to the concentration of the HE_{11} field in the axial region of the waveguide, and therefore high reflection coefficient is expected for smaller values of corrugation radius.

The necessity for a matching section is clearly illustrated in Figure (5.20), where it is seen that in a 4.0 cm corrugation radius waveguide, the V.S.W.R. of the junction is greater than 1.2, when a 1.0 cm core mode filter is used. This figure is unacceptable. The V.S.W.R.

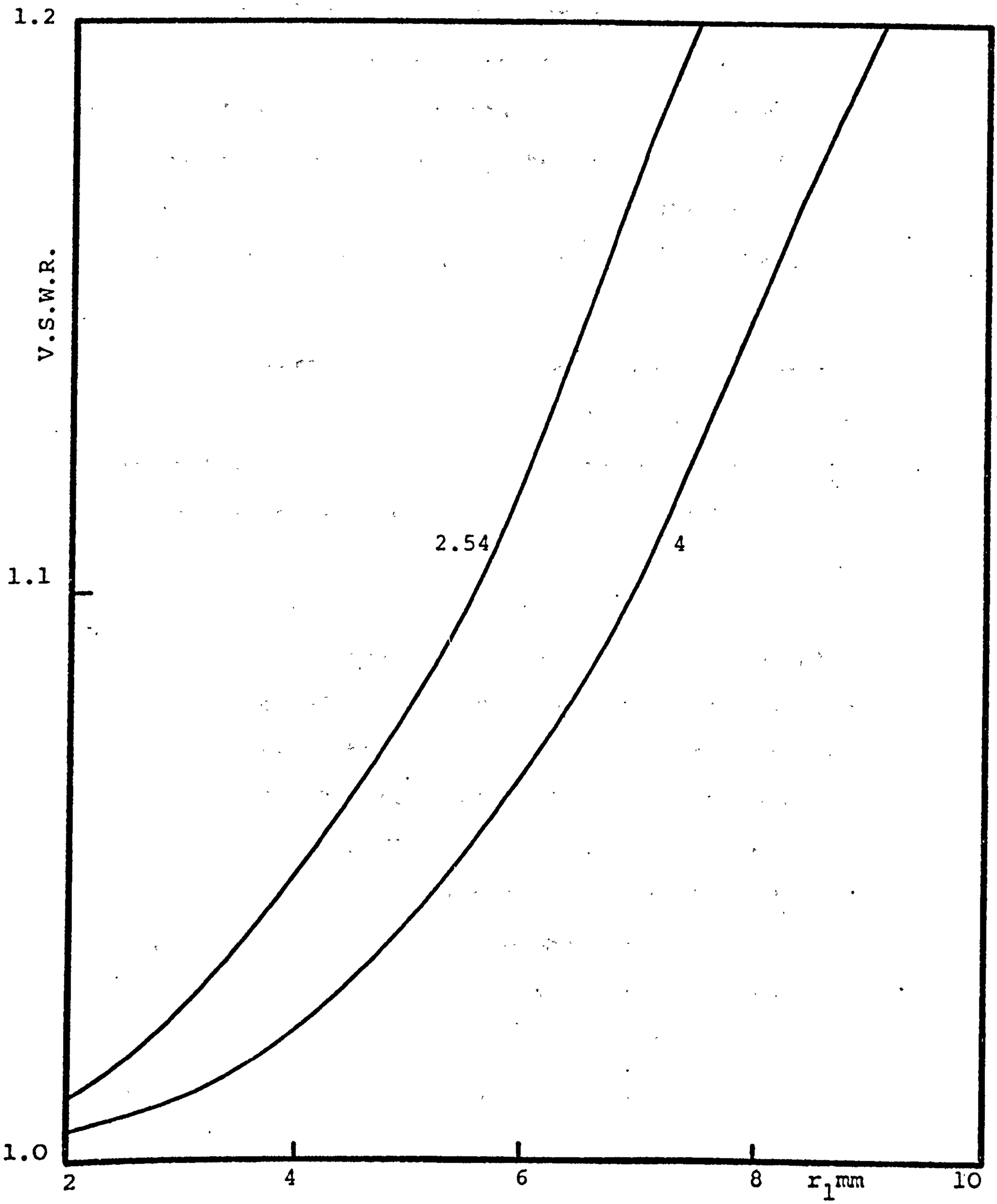

Figure (5.20) Theoretical V.S.W.R. of a dielectric rod in a corrugated waveguide against rod radius.

$\bar{\varepsilon}_1 = 2.25$ f = 9.0 GHz

Parameter (r_2)

at a junction between two similar corrugated waveguides containing axial core regions of different radii is shown in Figure (5.21). With the corrugation radius r_2 equal to 4 cm, x_q and x_{q-1} being the radii of the q-1 and q-th region of Figure (5.17). The computation was carried out using {5.11} at a fixed frequency of 9 GHz.

The influence of the core size on the junction V.S.W.R. is illustrated in Figure (5.21), where it is seen that for large values of x_q the junction V.S.W.R. becomes very sensitive to small changes in the value of x_{q-1}. Figure (5.21) is used in selecting the junction V.S.W.R. required for different steps of the quarter-wave transformer shown in Figure (5.17). These values are then inserted in the insertion loss expression and the overall reflection coefficient of the transformer is calculated. The radii of individual steps are therefore obtained. The electric length θ of each section of the transformer was assumed to be $\pi/2$, at the design frequency, thus the physical length $\lambda g/4$, ($\lambda g=2\pi/\beta$), can easily be calculated using Figure (5.22), where the guide wavelength λg is plotted as a function of the core radius r_1. Values of λg are obtained at a frequency of 9 GHz, with r_2 being equal to 4.0 cm.

5.7.5 Transformer Design

Figures (5.20) and (5.21) are used to select the V.S.W.R. at the first junction and at all consecutive

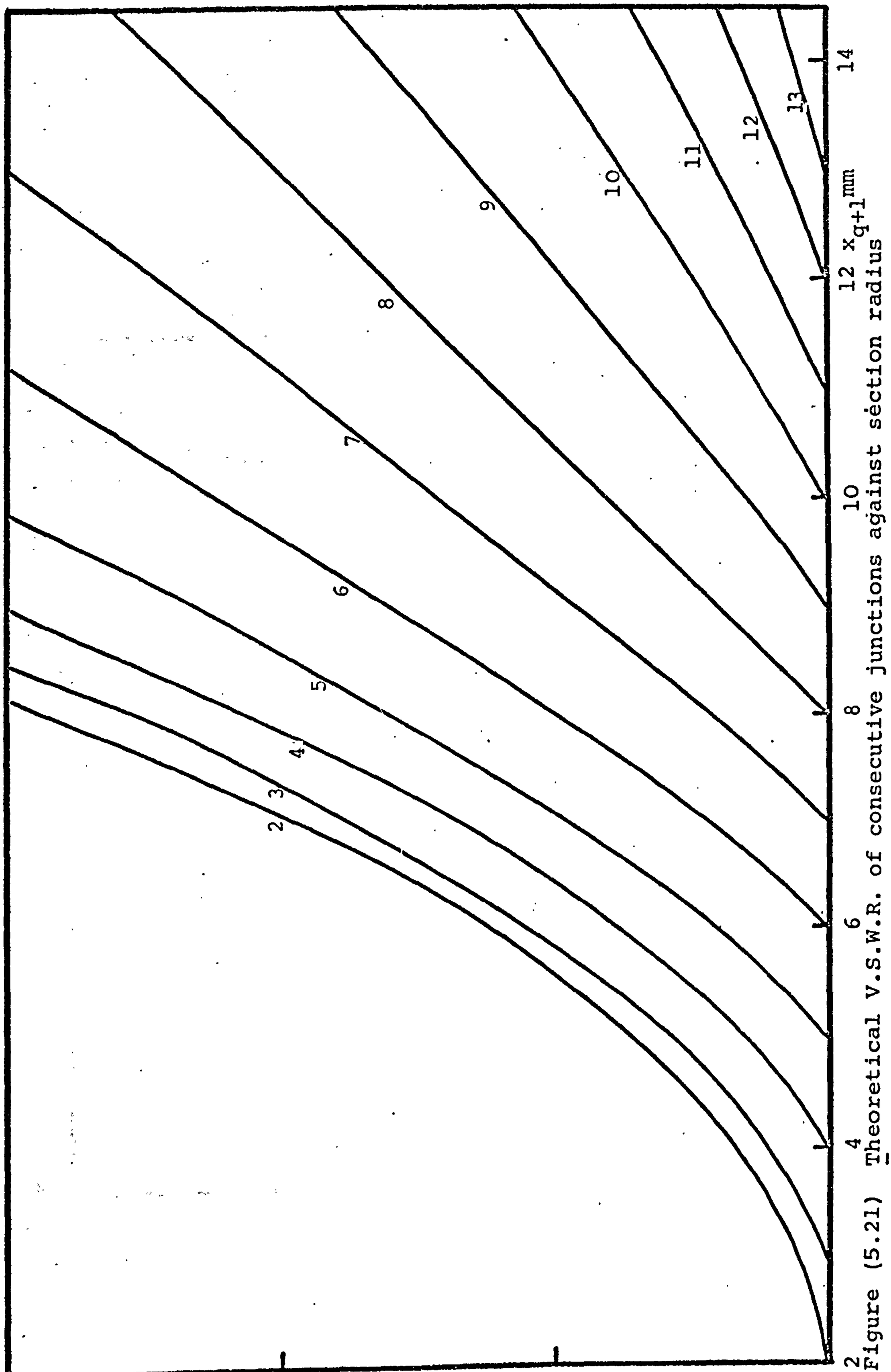

Figure (5.21) Theoretical V.S.W.R. of consecutive junctions against section radius
ε_1 = 2.25 r_2 = 4cm f = 9.0 GHz
Parameter (x_q)

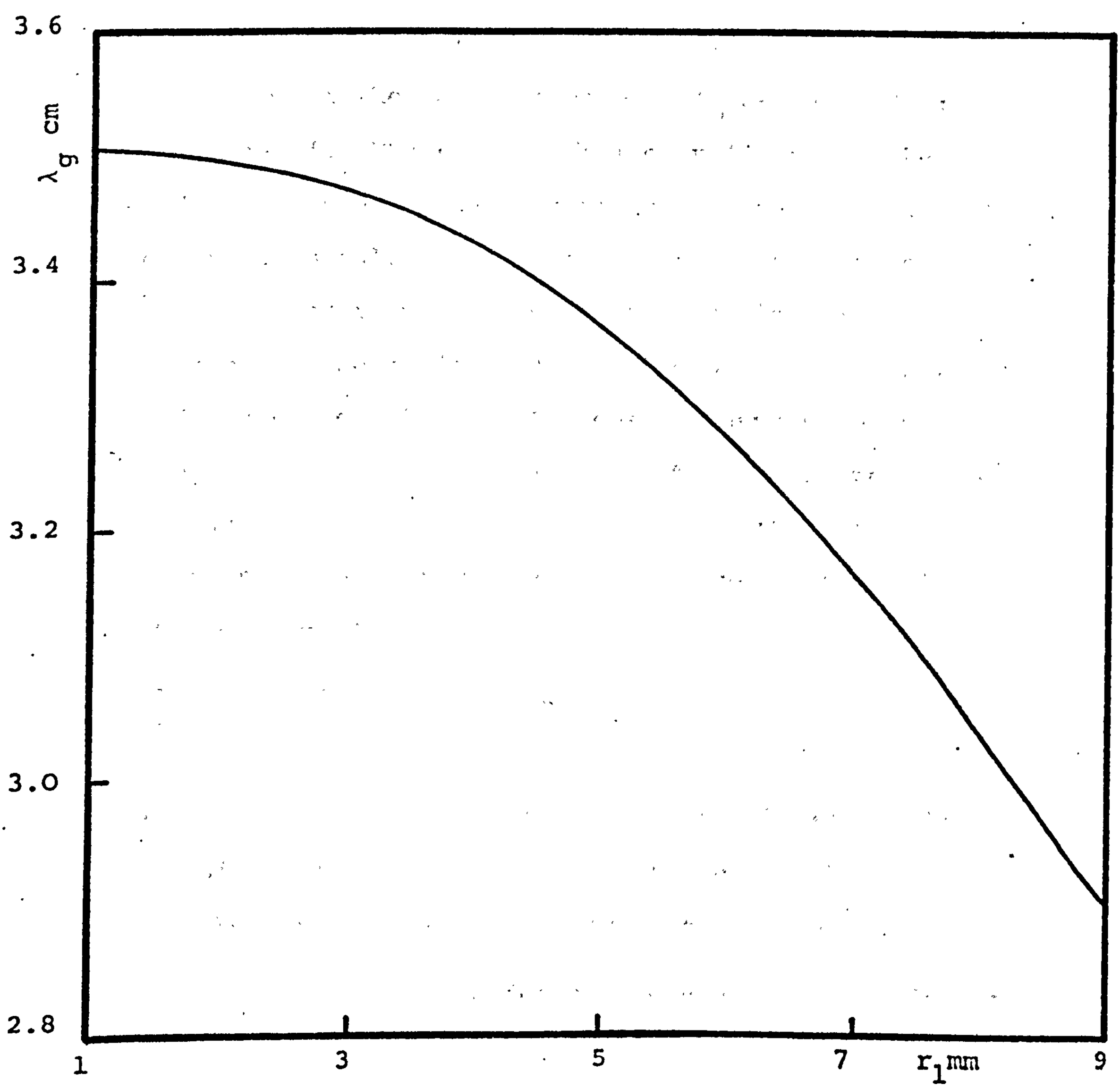

Figure (5.22) Guide wavelength of a loaded corrugated circular waveguide against rod radius

$\bar{\varepsilon}_1 = 2.25$ $r_2 = 4$cm f = 9.0 GHz.

junctions. The criterion used in selecting the V.S.W.R. values is that at all junctions, this quantity must be as small as possible provided that the last section of the transformer is matched to the core region of the mode filter with a low V.S.W.R. A computer program was developed to provide the overall V.S.W.R. of an n-section transformer at the design frequency f_o and at different frequencies f. The range (f/f_o) of validity of the results is based on the assumption that the V.S.W.R. of the junctions calculated at f_o will remain constant throughout the range. This assumption also implies that the value of the guide wavelength λg obtained at f_o, for the different sections, will remain constant for the range. A defined polynomial was not used to synthesise the transformer performance in this instance because of the error introduced in the calculations of the V.S.W.R. at the multi-section transformer, i.e.

$$\frac{Z_1}{Z_o} \cdot \frac{Z_2}{Z_1} \cdot \frac{Z_3}{Z_2} \; - - - - \; \frac{R}{Z_n} \neq \frac{R}{Z_o} \qquad \{5.12\}$$

The equality of this expression form the bases of the synthesis procedure, and accurate values of the radii x_q of the different sections were not obtainable.

Computed results for a three-section transformer are shown in Figure (5.23), where the V.S.W.R. of different junctions is chosen rather arbitrary to give best performance at and near the designed frequency f_o. The transformer is designed to match a 1.0 cm core radius mode filter situated in a corrugated waveguide with r_2

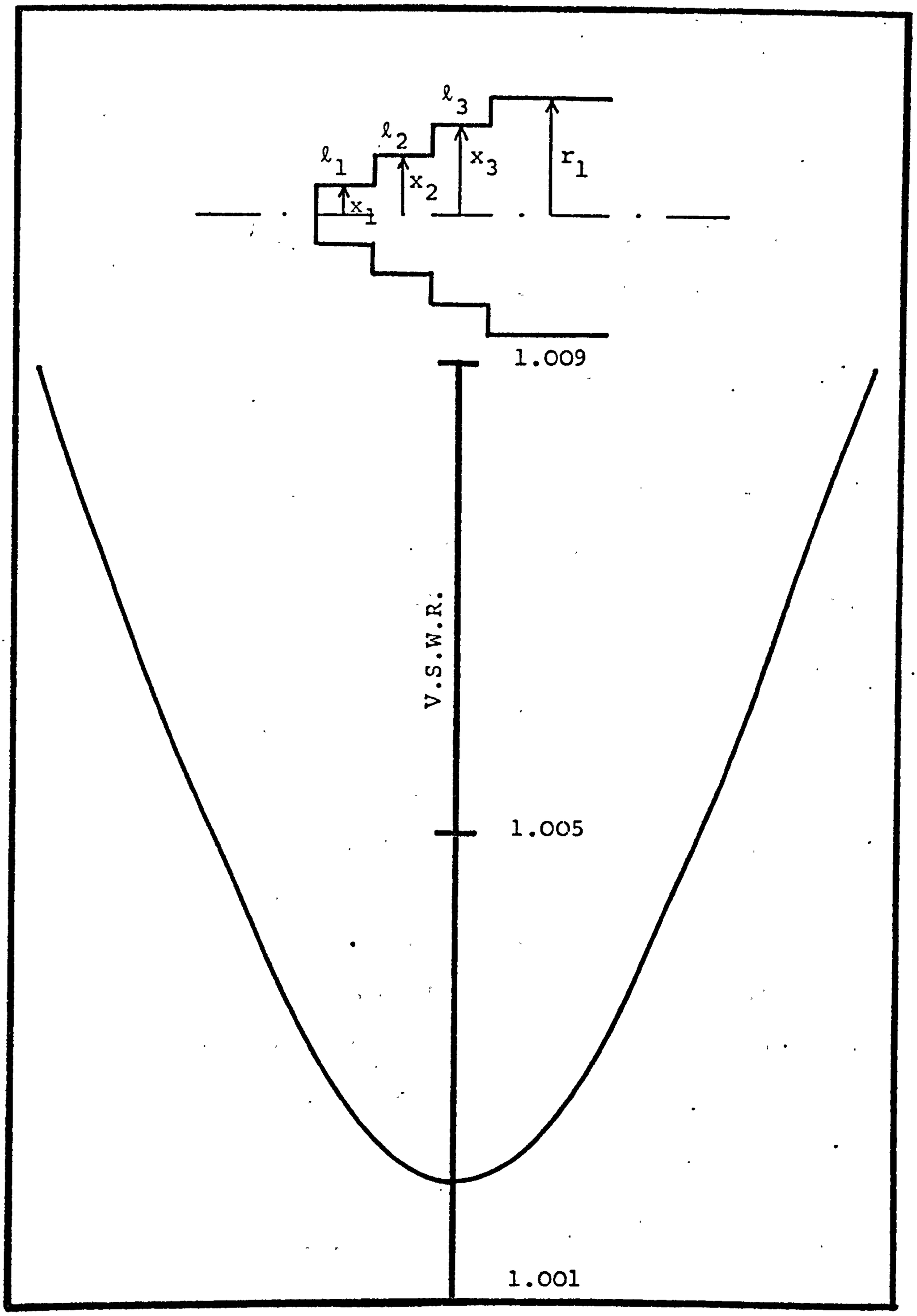

Figure (5.23) Theoretical V.S.W.R. of a three section transformer against normalised frequency .

$\bar{\varepsilon}_1 = 2.25$ $r_1 = 1cm$ $r_2 = 2.54cm$ $f_o = 9.0$ GHz

$\ell_1 = 9.4mm$ $\ell_2 = 8.8mm$ $\ell_3 = 7.7mm$

$x_1 = 1mm$ $x_2 = 2.5mm$ $x_3 = 4mm$

equal to 2.54 cm.

The product of the V.S.W.R. at different junctions is equal to 1.23, while in the absence of the transformer, the junction V.S.W.R. at the 1.0 cm core radius will be 1.30. The difference between the two results clearly demonstrates the inequality sign in the expression {5.12} and is due to the error explained above. A cross-sectional view of the transformer is shown in the insert of Figure (5.23), the lengths of different sections are calculated from a knowledge of the values of λg at different sections of the waveguide.

5.8 EXPERIMENTAL OBSERVATIONS

Two mode filters of the type described in previous sections were designed, constructed and tested in existing corrugated circular waveguides. Figure (5.24) shows a three-step transformer section at either end of the core region of the mode filter. The core region is contained in an annulus of expanded polystyrene. The outer absorbing layer, not shown in the photograph, was created first by winding two layers of flexible absorber (Emerson and Cumming Ecosorb VF10) around the outside of the expanded polystyrene. The loss tangent of the absorber is about equal to unity and its relative permittivity is slightly greater than $\bar{\varepsilon}_2$(=1.02), Figure (5.25) a, b shows swept frequency measurements made both with and without the mode filter. Elimination of the unwanted modes trapped resonance is clearly observed.

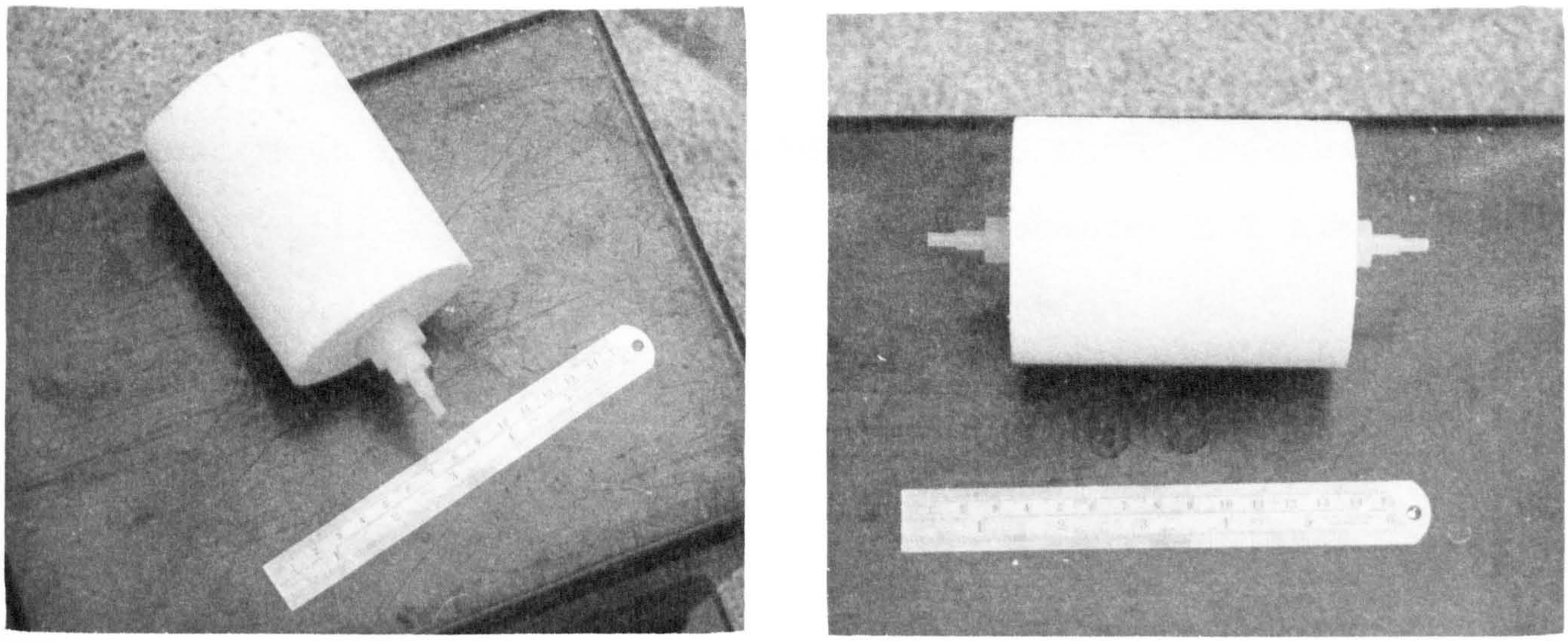

Figure (5.24)

Propsed Mode Filter For Corrugated Circular Waveguides

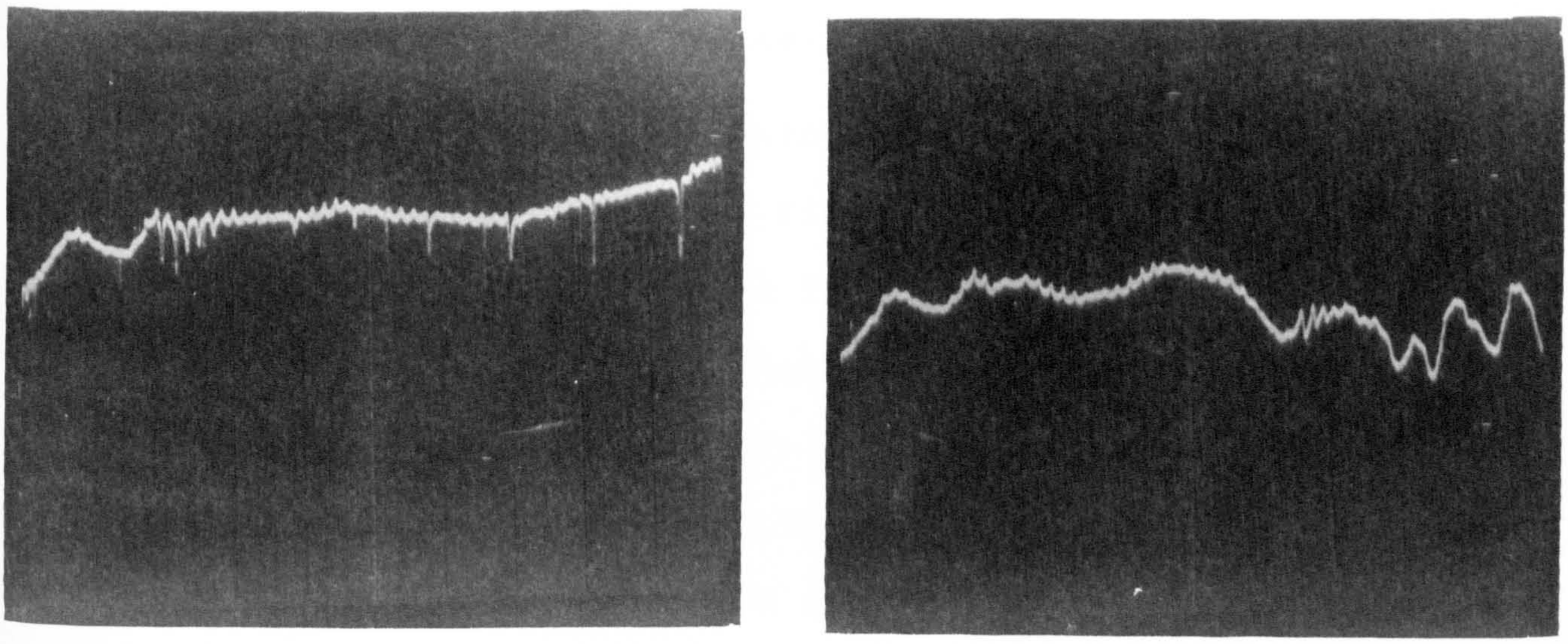

Horizontal Scale 8.0-10.0 GHz.

(a) (b)

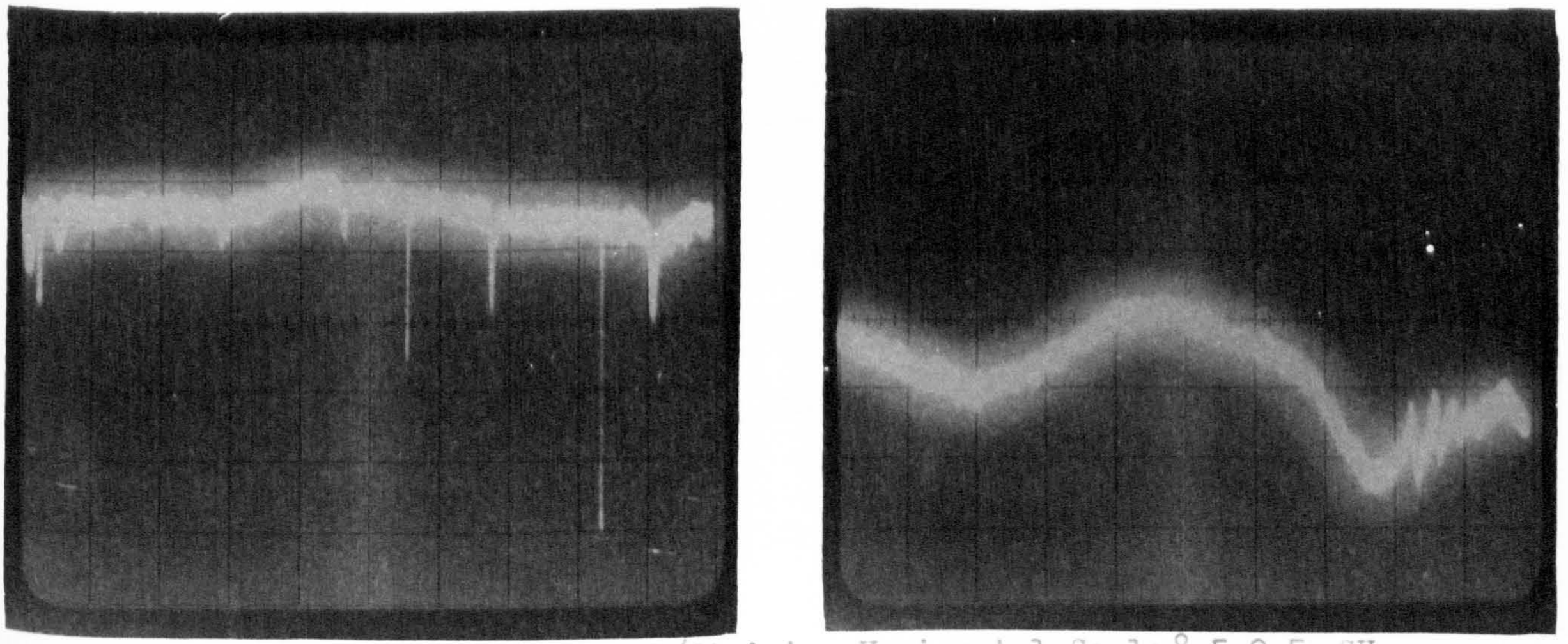

Vertical Scale 0.5dB/division Horizontal Scale 8.5-9.5 GHz.

Figure (5.25)

(a) Without Mode Filter. (b) With Mode Filter-Lossy Layer.

Subsequent reduction to one fold of the outer absorbing layer still eliminated the trapped resonances but almost halved the additional HE_{11} mode attenuation. An alternative very thin absorbing layer was made of solidified 'Emerson and Cummings' lossy paint. Its effect on the HE_{11} mode was observed to be even less, while the elimination of the trapped resonance was still achieved. Experimenting with different absorbing materials gave satisfactory results for the overall performance of the mode filter.

The low mismatch achieved by the transformer section is clearly shown in Figure (5.25) b, where it is seen that at the designed frequency, 9 GHz, the mismatch is minimum. The high mismatch observed at frequencies above 9 GHz, merely confirms the power concentration of the HE_{11} mode in the central region of the waveguide, and therefore a high reflection coefficient at these frequencies is noticed. On the other hand, at frequencies below 9 GHz, the mismatch does not result in high reflection coefficient because of the weak concentration of the HE_{11} mode power in the central region of the waveguide.

Due to the circular symmetry of the mode filter, it was observed that its influence on the cross-polarised components was exactly the same.

CHAPTER SIX

DIELECTRIC-LINED CIRCULAR WAVEGUIDES

6.1 INTRODUCTION

The investigations of corrugated circular waveguidesby Clarricoats and Olver < 2 > show that one reason for low attenuation lies in the low field strength near the wall in the case of the lowest order linearly polarised mode. The condition is achieved because a reactive boundary is created in the corrugated waveguide by a slot of approximately one quarter wavelength in depth. As corrugations are difficult to fabricate it was natural to wonder whether a dielectric-lined waveguide might exhibit low-attenuation and evidence in favour of this surmise is demonstrated in this chapter.

Barlow et al <49> have discussed the use of a dielectric-lined waveguide for long distance communication utilising the TE_{01} mode. In 1971 Carlin and D'Agostino < 5 >, < 6 > extended the analysis reported by Unger <18 > to include higher order circularly symmetric electric and magnetic modes of the lined waveguide. These authors have demonstrated that the attenuation of the TM_{0m} modes may be reduced under certain conditions. Furthermore, they show that under the same conditions, the TE_{0m} modes of the lined waveguide exhibit high losses. However, these authors were unaware of a previous study of the same structure by Brayer <20>, who had not only made the above observation but had also found low-attenuation bandpass characteristics in a linearly polarised wave supported by the lined structure.

Falicasecca and Prandi <50> calculated the complex propagation coefficient of the lined waveguide for the circularly symmetric modes using Rayleigh-Schroedinger power expansion technique. Their dispersion and attenuation results were found to be in good agreement with those obtained in < 5 > where first order perturbation techniques were used.

From the above description, one would not expect a low-attenuation region for the azimuthally dependent modes, since, as is well known <51>, the boundary conditions at $r = r_1$, Figure (6.1), couple E and H-type fields together to form hybrid modes. These boundary conditions would not appear to be simultaneously favourable to both E and H-type fields.

In April 1973 Carlin and D'Agostino <52> extended their investigations of the dielectric lined waveguide to include the azimuthally dependent modes. They illustrated the dispersion and attenuation characteristics of a number of modes supported by the structure. Apparently, these authors were unaware of our Electronics Letter, August 1972, where the attenuation characteristics of the two lowest order hybrid modes of the lined waveguide are reported.

In this chapter, it is shown that at the low-attenuation condition, the EH_{11} mode of the lined waveguide exhibits properties similar to those of the HE_{11} mode in a corrugated circular waveguide. Under this condition it is found that the HE_{11} mode of the lined

structure exhibits maximum-attenuation condition. The mode designated HE_{11} in corrugated circular waveguide is so named because the fields in the interior region ($r < r_1$, Figure (4.1)) closely resemble those of the HE_{11} mode of a dielectric rod which was the first hybrid mode structure to be studied in depth. However, examining the field over the total waveguide cross-section including the slot region, it is easy to identify the mode with the EH_{11} mode and the correspondence with that mode in dielectric lined waveguide follows naturally. In the last part of this chapter it is shown that the EH_{11} mode could be more readily excited than the circularly symmetric modes, and thus we believe that this mode could find applications at millimetre wavelengths, where the metal wall loss of an unlined waveguide is normally very high.

6.2 FORMULATION OF THE PROBLEM

6.2.1 Introduction

The waveguide structure under investigation is shown in Figure (6.1). It is a perfectly conducting cylinder of radius r_2 to which a lossless dielectric of relative permittivity $\bar{\varepsilon}$ and thickness d is bonded.

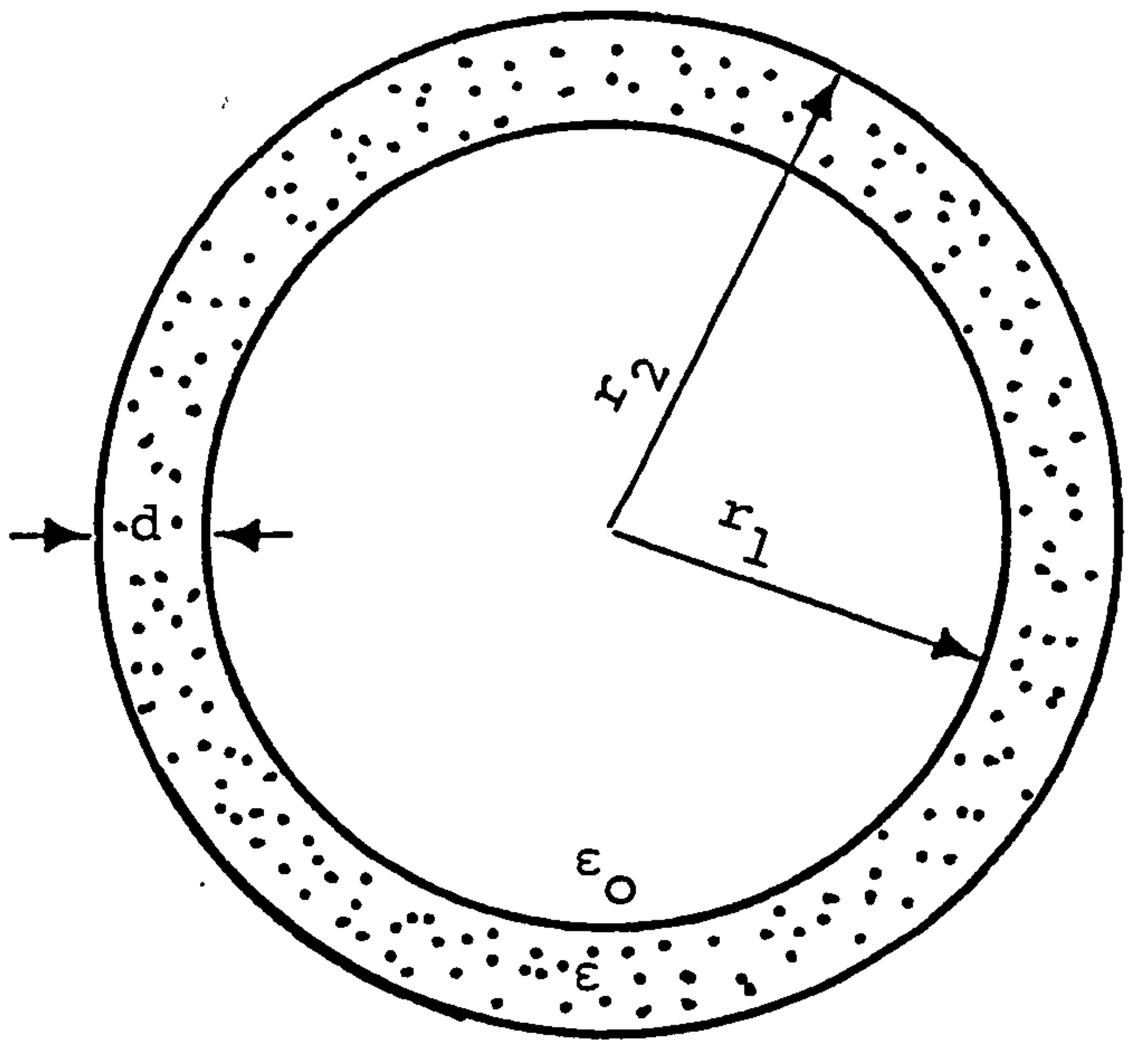

Figure (6.1) Dielectric Lined Waveguide

The interior region ($r < r_1$) is to be filled with Noble gas whose electrical properties are those of free-space over the frequency range of interest. Solutions of the wave equation in the two regions are obtained and on applying appropriate boundary conditions the characteristic equation of the structure is obtained. As the structure is assumed lossless, the transverse wave number, as given by the solution of the characteristic equation, is either real or pure imaginary.

The normal mode azimuthal dependent fields of the structure are not pure transverse electric or magnetic as in a hollow metallic waveguide, rather they are hybrid HE or EH modes. On the other hand, the circularly symmetric modes are pure TE or TM modes. This will be

demonstrated using the transverse network representation of the structure.

6.2.2 Characteristic Equation

Solutions of the wave equation in the two regions shown in Figure (6.1) have the form;

$$0 < r < r_1 \qquad {}_1E_z = A_1 J_n(K_1 r)\cos(n\theta)$$

$$ {}_1H_z = B_1 Y_o J_n(K_1 r)\sin(n\theta) \qquad \{6.1\}$$

$$r_1 < r < r_2 \qquad {}_2E_z = A_2 \frac{\S D_n(K_2 r, K_2 r_2)}{Y_n(K_2 r_2)} \cos(n\theta)$$

$$ {}_2H_z = B_2 Y_o \frac{\P D_n(K_2 r, K_2 r_2)}{Y_n'(K_2 r_2)} \sin(n\theta) \qquad \{6.2\}$$

The transverse wavenumbers are related by;

$$K_1^2 = \omega^2 \mu_o \varepsilon_o - \beta^2 \qquad K_2^2 = \omega^2 \mu_o \bar{\varepsilon} \varepsilon_o - \beta^2$$

where β is the phase-change coefficient, $Y_o = \sqrt{\varepsilon_o/\mu_o}$.

$$R_n(x,y) = x \frac{\P N_n(x,y)}{\P D_n(x,y)} \equiv x \frac{J_n'(x)Y_n'(y) - J_n'(y)Y_n'(x)}{J_n(x)Y_n'(y) - J_n'(y)Y_n(x)} ,$$

$$S_n(x,y) = x \frac{\S N_n(x,y)}{\S D_n(x,y)} \equiv x \frac{J_n'(x)Y_n(y) - J_n(y)Y_n'(x)}{J_n(x)Y_n(y) - J_n(y)Y_n(x)} ,$$

A_1, A_2, B_1 and B_2 are amplitude coefficients.

The primed Bessel functions mean first derivations with respect to their arguments.

The term expj$(\omega t - \beta z)$ is assumed in the field expressions.

The field expressions written in the form {6.1} and {6.2} satisfy the boundary conditions;

(i) Finite field intensity at the origin r = 0.

(ii) Vanishing tangential electric field intensity at the metal wall $r = r_2$.

(iii) Vanishing normal magnetic field intensity at the metal wall $r = r_2$.

The transverse field components in the two regions are obtained using Appendix I with $\ell_1 = 1$, $\ell_2 = r$, and the appropriate value of the transverse wavenumber in the two regions.

In the region $0 < r < r_1$;

$$ {}_1E_r = -j\left[A_1 \frac{(\beta r)|K_1 r|}{(K_1 r)^2} J_n'(K_1 r) + B_1 \frac{n\bar{r}}{(K_1 r)^2} J_n(K_1 r)\right]\cos(n\theta) $$

$$ {}_1H_r = -jY_o\left[A_1 \frac{n\bar{r}}{(K_1 r)^2} J_n(K_1 r) + B_1 \frac{(\beta r)|K_1 r|}{(K_1 r)^2} J_n'(K_1 r)\right]\sin(n\theta) $$

$$ {}_1E_\theta = j\left[A_1 \frac{n(\beta r)}{(K_1 r)^2} J_n(K_1 r) + B_1 \frac{\bar{r}|K_1 r|}{(K_1 r)^2} J_n'(K_1 r)\right]\cos(n\theta) $$

$$ {}_1H_\theta = -jY_o\left[A_1 \frac{\bar{r}|K_1 r|}{(K_1 r)^2} J_n'(K_1 r) + B_1 \frac{n(\beta r)}{(K_1 r)^2} J_n(K_1 r)\right]\sin(n\theta) $$

{6.3}

and in the dielectric region;

$$2E_r = -j\left[\frac{(\beta r)}{(K_2 r)} \frac{\S N_n(K_2 r, K_2 r_2)}{Y_n(K_2 r_2)} + B_2 \frac{n\bar{r}}{(K_2 r)^2} \frac{\P D_n(K_2 r, K_2 r_2)}{Y_n'(K_2 r_2)}\right]\cos(n\theta)$$

$$2H_r = -jY_o\left[A_2 \frac{n\bar{r}\bar{\varepsilon}}{(K_2 r)^2} \frac{\S D_n(K_2 r, K_2 r_2)}{Y_n(K_2 r_2)} + B_2 \frac{(\beta r)}{(K_2 r)} \frac{\P N_n(K_2, K_2 r_2)}{Y_n'(K_2 r_2)}\right]\sin(n\theta)$$

$$2E_\theta = j\left[A_2 \frac{n(\beta r)}{(K_2 r)^2} \frac{\S D_n(K_2 r, K_2 r_2)}{Y_n(K_2 r_2)} + B_2 \frac{\bar{r}}{(K_2 r)} \frac{\P N_n(K_2 r, K_2 r_2)}{Y_n'(K_2 r_2)}\right]\sin(n\theta)$$

$$2H_\theta = -jY_o\left[A_2 \frac{\bar{\bar{\varepsilon}}\bar{r}}{(K_2 r)} \frac{\S N_n(K_2 r, K_2 r_2)}{Y_n(K_2 r_2)} + B_2 \frac{n(\beta r)}{(K_2 r)} \frac{\P D_n(K_2 r, K_2 r_2)}{Y_n'(K_2 r_2)}\right]\cos(n\theta$$

{6.4}

where $\bar{r} = \omega r\sqrt{\varepsilon_o \mu_o}$.

The general solutions of the field are then introduced with the boundary conditions;

at $r = r_1$

$$1E_z = 2E_z \qquad 1H_z = 2H_z$$

$$1E_\theta = 2E_\theta \qquad 1H_\theta = 2H_\theta$$

and after some cumbersome algebra a homogeneous system of equations for the amplitude coefficients is obtained. From the condition of non-triviality of the solution of the system obtained, the characteristic equation of the

lined waveguide is obtained, which after simplification can be written in the form

$$\left[\frac{F_n(K_1r_1)}{(K_1r_1)^2} - \frac{R_n(K_2r_1,K_2r_2)}{(K_2r_1)^2}\right]\left[\frac{F_n(K_1r_1)}{(K_1r_1)^2} - \frac{S_n(K_2r_1,K_2r_2)}{(K_2r_1)^2}\right]$$

$$= (n\bar{\beta})^2\left[\frac{1}{(K_1r_1)^2} - \frac{1}{(K_2r_1)^2}\right] \qquad \{6.5\}$$

where $F_n(x) = x\,\dfrac{J_n'(x)}{J_n(x)}$ and $\bar{\beta} = \dfrac{(\beta r)}{\bar{r}}$.

The above characteristic equation is valid when the transverse wavenumber is real, i.e. $\bar{\beta} < 1$.

When K_1 becomes pure imaginary the characteristic equation has the form

$$\left[\frac{F_n(K_1' r_1)}{(K_1' r_1)^2} + \frac{R_n(K_2r_1,K_2r_2)}{(K_2r_1)^2}\right]\left[\frac{F_n(K_1' r_1)}{(K_1' r_1)^2} + \frac{S_n(K_2r_1,K_2r_2)}{(K_2r_1)^2}\right]$$

$$= (n\bar{\beta})^2\left[\frac{1}{(K_1' r_1)^2} + \frac{1}{(K_2r_1)^2}\right]^2$$

where $F_n(x) = x\,\dfrac{I_n'(x)}{I_n(x)}$ and $K_1 = jK_1'$

The amplitude coefficients can be expressed in terms of A_1 using the relationships

$$A_2 = A_1 \frac{J_n(K_1 r_1) Y_n(K_2 r_2)}{\S D_n(K_2 r_1, K_2 r_2)}$$

$$B_2 = B_1 \frac{J_n(K_1 r_1) Y_n'(K_2 r_2)}{\P D_n(K_2 r_1, K_2 r_2)}$$

$$B_1 = A_1 \left[\frac{\omega \varepsilon_o F_n(K_1 r_1)}{(K_1 r_1)^2} - \omega \bar{\varepsilon} \varepsilon_o \frac{S_n(K_2 r_1, K_2 r_2)}{(K_2 r_1)} \right] \left[\frac{n \beta}{(K_1 r_1)^2} - \frac{n\beta}{(K_2 r_1)^2} \right]^{-1}$$

{6.6}

6.2.3 Transverse-Network Representation

The electromagnetic behaviour of the dielectric lined circular waveguide can also be described by the use of the transverse network representation. A summary of the theory is given here, the details of development can be found in <51> and <53>. The transverse-network shown in Figure (6.2) corresponds to the physical structure shown in Figure (6.1). The electric and magnetic field components of the lined waveguide are expressed in terms of voltages and current analogies. The electromagnetic behaviour is described in terms of the transfer admittances and impedances. In the E-line, the admittances at the boundary $r = r_1$ are given by;

$$\overleftarrow{Y}_{a,a} = -j \frac{\omega \varepsilon_o}{K_1^2} F_n(K_1 r_1)$$

$$\overrightarrow{Y}_{a,a} = j \frac{\omega \bar{\varepsilon} \varepsilon_o}{K_2^2} S_n(K_2 r_1, K_2 r_2)$$

and for the H-line the impedances at the boundary $r = r_1$ are given by;

$$\overleftarrow{Z}_{b,b} = -j \frac{\omega\mu_o}{K_1^2} F_n(K_1 r_1)$$

$$\overrightarrow{Z}_{b,b} = j \frac{\omega\mu_o}{K_2^2} R_n(K_2 r_1, K_2 r_2)$$

The impedances and admittances are evaluated looking in the positive radial direction.

At the junction i.e. at the boundary $r = r_1$, the radial transmission lines are related by

$$(\overleftarrow{Z}_{b,b} + \overrightarrow{Z}_{b,b})(\overleftarrow{Y}_{a,a} + \overrightarrow{Y}_{a,a}) = N^2 \qquad \{6.7\}$$

where N represents the transformer ratio, and is given by;

$$N^2 = -n^2\beta^2\left[\frac{1}{K_1^2} - \frac{1}{K_2^2}\right]^2$$

Substituting for the impedances and admittances in {6.7} leads to the same characteristic equation obtained in {6.5}.

When n = 0, the coupling transformer is removed, and no coupling between the E and H lines occurs. Thus, circularly symmetric modes can be supported by the lined waveguide.

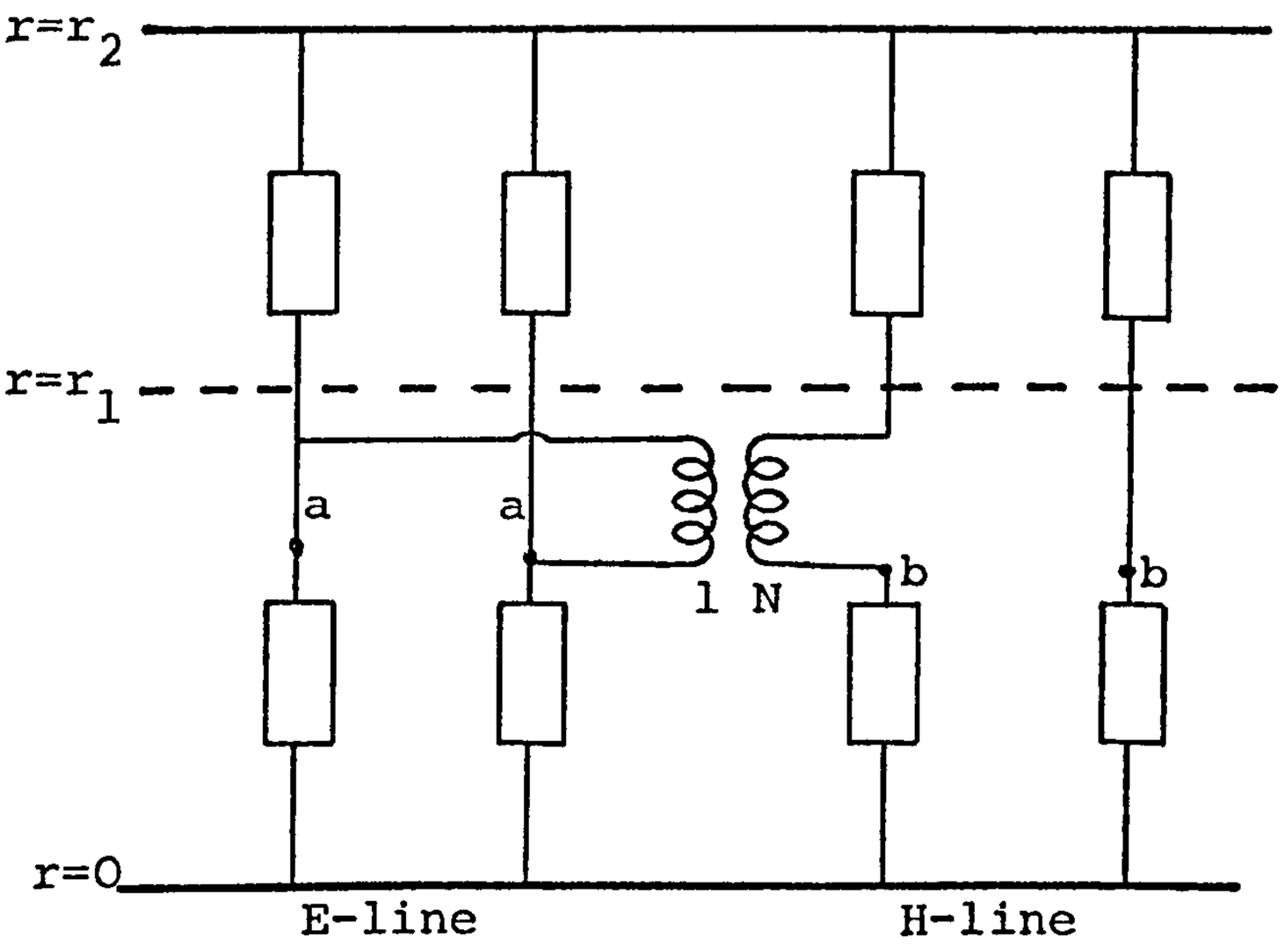

Figure (6.2)

Transverse network representation of the lined waveguide

6.2.4 Classifications of Modes

When analysing the lined waveguide Unger <18> used the notation $TE_{om}(TM_{om})$ for circularly symmetric modes to correspond to the $TE_{om}(TM_{om})$ modes in a hollow conducting circular waveguide, when the lining thickness is reduced to zero. The same notation was later adopted by Carlin and D'Agostino < 5 > and < 6 >, when studying the attenuation characteristics of the circularly symmetric modes in the lined waveguide. However, the existence of a pure TE_{nm} and TM_{nm} mode for n > 0 is no longer possible in the lined waveguide due to the coupling

mechanism introduced by the boundary at $r = r_1$. This is illustrated by the presence of the transformer in the transverse network representation described in the previous section.

Unger <54> used the term hybrid $TE_{nm}(TM_{nm})$ modes for the azimuthally dependent modes in the lined waveguide which correspond to the $TE_{nm}(TM_{nm})$ modes in a hollow conducting circular waveguide, when the lining thickness is reduced to zero. When analysing the same structure Brayer <20> used the same notation given by Unger for the circularly symmetric modes, but used the term hybrid $HE_{nm}(EH_{nm})$ modes for the azimuthally dependent modes, which correspond to the $TE_{nm}(TM_{nm})$ modes in the hollow waveguide, when the lining thickness is reduced to zero. Since the azimuthally dependent hybrid modes are due to contributions of both TE and TM modes, Brayer's hybrid mode notation will be adopted in naming the modes.

Recently, Carlin and D'Agostino <52>, reported some properties of the hybrid modes in the lined waveguide, the notation they used in naming the modes was that due to Unger. The suffix n, is the azimuthal dependence of the mode, and $n > 0$, indicates the order of the hybrid mode. The suffix m will indicate the m-th parametric root of the characteristic equation.

Table (6.1) summarises the mode nomenclature and notation used by different authors.

Wave-guide	Unger, Carlin and D'Agastino	Brayer
Hollow	TE_{om} TM_{om} TE_{nm} TE_{om}	TM_{om} TE_{nm} TM_{nm}
Lined	TE_{om} TM_{om} TE_{nm} TM_{om}	TM_{om} HE_{nm} EH_{nm}

Table (6.1)

6.2.5 Circularly Symmetric Modes

When the azimuthal order n = 0, the characteristic equation of the lined waveguide {6.5}, splits into two equations;

for $\bar{\beta} < 1$

$$\frac{F_o(K_1 r_1)}{(K_1 r_1)^2} - \frac{R_o(K_2 r_1, K_2 r_2)}{(K_2 r_1)^2} = 0$$

and

$$\frac{F_o(K_1 r_1)}{(K_1 r_1)^2} - \frac{\bar{\varepsilon} S_o(K_2 r_1, K_2 r_2)}{(K_2 r_1)^2} = 0$$

for $\bar{\beta} > 1$

$$\frac{F_o(K_1' r_1)}{(K_1' r_1)^2} + \frac{R_o(K_2 r_1, K_2 r_2)}{(K_2 r_1)^2} = 0$$

and

$$\frac{F_o(K_1' r_1)}{(K_1' r_1)^2} + \frac{\bar{\varepsilon} S_o(K_2 r_1, K_2 r_2)}{(K_2 r_1)^2} = 0$$

representing the TE_{om} and TM_{om} modes respectively.

The radial propagation constant for a TE_{om} (TM_{om}) mode in the lined waveguide equal to that of a TE_{om-1} (TM_{om-1}) mode in an unlined waveguide, when the lining is equivalent to half wavelength in thickness. For the TM_{01} mode, the radial propagation constant decreases rapidly to zero as the lining thickness increases and then becomes imaginary. This indicates that the TM_{01} mode propagates as a surface wave closely bound to the lining region. The other circularly symmetric modes exhibit the same surface wave behaviour for thicker linings. The attenuation characteristics of the circularly symmetric modes will be discussed in section (6.4).

6.3 DISPERSION CHARACTERISTICS

Unger <18> treated the hybrid modes of the lined waveguide, with very thin lining, as perturbed TE_{nm} and TM_{nm} modes of the hollow circular waveguide. Perturbation formulae obtained for the phase-change coefficient were valid for small lining thicknesses.

A computer program was developed to obtain exact solutions of the characteristic equation {6.5} using an iteration process, for values of $\bar{\beta}$ greater than and less than unity. The validity of the results obtained did not depend on the lining thickness chosen, as no approximations of the field were used in the formulation of the characteristic equation. For a fixed frequency 7.3 GHz, the effect of increasing the lining thickness

on the normalised phase-change coefficient of different hybrid modes is shown in Figure (6.3), with the waveguide's outer radius r_2, being fixed at 8.6 cm and perspex is used for the lining, $\bar{\varepsilon} = 2.56$.

At the two extremesof the r_1/r_2 axis, the values of the normalised phase-change coefficient coincide with those obtained in a circular waveguide filled with a homogeneous dielectric of relative permittivity $\bar{\varepsilon}$;

$$\bar{\beta} = \sqrt{\bar{\varepsilon} - (\frac{P_{nm}}{\bar{r}_2})^2} \qquad \{6.9\}$$

where P_{nm} is the m-th parametric root of $J_n = 0$ for TM_{nm} (EH_{nm}) modes, and is the m-th parametric root of $J_n' = 0$ for $TE_{nm}(HE_{nm})$ modes.

$$\bar{r}_2 = \omega r_2 \sqrt{\varepsilon_o \mu_o}$$

6.4 ATTENUATION CHARACTERISTICS

6.4.1 Introduction

The attenuation characteristic of the TE_{01} mode in a thinly lined circular waveguide was first determined by Unger <18>. His work was later extended by Carlin and D'Agastino < 5 >, where attenuation results of circularly symmetric modes are reported. It is shown that the attenuation of the TM_{om} modes may be reduced when the dielectric thickness is equal to $(2m-1)\frac{\lambda'}{4}$, where λ' is the effective transverse wavelength in the dielectric.

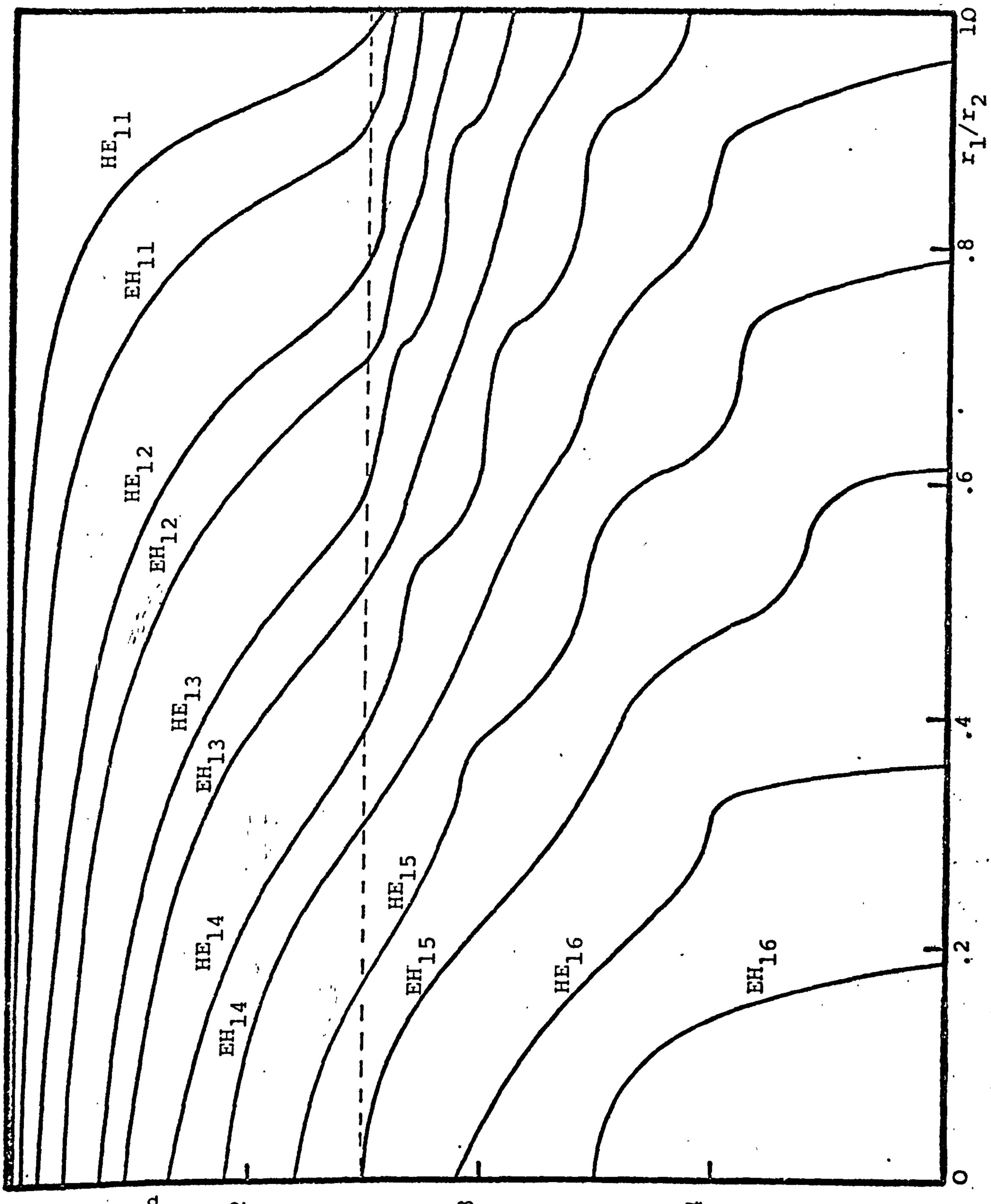

Figure (6.3) Normalised phase-change coefficient against r_1/r_2 for a dielectric lined circular waveguide

They provide an explanation of the phenomena in terms of the creation of a magnetic-wall at the boundary $r = r_1$, a condition which causes the familiar low-attenuation properties of the TE_{om} modes in a hollow waveguide.

Furthermore, they show that the TE_{om} modes, exhibit high loss under the $(2m-1)\frac{\lambda'}{4}$ conditions. The low-attenuation condition of the TE_{om} modes corresponds to $d = (m-1)\frac{\lambda'}{2}$, provided that, when $m > 1$, surface wave conditions do not predominate. From the above description, one would not expect a low-attenuation region for the azimuthally dependent modes, due to the coupling mechanism of the E-type and H-type fields described in section (6.2). However, evidence to the contrary is given by Brayer <20>, who observed that, under certain conditions, the EH_{11} mode could exhibit low-attenuation. In what follows, the above inconsistency is resolved by demonstrating that when low-attenuation occurs, the EH_{11} mode exhibits nearly pure E mode properties. The influence of dielectric permittivity and loss tangent on the attenuation of the EH_{11} mode will be discussed and an optimum dielectric thickness to produce the low attenuation condition is found. The low-loss behaviour of the EH_{11} mode will be discussed in terms of surface currents induced in the metal walls by different field components.

6.4.2 Power-Losses

In the lined waveguide, the power losses consist of two parts;

P_m : due to induced currents in the metal wall of the structure at $r = r_2$, and

P_d : due to dielectric loss.

The two components are formulated separately and the overall power-loss of the waveguide is obtained by numerically summing the two contributions.

For hybrid EH_{nm} and HE_{nm} modes the power-loss components are given below.

The metal wall power-loss/unit length of the waveguide is given by;

$$P_m = \frac{R_s}{2} \int_0^{2\pi} ({}_2H_z \cdot {}_2H_z^* + {}_2H_\theta \cdot {}_2H_\theta^*)\Big|_{r=r_2} r_2 d\theta \qquad \{6.10\}$$

where R_s is the surface resistivity of the metal wall. Using the expressions for ${}_2H_z$ and ${}_2H_\theta$ given in {6.2} and {6.4}, and expressing the coefficients A_2 and B_2 in terms of A_1 {6.6}, the metal wall power-loss can be found in terms of A_1.

To formulate the dielectric power-loss, the field components in the lining are assumed to be unperturbed by the loss component of the permittivity as shown below;

writing

$$K_2 = K_2' - jK_2'' = \omega\sqrt{\mu_o \varepsilon_o}\ (\bar{\varepsilon} - j\bar{\varepsilon}'')^{\frac{1}{2}},$$

then

$$\frac{K_2''}{K_2'} \simeq \frac{\bar{\varepsilon}''}{2(\bar{\varepsilon}-1)} = 0.0001 \quad , \quad \text{when } \bar{\varepsilon}'' = 0.0002,\ \bar{\varepsilon} = 2.$$

Thus, when using very small loss tangent dielectrics, the complex aspect of the field is unimportant. The dielectric power-loss/unit length of the waveguide is given by;

$$P_d = \frac{\omega \varepsilon_o \bar{\varepsilon} \tan\delta}{2} \int_0^{2\pi} \int_{r_1}^{r_2} ({}_2E_r \cdot {}_2E_r^* + {}_2E_\theta \cdot {}_2E_\theta^* + {}_2E_z \cdot {}_2E_z^*) r\,dr\,d\theta \qquad \{6.11\}$$

where δ is the loss angle of the lining.

Using the expressions for the electric field components given in {6.3} and{6.4}, and substituting for the coefficients A_2 and B_2 in terms of A_1 {6.6}, the dielectric power-loss can be found in a closed form in terms of the amplitude coefficient A_1.

6.4.3 Power-Flow

The average power flowing through the waveguide for a given mode is given by;

$$P_o = \tfrac{1}{2}\ \mathrm{Re} \int_S (\underset{\sim}{E} \times \underset{\sim}{H}^*) . \underset{\sim}{z}\ dS \quad ,$$

where S is the cross-sectional area of the waveguide.

The power flow expression is formulated in two parts using appropriate field expressions in the two regions.

$$P_o = \tfrac{1}{2}\int_0^{2\pi}\int_0^{r_1} ({}_1E_{r1}{}_1H_\theta^* - {}_1E_{\theta 1}{}_1H_r^*)\,r\,dr\,d\theta + \tfrac{1}{2}\int_0^{2\pi}\int^{2} ({}_2E_{r2}{}_2H_\theta^* - {}_2E_{\theta 2}{}_2H_r^*)\,r\,dr\,d\theta$$

The field expressions given in {6.3} and {6.4} are substituted in {6.12} and the amplitude coefficients B_1, A_2 and B_2 are expressed in terms of A_1 {6.6}. The average power flow in the two regions can be found in a closed form in terms of the amplitude coefficient A_1.

For the circularly symmetric modes the two power-loss expressions and the average power-flow expression have a much simpler form, due to the non-existence of some of the field components.

The attenuation coefficient, α, for the hybrid modes is formulated using the above power-loss and power-flow expressions;

$$\alpha = \frac{P_m + P_d}{2P_o} \times 8.68 \text{ dB/m}$$

when r_1 and r_2 are measured in meters.

6.4.4 HE_{11} Mode Characteristic

Figure (6.4) shows computed attenuation due to the metal wall-loss for the HE_{11} mode as a function of dielectric thickness. At the two extreme points $r_1/r_2 = 1$ and $r_1 = 0$, the attenuation coefficient of the hybrid mode is in agreement with that of a TE_{11} mode in a circular

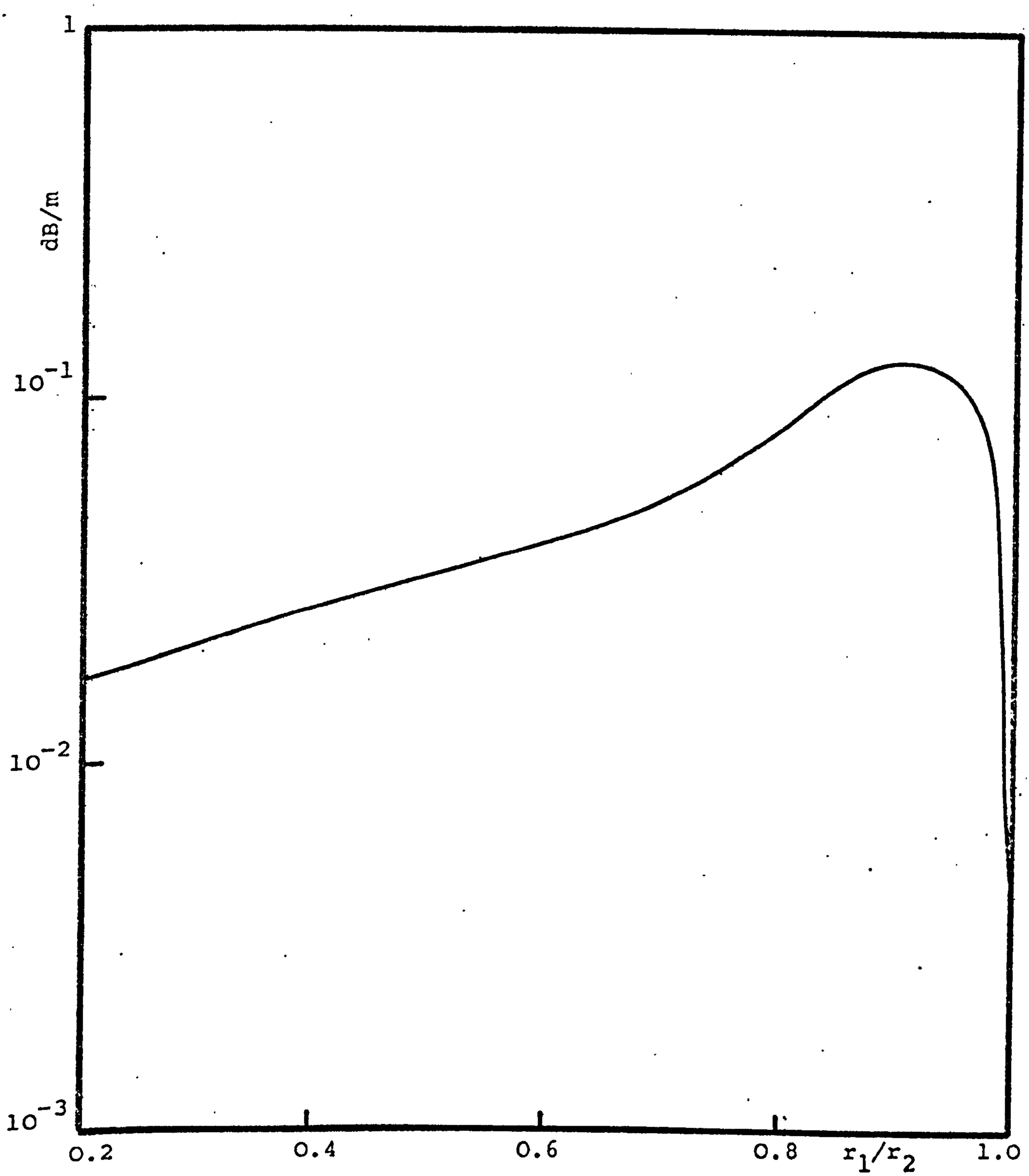

Figure (6.4) Attenuation due to loss in the metal wall against lining thickness
HE_{11} mode
r_2 = .086m $\bar{\varepsilon}$ = 2.25 f = 7.3 GHz
$\sigma = 1.57 \times 10^7$ S/m

waveguide filled with a lossless dielectric of relative permittivity $\bar{\varepsilon}$, i.e.

$$\alpha = \frac{R_s}{r_2 Z_o \sqrt{\bar{\varepsilon} - (f_c/f)^2}} \left[(f_c/f)^2 + \frac{n^2 \bar{\varepsilon}}{p_{nm}^2 - n^2} \right] x\ 8.68\ \text{dB/m}$$

where f_c is the cut-off frequency, $Z_o = \sqrt{\mu_o/\varepsilon_o}$.

As the lining thickness increases the metal wall-loss of the HE_{11} mode rises rapidly. This is due to surface wave phenomena exhibited by this mode. The metal wall-loss reaches a maximum when $d \simeq \frac{\lambda'}{4}$, and further increase in lining thickness reduces the wall-loss as illustrated in Figure (6.4). The attenuation behaviour of the HE_{11} mode parallels that reported by Carlin and D'Agastino for the TE_{01} mode, which has minimum attenuation for zero lining thickness and reaches a maximum when $d \simeq \frac{\lambda'}{4}$.

6.4.5 EH_{11} Mode Characteristic

Figure (6.5) shows the computed attenuation due to the metal wall-loss for the EH_{11} mode as a function of dielectric thickness. At the two extreme points $r_1/r_2 = 1$ and $r_1 = 0$, the attenuation coefficient of the hybrid mode coincides with that of the TM_{11} mode in circular waveguide filled with a lossless dielectric of relative permittivity $\bar{\varepsilon}$, i.e.

$$\alpha = \frac{R_s \bar{\varepsilon}}{r_2 Z_o \sqrt{\bar{\varepsilon} - (f_c/f)^2}}\ x\ 8.686\ \text{dB/m.}$$

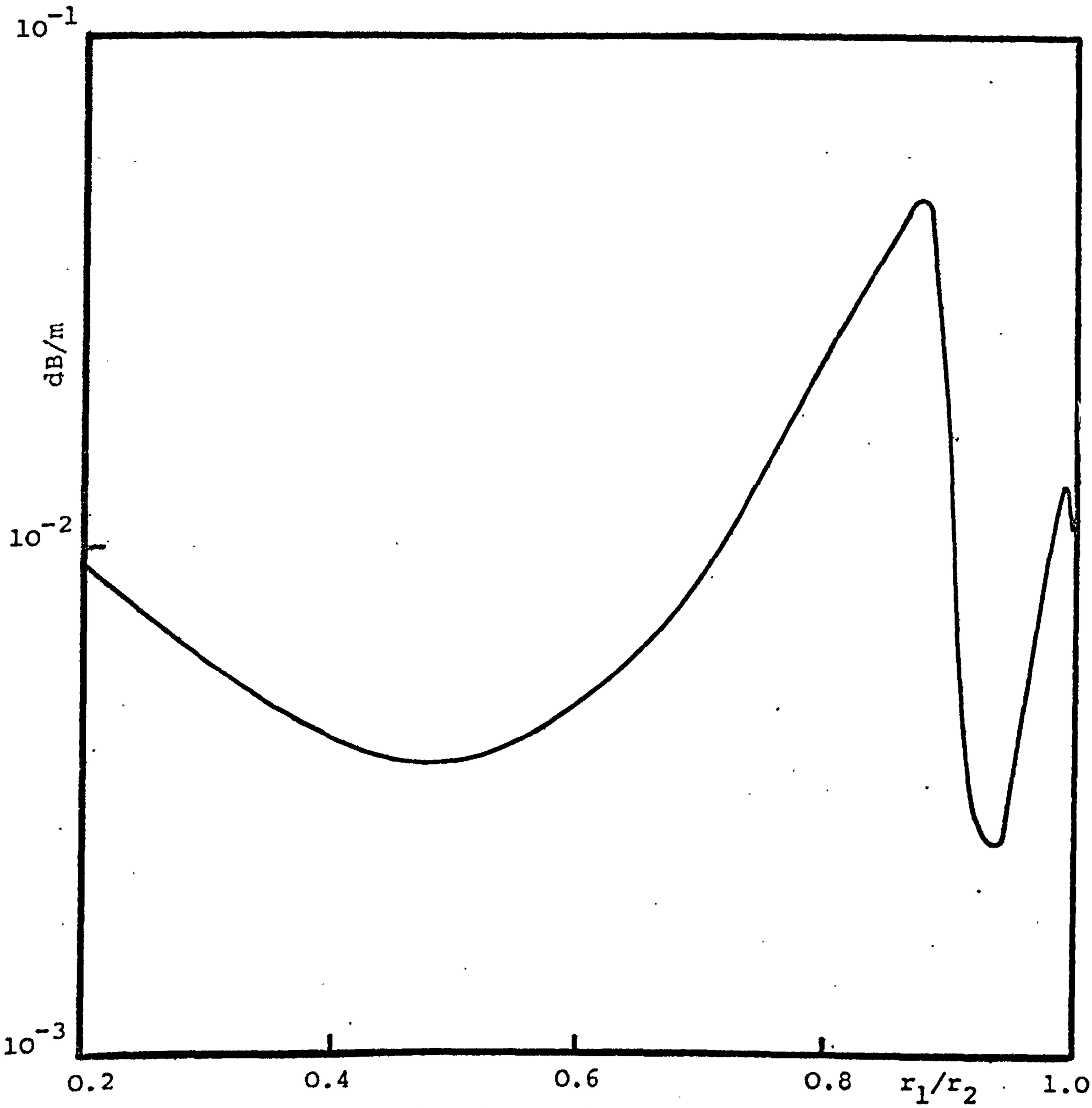

Figure (6.5) Attenuation due to loss in the metal wall against lining thickness
EH_{11} mode
r_2 = .086m $\quad \bar{\varepsilon}$ = 2.25 $\quad$ f = 7.3 GHz
$\sigma = 1.57 \times 10^7$ S/m

As the lining thickness is increased the metal wall-loss of the EH_{11} mode rises, but falls very rapidly for further increase in lining thickness, reaching a minimum when $d < \frac{\lambda'}{4}$. As the lining approaches one quarter wavelength thickness, the loss increases very rapidly. This rapid rise is due to surface wave phenomena that takes place when the lining is one quarter wavelength thickness. For a lining greater than $\frac{\lambda'}{4}$ thickness, the metal wall-loss decreases again and reaches a second minimum when $d \simeq 5\frac{\lambda'}{4}$, where the attenuation coefficient is nearly 40% higher than that reached at the first minimum. This rise is due to confinement of energy in the dielectric region of the waveguide. Further increase in lining thickness causes a third rise in the metal wall-loss and reaches that of the homogeneously filled waveguide at $r_1 = 0$.

6.4.6 Effect of Lining Loss Angle

The effect of the lining loss on the attenuation of the EH_{11} mode is shown in Figure (6.6), where computed attenuation due to the metal wall loss and metal loss plus dielectric loss is plotted as a function of dielectric thickness. The value of the loss tangent used in the computation is 4×10^{-4}. At the point of minimum attenuation it is seen that the lining loss contribution is 58% of the total waveguide attenuation. As the lining thickness cannot be reduced for obvious reasons, low-loss dielectrics must therefore be used for

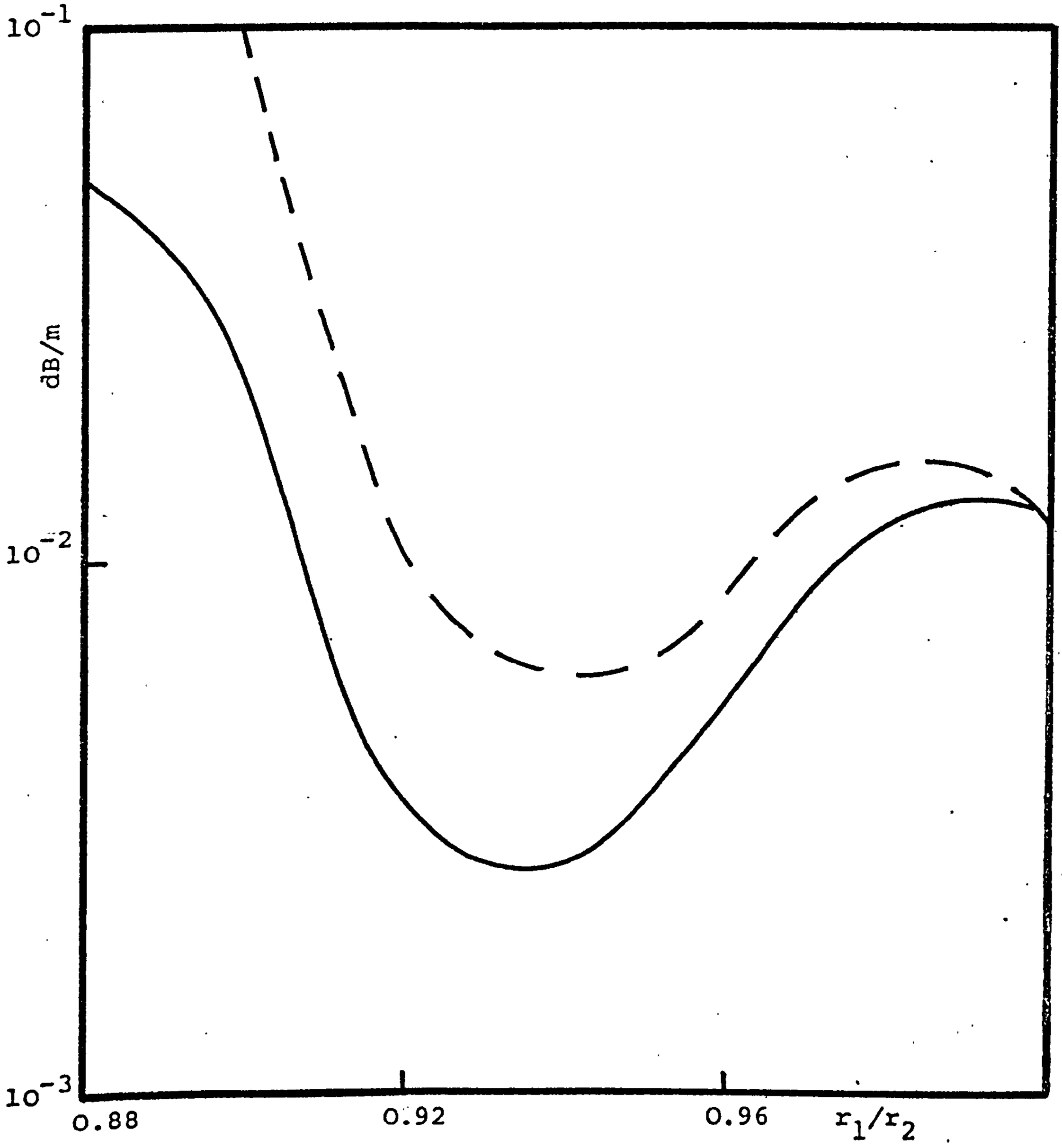

Figure (6.6) Attenuation in a dielectric lined waveguide against lining thickness
EH_{11} mode
r_2 = 0.086m $\bar{\varepsilon}$ = 2.25 f = 7.3 GHz

——— Metal wall loss only $\sigma = 1.57 \times 10^7$ S/m

------ Total loss $\tan\delta = 5 \times 10^{-4}$

the lining. The dielectric loss was formulated assuming the field components in the lining are unaffected by the loss component of the dielectric and {6.11} shows that the dielectric loss is directly proportional to the loss tangent of the lining. Therefore, a drastic reduction in this loss component is achieved if low loss dielectrics are used. For example, the 58% contribution of the lining loss can be reduced to 12% contribution if the lining had a loss tangent of 4×10^{-5} instead.

6.4.7 Effect of Lining Permittivity

The lining thickness required to achieve low-attenuation condition for the EH_{11} mode, is in the range $\frac{\lambda'}{4} > d > 0$, the upper limit is set to avoid the surface wave region. In order to obtain the necessary lining thickness required to produce minimum attenuation condition, the metal wall loss of the EH_{11} mode is computed using liningsof different permittivities. In the vicinity of the low-attenuation region, the value of $\bar{\beta}$ is nearly unity, and thus the relationship

$$\lambda' = \frac{\lambda}{\sqrt{\bar{\varepsilon}-1}} \qquad (\lambda=\text{free-space wavelength})$$

is used to obtain approximate values of lining thickness. Table (6.2) shows the thickness required to produce the minimum attenuation condition for various values of $\bar{\varepsilon}$.

$\bar{\varepsilon}$	1.56	2.56	3.56	4.56
λ'/d	5.68	5.76	5.44	5.56

Table (6.2)

The approximate lining thickness needed was found to be given by:

$$d \sim \frac{\lambda}{5.6\sqrt{\varepsilon-1}} \qquad \{6.13\}$$

6.4.8 Low-Loss Mechanism

In order to identify the phenomena underlying the low-loss property of the EH_{11} mode, the contribution of separate power-loss components is studied. For low-loss lining materials, it was shown that the power-loss contribution of the lining is very small, when compared with the conducting wall power-loss, and therefore the lining loss will not be considered.

The metal wall power-loss is separated into two components; that due to the azimuthal and that due to longitudinal components of the magnetid field at the boundary $r = r_2$. Computed normalised metal wall-loss components are shown in Figure (6.7) as a function of lining thickness. The expression for ${}_2H_\theta$ given in {6.4} consists of two parts; the first due to an E-type mode, while the second is due to an H-type mode. However, it can be seen from Figure (6.7), that in the region of interest, the H-type part is negligible when compared with that of the E-type contribution. Thus, after an initial rise, the subsequent reduction in ${}_2H_\theta$ component as the dielectric thickness increases is due to the trend towards a magnetic-wall condition at the boundary $r = r_1$, which occurs when $r_1/r_2 = A$, Figure (6.7). The dielectric thickness is then given by

$$d \simeq \frac{\lambda'}{4} = \frac{\lambda}{4\sqrt{\varepsilon-1}}$$

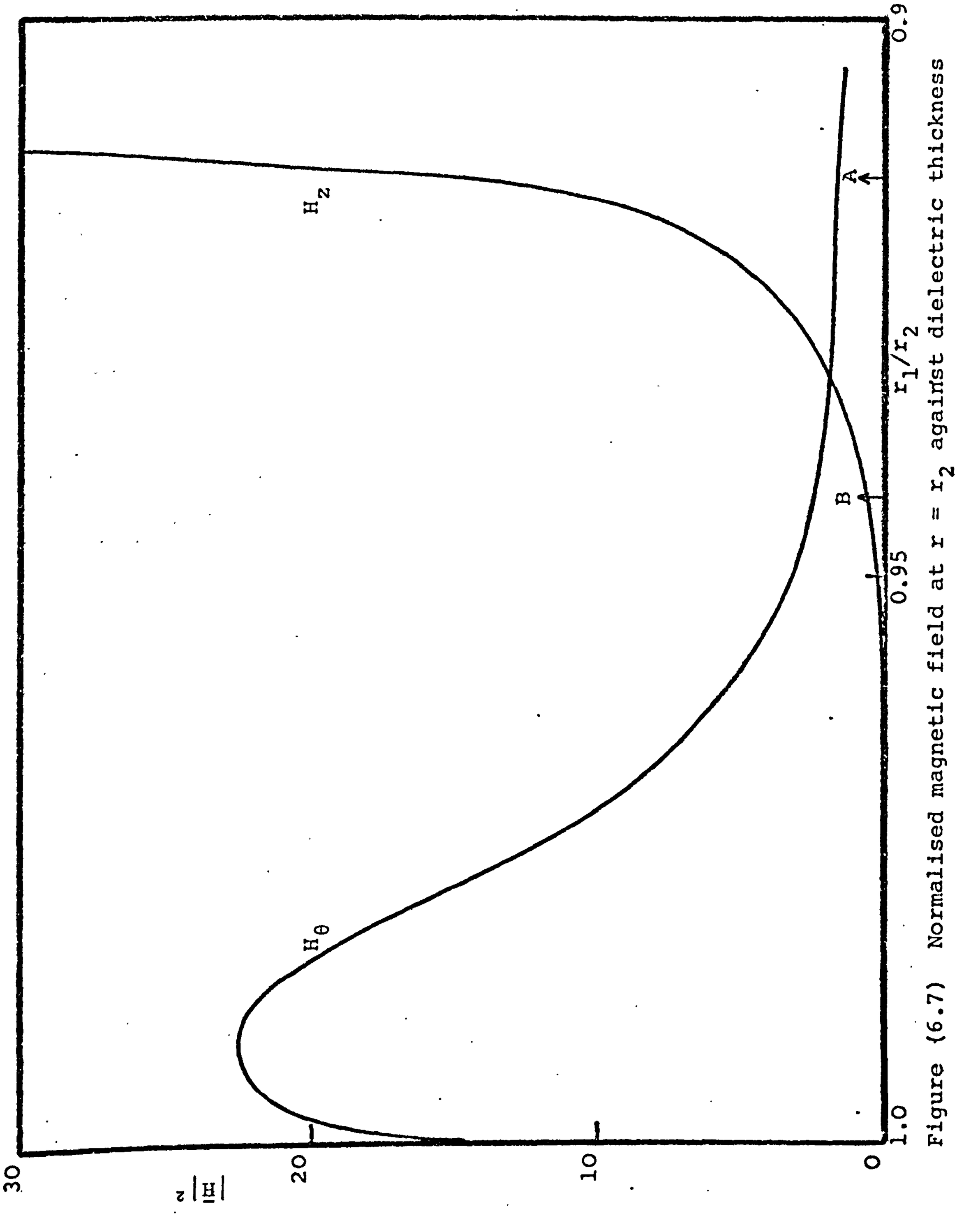

Figure (6.7) Normalised magnetic field at $r = r_2$ against dielectric thickness

The above behaviour parallels that reported by Carlin and D'Agostino < 5 >, for the TM_{02} mode, and if it were not for the H-type part of the hybrid field with its associated H_z component, the above condition would lead to an attenuation minimum. However, it can also be seen from Figure (6.7), that the $_2H_z$ component increases as d increases and the attenuation minimum condition occurs when $r_1/r_2 = B$, Figure (6.7), where the total metal wall-loss contribution is a minimum. The same agreement can be followed for the HE_{11} mode, which does not exhibit a minimum because the H_θ field has a stronger component associated with the H-type part of the field, and this reaches a maximum when $d \simeq \frac{\lambda'}{4}$, as is evident from the attenuation characteristic shown in Figure (6.4).

6.5 TRANSVERSE FIELD PATTERN

Two methods can be adopted in plotting the electric field lines in the transverse plane of a circular waveguide <24>.

The first method involves solving a differential equation governing the contours of electric field lines;

$$\frac{1}{r}\frac{dr}{d\theta} = \frac{E_r}{E_\theta}$$

The results can be obtained using Runge-Kutte process, with the appropriate conditions. In the lined waveguide two such differential equations must be solved in the appropriate regions, with the field expressions given in {6.3} and {6.4}. The second method requires to express

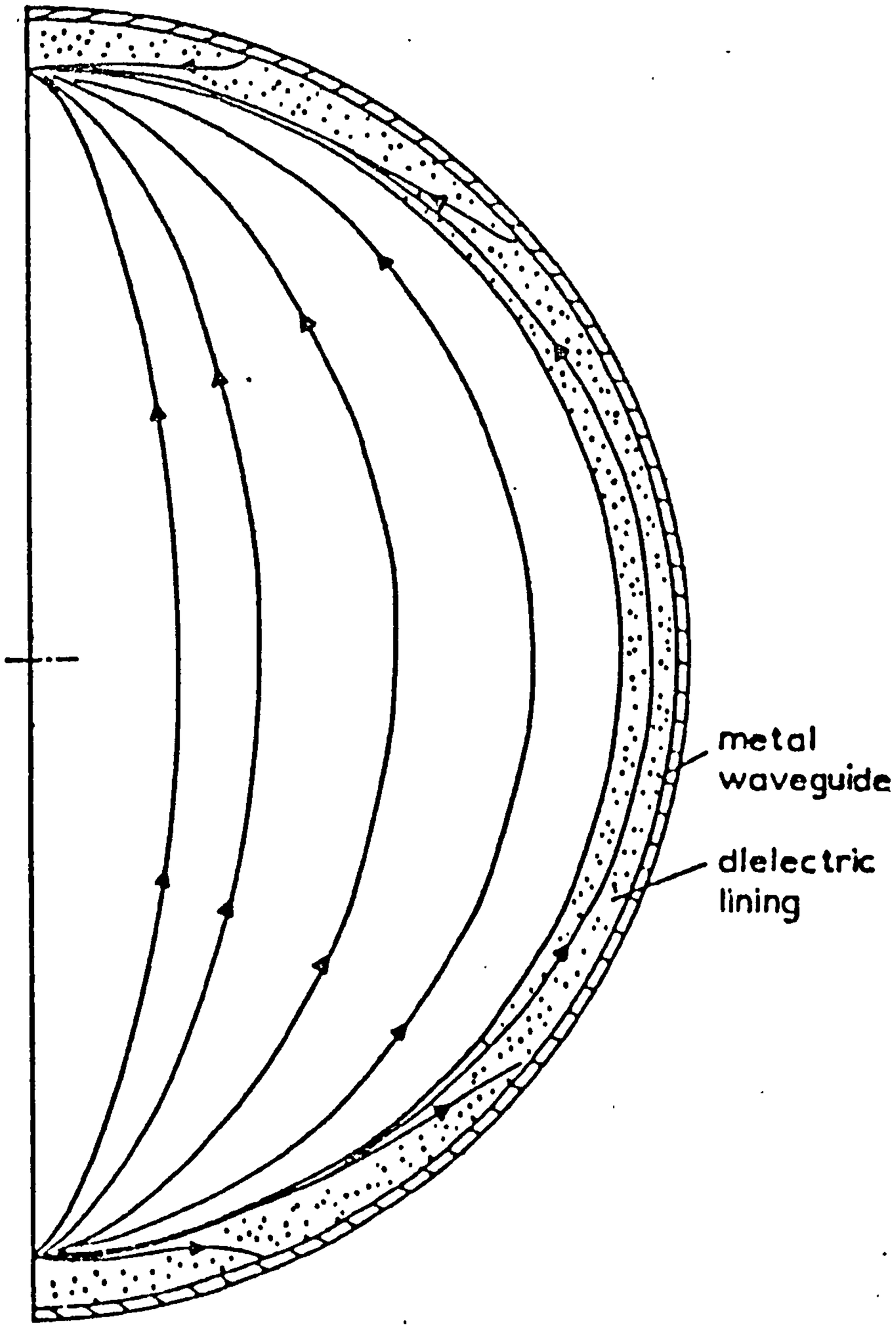

Figure (6.8) Transverse electric field configuration of the EH_{11} mode under optimum low-attenuation conditions.

the transverse field components in terms of cartesian components;

$$E_x = E_r \cos\theta - E_\theta \sin\theta$$

$$E_y = E_r \sin\theta + E_\theta \cos\theta$$

$$\phi = \tan^{-1}(E_x/E_y) \qquad \{6.14\}$$

The gradient of the electric field lines given in {6.14} can be found for a particular value of r and θ. This procedure is followed over the complete r, θ grid and the appropriate points are then joined to trace the electric field lines. In the lined waveguide, the second procedure is followed using the appropriate field expressions in the two regions.

Figure (6.8) shows the transverse-electric field configuration of the EH_{11} mode under the minimum attenuation condition. It can be seen that the lining drastically alters the field lines from those in a hollow waveguide. The position of the two nulls in the electric field configuration of the TM_{11} mode in a hollow circular waveguide, moves towards the boundary $r = r_1$, as the lining thickness increases. Over the central region of the waveguide, the field shows similarity to the field of the TE_{11} mode in a hollow waveguide of radius r_1 which suggests that the EH_{11} mode in the lined waveguide could be quite efficiently excited from a smooth wall waveguide.

CHAPTER SEVEN

CONCENTRIC DIELECTRIC WAVEGUIDES

7.1 INTRODUCTION

This chapter is concerned with an evaluation of cladded circular dielectric waveguides, as shown in Figure (7.1), for microwave communication. The dominant mode of the dielectric waveguide comprises a linearly polarised field <21>. It is designated HE_{11} and bears a close resemblance to the mode of similar designation found in corrugated circular waveguides investigated in chapters 4 and 5. By arranging that the central core has a permittivity only slightly greater than that of the surrounding cladding, it is possible to arrange that only the HE_{11} mode propagates with its field confined to the core region <21>. Other higher order modes, e.g. the TE_{01}, TM_{01}, HE_{21}, etc., have fields extending radially well beyond the core. Then if a lossy outer layer is provided, as shown in Figure (7.1) a substantial differential attenuation can be achieved between the desired HE_{11} mode and the higher order modes. Provided the lossy region is not brought too close to the core, its influence on the HE_{11} mode can be rendered almost negligible. Then the attenuation of that mode is given, to a good approximation, by

$$\alpha = \frac{\pi}{\lambda_g} \tan\delta \qquad \text{nepers/m}$$

where λ_g is the guide wavelength and $\tan\delta$ the loss tangent of the interior regions. As an example, with $\lambda_g \simeq 1$ cm (f = 30 GHz), the attenuation coefficient is

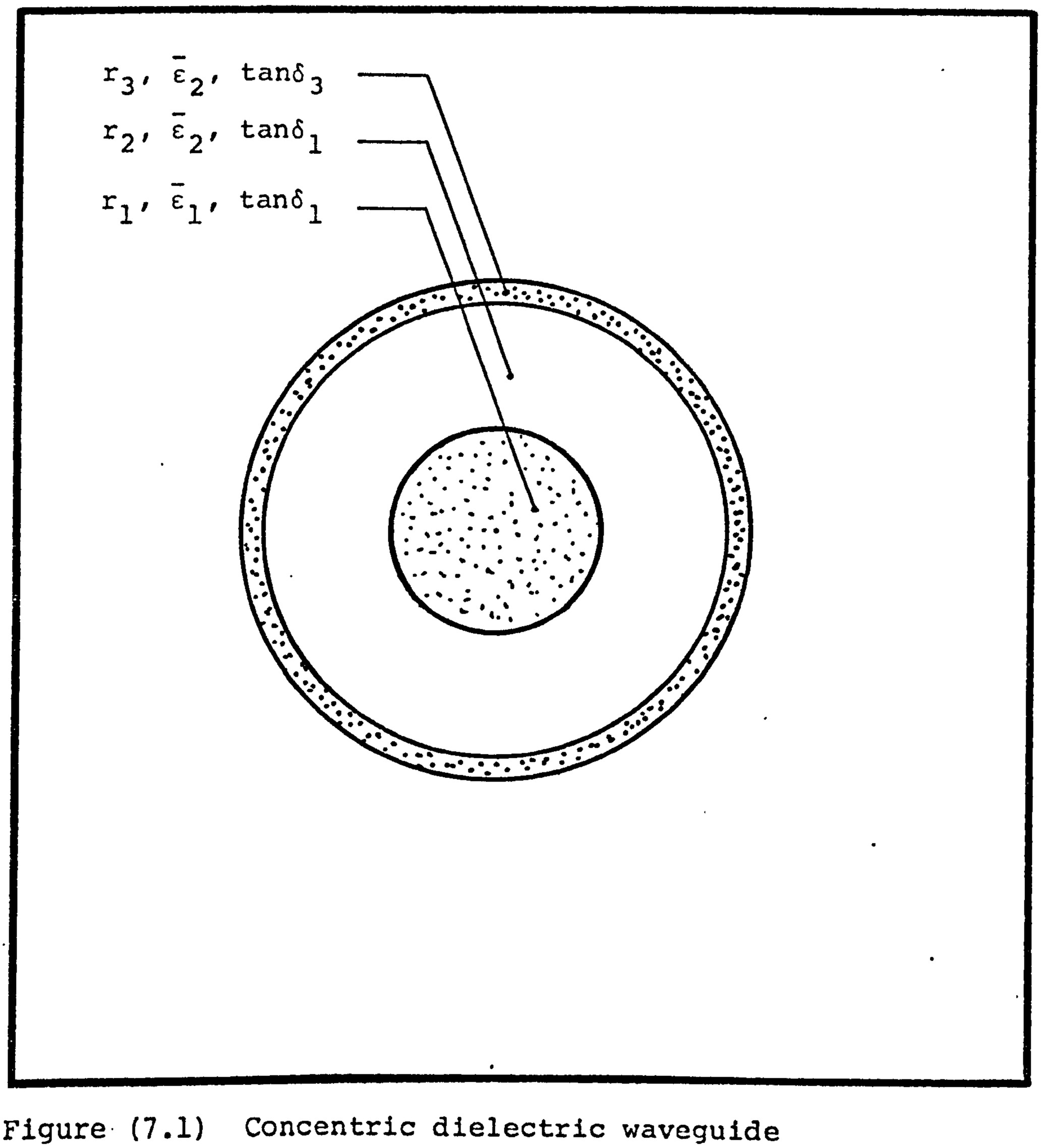

Figure (7.1) Concentric dielectric waveguide

approximately 30 dB/km when $\tan\delta = 10^{-5}$. Loss tangents of this order have been measured for commercial polystyrene foam <22> and solid polypropylene also has a loss tangent of this order < 3 >. By comparison, copper waveguides exhibit <55> measured attenuation of about 1 dB/m at f = 35 GHz, which suggests that dielectric waveguides could find an important place in future communication systems operating at higher microwave frequencies.

It is noteworthy that a comparable waveguide is being developed for optical communication in U.S.A., U.K., Japan and Germany <56>. To date, the best attenuation figure reported for optical waveguides is 4 dB/km at a wavelength of 0.8μm, furthermore, there is good reason to anticipate an ultimate limit of about 2dB/km. The prospect of such exceedingly low attenuation in waveguides inevitably influences long-term systems planning and may result in impact on the microwave communication industry during this decade. However, because of the requirements for a substantial capital investment, there seems a likelihood that conventional microwave communication systems will survive into the more distant future although there will be increased use of higher microwave frequencies. At these frequencies dielectric waveguides may find an important place.

This chapter aims to identify suitable parameters for a concentric dielectric waveguide for use in the frequency band 30-40 GHz. The general principles can also

be applied at other frequencies. Our proposals are based mainly on electrical rather than mechanical considerations, and this should be borne in mind when the ultimate assessment is made. We begin by illustrating the attenuation and dispersion characteristics of the lowest order modes of the waveguide and then discuss the choice of parameters for monomode operation. We indicate a prospect for efficient input/output transducers and show favourable group delay characteristics. Because the detailed formulation of the electromagnetic problems underlying this study have been extensively described elsewhere <21>, we refrain from discussing mathematical aspects here.

7.2 CHARACTERISTIC EQUATION

Figure (7.1) shows a view of the concentric dielectric waveguide. The central core of radius r_1 comprises a dielectric of relative permittivity $\bar{\varepsilon}_1$. The function of the cladding, $r_1 < r < r_2$, of relative permittivity $\bar{\varepsilon}_2$, $(\bar{\varepsilon}_2 < \bar{\varepsilon}_1)$, is to act as a low-loss support for the central core. Also shown is a thin lossy layer, $r_2 < r < r_3$, which might be made from plastic of relative permittivity $\bar{\varepsilon}_2$. The dielectric loss angles of the core, cladding and the lossy layers are δ_1, δ_1 and δ_3 respectively, where $\delta_3 >> \delta_1$. As the lossy layer is very thin and its permittivity is matched to that of the cladding layer, its effect may be considered as a perturbation of the lossless structure of radius r_3.

The characteristic equation of a lossless multi-layer dielectric waveguide has been formulated by Chan <21>, while investigating the propagation characteristics of the optical waveguide. General field components in different layers are derived for the azimuthal dependent hybrid and circularly symmetric pure modes. On matching the tangential electric and magnetic field components at the interface of the different layers, a homogeneous system of equations for the amplitude coefficients in the different layers is derived. From the condition of non-triviality of the solutions of the homogeneous system, the characteristic equation of the structure is obtained.

Symbolically, it has the form;

$$F(\beta, \omega, r_1, r_3, \bar{\varepsilon}_1, \bar{\varepsilon}_2, n) = 0 \qquad \{7.1\}$$

where, β is the phase-change coefficient, ω is the angular frequency, and n being the azimuthal order of the mode.

7.3 DISPERSION CHARACTERISTICS

If the boundary $r = r_3$ is assumed to be infinite, the characteristic equation {6.1} simplifies to a form given in < 21 >. The normalised phase-change coefficient for all the modes lies in the range

$$\sqrt{\bar{\varepsilon}_2} < \bar{\beta} < \sqrt{\bar{\varepsilon}_1}$$

where $\bar{\beta} = \beta/k$, $k = \omega\sqrt{\varepsilon_o \mu_o}$.

The propagation characteristics of such structures are independent of the change in the difference in permittivities between the core and the surrounding medium. A normalised frequency, V, has been used extensively in describing surface wave behaviour on dielectric rods <57>, and optical waveguides <58>, which is defined as

$$V = \frac{2\pi r_1}{\lambda} \sqrt{\bar{\varepsilon}_1 - \bar{\varepsilon}_2} \qquad \{7.2\}$$

where λ is the free space wavelength.

The normalised cut-off frequency for different modes based on an infinite cladding assumption are given in table (7.1), where it can be seen that, except for the HE_{11} hybrid mode, all other modes have finite cut-off frequencies. For the HE_{11} mode, propagation exists down to zero frequency. In surface waves, the cut-off is defined as the condition at which the phase velocity of the wave is equal to that of a plane wave in the infinite homogeneous surrounding medium, i.e. when $\bar{\beta} = \sqrt{\bar{\varepsilon}_2}$.

MODE	Cut-off V
HE_{11}	0
TE_{01} TM_{01}	2.405
HE_{21}	2.80
HE_{12} EH_{12}	3.83

Table (7.1)

Cut-off V value of dielectric rod

However, an infinite cladding radius cannot be assumed when studying the propagation characteristics of a realistic dielectric waveguide at microwave frequencies. The exact characteristic equation for a three layer concentric dielectric waveguide is thus solved. The normalised phase-change coefficient for all the modes lies in the ranges;

$$1 \leq \bar{\beta} \leq \sqrt{\varepsilon_2} \quad , \quad \sqrt{\varepsilon_2} < \bar{\beta} < \sqrt{\varepsilon_1}$$

The first range, cannot exist when employing the infinite cladding assumption, as the modes will be cut-off for such values of $\bar{\beta}$. This part of the range is known as cladding mode approximation, as most of the energy carried by the modes lies outside the core region, and thus the existence of the core will have very little influence on the propagation characteristics. In the second part of the range, very good agreement is found <21>, between values of $\bar{\beta}$ obtained by solving {7.1}, and those obtained using the infinite cladding approximation. This agreement is in accord with the observed concentration of the energy carried by the modes, in the core region of the waveguide. However, the cut-off frequencies of the different modes will obviously be different from those obtained using the infinite cladding approximation. The energy carried by the dominant HE_{11} mode will be mainly distributed in the cladding region for values of V near cut-off (V=O). As frequency increases the field concentration of the HE_{11} mode increases in the core region. For the higher order

modes, the core field concentration will occur when the infinite cladding approximation can be applied, i.e. $V > 2.405$. Therefore in order to operate the concentric dielectric waveguide such that only the field of the dominant mode is confined to the core region, while the fields of the higher order modes extend outside the core region, the V value must lie in the range

$$2.405 > V >> 0$$

Figure (7.2) shows, computed results for the normalised phase-change coefficient as a function of frequency, for the dominant HE_{11} mode and mode of the first higher order triplet (HE_{21}, H_{01}, E_{01}).

7.4 ATTENUATION CHARACTERISTICS

The dielectric power-loss of the waveguide is formulated by assuming that the field components are similar to those obtained in a lossless structure, and then using the well known perturbation expression for the power-loss per unit length;

$$P = \frac{\omega\bar{\varepsilon}\tan\delta}{2} \int_S |\underline{E}|^2 dS \qquad \{7.3\}$$

where, for a hybrid mode $|\underline{E}|^2 = E_r^2 + E_\theta^2 + E_z^2$ and S is the waveguide cross-section. The dielectric power-loss in the different layers is obtained using appropriate field components and corresponding values of $\bar{\varepsilon}$, δ and S.

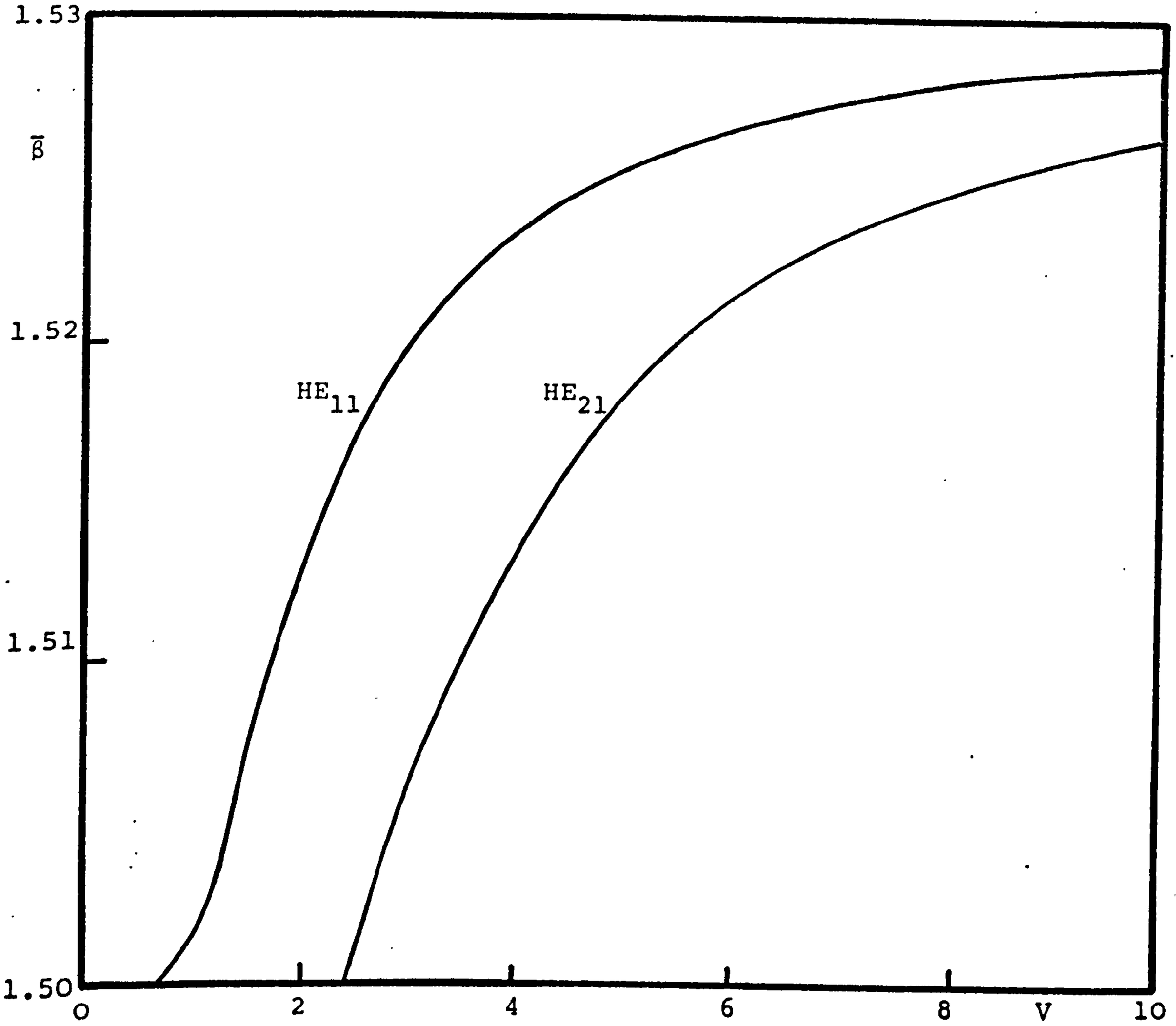

Figure (7.2) Dispersion characteristics of a dielectric waveguide

$\bar{\varepsilon}_1 = 2.341$ $\bar{\varepsilon}_2 = 2.25$

The dielectric power-loss of the outer lossy layer is formulated using the field components in the cladding region, and integrating over the area enclosed between r_2 and r_3. This procedure will no longer apply when the lossy layer has a large value of δ_3. For such a situation the problem must be formulated taking into account the complex permittivity of the layers. The average power flow in the waveguide is formulated by integrating the appropriate Poynting vectors over separate layers and then numerically summing the results. The attenuation coefficient is finally formulated from the knowledge of the average power flow and the power-loss of individual layers. Figure (7.3) shows, as a function of frequency, computed curves of attenuation for three waveguides with permittivity values of core and cladding corresponding to two expanded polystyrene foams of different density <59>. The loss tangents of the foams correspond to those measured using low-loss cavity techniques. Figure (7.3) also shows that, over a broad frequency band, the attenuation of the first higher-order mode HE_{21} is significantly greater than that of the dominant HE_{11} mode.

7.5 PARAMETRIC STUDY

7.5.1 Introduction

The choice of waveguide parameters is governed principally by the operating frequency and the availability of dielectric materials with low losses.

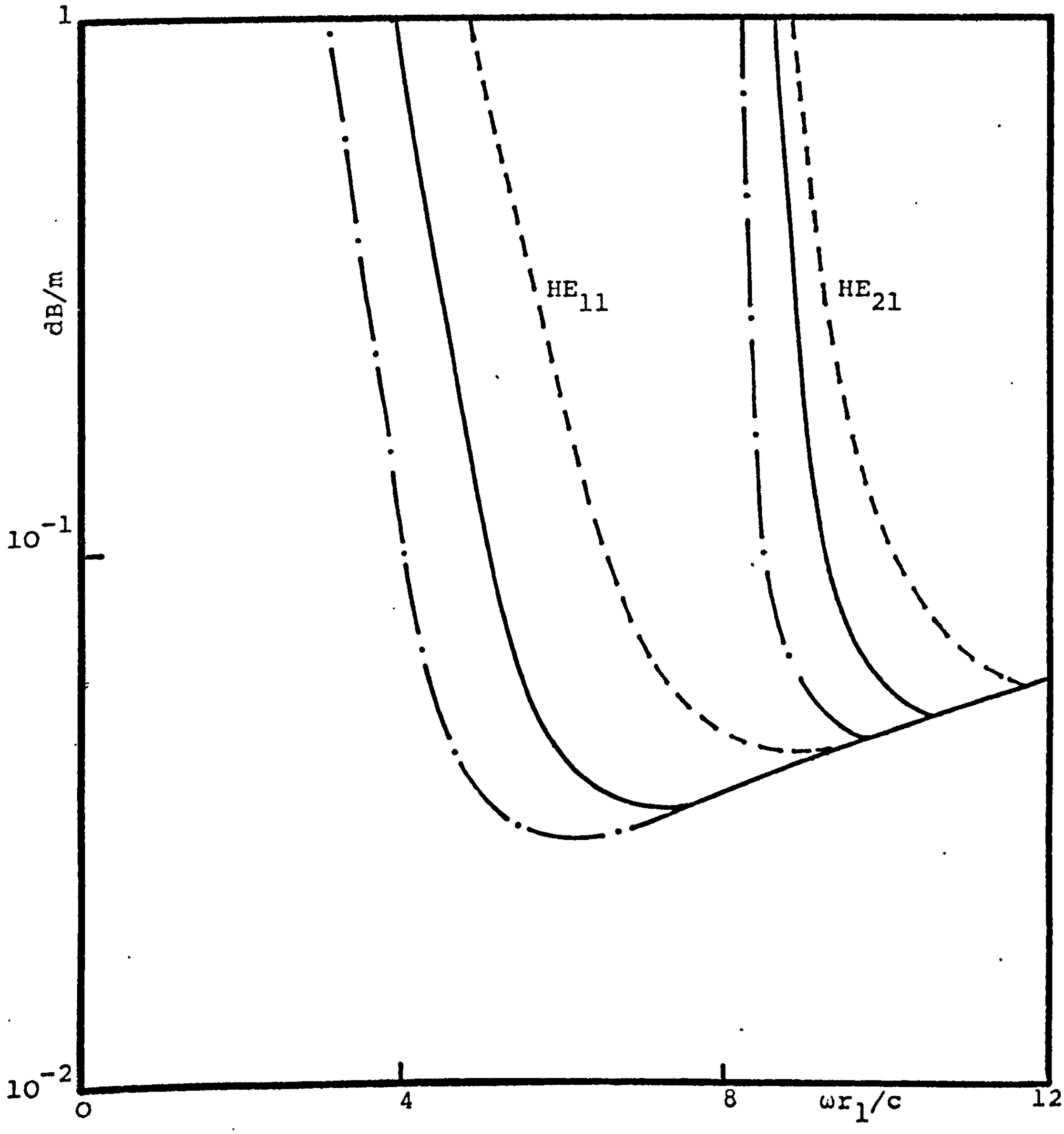

Figure (7.3) Attenuation characteristics of a dielectric waveguide

r_1 = 1cm $\quad \bar{\epsilon}_1 = 1.11 \quad \bar{\epsilon}_2 = 1.01$

$\tan\delta_1 = 10^{-5} \quad \tan\delta_3 = 0.1$

-.-.-.- r_2 = 6cm $\quad r_3$ = 7cm

——— r_2 = 4cm $\quad r_3$ = 5cm

------- r_2 = 3cm $\quad r_3$ = 3.4cm

The aim of this study is to find suitable parameters for the dielectric concentric waveguide to fulfil the following criteria for the range of frequencies of interest;

(a) Dominant mode operation:

In order to achieve dominant mode operation only the field of the HE_{11} mode must be confined to the core region. Then because of the outer lossy layer, higher-order modes are strongly attenuated, as their fields extend radially well beyond the core. Therefore, the parameters $\bar{\varepsilon}_1$, $\bar{\varepsilon}_2$, r_1 must be chosen to assure the confinement of the HE_{11} mode field in the core region.

(b) Minimum outer radius:

At optical wavelengths, the ratio of the cladding radius r_2 to core radius r_1 is chosen in the range 20-50 mainly for reasons of mechanical strength. At millimetre wavelengths and even more so at centimeter wavelengths, r_2/r_1 must be restricted otherwise the outer radius of the waveguide will be inconveniently large. Therefore, the core radius r_2 must be chosen to minimise the effect of the lossy layer $r > r_2$ on the dominant mode field and to maximise its effects on the higher order modes.

(c) Minimum-attenuation for the HE_{11} mode:

In the above range of operation the attenuation of the HE_{11} mode is dependent only on the losses in the core and cladding regions. Therefore, the core must be chosen of dielectric materials with very low loss angle.

(d) Maximum-attenuation for the higher-order modes:

A substantial differential attenuation can be achieved between the desired HE_{11} mode and the higher-order modes if the thickness of the lossy layer and the loss angle δ_3 are chosen correctly.

(e) Group delay:

In communication systems, it is desirable to reduce the delay distortion arising from the waveguide effects. Chan < 21 >, shows that the group delay change in the optical waveguide is proportional to the core-cladding permittivity difference. Therefore, for the concentric dielectric waveguide the difference in permittivity must be chosen to be as small as possible consistent with acceptable waveguide dimensions.

(f) Maximum excitation efficiency:

When assessing the overall power-loss of a communication system employing the concentric dielectric waveguide as the guiding medium, the power-loss due to the input/output transitions of the waveguide must be taken into account. Obviously the transition reflection loss must be well below the power-losses in the waveguide, which are themselves very small. Therefore maximum excitation efficiency of the dominant HE_{11} mode must be sought. A corrugated circular waveguide can be used to efficiently excite the concentric dielectric waveguide, because of the similarity between the HE_{11} mode fields in both waveguides. Clarricoats and Salema <60>, show that for the range of frequencies of interest, the excitation

efficiency of such a configuration depended on permittivity difference, core radius, and the inner radius of the corrugated waveguide R. Therefore, when choosing the permittivity difference and the core radius of the waveguide, the excitation efficiency must be taken into consideration.

Due to the number of parameters involved and the wide range of each parameter, a straight forward optimisation technique cannot be followed to obtain suitable parameters for a particular range of frequencies. The influence of the relevant parameter on performance is studied. The overall parameters of the concentric dielectric waveguide are then chosen to best satisfy the desired performance criterion.

7.5.2 Choice of Core Radius

The choice of core size determines the frequency band of operation. It is desirable to operate below the frequency at which higher order modes begin to have their field concentration in the core region. This condition will lead to a choice of normalised frequency $V < 2.405$. If the operating frequency is chosen to be slightly below this frequency, e.g. $V = 2.2$, then r_1 can be determined in terms of $\Delta\bar{\varepsilon}$ as shown in Figure (7.4), for a frequency of 40 GHz; this frequency is chosen as a convenient upper bound, $\Delta\bar{\varepsilon} = \bar{\varepsilon}_1 - \bar{\varepsilon}_2$.

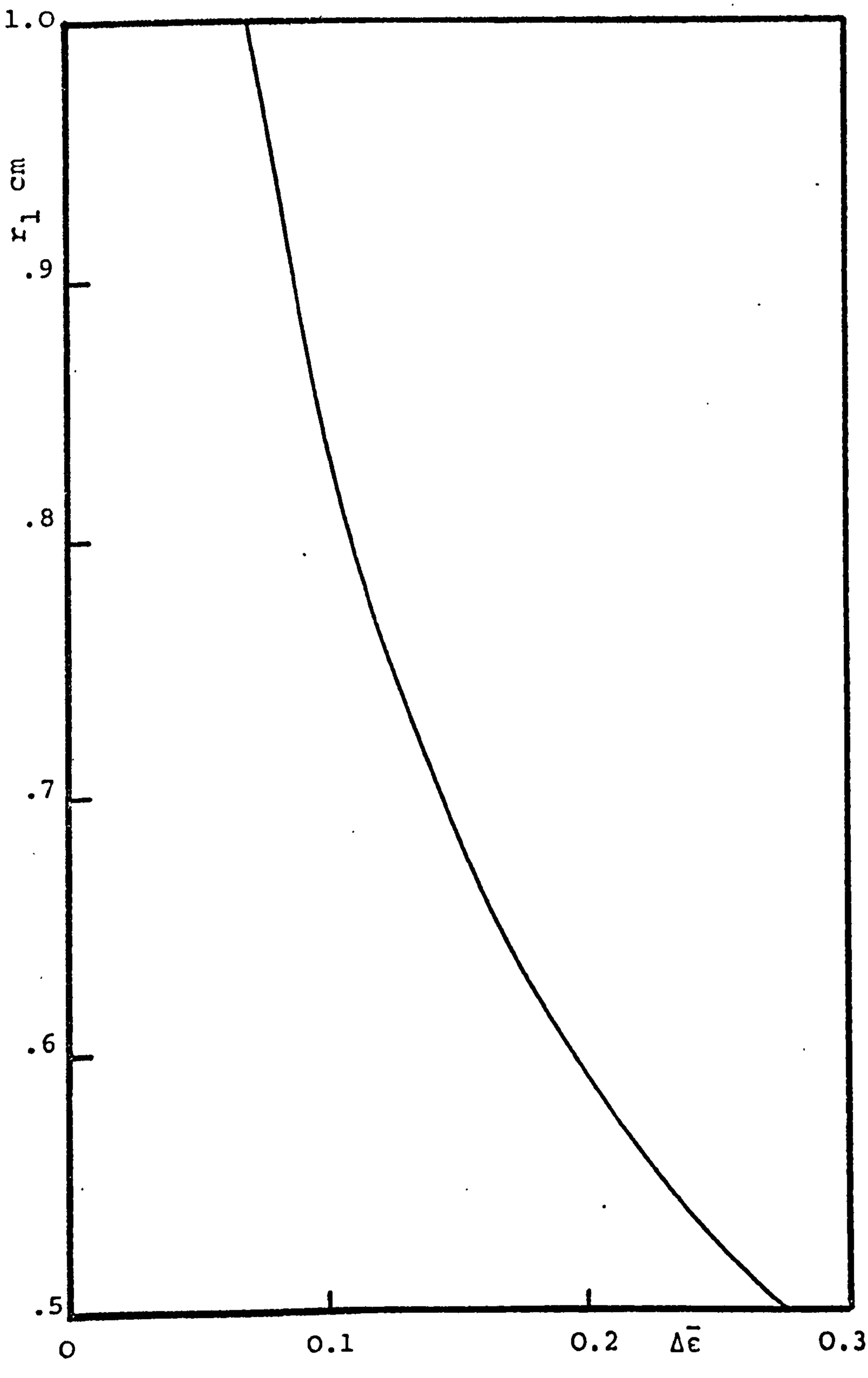

Figure (7.4) Choice of core radius and relative permittivity difference between core and cladding regions

7.5.3 Choice of Loss Angle δ_1

The influence of the loss angle δ_1, is shown in Figure (7.5), where it is observed that at frequencies above and slightly below the frequency of minimum-attenuation, the core and cladding loss only influences the HE_{11} mode attenuation. This criterion confirms the confinement of the dominant mode power to the central region of the waveguide. It was found that when the loss is the same in the core and cladding regions, the attenuation coefficient α, is then given, to close approximation, by the expression

$$\alpha = \frac{\pi}{\lambda g} \tan\delta_1 \qquad \text{nepers/m} \qquad \{7.4\}$$

where λg is the wavelength of a plane wave in the core region, whose permittivity is assumed to be nearly the same as that of the cladding. Computed results using {7.4} are also shown in Figure (7.5) for different values of δ_1.

7.5.4 Choice of Cladding Radius

The criterion applied in selecting the outer cladding radius r_2, is that at the frequency when the dominant HE_{11} mode has minimum attenuation, the attenuation of the higher order modes shall exceed that of the HE_{11} mode by at least one hundred times. Figure (7.4) is used to select values of core and cladding permittivities for a particular value of core radius r_1. For this set of

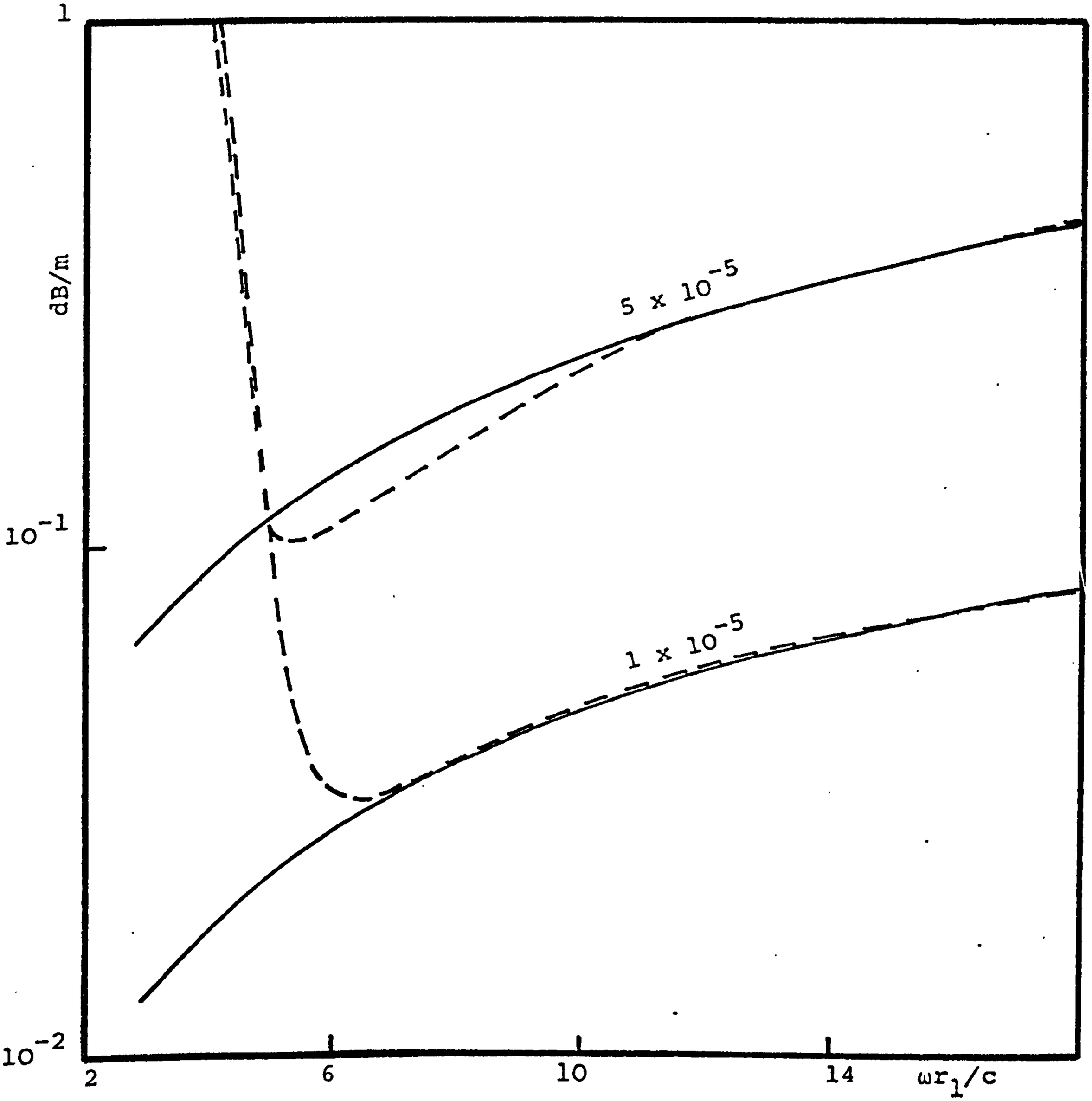

Figure (7.5) Attenuation characteristics of the HE_{11} mode

$r_1 = 1.0cm \quad r_2 = 6.0cm \quad r_3 = 7.0cm$

$\bar{\varepsilon}_1 = 1.11 \quad \bar{\varepsilon}_2 = 1.01$

Parameter $(\tan\delta_1)$

——— Exact analysis ----- Approximate formulae

parameters, the cladding radius r_2 is increased gradually until the above differential attenuation criterion is fulfilled.

In Figure (7.6) it is assumed rather arbitrarily that the thickness of the outer lossy layer is $r_2/10$ when $r_2 > 2.7$ cm and $r_2/5$ when $r_2 < 2.7$ cm, as there is a substantial tolerance on this parameter. It is also assumed that the loss tangent of the lossy layer is to have the value $\tan \delta_3 = 0.1$. The characteristics shown in Figure (7.6) are consistent with differences in the nature of the transverse electric field of the HE_{11} and HE_{21} modes. For a core V value of about 2, the field of the HE_{11} mode in the lossy region is of the form $\exp -V(r/r_1 - 1)$, whereas that corresponding to the HE_{21} mode is of the form $J_1\{\frac{2\pi r}{\lambda} (\bar{\varepsilon}_1 - 1)^{\frac{1}{2}}\}$. As V is constant throughout Figure (7. 6) and the slope of J_1 Bessel function is negative, r_1 and $\bar{\varepsilon}_1$ are inversely proportional if the field and attenuation ratios are to remain constant. The permittivities of the core region, shown in Figure (7.6), are representative of both solid and expanded types and extrapolation between them can be made easily. For $\bar{\varepsilon}_1 = 1.1$, the limit in the value of r_1 is due to the choice of $\Delta\bar{\varepsilon}$ in Figure (7.4).

7.5.5 Coupling Efficiency

Salema <59>, studied the excitation of the HE_{11} mode in a dielectric rod using, square, circular and corrugated circular waveguides as launchers. The

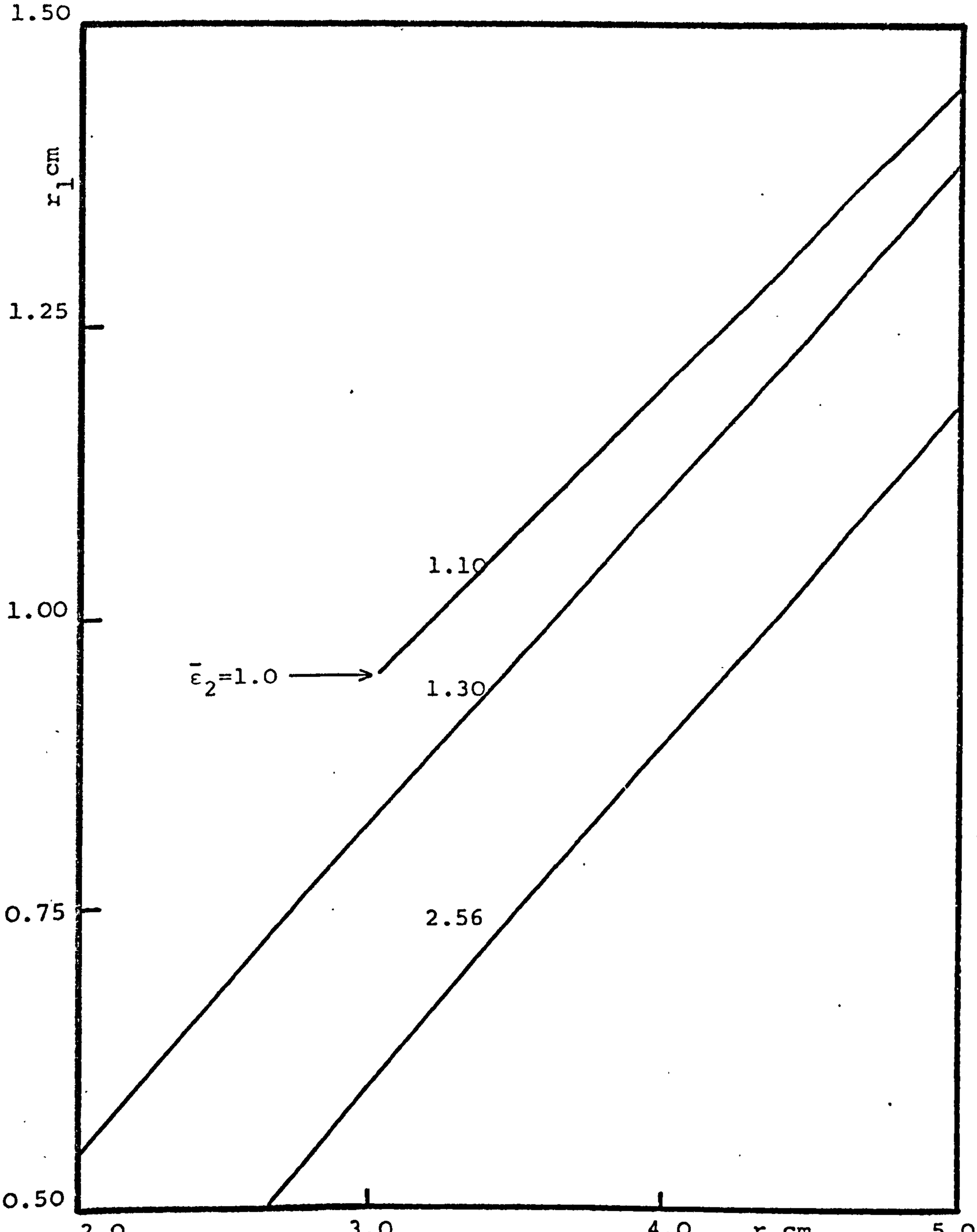

Figure (7.6) Choice of cladding radius and relative permittivity of core region

Parameter ($\bar{\varepsilon}_1$)

corrugated circular waveguide is found to give the best coupling efficiency; this is due to the similarity between the HE_{11} mode fields in both waveguides. Further, satisfactory transitions between conventional smooth-wall waveguides and corrugated waveguides have been manufactured in the millimetre regime, <61>, lending confidence to the practicability of the above choice. The coupling efficiency of such a transition, shown in the insert of Figure (7.7), is calculated using modal matching method <62>, and computed results for two values of $\Delta\bar{\varepsilon}$ are displayed in Figure (7.7). From the given data, it is possible to calculate the coupling efficiency as a function of the frequency or the corrugated waveguide inner radius R, for a particular value of core radius r_1.

From Figure (7.7) three important practical conclusions can be drawn.

(i) Over a wide frequency band, the excitation efficiency exceeds 70%. This implies a total transition loss at the input and output of less than 3 dB. The loss of the concentric dielectric waveguide shown in Figure (7.1) is of the order of 40 dB/km, thus the contribution due to the transitions is almost negligible if kilometer lengths are envisaged.

(ii) The lower the frequency and the dielectric permittivity, the larger the ratio between the launcher and the rod cross section for maximum efficiency.

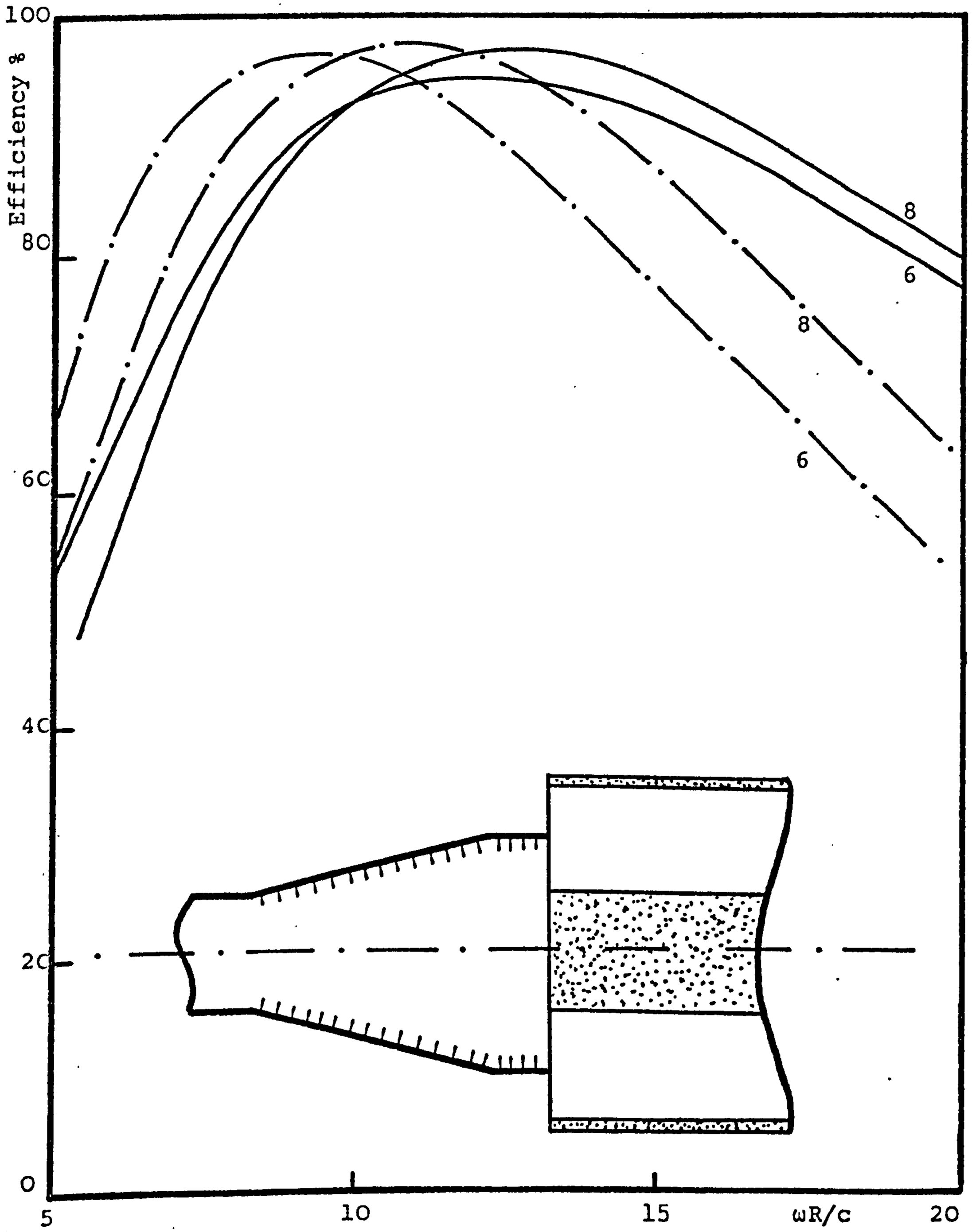

Figure (7.7) Coupling efficiency between a dielectric waveguide and a corrugated conical horn. Insert shows proposed configuration

——— $\Delta\bar{\varepsilon} = 0.1$ —.—.—.—. $\Delta\bar{\varepsilon} = 0.2$

Parameter ($\omega r_1/c$)

(iii) The aperture of the coupling corrugated waveguide should exceed that of the core by about 1.5 times for maximum efficiency, a result which is to be expected when consideration is given to the nature of the fields in the two waveguides.

7.5.6 Group Delay Consideration

When formulating the group delay characteristic of dielectric waveguides two factors must be taken into consideration <63>. First, due to the material dispersion, which is neglected in this study because of the assumption that the permittivity is frequency independent, and secondly, the group delay on account of waveguide dispersion, which can be calculated from a knowledge of the dispersion characteristic of the waveguide.

Computed results of the differential change in group delay with differential change in frequency, $\frac{\partial \tau}{\partial f}$, is shown in Figure (7.8), for dielectric waveguides with different values of core and cladding permittivities, where

$$\frac{\partial \tau}{\partial f} = - \frac{1}{V_g^2} \frac{\partial V_g}{\partial f} \qquad V_g = \text{group velocity}$$

It can be seen that $\frac{\partial \tau}{\partial f}$ decreases rapidly as the frequency is increased, and at approximately V = 2.6, there is a singularity which implies no signal distortion. Theoretically this means infinite bandwidth, which, however, in practice, will be limited because of material

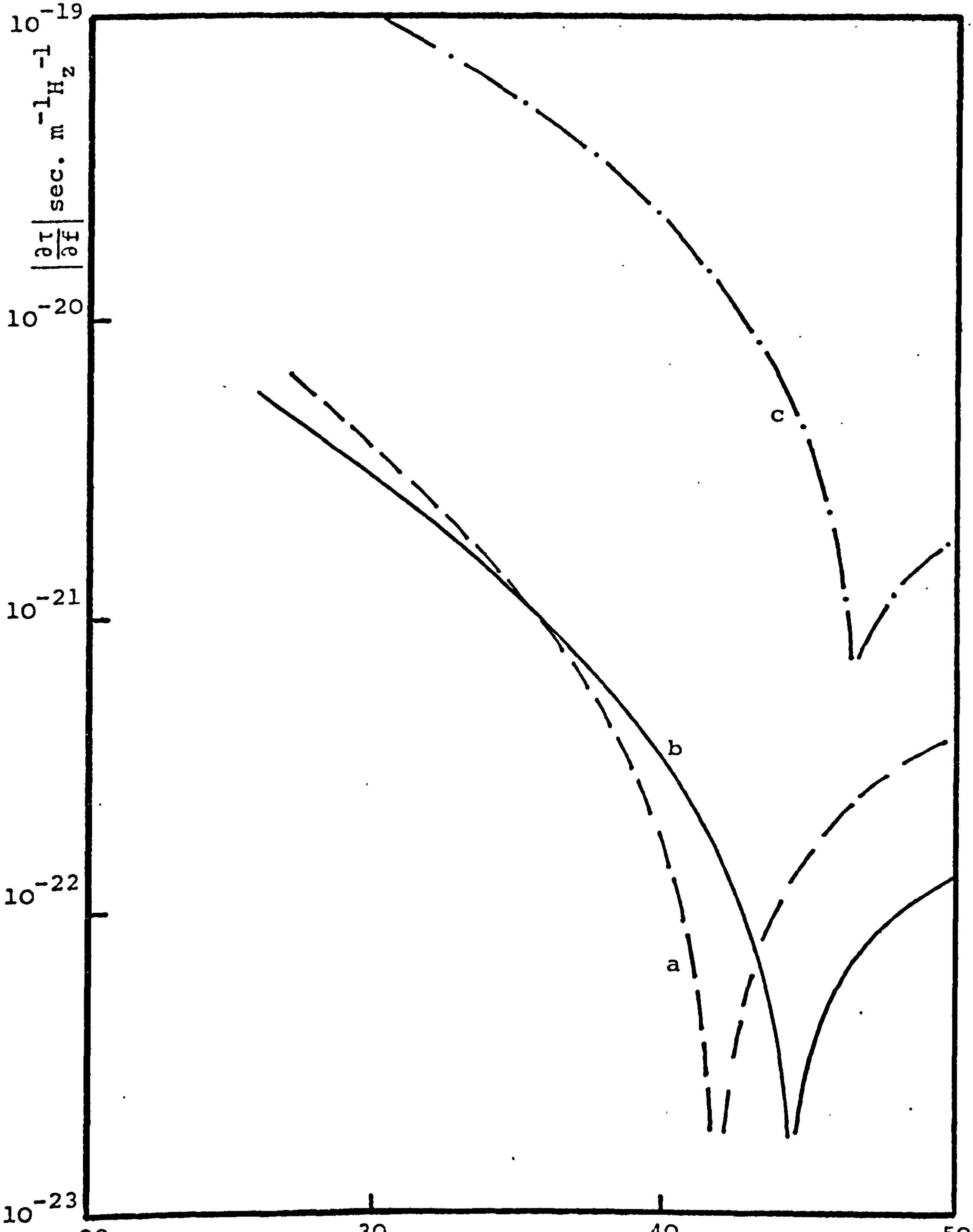

Figure (7.8) Differential change in group delay with frequency against frequency

——— r_1 = 1.0cm r_2 = 3.2cm r_3 = 3.4cm $\bar{\varepsilon}_1$ = 1.11 $\bar{\varepsilon}_2$ = 1.01

------ r_1 = 0.6cm r_2 = 3.0cm r_3 = 3.2cm $\bar{\varepsilon}_1$ = 2.56 $\bar{\varepsilon}_2$ = 2.25

–.–.–. r_1 = 0.25cm r_2 = 1.6cm $\bar{\varepsilon}_1$ = 2.26 $\bar{\varepsilon}_2$ = 1.01 <64>

dispersion mentioned above. Unfortunately, this value of V is higher than the upper limit for dominant mode operation, i.e. V = 2.4, this operating point is therefore not adopted. The influence of the dielectric difference $\Delta\bar{\varepsilon}$ is also illustrated in Figure (7.8), where it is seen that for case (a), $\Delta\bar{\varepsilon}$ = .1, the group delay change is 0.35 ns/km over 1GHz bandwidth centred at 40 GHz. Recently, Ravenscroft and Jackson <64> have described a single mode dielectric-rod waveguide suitable for microwave transmission at millimetre wavelengths. Their waveguide resembles the structure shown in Figure (7.1), with the central core, r_1 = 2.5 cm, comprising polypropylene, $\bar{\varepsilon}_1$ = 2.26, and surrounded by polypropylene foam of finite radius. The group delay characteristic of the waveguide is shown in Figure (7.8) case (c), where it is seen that their waveguide has a group delay change of 20 ns/km over 1 GHz bandwidth centred at 40 GHz. Evidently, waveguide (a) has superior group-delay properties, although it has twice the diameter of (c).

It may be concluded that group delay dispersion is unlikely to present a problem in the design of dielectric waveguides of the kind envisaged here.

7.6 CONCLUSIONS

We have presented the results of a parametric study which suggest that a homogeneous dielectric waveguide of outer diameter between 5 - 7 cm, could

exhibit low-attenuation at wavelengths in the range 0.75 - 1.0 cm, where metal waveguides begin to exhibit unreasonably high attenuation. To summarise the anticipated waveguide performance, Figures (7.9)(a) and (b) show attenuation curves appropriate to optimum designs for two different values of core permittivity. The design parameters have been taken from Figures (7.4) and (7.6). The overall properties of waveguide (a) are shown in the table below, for operating frequency of 40 GHz.

Choice of Parameters:

PARAMETER	VALUE	REMARKS
Core relative permittivity $\bar{\varepsilon}_1$	1.11	Specified
Cladding relative permittivity $\bar{\varepsilon}_2$	1.01	Specified
Core, cladding loss $\tan\delta_1$	10^{-5}	Specified
Outer layer loss $\tan\delta_3$	10^{-1}	Specified
Core radius r_1	1.0 cm	Figure (7.4)
Cladding radius r_2	3.2 cm	Figure (7.6)
Lossy layer radius r_3	3.4 cm	Figure (7.6)
Launcher radius R	1.6 cm	Figure (7.7)

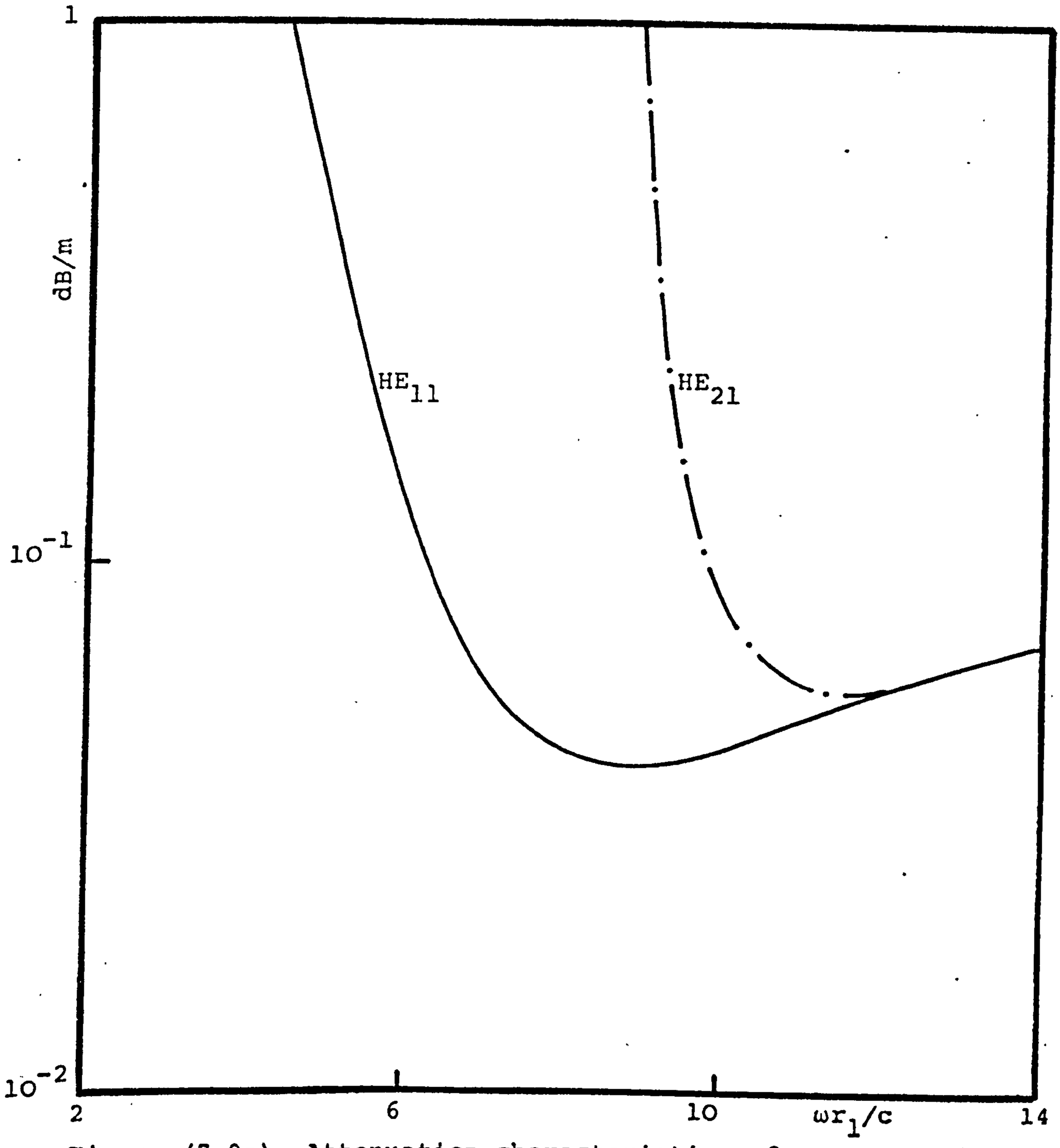

Figure (7.9a) Attenuation characteristics of a concentric dielectric waveguide

r_1 = 1.0cm r_2 = 3.2cm r_3 = 3.4cm

$\bar{\varepsilon}_1$ = 1.11 $\bar{\varepsilon}_2$ = 1.01

$\tan\delta_1 = 10^{-5}$ $\tan\delta_3$ = 0.1

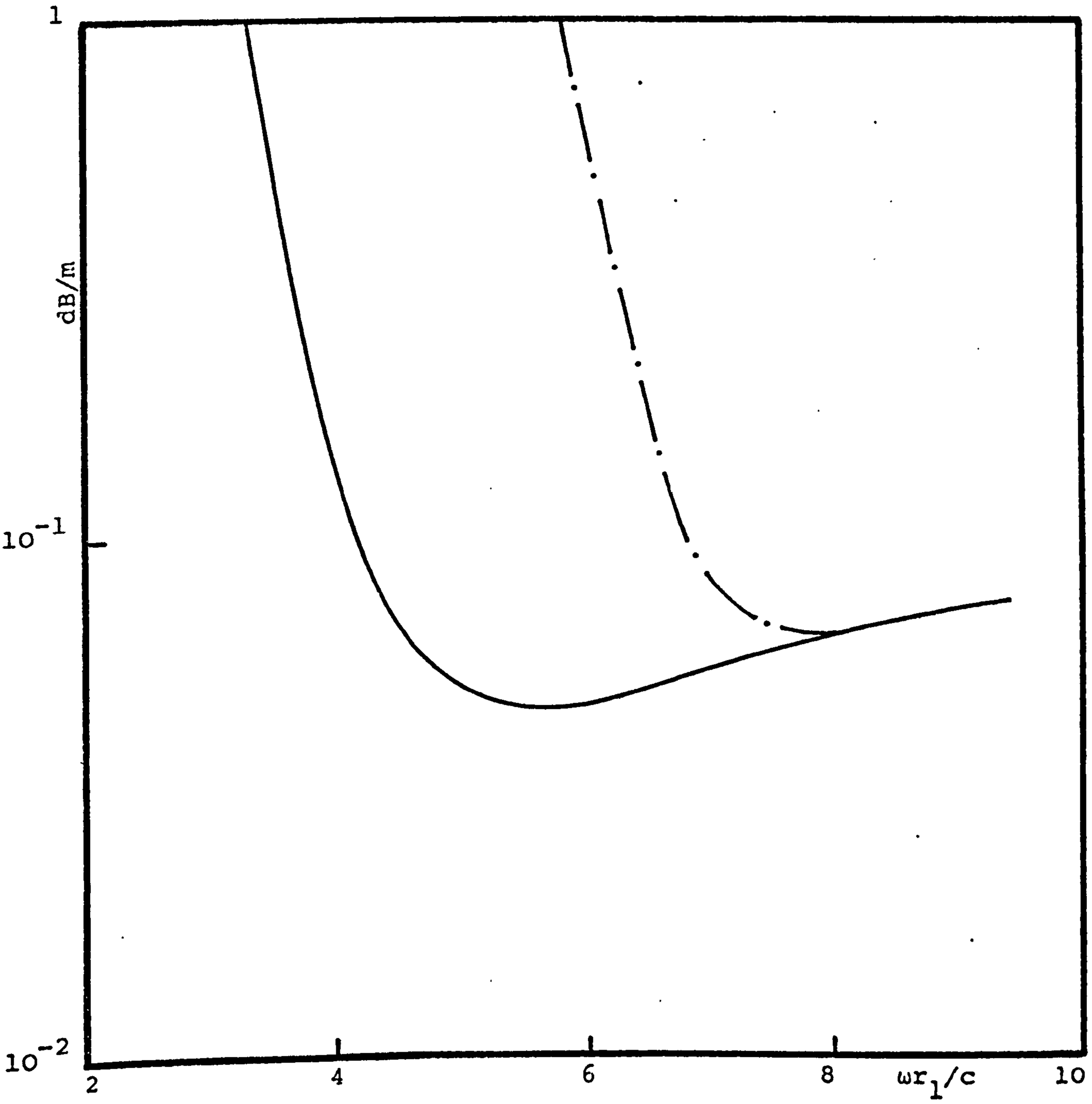

Figure (7.9b) Attenuation characteristics of a concentric dielectric waveguide

$r_1 = 0.6cm \quad r_2 = 2.3cm \quad r_3 = 2.5cm$

$\bar{\varepsilon}_1 = 1.31 \quad \bar{\varepsilon}_2 = 1.01$

$\tan\delta_1 = 10^{-5} \quad \tan\delta_3 = 0.1$

Performance:

PARAMATER	VALUE	REMARKS
Attenuation coefficient HE_{11}	42dB/km	Figure (7.9a)
Attenuation coefficient HE_{21}	5000dB/km	Figure (7.9a)
Excitation efficiency	95% .2dB	Figure (7.7)
Group delay change	0.35ns/km	Over 1 GHz B.W. Figure (7.8)

The performance of the concentric dielectric waveguide system, while not as good as either the optical or TE_{01} mode systems, deserves consideration for use in telecommunication applications at higher microwave frequencies.

In a practical system, protection against moisture penetration into the dielectric waveguide could be achieved by introducing a weather resistant layer around the outer lossy layer or alternatively by making that layer itself weather resistant. Besides application in digital microwave-communication systems, as discussed by Ravenscroft and Jackson <64>, dielectric waveguides may find use in millimetre radioastronomy <65> and in millimetre-wavelength microwave-antenna systems, where conventional metallic waveguides exhibit prohibiting high losses. The waveguides we have described are similar to

those investigated in <60> as feeds for microwave antennas, and these are known to exhibit little mechanical flexibility; for this reason we have not addressed the problem of radiation losses arising owing to bends. Nevertheless, the problem has been considered recently by Lewin <66>, and his analysis could be used if sharp bends were envisaged as forming part of a practical dielectric-waveguide system.

Another factor that we have not considered here is the loss arising from scattering due to inhomogeneities. This problem has been discussed by Clarricoats and Chan <67> in the context of optical waveguides. The extension of their results is probably well justified for solid dielectric materials but may be questioned in the case of low permittivity foam materials. At millimetre wavelengths, scattering losses due to inhomogeneities will be significant and extrapolation of the results presented here to wavelengths around 2 mm should be made cautiously if the use of foam material is envisaged. However, in the absence of reliable data on the nature of inhomogeneities in foam materials, we have deferred this problem.

Finally, recognising the conclusion reached by Yeh <36> that a thin elliptical dielectric rod operating in the dominant even HE_{11} mode has much lower loss than a circular rod of identical cross-sectional area. A concentric dielectric waveguide of elliptical cross-section with high eccentricity might provide lower attenuation values at microwave frequencies than the

waveguide studied.

It is reported <22> that Imperial Chemical Industries (U.K.) are developing an ultra low attenuation polypropylene and, conceivably before the end of the century, the era of the metallic waveguide will have passed.

CHAPTER EIGHT

CORRUGATED RECTANGULAR WAVEGUIDES

8.1 INTRODUCTION

Elliptical and circular structures with modified boundaries have been investigated in previous chapters. In this chapter the concept is extended to the rectangular structure with the aim of identifying configurations having favourable propagation and attenuation characteristics.

The rectangular corrugated waveguide with corrugation on two opposite sides, Figure (8.4), could be easier to manufacture than the circular corrugated waveguide and also have the advantage of stable modes, whereas the latter has the problem of mode polarisation rotation associated with slightly elliptical cross-section.

In section 2 the major power-loss components of the dominant mode in a smooth wall rectangular waveguide are identified and the nature of wall modifications, needed to reduce these losses, are discussed. The most promising structure is shown to have transverse corrugations on the two walls perpendicular to the electric field. The possibility of obtaining a closed form solution <68> of Maxwell's equations in the rectangular structure with impedance walls is also discussed in this section.

Field expressions and the characteristic equation of the corrugated waveguide are formulated in section 3, and the existence of two types of waves is explained.

The behaviour of the solutions of the characteristic equation are discussed and the dispersion characteristics of the waveguide are obtained.

In section 4 the attenuation coefficient of the corrugated structure is formulated and published attenuation results of Baldwin and McInnes < 9 > are shown to be in error. The major power-loss components are identified and it is shown that a tall corrugated waveguide could have an advantage, in attenuation, over the smooth wall circular and rectangular waveguides. It is also shown that the corrugated circular waveguide has an attenuation advantage over the rectangular corrugated structure. This is attributed, in part, to higher relative field strengths in the slot and to the presence of an additional loss component in the rectangular structure.

The chapter is concluded with experimental verification of the theoretical results obtained in sections 3 and 4, using a resonant cavity.

8.2 CHOICE OF WAVEGUIDE

The attenuation of the dominant TE_{10} mode (neglecting surface roughnesses) in a smooth wall rectangular waveguide is given by the expression <55>

$$\frac{8.686R_s}{Z_o\sqrt{1-(f_c/f)^2}}\{1/b + 2(f_c/f)^2/a\} \text{ dB/m}$$

where the electric vector is normal to the side a.

The first term is the contribution of the two horizontal walls, while the second term is due to vertical walls. It is evident that at frequencies above cut-off (f_c), the contribution of the first term will be predominant. The horizontal and vertical wall losses in a square waveguide are shown in Figure (8.1) where it is seen that in order to achieve lower losses the search must be directed towards finding a structure which will provide weaker fields at the two horizontal walls.

8.2.1 Walls Modification

There are four possible ways of modifying the fields near the two horizontal walls:

(a) Coating the horizontal walls with a dielectric material:

By choosing appropriate thicknesses and permittivities of a low loss dielectric material, it would be possible to create a quarter-wave transformer action, and hence reducing the field strength at the metal-dielectric interface. Experience with the lined circular waveguide, chapter six, suggests the possibility of obtaining lower attenuation figures, but not as attractive as figures offered by other structures.

(b) Extending the height of the waveguide:

This will cause an appreciable drop in the attenuation, but suffers the disadvantage of permitting a large number of modes to propagate <55>.

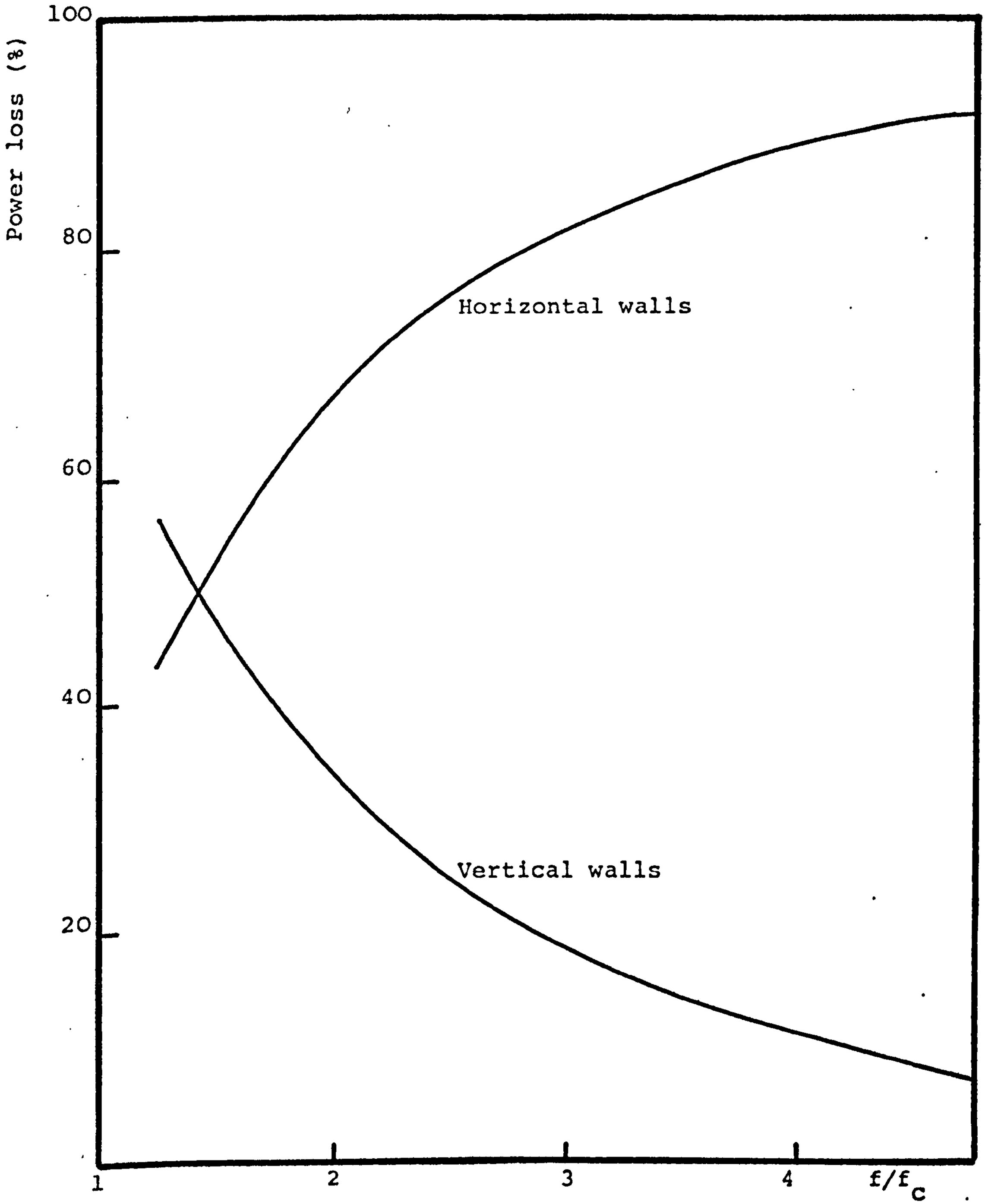

Figure (8.1) TE_{10} mode power loss in square smooth wall waveguide
a = 4cm, b = 4cm

(c) Longitudinal Corrugation:

When the waveguide is operating in the TE_{10} mode there exist two magnetic field components, axial, H_z acting at the four walls and transverse, H_x at the two horizontal walls. The loss due to the H_x component is very much greater than the loss due to the H_z component at the two horizontal walls as shown in Figure (8.2). Longitudinal corrugations of appropriate depth can reduce the power-loss due to the transverse current flow in the walls. As its contribution is very small, one would not expect a large decrease in attenuation due to the presence of longitudinal corrugations.

(d) Transverse Corrugation:

From Figure (8.2) it would seem that transverse corrugations having quarter wavelength depth would be the most feasible method for reducing the longitudinal currents due to H_x. Furthermore, if the corrugations reduced the number of modes existing in the waveguide, then method (b), could simultaneously be utilised.

From the above discussions it was decided to study in detail a rectangular structure with transverse corrugations on the two horizontal walls.

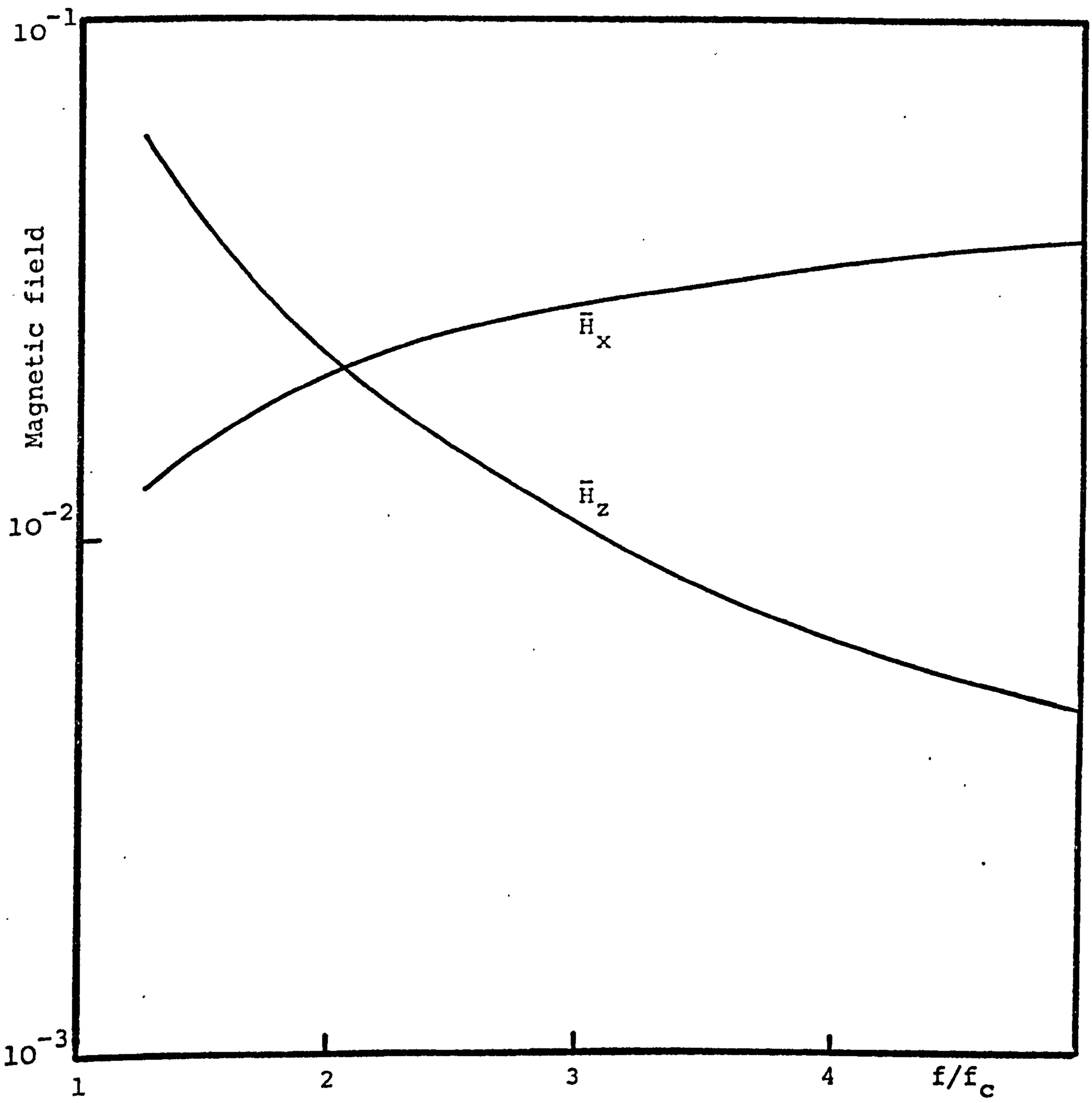

Figure (8.2) TE_{10} mode normalised magnetic field at the walls of a square waveguide
a = 4cm, b = 4cm

8.2.2 Rectangular Waveguide with Impedance Walls

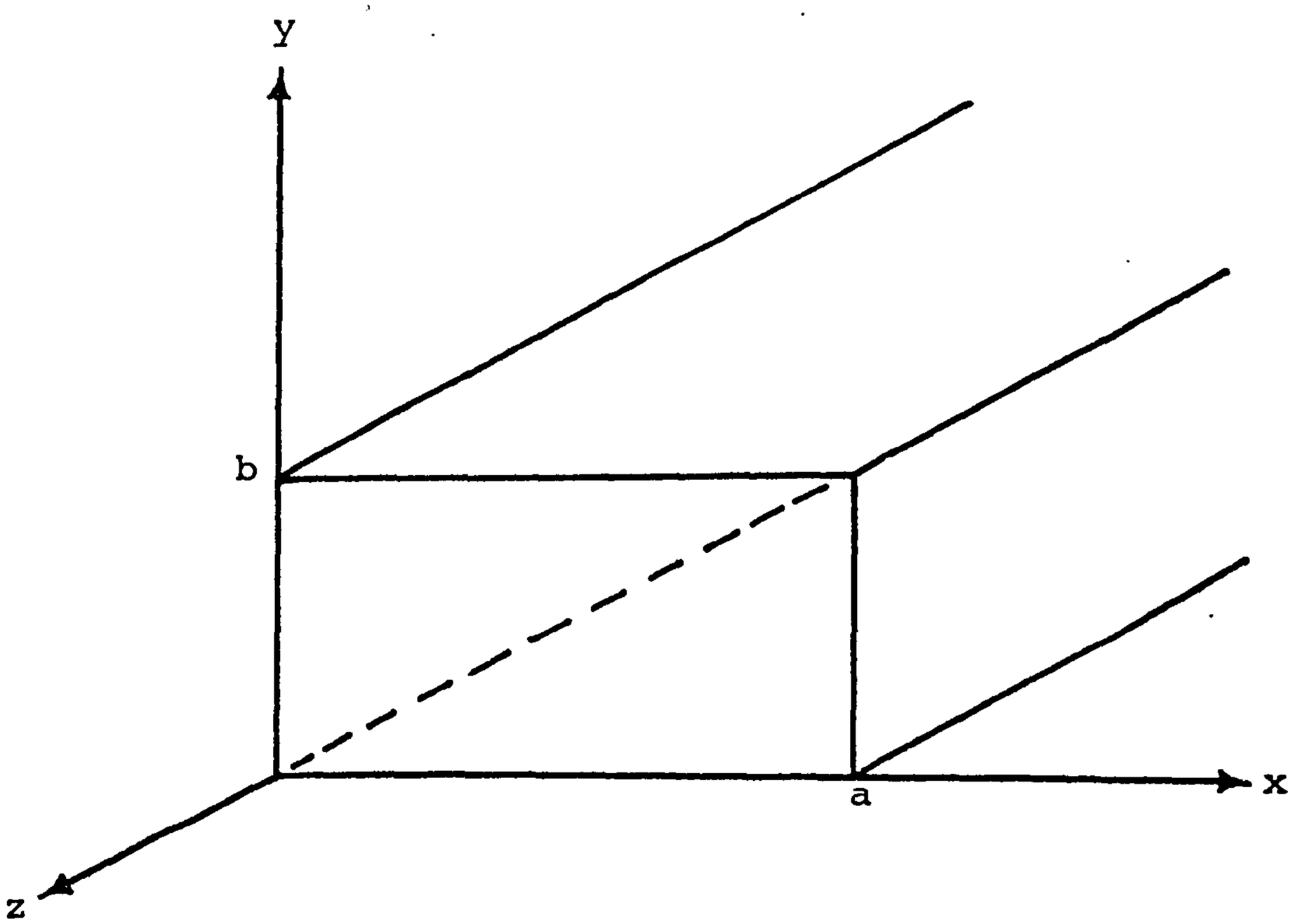

Figure (8.3)

Figure (8.3) shows a rectangular structure with impedance boundaries Z_1, Z_2, Z_3 and Z_4 where

$$Z_1 = \pm E_x/H_z \qquad Z_2 = \mp E_z/H_x \qquad y = o, b$$

$$Z_3 = \pm E_z/H_y \qquad Z_4 = \mp E_y/H_z \qquad x = o, a$$

The impedance boundaries could be either

isotropic $Z_1 = Z_2$, $Z_3 = Z_4$ e.g. proposal (a) or

anisotropic $Z_1 \neq Z_2$, $Z_3 \neq Z_4$ e.g. proposal (c) and (d) section (8.2.1).

The field equations in the above structure will have a closed form solution if and only if the condition

$$Z_1Z_3 - Z_2Z_3 + Z_2Z_4 = 0 \qquad \{8.1\}$$

is satisfied <68>. The choice of transverse corrugations at y = 0 and b, creates impedance walls having $Z_1 = 0 = Z_3 = Z_4$, and therefore a closed form solution of the field equations is possible in the structure. However, the field equations of a rectangular structure with transverse corrugations on all four walls cannot be written in a closed form.

8.3 Rectangular Corrugated Waveguide

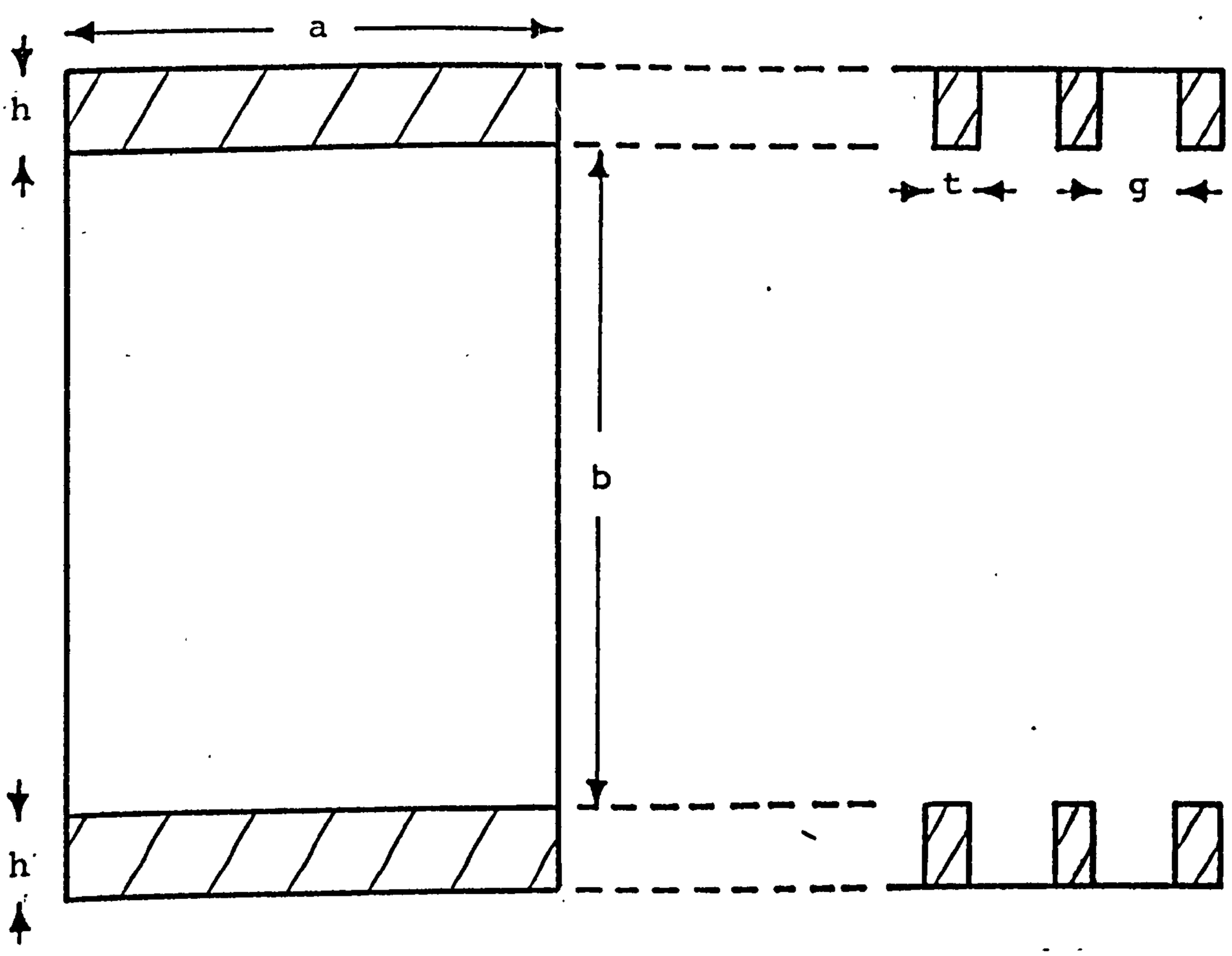

Figure (8.4)

The geometry of the rectangular corrugated waveguide used in this study is depicted in Figure (8.4). The origin of the cartesian system of co-ordinates is chosen to be at the centre of the waveguide,and the structure is divided in two regions;

region 1	$-b/2 \leq y \leq b/2$	$-a/2 \leq x \leq a/2$
region 2	$-(b/2+h) \leq y < -b/2$	
	$(b/2+h) \geq y > b/2$	

The analysis to be derived neglects the dependence of the solution on the width of the slots and the thickness of the teeth. The interaction of modes between consecutive slots is also neglected. Higher-order space harmonics are neglected in region 1. The phase-change coefficient of the first spatial harmonic β_z will be used in the analysis, where the phase-change coefficient β_{zn} of the $(n+1)^{th}$ spatial harmonic is given by

$$\beta_{zn} = \beta_z + \frac{(2n\pi)}{g+t}$$

The boundary condition at $y = \pm b/2$ is assumed to be a continuous impedance transverse to the slots, $z_1 = 0$. Thus the only fixed boundary condition assumed is that the electric field parallel to the corrugation edge at $y = \pm b/2$ is zero. This boundary condition is independent of the type of modes supported by the structure.

8.3.1 Field Equations

Solution of the wave equation, in region 1 is of the form

$$ {}_1E_z = C_1 \sin(K_x x+\theta)\sin(K_y y+\gamma) $$

where

$K_x = m\pi/a$ m = 0, 2, 4, θ = 0 asymmetric modes

m = 1, 3, 5, $\theta = \pi/2$ symmetric modes

and when the slot depth h is one quarter of a slot wavelength

$K_y = r\pi/b$ r = 0, 2, 4, γ = 0

r = 1, 3, 5, γ = /2

C_1 is an amplitude coefficient.

Two types of waves can be supported by this structure depending on whether K_y is real or imaginary. In the former case the modes supported are similar to those supported by the smooth wall waveguide, while in the latter case the modes do not exist in the ordinary rectangular waveguide, and their energy is bound to the corrugated surface and decay in an exponential manner towards the centre of the waveguide, i.e. in a manner similar to a surface wave structure.

The field components are obtained using App. I with $\ell_1 = \ell_2 = 1$. Assuming the guide is excited by a vertically polarised field ${}_1E_x = 0$, then

$$ {}_1H_z = - \frac{\beta_z}{\omega\mu_o} \int \frac{\partial {}_1E_z}{\partial x}\, dy $$

$$ = C_1 \frac{\beta_z K_x}{\omega\mu_o K_y} \cos(K_x x+\theta)\cos(K_y y+\gamma) $$

$$ {}_1H_x = jC_1 \frac{\beta_m{}^2}{\omega\mu_o K_y} \sin(K_x x+\theta)\cos(K_y y+\gamma) $$

$$ {}_1H_y = -jC_1 \frac{K_x}{\omega\mu_o} \cos(K_x x+\theta)\sin(K_y y+\gamma) $$

$$ {}_1E_y = -jC_1 \frac{\beta_z}{K_y} \sin(K_x x+\theta)\cos(K_y y+\gamma) $$

where

$$ K_c{}^2 = k^2 - \beta_z{}^2 = K_x{}^2 + K_y{}^2 , \quad \beta_m{}^2 = k^2 - K_x{}^2 \qquad \{8.2\} $$

and $k = \omega\sqrt{\mu_o\varepsilon_o} = 2\pi/\lambda$.

For the case $K_y = jK_y'$, solution of the wave equation in region 1 has the form

$$ {}_1E_z = C_1'\sin(K_x x+\theta)\sinh(K_y' y+j\gamma') $$

where

$\gamma' = 0$ or $\pi/2$. $K_c{}^2 = k^2 - \beta_z = K_x{}^2 - (K_y')^2$

The slots are thought of as rectangular waveguides supporting an infinite number of modes, producing standing waves in the slots. Experience with the corrugated circular waveguide and the discussions in <4>, indicate that it is a good approximation to assume TE_{mo} modes in the slots, i.e. modes with E_z, H_x and H_y

field components as compared with E_z, H_θ and H_r in the corrugated circular waveguide.

As the slot width, g, is very much smaller than the guide wavelength, the reasonable assumption is made that only the dominant TE_{10} mode will be sufficiently unattenuated to be reflected from the outer metal wall of the slot and so produce a standing wave in the slot. The condition $g << \lambda_g$ is also being made use of in removing the z variation of the slot fields.

The field components in region 2 are therefore given by;

$$_2E_z = C_2 \sin(K_x x+\theta)\sin\{\beta_m(b/2+h-y)\}$$

$$_2H_x = -jC_2 \frac{\omega\epsilon_o\beta_m}{k^2} \sin(K_x x+\theta)\cos\{\beta_m(b/2+h-y)\}$$

$$_2H_y = -jC_2 \frac{\omega\epsilon_o K_x}{k^2} \cos(K_x x+\theta)\sin\{\beta_m(b/2+h-y)\}$$

The time factor $\exp(j\omega t)$ is assumed in the above expressions. The assumption that only the TE_{10} mode exists in the slots implies that only modes with single x-variation dependence will be supported in the propagating region, i.e. m = 1.

8.3.2 Characteristic Equation

The characteristic equation of the structure is obtained by equating the surface impedance Z_2 of region 1 to that of region 2, at the boundary $y = \pm b/2$.

K_y real → $\beta_1 \tan(\beta_1 h) = -K_y \tan(K_y b/2+\gamma)$

K_y imaginary → $\beta_1 \tan(\beta_1 h) = K_y' \tanh(K_y' b/2+j\gamma')$

The modes generated in the case $\gamma = 0 = \gamma'$ are designated EH_{1n} modes, and those generated by setting $\gamma = \pi/2 = \gamma'$ are designated HE_{1n} modes, where the integer $n \geq 0$ shows the n^{th} root of either of the two cases above. Typical dispersion characteristics of the corrugated structure are shown in Figure (8.5), where a = 0.0228m, b = h = 0.0101 m.

For each particular mode there are three points which can be evaluated using simple algebra. The table below shows values of β_1 at these special points and with the aid of equation {2.8} the appropriate frequencies can easily be found.

MODE	$\beta_z = 0$ Low frequency cut-off	$\beta_z = \beta_1$ K_y becomes jK_y'	$\beta_z \to \infty$ High frequency cut-off
HE_{mn}	$\frac{n\pi}{h+b/2}$	$\frac{n\pi}{h}$	$\frac{(2n+1)\pi}{2h}$
EH_{mn}	$\frac{(2n+1)\pi}{2h+b}$	$\beta_1 \tan(\beta_1 h) = 2/b$	$\frac{(2n+1)\pi}{2h}$

Table (8.1)

The "cross over point" ($K_y \to jK_y'$) shown above is not the point at which $\beta_z = k$, i.e. the mode becomes a slow wave with increasing frequency, this point occurs beyond the

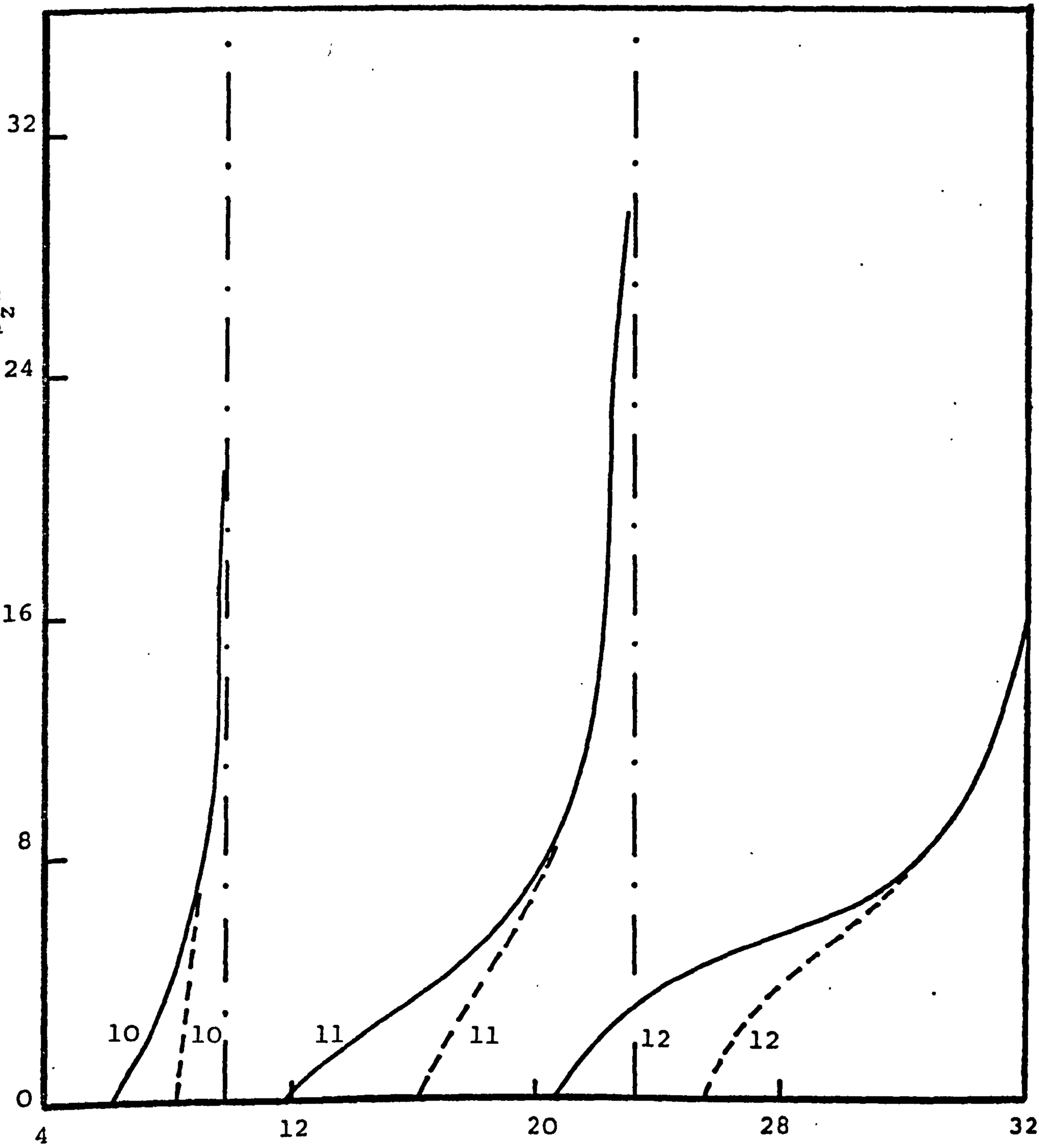

Figure (8.5) Dispersion characteristics of corrugated rectangular waveguide

a = 2.28cm b = 1.01cm, h = 1.01cm

——— HE mode ------ EH mode

-.-.-. High frequency cut-off

Parameter (mode number)

the cross over point, and it approaches the fast-slow wave point in the limit $a \to \infty$.

The above table shows that the cut-off frequencies of the corrugated guide coincide with those of a smooth wall guide of height (2h+b) and width a. In the case $\gamma = 0$ the cut-off frequencies are those of modes with suffix (m, 2n) and for $\gamma = \pi/2$ they coincide with modes having (m, 2n+1) suffix.

8.3.3 Mode Recognition

Mode recognition based on the nature of the modes at cut-off is not very profound in the case of the corrugated rectangular structure, as all modes will have a TM type cut-off ($H_z = 0$) when $\beta_z = 0$, except for the case n = 0, when it is a TE_{10} type cut-off. This phenomena occurs due to the setting of $E_x = 0$, in the original analysis, as explained below.

In a smooth wall rectangular guide the following field components remain finite at cut-off:

$$TM \to E_z,\ H_x,\ H_y$$

$$TE \to H_z,\ E_x,\ E_y$$

But in the analysis we have assumed that $E_x = 0$ for all modes, and hence a $TE_{mn}(n>0)$ type mode will not exist at cut-off in the corrugated rectangular waveguide. While for a smooth wall circular waveguide the fields components that remain finite at cut-off are:

$$TM \rightarrow E_z,\ H_\theta,\ H_r$$

$$TE \rightarrow H_z,\ E_\theta,\ E_r$$

and as none of the components is set to zero in the analysis of the corrugated circular waveguide <33>, modes possessing TE or TM type cut-off exist in the corrugated circular waveguide.

Mode recognition based on the modes's nature when the slot depth is one quarter of a slot wavelength deep seems to give a better picture in naming the modes;

at $y = \pm b/2$ $\quad \gamma = 0 \rightarrow H_z = 0$ thus HE type

$\gamma = \pi/2 \rightarrow E_z = 0$ thus EH type

8.3.4 Single Mode Operation

The operating frequency for low loss condition must be well below the cross-over frequency $K_y \rightarrow jK_y'$, as at frequencies above this most of the mode's power is carried near the corrugated surface, and high losses are expected.

For wide-band low loss unimode operation it is adequate to ensure that the cross-over frequency of the HE_{1n} mode is below the low frequency cut-off of the EH_{1n} mode. Furthermore, the high frequency cut-off of the $HE_{1(n-1)}$ must be below the low frequency cut-off of the HE_{1n} mode. The first condition yields $h > nb$, and the latter gives $h > b(2n+1)/3$, which is implied in the first results for $n \geq 1$. The choice of slot depth might prove

useful in providing a unimode region, but does not imply low loss condition.

Clarricoats and Olver < 2 > demonstrated that the point of minimum attenuation, in a corrugated circular waveguide, occurs at a frequency when the slot depth is between $\lambda/3$ and $\lambda/4$.

As the slot wavelength differs from the free space wavelength, then we must ensure that the mode will not start to propagate beyond a frequency where the slot depth is one quarter of a slot wavelength. For the HE type modes, the cut-off frequency occurs when $\beta_1 h = n\pi/(1+\varepsilon)$, where $\varepsilon = b/2h$.

The quarter wavelength condition, $\beta_1 h = \pi/2$, for the HE_{11} mode is satisfied if $\varepsilon > 1$, which is contradictory to the wide-band unimode condition derived above.

8.4 ATTENUATION

The corrugated rectangular structure was analysed by Baldwin and McInnes < 9 >, and their results showed a substantial advantage in attenuation over the TE_{10} mode propagating in a smooth wall rectangular waveguide of comparable dimensions. For certain values of slot depth they reported an attenuation figure of ~10dB/Km, as compared with ~110dB/Km for the smooth wall waveguide. They also derived an approximate attenuation formula for the corrugated structure under special conditions.

A numerical error was discovered in their attenuation results, which eroded away the attenuation advantage over the smooth wall rectangular waveguide. Their approximate formula was found to be incorrect, as they have neglected a substantial loss component.

In this section we will discuss the conditions leading to an improvements, in attenuation, over the smooth wall waveguide.

8.4.1 Power Expressions

The expression for the power flow in region 1 is formulated in the usual manner and expressions for the wall loss are derived using perturbation techniques. Surface roughnesses are not included. Expressions for the power losses over a single slot are given below for the two cases K_y real and imaginary, with the appropriate values of γ and γ'. The attenuation coefficient, α, is finally obtained using the expression;

$$\alpha = \frac{8.686}{2(g+t)} \quad \frac{\sum_{i=1}^{5} P_i}{P_o} \quad \text{dB/m.}$$

P_o = Power flow in region 1, over the area (axb)

$$P_o = \frac{ab\beta_m{}^2\beta_z}{8\omega\mu_o K_y} C_1{}^2\{1+\cos(2\gamma)\,\mathrm{sinc}(bK_y)\}$$

$$P_o = \frac{ab\beta_m{}^2\beta_z}{8\omega\mu_o K_y{}'^2} C_1{}'^2\{\cos(2\gamma')+\mathrm{sinhc}(bK_y')\}$$

P_1 = Power loss on the transverse slot walls, over the area 4(axh)

$$P_1 = \frac{\omega^2 \varepsilon_o{}^2 a h R_s}{2k^4} C_2{}^2 \{k_o{}^2 + (\beta_m{}^2 - K_x{}^2) \operatorname{sinc}(2\beta_m h)\}$$

P_2 = Power loss on the slot base, over the area 2(axg)

$$P_2 = \frac{\omega^2 \varepsilon_o{}^2 R_s a g \beta_m{}^2}{2k^4} C_2{}^2$$

P_3 = Power loss on the axial slot walls, over the area 4(hxg)

$$P_3 = \frac{\omega^2 \varepsilon_o{}^2 g h K_x{}^2 R_s}{k^4} C_2{}^2 \{1 - \operatorname{sinc}(2\beta_m h)\}$$

P_4 = Power loss on the teeth edge, over the area 2(axt)

$$\frac{at \cos^2(K_y b/2+\gamma) R_s}{2\omega^2 \mu_o{}^2 K_y{}^2} C_1{}^2 \{K_x{}^2 \beta_z{}^2 + \beta_m{}^4\}$$

P_4 =

$$\frac{at \cosh^2(K_y' b/2+j\gamma') R_s}{2\omega^2 \mu_o{}^2 K_y'{}^2} C_1'{}^2 \{K_x{}^2 \beta_z{}^2 + \beta_m{}^4\}$$

P_5 = Power loss on the vertical smooth walls, over the area 2{bx(g+t)}

$$\frac{K_x{}^2 (g+t) b R_s}{2\omega^2 \mu_o{}^2 K_y{}^2} C_1{}^2 \{\beta_m{}^2 + (\beta_z{}^2 + K_y{}^2) \cos(2\gamma) \operatorname{sinc}(K_y b)\}$$

P_5 =

$$\frac{K_x{}^2 (g+t) b R_s}{2\omega^2 \mu_o{}^2 K_y'{}^2} C_1'{}^2 \{\beta_m{}^2 \cos(2\gamma') + (\beta_z{}^2 + K_y{}^2) \operatorname{sinhc}(K_y' b)\}$$

where $C_1/C_2 = \sin(\beta_m h)/\sin(K_y \frac{b}{2}+\gamma)$

$$C_1'/C_2 = \sin(\beta_m h)/\sinh(K_y' \frac{b}{2}+j\gamma')$$

The ratio of the constants C_1/C_2 and C_1'/C_2 were obtained by equating the E_z components at $y = \pm b/2$. At this value of y the assumption that the slot width g is very much smaller than the guide wavelength in region 1, permits the existence of a continuous constant axial surface impedance, thus removing the field dependence in region 1 of the propagation direction. The common factor $\exp j(\omega t-\beta_z z)$ is therefore replaced by $\exp j(\omega t)$ at this value of y.

8.4.2 Low Attenuation Characteristic

In order to identify modes possessing the property of low attenuation, over a reasonable band width, and which will propagate with the least possible number of propagating modes, our attention must be focussed on the following:

(a) K_y must be real; thus avoiding the slow wave region where most of the power is carried near the corrugation surfaces, giving rise to high losses.

(b) The tangential fields at $y = \pm b/2$ must be weak; this condition is fulfilled by the HE type mode.

(c) Least possible number of propagating modes; the influence of normalised slot depth on the normalised high frequency cut-off is shown in Figure (8.6), which

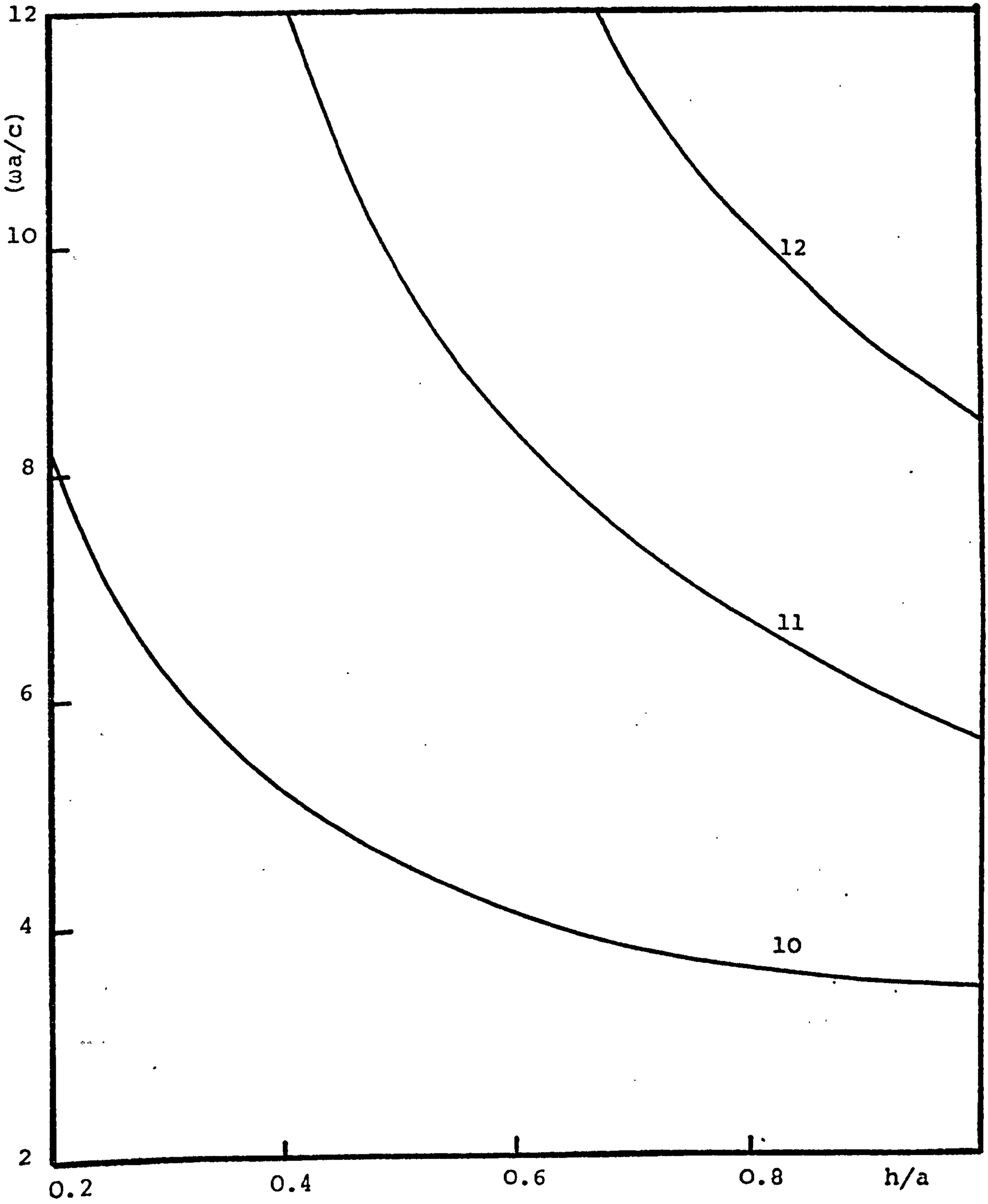

Figure (8.6) High frequency cut-off of corrugated rectangular waveguide against normalised slot depth

Parameter (mode number of either HE or EH mode)

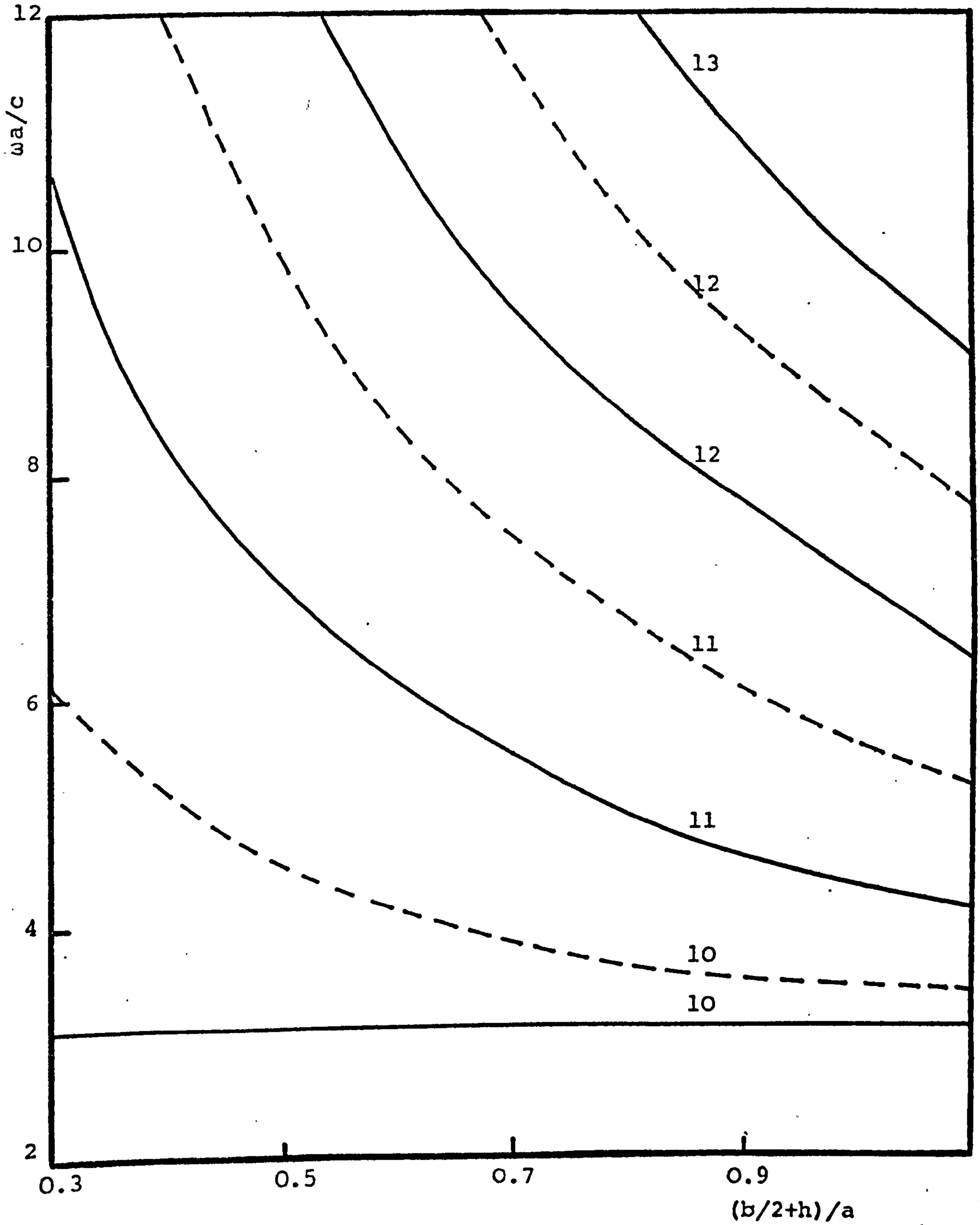

Figure (8.7) Low frequency cut-off of corrugated rectangular waveguide against normalised waveguide height

Parameter (mode number)

——— HE mode ------ EH mode

could be made use of in conjunction with the normalised low frequency cut-off, Figure (8.7), to minimise the number of propagating modes at a particular value of ωa/c.

(d) Large values of h must be avoided; as this will cause high slot losses.

8.4.3 Attenuation Characteristic

The attenuation characteristic of the first few modes supported by the corrugated structure are shown in Figure (8.8) for a waveguide with a = 0.0228m, b = 0.0101m, h = 0.0101m, g = 0.005m, t =0.0005m. All modes have a minimum of attenuation. Beyond the frequency for minimum attenuation the modes, except HE_{10}, approach their cross over frequencies, where high losses are expected. The losses of the EH modes are higher due to their rapid approach to the cross over point as seen in Table (8.1) and Figure (8.5).

The slow wave nature of the HE_{10} mode, and its rapid approach to the high frequency cut-off makes this mode unsuitable for communication purposes.

The HE_{11} mode is used in corrugated rectangular horns due to its uniform polarisation and has been studied by several authors <10>. For long distance communication this mode would be used because of its low attenuation property, and it could be supported with minimum overmoding.

The attenuation advantage of the HE_{12} mode cannot be utilised as at such high frequencies the waveguide

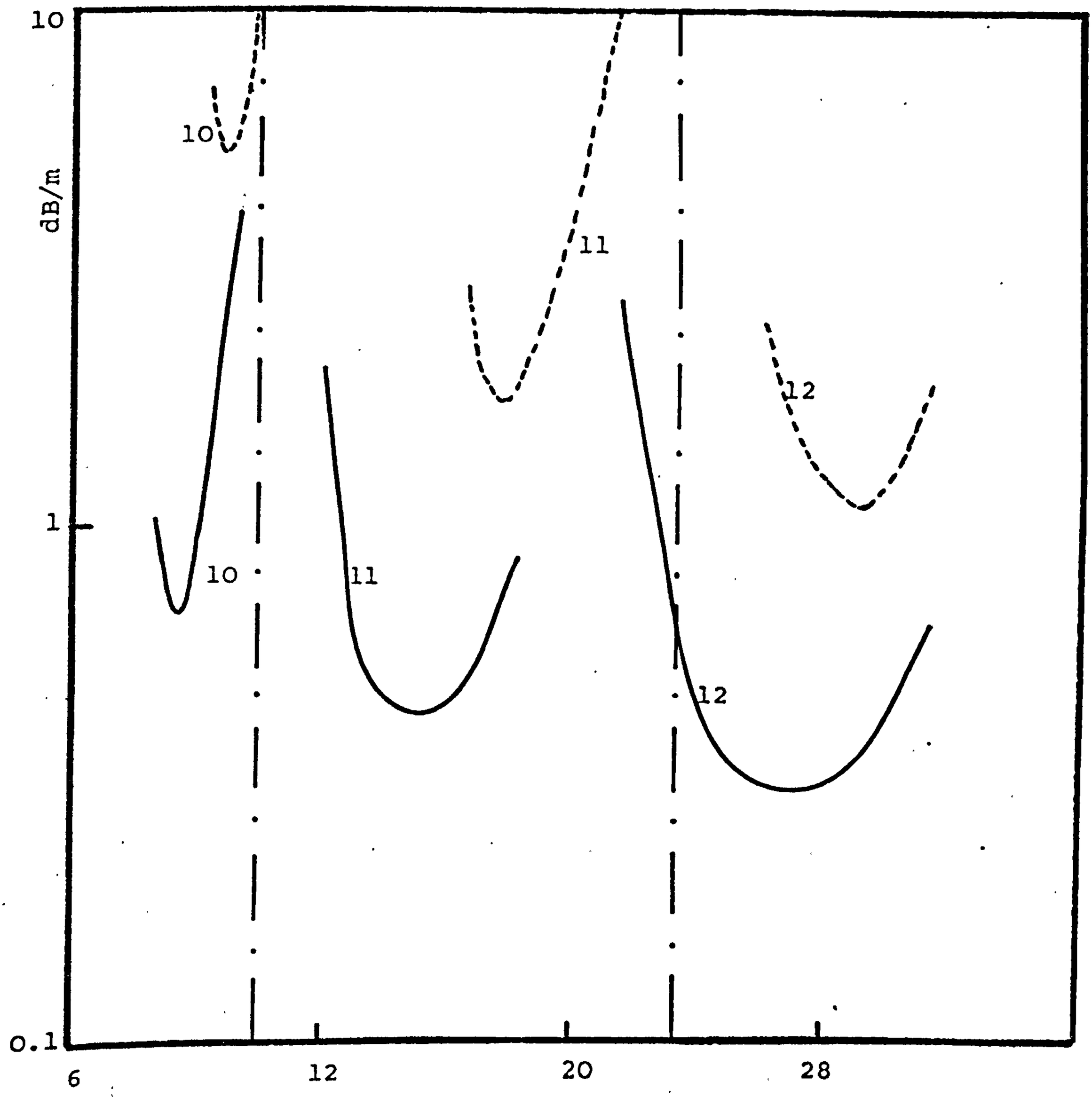

Figure (8.8) Attenuation characteristics of brass corrugated rectangular waveguide

a = 2.28cm b = 1.01cm h = 1.01cm g = .5cm

t = g/10

——— HE mode ------ EH mode

Parameter (mode number)

will be grossly overmoded.

In the sections to follow the properties of the HE_{11} mode will be investigated.

8.4.4 Comparison with Published Results

Attenuation results in dB/m for a corrugated rectangular waveguide are plotted for various slot depths in Figure (8.9). On the same figure, the attenuation results obtained by Baldwin <10> are also shown.

Two significant errors were found in Baldwin's work:

(a) A numerical error was discovered in the calculations of the attenuation coefficient.

(b) A false assumption for narrow-slots under the quarter slot-wavelength condition.

(i) The dispersion characteristics obtained were in agreement with Baldwin's available characteristics. His expressions for the losses of the HE_{11} mode were found to be correct, but when calculating the attenuation coefficient a very large difference in the numerical values was observed, as shown in Figure (8.9).

Using Baldwin's available results an approximate correction factor for his attenuation results was found to be (Z_o/h), $Z_o = \sqrt{\mu_o/\varepsilon_o}$, h is slot depth in mm.

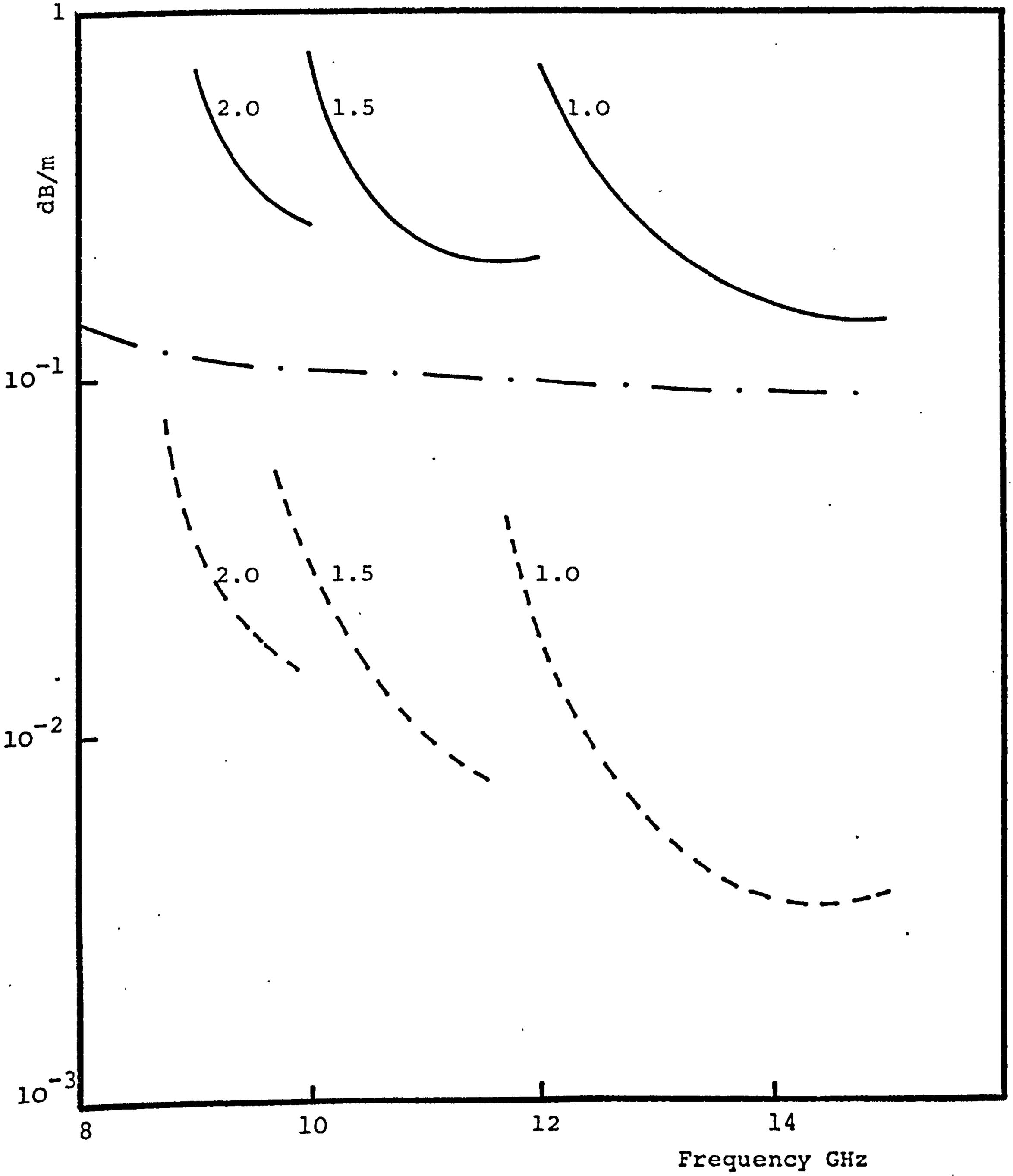

Figure (8.9) HE_{11} mode attenuation characteristics of copper rectangular corrugated waveguide, inner dimensions as WG 16.

------ Baldwin <10> Parameter (slot depth cm)

——— Corrected theory

------ TE_{10} mode in WG 16

$$\text{i.e. } \alpha_{BALDWIN} \times (Z_o/h) = \alpha_{CORRECT}$$

(ii) Baldwin suggested that under the quarter wavelength slot depth condition, the only significant loss component was that due to the broad walls of the slot, P_1, and hence arrived at an approximate expression for the attenuation coefficient. The invalidity of this assumption is demonstrated in Figure (8.10), where the normalised power loss components of a square corrugated waveguide are shown. It is seen that at the frequency where the slot depth is one quarter of a slot-wavelength, the contributions of the vertical smooth walls P_5, and of the slot base P_2, are of the same order as the broad wall base P_1, and thus the former two components cannot be neglected.

8.4.5 Parametric Study

The influence, on the attenuation coefficient, of different parameters has been studied in order to find circumstances leading to an advantage in attenuation over the smooth wall waveguide. The difficulty in finding an optimum slot depth was the optimisation of the two dimensions a and b at a particular frequency. For small values of b/λ ($\lambda=2\pi/k$), the optimum slot depth was found to be very sensitive to changes in the value of $\omega a/c$, as shown in Figure (8.11), and deep slots were necessary to obtain the minimum attenuation condition. The overall slot loss was therefore high and a disadvantage in

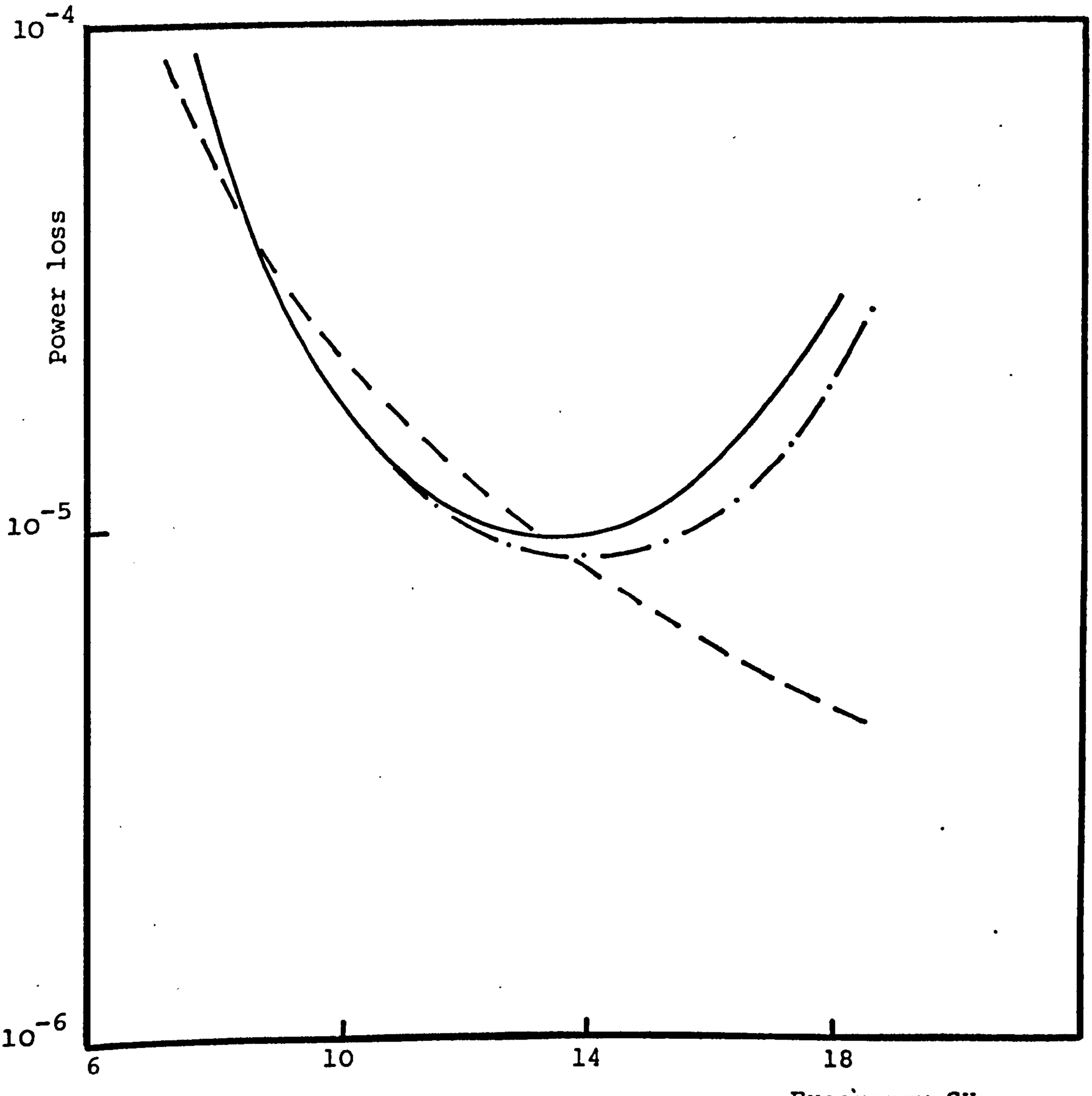

Figure (8.10) HE_{11} mode normalised power loss in square corrugated waveguide

a = 4.0cm b = 4.0cm h = .8cm

——— P_1 -.-.-. P_2 ------ P_5

attenuation was observed.

The sensitivity of the slot depth for large values of b/λ was found to be less and shallower slots were needed to produce the minimum attenuation condition as shown in Figure (8.12). Due to the decrease in slot depth, and weaker fields near the slot edge, the attenuation coefficient had lower values for corresponding values of $\omega a/c$.

8.4.6 The Tall Waveguide

The major loss components of a corrugated square waveguide are shown in Figure (8.10). It is clear that in order to obtain lower values of the attenuation coefficient, a means must be found to reduce these losses, preferably the slot losses, as this consists of two components. In order to specify the means by which the losses can be reduced, we will study the normalised loss expressions when the waveguide's slot depth is one quarter of a slot wavelength, i.e.

$$\beta_m h = \pi/2 \quad , \quad K_y b = \pi \quad \text{when } \gamma = 0 \text{ (HE modes)}$$

After simplification it can be shown that the significant normalised losses are proportional to;

$$P_1/P_o \; \alpha l/(b^3\beta_z) \quad , \quad P_2/P_o \; \alpha l/(b^3\beta_z) \text{ and } P_5/P_o \; \alpha l/\beta_z$$

As increasing the b dimension will cause a decrease in the value of K_y and hence an increase in the value of

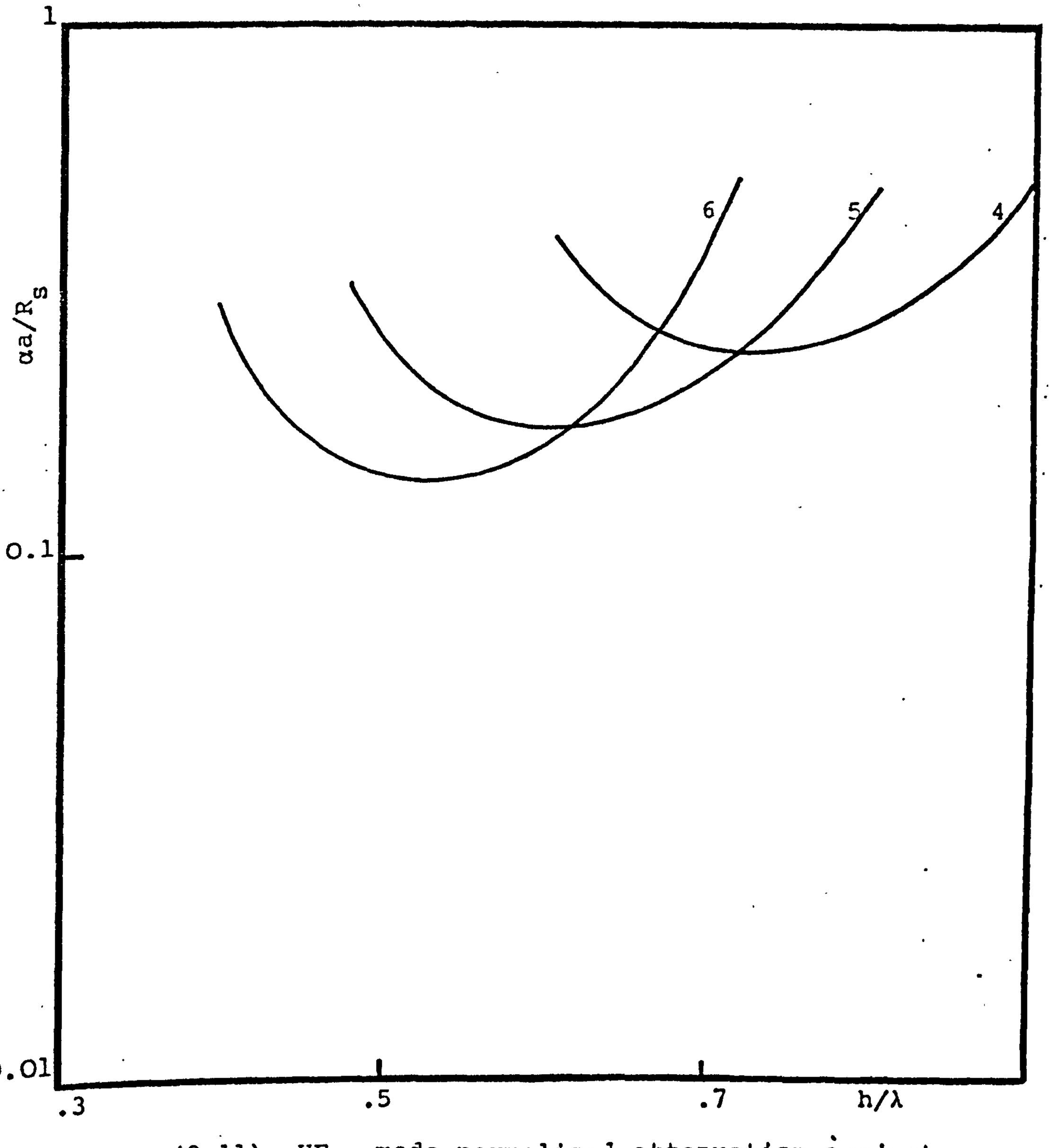

Figure (8.11) HE_{11} mode normalised attenuation against normalised slot depth

$b/\lambda = 0.40$ $g/\lambda = 0.30$ $g/t = 10$

Parameter ($\omega a/c$)

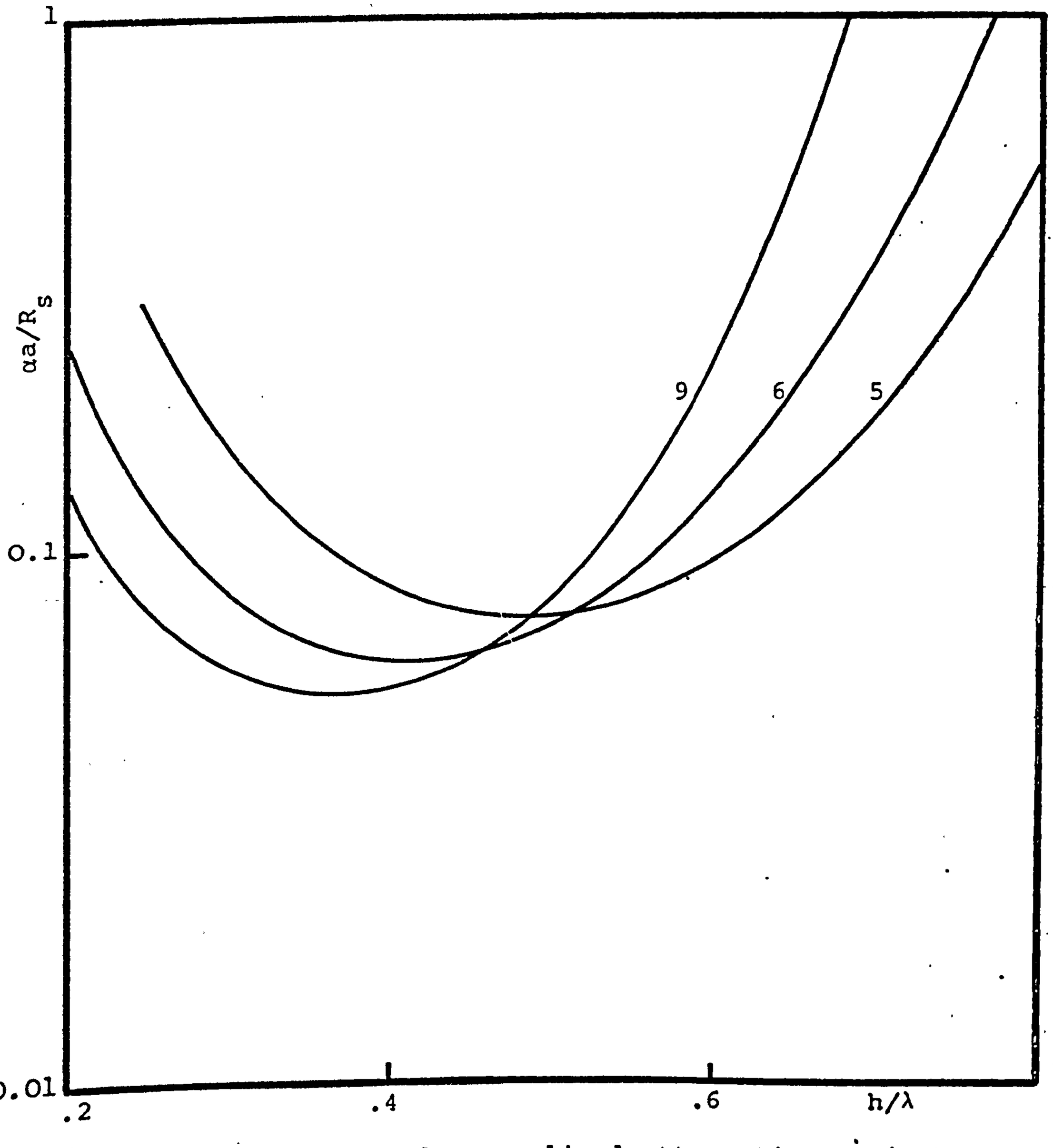

Figure (8.12) HE_{11} mode normalised attenuation against normalised slot depth

$b/\lambda = 0.80$ $g/\lambda = 0.30$ $g/t = 10$

Parameter ($\omega a/c$)

β_z, eqn. {8.2}, it follows that increasing the b dimension of the corrugated waveguide will cause a substantial decrease in the slot losses and a marginal decrease in the vertical smooth wall loss. The normalised losses of a corrugated tall waveguide are shown in Figure (8.13), where a decrease in all components is seen when compared with those of a square corrugated waveguide, Figure (8.10).

There are two more advantages in increasing the b dimensions:

(1) Due to the decrease in the value of K_y the frequency at which the minimum slot loss condition occurs will move further away from the cross-over frequency, $K_y = 0$, thus occurring at lower frequencies.

(2) The low frequency cut-off of the HE_{11} mode is lowered, which provides a larger bandwidth of propagation as the cross-over frequency is not altered.

A disadvantage in increasing the b dimension is the increase in the number of propagating modes as shown in Figure (8.7).

8.5 COMPARISON OF WAVEGUIDES

8.5.1 Smooth Wall Waveguides

In order to visualise the advantages, or disadvantages, offered by the corrugated rectangular waveguide two comprisons can be made;

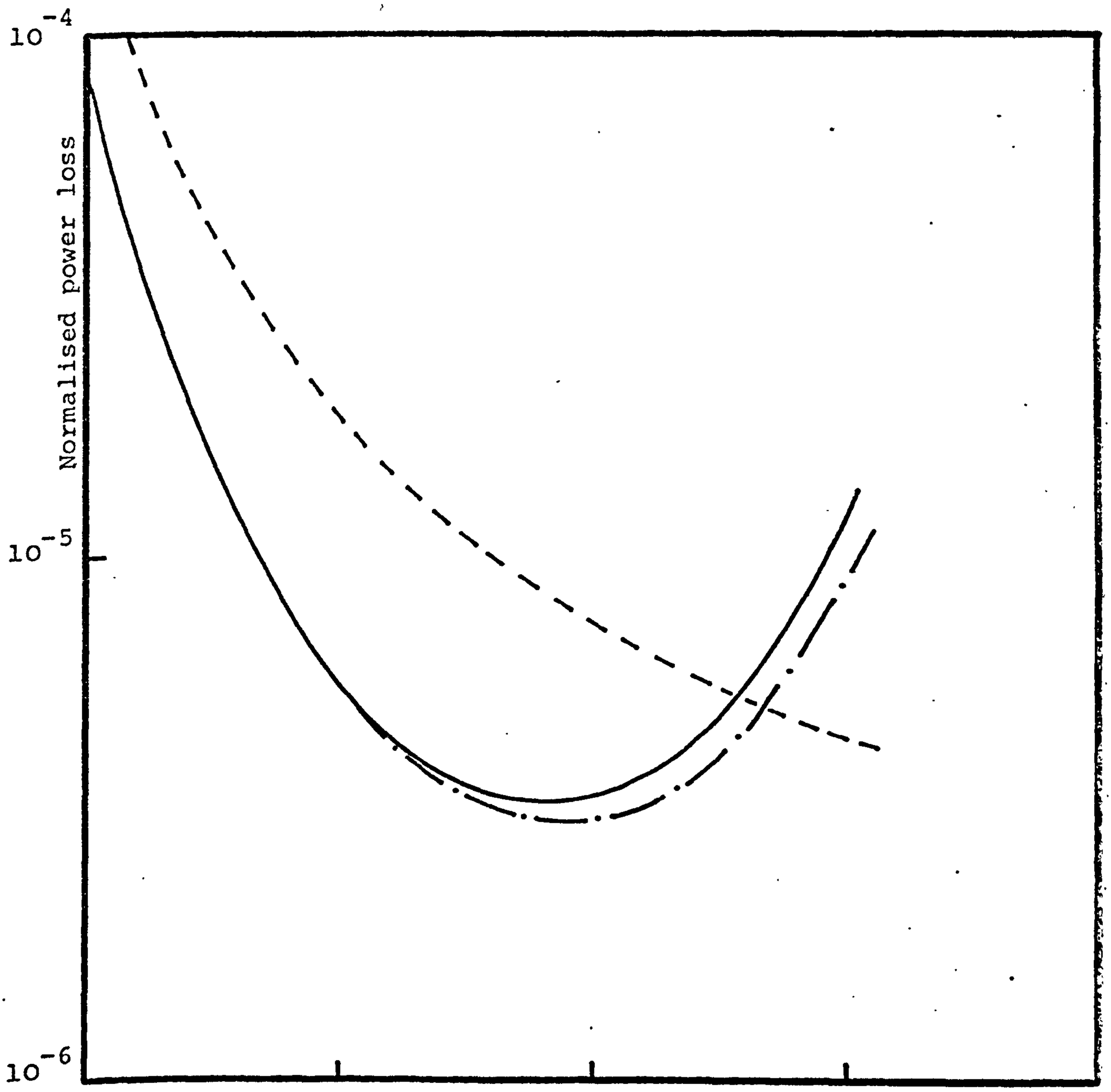

Figure (8.13) HE_{11} mode normalised power loss in rectangular corrugated waveguide

a = 4.0cm b = 6.0cm h = 0.8cm

——— P_1 -.-.-. P_2 ------ P_5

(a) The decrease, or increase in the attenuation coefficient when compared with that of an uncorrugated rectangular waveguide operating in the TE_{10} mode.

(b) The decrease, or increase, in the number of modes supported by the corrugated structure when compared with the smooth wall structure.

Both comparisons should be made at the same frequency and between structures of comparable dimensions. The two comparisons are shown in Figure (8.14) where the attenuation coefficient of the TE_{10} mode in a smooth wall rectangular waveguide is plotted as a function of the waveguide height. The operating frequency is maintained at 9.0 GHz. On the same graph is shown the attenuation coefficient of the HE_{11} mode in a corrugated waveguide possessing the same internal dimensions. The total number of propagating modes in the two types of waveguides are also given in Figure (8.14), with the assumption made that these are the TE_{lm}, TM_{lm}, HE_{lm} and EH_{lm} modes. So, by corrugating the two surfaces of a smooth wall waveguide, an advantage in attenuation is achieved and a reduction in the number of propagating modes is observed. A much greater advantage in attenuation is seen if the comparison is based on structures supporting the same number of propagating modes.

Figure (8.15) shows an alternative attenuation comparison, illustrating the frequency dependence,

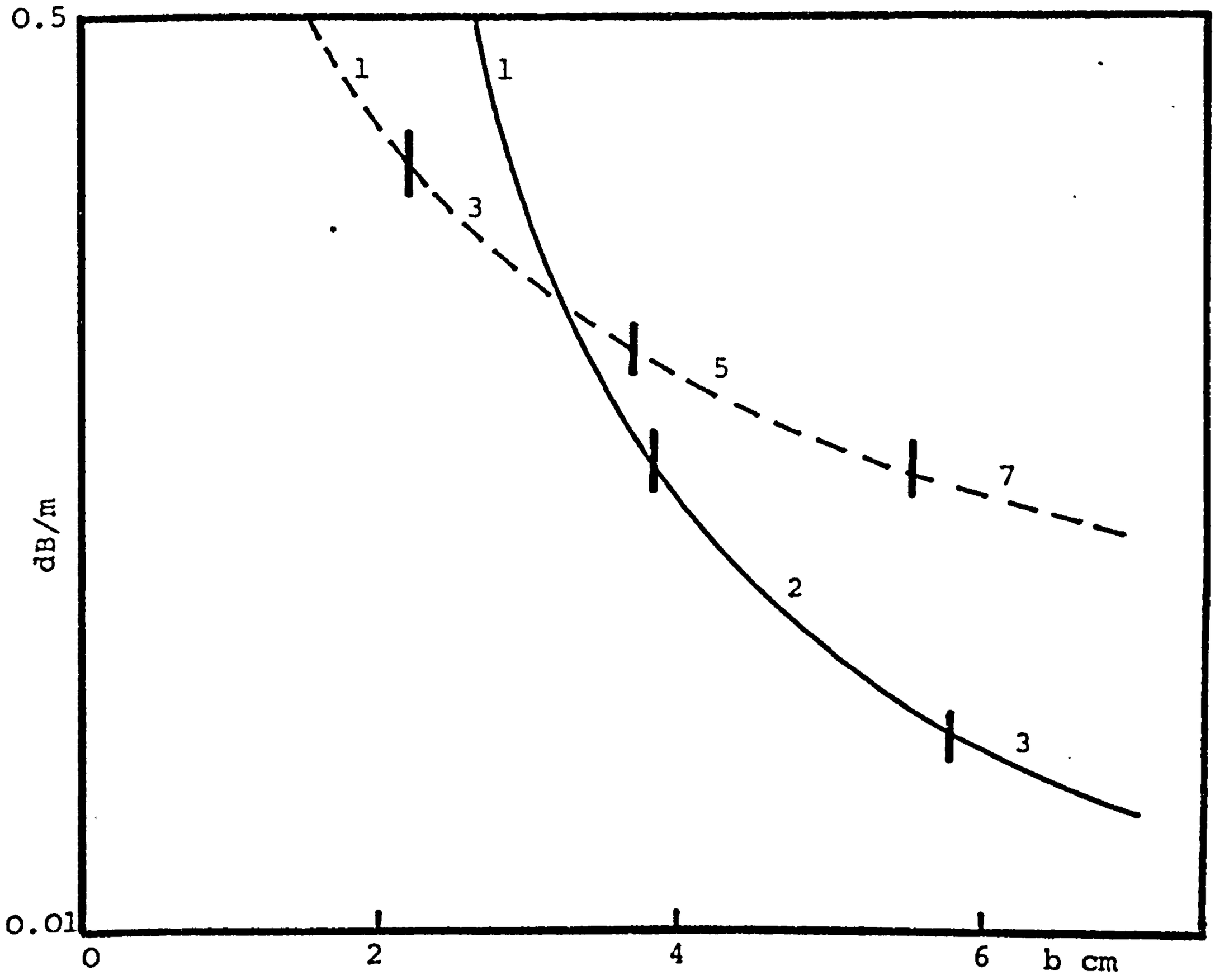

Figure (8.14) Attenuation in brass smooth and corrugated rectangular waveguide against waveguide height at 9.0 GHz

a = 4cm h = .92cm g = .15cm t = .2g

Parameter (number of propagating modes)

(It is assumed that higher order modes of TE_{mn}, TM_{mn}, HE_{mn}, EH_{mn} types for m>1 are not excited).

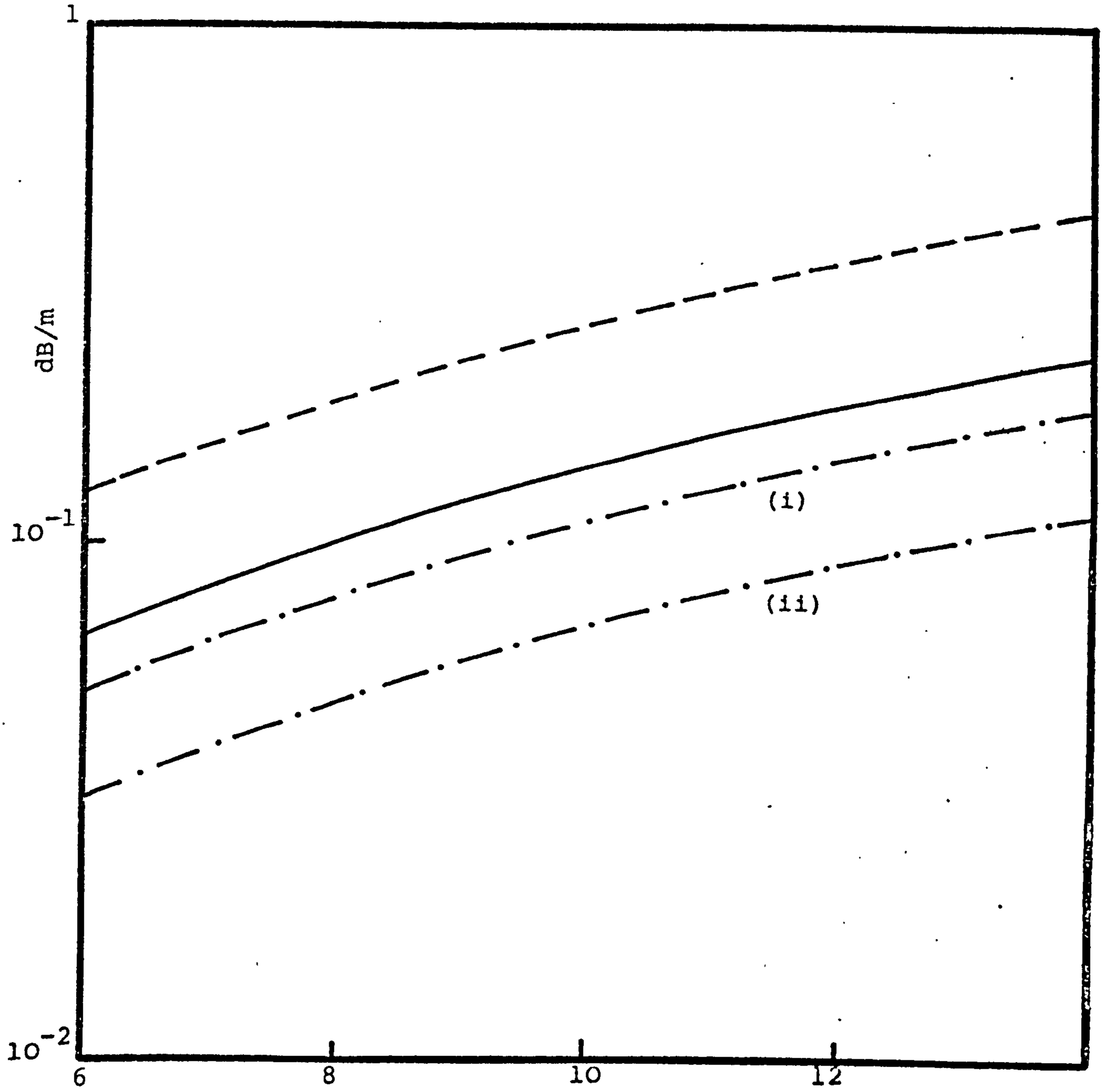

Figure (8.15) Attenuation characteristic of various waveguides
$\sigma = 1.57 \times 10^{7}$ S/m

------ TE_{10} mode in a rectangular waveguide $f = 1.35\ f_c$

——— TE_{11} mode in a circular waveguide $f = 1.35\ f_c$

-.-.-. HE_{11} mode in a corrugated rectangular waveguide

(i) single mode $a \backsim b$ (ii) overmoded $a < b$

in which single mode operation is maintained for the smooth wall rectangular, circular and the corrugated rectangular waveguide. It is observed that the rectangular corrugated waveguide offers an attenuation advantage over both most commonly used waveguides. Unfortunately, the size of the new waveguide is large and the cost of producing the waveguide might erode the attenuation advantage gained by corrugating the surfaces.

8.5.2 Corrugated Waveguides

Although the corrugated rectangular waveguide can exhibit an attenuation advantage over the smooth wall circular and rectangular waveguides, Figure (8.16) shows that the attenuation is always higher than that of a corrugated circular waveguide having the same perimeter.

In order to give a physical explanation of the lower attenuation characteristics of the circular waveguide, the power-losses at the slot base and the slot sides of the corrugated waveguide are plotted as a function of frequency in Figure (8.17). When comparing these losses with the losses obtained in a corrugated square waveguide, Figure (8.10), it is immediately recognised that the loss contribution of the uncorrugated sides P_5, causes the large degradation in the attenuation coefficient of the square waveguide. The magnitudes of the normalised electric field strength in the square, rectangular and circular corrugated waveguides are plotted in Figure (8.18) as a function of normalised

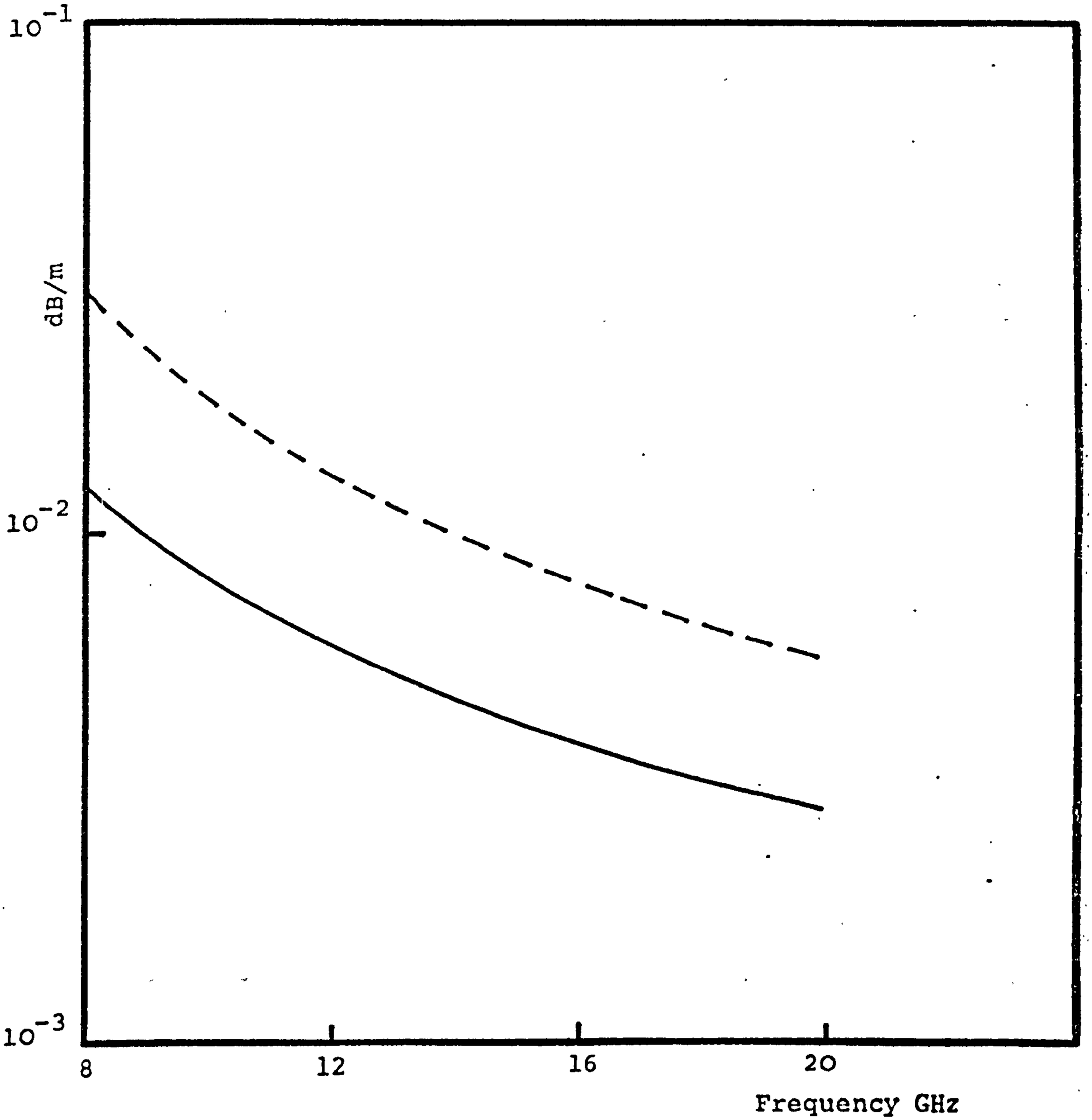

Figure (8.16) Attenuation in corrugated circular and corrugated square brass waveguides against frequency

——— HE_{11} circular $r_1 = 2.55cm$ $h = .25\lambda$
$g = 0.3\lambda$ $t = 0.1g$

------ HE_{11} square $a = 4.0cm$ $h = 0.25\lambda_s$
$g = 0.3\lambda$ $t = 0.1g$

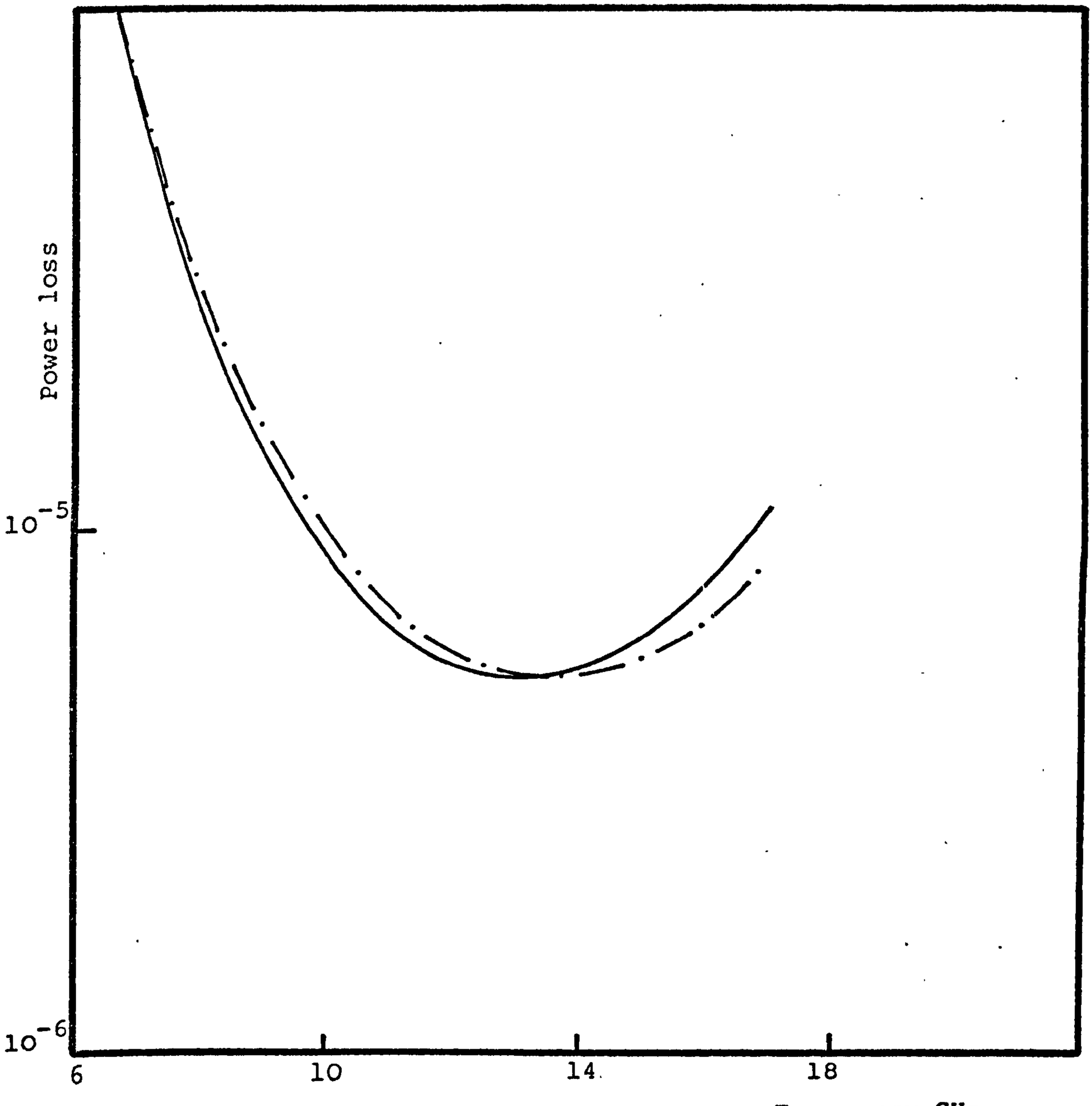

Figure (8.17) HE_{11} mode normalised power loss in a circular corrugated waveguide
r_1 = 2.25cm $r_o - r_1$ = .8cm

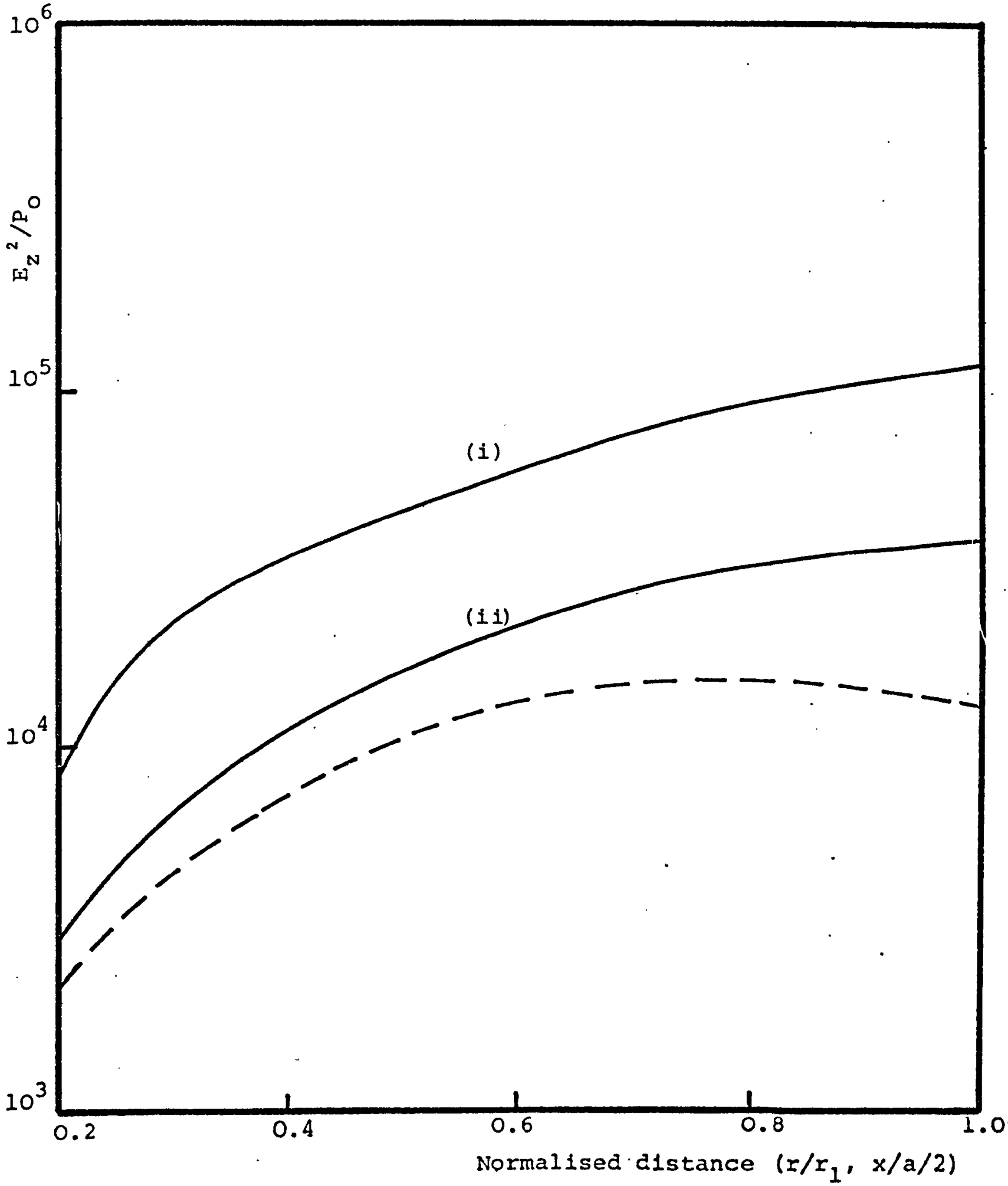

Figure (8.18) Field strength distribution in corrugated waveguides.

——— HE_{11} mode in a corrugated rectangular waveguide

(i) a = 4cm b = 4cm (ii) a = 4cm b = 6cm

------ HE_{11} mode in a corrugated circular waveguide

r = 2.25cm

waveguide dimension. The average electric field strength at the slot edge ($y=\pm b/2$, $r=r_1$) is found to vary in proportion to the slot power loss in the individual waveguides. The decrease in the field strength for the tall rectangular waveguide is clearly illustrated, and it is also observed that the field strength at the corrugation edge of the circular waveguide is the lowest.

8.5.3 Fully Corrugated Rectangular Waveguide

So far we have demonstrated the feasibility of the method described in section 8.2 in reducing the losses of a smooth wall waveguide by corrugating the two surfaces normal to the electric field and by increasing the dimensionsof the other two sides.

In order to further reduce the losses of the tall corrugated waveguide a method similar to the one described in section 8.2 must be adopted. The part played by the dimensionsof the smooth surfaces in lowering the losses of the corrugated surfaces was described in section 8.4 where it was also shown that the contribution of the smooth surfaces was very significant. Therefore modification of the remaining smooth surfaces must be made in accordance with the contributions of the axial and transverse currents. The smooth wall loss expression P_5, derived in section 8.4 shows that the ratio of axial to transverse magnetic field is of the form $\sin(K_y b)/(K_y b)$ which is always less

than 1 for $K_y b > 0$. Thus by transversely corrugating the two vertical walls a reduction in the loss component P_5 is probably expected, particularly at frequencies well below the cross-over frequency. Therefore the fully transversely corrugated tall structure is expected to provide lower losses for the same modes supported by the tall corrugated waveguide described in the previous sections.

The condition {8.1} described in section 8.2 is not satisfied for the fully transversely corrugated structure as this configuration requires $Z_1 = 0 = Z_4$, $Z_2 \neq 0$ and $Z_3 \neq 0$, thus it is not possible to obtain a modal solution in such structure. Bryant < 7 > has presented an analysis for the fully corrugated waveguide. This is in error; the author has overlooked the boundary condition corresponding to Z_2.

8.6 EXPERIMENTAL RESULTS

Due to the low values of the attenuation coefficient of the corrugated rectangular waveguide and manufacturing difficulties in construction of long sections of the waveguide, a method employing short sections of the waveguide must be adopted for measuring the predicted attenuation coefficient. One simple method is to form a resonant cavity out of a short section of the waveguide. The losses of such resonating system can easily be related to the resonant frequency of the system, thus enabling the assessment of the attenuation

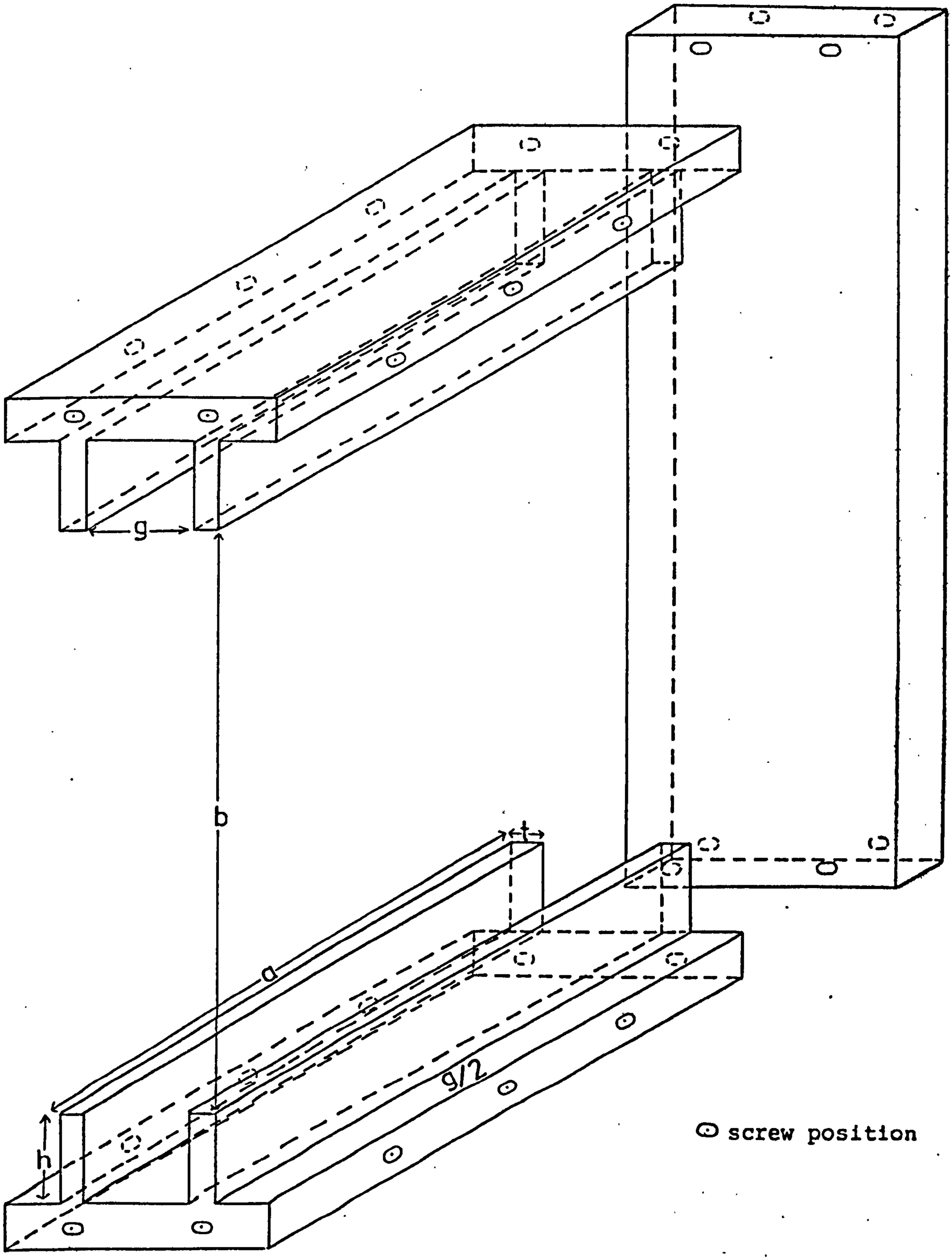

Figure (8.19) Section of the resonant cavity

a = 4 b = 6.566 h = .917 g = .8

t = .15 dimensions in cm.

coefficient of the waveguide.

A section of a waveguide, L, sandwiched between two short circuited plates, providing coupling to the waveguide's wavelength by the equality $L = m\lambda_g/2$, {8.3}, m is an integer. A measure of the strength of the resonance is given by the 'Q' = $f_o/\Delta f$, f_o being the resonant frequency specified by eqn. {8.3} and Δf is the difference between the two frequencies where the power output has fallen to half its peak value, Δf is solely determined by the losses in the cavity, and consists of two parts $\Delta_1 f$ and $\Delta_2 f$. The former is due to wall losses and is given by $\alpha = \frac{\pi \Delta_1 f}{v_g}$, v_g = group velocity, while the latter is due to the coupling holes and the losses on the end plates, which is inversely proportional to the length of the cavity <23>. Thus,

$$\Delta f = \Delta_1 f + \Delta_2 f$$

The attenuation coefficient (αx8.686)dB/m is readily obtained from a plot of Δf against 1/L.

A multi-section cavity was designed to be resonant at a frequency of 9 GHz, a section of which is shown in Figure (8.19). The edges of each section were then painted with silver paint, ensuring good electrical contact, and added to previous sections placed in the circuit shown in Figure (8.20). The resonant frequency was located by using a swept frequency source. A stable

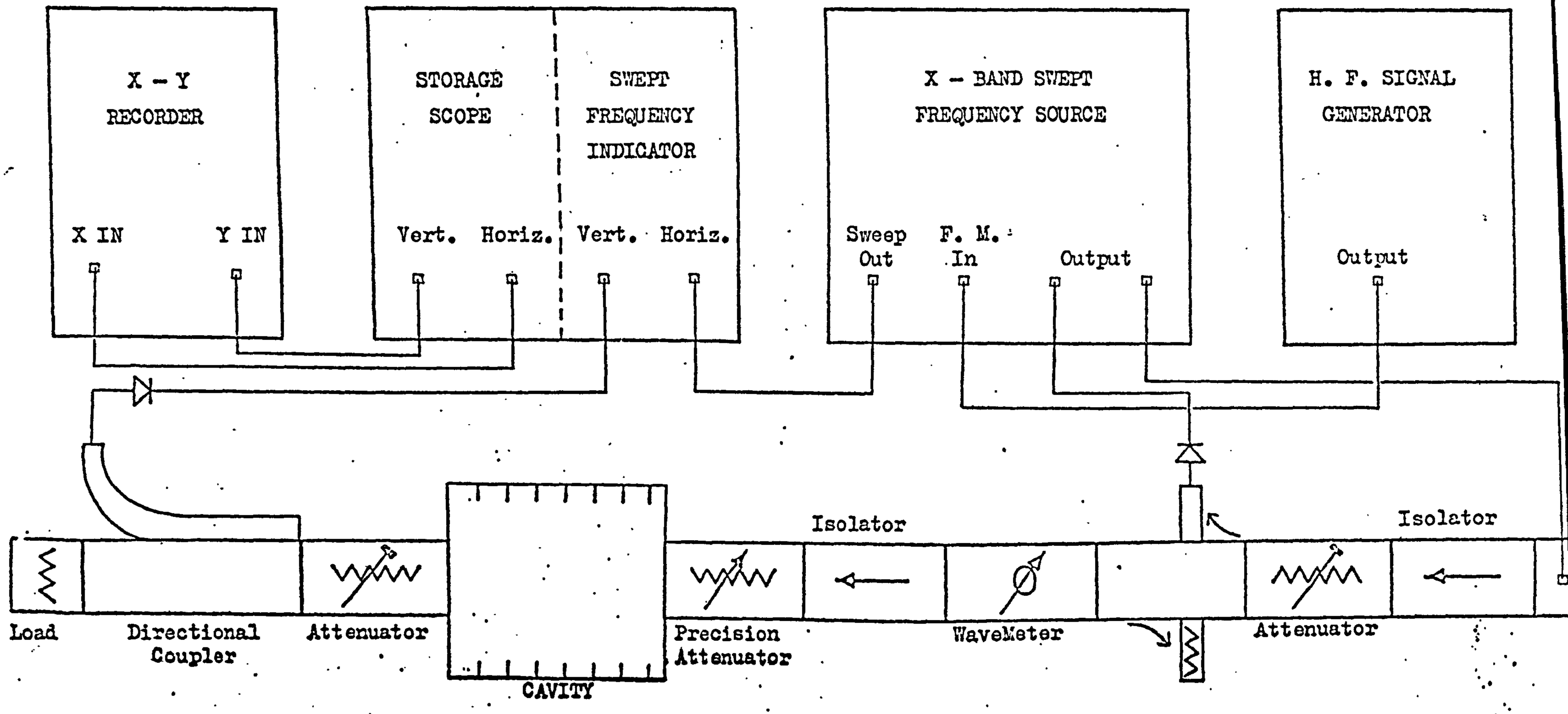

Figure (8.20) Arrangement for measuring resonant cavity properties by swept frequency techniques

H.F. signal generator, producing a frequency f_1 was introduced to frequency modulate the backward wave oscillator of the swept frequency source. The swept frequency source was then generating three frequencies at any given time, f_o, f_o-f_1, f_o+f_1. The sidebands could be used to calibrate the frequency scale. The half power points are found by inserting 3 dB attenuation in the circuit. These points for cavities of different lengths are plotted against the inverse of the length in Figure (8.21) and the ordinate interception was found using a least-squares fit using first order orthogonal polynomials.

A very good agreement was obtained between the designed resonant frequency and the observed resonant frequency, thus confirming the calculated guide wavelength. The predicted attenuation coefficient using the analysis presented in the previous sections was found to be 1.601×10^{-2} dB/m. The calculated coefficient using the experimental results was found to be 1.8×10^{-2} dB/m.

The experimental error introduced by the swept frequency technique is of the order of 5% <23 >. The percentage difference between measured and theoretical results is nearly 12%. A nominal value for the conductivity was used in the calculations, this value is slightly higher than the value obtained from measurements of conductivity. The correct value of the conductivity will thus increase the surface resistivity of the material bringing the theoretical attenuation value closer to the experimental value.

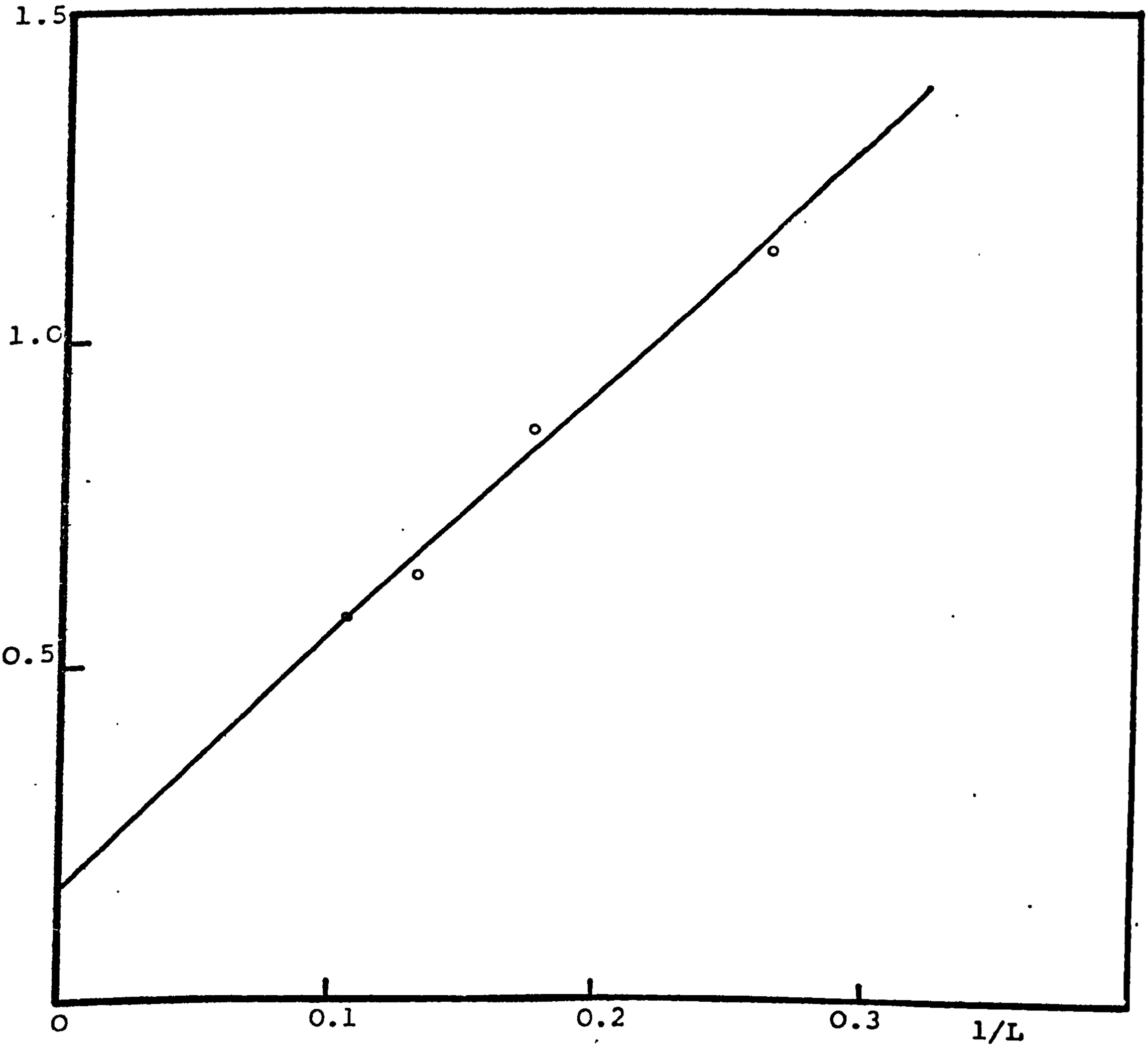

Figure (8.21) Half power bandwidth against reciprocal of cavity length

Resonance at 9.0 GHz

O Experimental point

CHAPTER NINE

CONCLUSIONS

9.1 SUMMARY OF MAIN CONTRIBUTIONS

In preceding chapters a variety of cylindrical structures guiding electromagnetic energy have been investigated. The main concern of the study was to describe the effects of the shape and the nature of the boundary on the propagation characteristics of the guided waves, leading to favourable attenuation characteristics.

The main contributions of the individual chapters (identified by number) are given below:-

2. Smooth Wall Elliptical Waveguides;

(i) Basic correction to the classic attenuation results obtained by Chu <14>.

(ii) Correction to the surface impedance formulae derived by Falciasecca, et al <15>.

(iii) Formulation of the surface curvature-dependent effect on the attenuation and surface impedance in waveguides.

(iv) Identification of a family of Mathieu functions, different from the established ones, which appear to have been almost overlooked in the literature.

The last contribution stems from a discussion on Mathieu functions related to the elliptical waveguide problem and it appears in Appendix III.

3. Corrugated Elliptical Waveguides;

(i) Formulation and solutions of the characteristic equation.

(ii) Mode classifications and attenuation results.

4. Influence of Slot Shape on the Performance of a Corrugated Circular Waveguide;

(i) The principal effect of non-rectangular corrugations is on the slot depth required to produce the open-circuit condition in the surface-impedance-model.

(ii) The attenuation and radiation characteristic of the corrugated waveguide with non rectangular slots.

5. A New Mode Filter for use in Corrugated Circular Waveguides;

(i) The monomode optical waveguide features are applied successfully in the design of a mode filter for use in overmoded corrugated circular waveguides.

(ii) Elimination of the undesired modes is illustrated.

6. Dielectric-Lined Circular Waveguides;

(i) An explanation is given for the low-attenuation characteristics of a hybrid mode in a dielectric-lined circular waveguide. This contribution preceded a similar study undertaken at Bell Laboratories.

7. Concentric Dielectric Waveguides;

(i) Appropriately designed concentric dielectric waveguides can have favourable attenuation, group-delay and excitation characteristics, and therefore can find future applications for millimetre-wavelength microwave transmission.

8. Corrugated Rectangular Waveguides;

(i) An error in earlier predictions of the attenuation coefficient is corrected.

(ii) The region is identified in which the corrugated waveguide exhibits an attenuation advantage over comparable smooth wall waveguides.

Except for some of the results of chapter two, most of the theoretical results have required substantial computer program development. The results given here should prove useful in the early stage of the waveguide design.

The attenuation results compared here and elsewhere <9>, <10>, with those obtained in smooth wall waveguides, clearly illustrate the need for the presence of a hybrid mode in the waveguide in order to achieve the low attenuation characteristics. The nature of the boundary created to produce the hybrid mode is, unfortunately, always frequency dependent. Thus, in metal waveguides, the low-attenuation phenomenon occurs over a relatively narrow, but useful, frequency band.

The low-attenuation property of the hybrid mode can be made use of either in the centimetre or the millimetre-wavelength regime. Corrugated, circular, elliptical and rectangular waveguides can offer an attenuation advantage in the former range, while in the millimetre range the use of the dielectric-lined waveguide has been envisaged by workers at the Bell System Laboratories <69> and the use of the concentric dielectric waveguide also by researchers at the British Post Office <64>.

9.2 SUGGESTIONS FOR FURTHER WORK

Although the existence of a low-attenuation hybrid mode in corrugated and lined waveguides has been illustrated, structures with different boundaries might provide an even lower attenuation coefficient or prove more economic to manufacture. Clarricoats <70> has proposed a hybrid mode waveguide comprising dielectric washers spaced periodically along a metal cylindrical waveguide, while Barlow < 71 > is investigating the propagation of dipole-modes in a circular grid of longitudinal lossy conductors insulated from each other. More recently Clarricoats <72> has proposed a modified version of the corrugated circular waveguide in which the metal boundary at $r = r_o$, Figure (4.1) is being replaced by four longitudinal metal strips at 90^o angles. The advantages offered by this structure is the lowering in weight and comparative ease of manufacture. While a

general mathematical formulation of the attenuation coefficient in smooth wall waveguides is possible <73>, the formulation, for obvious reasons, cannot be extended for the hybrid modes in an anisotropic wall waveguide. The only physical criterion that can be searched for in order to achieve low-losses, is the influence of the new boundaries on the field strength near the new metal surfaces. Moreover, the new metal boundaries must be shaped such that only sufficient metal surface-area is present to provide a current path, thus removing any unnecessary metal loss.

Apart from the general research into an optimum waveguide boundary, directions for further work, on the individual structures studied in this thesis are described below:-

With regard to the anomolous property of the Mathieu functions, further mathematical work should prove generally useful. Experimental work to determine the accuracy of the attenuation formula derived in chapter two are required and will demonstrate the curvature-dependent effect.

A more exact formulation of the attenuation coefficient of the corrugated elliptical waveguide is very important before any experimental work can be carried out. Elliptical corrugated horns employed in microwave antennas have not been analysed on a rigorous basis. The theory developed by Jansen and Jeuken <74>

to describe their radiation characteristics is only applicable under very special conditions. The analysis presented in chapter three can be extended to predict the radiation characteristics of elliptical corrugated horns.

Resonant cavity techniques can be employed to measure the attenuation coefficient of the dominant mode in the concentric dielectric waveguide. The effect of the lossy layer on the higher order modes can also be illustrated in a manner similar to that described during the mode filter experiments.

Large scale production of corrugated waveguides has been impeded by manufacturing difficulties. However, the results presented in chapter eight could be utilised in the manufacture of low-loss flexible rectangular waveguides. Finally, the low-loss rectangular corrugated waveguide could be employed in the manufacture of waveguide components for use in the millimeter range.

APPENDICES

APPENDIX I

Field Equations in General System of Co-ordinate (ϕ_1, ϕ_2, Z)

$$E_{\phi_1} = -j \frac{\beta}{\ell_1 K^2} \frac{\partial E_z}{\partial \phi_1} - j \frac{\omega\mu}{\ell_2 K^2} \frac{\partial H_z}{\partial \phi_2}$$

$$E_{\phi_2} = -j \frac{\beta}{\ell_2 K^2} \frac{\partial E_z}{\partial \phi_2} + j \frac{\omega\mu}{\ell_1 K^2} \frac{\partial H_z}{\partial \phi_1}$$

{1}

$$H_{\phi_1} = j \frac{\omega\varepsilon}{\ell_2 K^2} \frac{\partial E_z}{\partial \phi_2} - j \frac{\beta}{\ell_1 K^2} \frac{\partial H_z}{\partial \phi_1}$$

$$H_{\phi_2} = -j \frac{\omega\varepsilon}{\ell_1 K^2} \frac{\partial E_z}{\partial \phi_1} - j \frac{\beta}{\ell_2 K^2} \frac{\partial H_z}{\partial \phi_2}$$

Co-ordinate System	ϕ_1	ϕ_2	ℓ_1	ℓ_2
Cartesian	x	y	1	1
Polar	r	θ	1	r
Elliptical	ξ	η	$h(\cosh^2\xi - \cos^2\eta)^{\frac{1}{2}}$	$h(\cosh^2\xi - \cos^2\eta)^{\frac{1}{2}}$

where

$$\frac{\partial}{\partial z} = -j\beta, \quad K^2 = k^2 - \beta^2, \quad k = 2\pi/\lambda$$

$$h = a.e$$

a = Semi-major ellipse axis

e = Ellipse eccentricity

λ = Free space wavelength

APPENDIX II

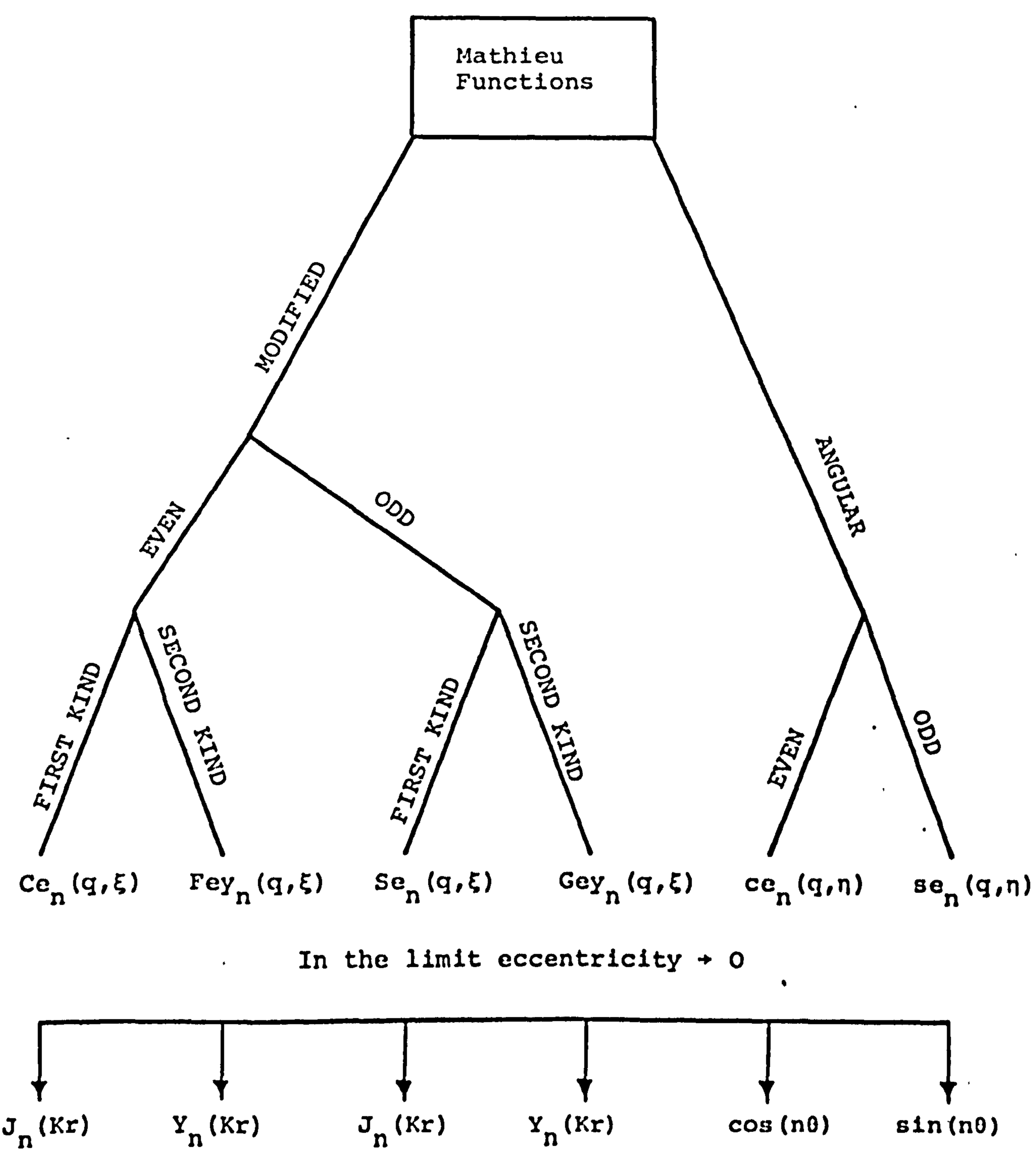
Mathieu Functions
MODIFIED
ANGULAR
EVEN
ODD
EVEN
ODD
FIRST KIND
SECOND KIND
FIRST KIND
SECOND KIND
EVEN
ODD
$Ce_n(q,\xi)$
$Fey_n(q,\xi)$
$Se_n(q,\xi)$
$Gey_n(q,\xi)$
$ce_n(q,\eta)$
$se_n(q,\eta)$
In the limit eccentricity → 0
$J_n(Kr)$
$Y_n(Kr)$
$J_n(Kr)$
$Y_n(Kr)$
$\cos(n\theta)$
$\sin(n\theta)$

II.1 Angular Mathieu Functions

$$ce_{2n}(q,\eta) = \sum_{r=0}^{\infty} A_{2r}^{(2n)} \cos 2r\eta$$

$$ce_{2n+1}(q,\eta) = \sum_{r=0}^{\infty} A_{2r+1}^{(2n+1)} \cos(2r+1)\eta$$

$$se_{2n+1}(q,\eta) = \sum_{r=0}^{\infty} B_{2r+1}^{(2n+1)} \sin(2r+1)\eta$$

$$se_{2n+2}(q,\eta) = \sum_{r=0}^{\infty} B_{2r+2}^{(2n+2)} \sin(2r+2)\eta$$

II.2 Modified Mathieu Functions

$$Ce_{2n}(q,\xi) = \frac{ce_{2n}(q,0)}{A_0^{(2n)}} \sum_{r=0}^{\infty} A_{2r}^{(2n)} J_{2r}(2k\sinh\xi)$$

$$Fey_{2n}(q,\xi) = \frac{ce_{2n}(q,0)}{A_0^{(2n)}} \sum_{r=0}^{\infty} A_{2r}^{(2n)} Y_{2r}(2k\sinh\xi)$$

$$Se_{2n+2}(q,\xi) = \frac{se'_{2n+2}(q,0)}{k^2 B_2^{(2n+2)}} \coth\xi \sum_{r=0}^{\infty} (2r+2) B_{2r}^{(2n+2)} J_{2r+2}(2k\sinh\xi)$$

$$Gey_{2n+2}(q,\xi) = \frac{se'_{2n+2}(q,0)}{k^2 B_2^{(2n+2)}} \coth\xi \sum_{r=0}^{\infty} (2r+2) B_{2r+2}^{(2n+2)} Y_{2r+2}(2k\sinh\xi)$$

where A and B are functions of q and $k^2 = q > 0$.

II.3 Orthogonality of the Angular Mathieu Functions

$$\int_0^{2\pi} ce_{2n}^2(q,\eta)\,d\eta = 2\pi\left[A_0^{(2n)}\right]^2 + \pi \sum_{r=1}^{\infty}\left[A_{2r}^{(2n)}\right]^2$$

$$\int_0^{2\pi} ce_{2n+1}^2(q,\eta)\,d\eta = \pi \sum_{r=0}^{\infty}\left[A_{2r+1}^{(2n+1)}\right]^2$$

$$\int_0^{2\pi} se_{2n+1}^2(q,\eta)\,d\eta = \pi \sum_{r=0}^{\infty}\left[B_{2r+1}^{(2n+1)}\right]^2$$

$$\int_0^{2\pi} se_{2n+2}^2(q,\eta)\,d\eta = \pi \sum_{r=0}^{\infty}\left[B_{2r+2}^{(2n+2)}\right]^2$$

$$\int_0^{2\pi} ce_\nu(q,\eta)\,ce_\mu(q,\eta)\,d\eta = \int_0^{2\pi} se_\nu(q,\eta)\,se_\mu(q,\eta)\,d\eta$$

$$= \int_0^{2\pi} ce_\nu(q,\eta)\,se_\mu(q,\eta)\,d\eta = 0$$

for $\nu \neq \mu$ in the first two integral

APPENDIX III

MATHIEU FUNCTION FORMULA

III.1 Asymptotic Expansion for Large q

Asymptotic expressions of the modified Mathieu function for large q exist <16>, and are referred to as Goldstein's expansion <13>. They have an exponent dominated by $-2jq^{\frac{1}{2}}$ sinh z and are the form used and needed in chapter 2. We give here a brief derivation, and draw attention to a peculiar anomoly in the determination of the characteristic values associated with these functions. It should be mentioned that in <13> the expansion is given for real q > 0 whereas we need q complex and nearly imaginary. McLachlan <16> in his section 3.43 takes q pure imaginary, and uses the corresponding Goldstein equation to derive the characteristic number. It is here that the anomolous features make their appearance, as discussed more fully, in the next section.

The equation to be solved is

$$\frac{\partial^2 V}{\partial \xi^2} + \frac{\partial^2 V}{\partial \eta^2} + k^2h^2(\cosh^2\xi - \cos^2\eta) = 0 \qquad \{1\}$$

Putting V = XY and decomposing in the usual way gives

$$\frac{d^2 Y}{\partial \eta^2} + k^2h^2Y(\beta - \cos^2\eta) = 0 \qquad \{2\}$$

$$\frac{d^2 X}{d\xi^2} + k^2h^2X(\cosh^2\xi - \beta) = 0 \qquad \{3\}$$

where β is a separation constant. The standard form comes by putting $k^2h^2 = 4q$ and $\beta = \frac{1}{2} + a/k^2h^2$, where $\underline{a}$ is known as the characteristic number. (Confusion with the use of $\underline{a}$ for the ellipse semi-major axis should not arise). It is determined by the requirement that physical solutions of {2} be periodic with period π or 2π, and it is a function of q and of n, the order of the function. For n even, $\underline{a}$ is treated as an even function of q; that is, the series expansion of $\underline{a}$ as a function of q, convergent for small q, has q occurring only in even powers. However, we are here concerned with asymptotic expansions for large q and the way in which q enters the formula has to be watched carefully. In the case of a non-conducting wall material q is pure real and positive. As σ increases q moves directly into the fourth quadrant, approaching the negative imaginary axis. Hence, for physical wall materials we are interested in that solution which, in the non-conducting case, gives q real and positive. For this case it is known that the established Mathieu function solutions have

$$a \sim -2q + 2(2n+1)q^{\frac{1}{2}} + - - - \quad \text{as } q \to \infty \qquad \{4\}$$

so that $\beta \to 0$ for large q, since $\beta = \frac{1}{2} + a/4q$.

We are here interested only to demonstrate the dominant part of the exponents for X and Y, and to this end we write $Y = e^y$ and $X = e^x$. The equations for y and x are then

$$y'' + y'^2 = 4q(\cos^2\eta - \beta) \qquad \{5\}$$

$$x'' + x'^2 = -4q(\cosh^2\xi - \beta) \qquad \{6\}$$

If we assume, as in <16> section 11.43 the existence of solutions in descending powers of $q^{\frac{1}{2}}$ (this is the Horn-Jefferys technique <31>), then the first-order solution of {5} gives $y' \sim 2q^{\frac{1}{2}}y_o'$ where

$$y_o'^2 = (\cos^2\eta - \beta) \qquad \{7\}$$

This equation has <u>two</u> values of β which apparently could lead to periodic solutions, namely 0 and 1. Since we know that $\beta \to 0$ for large q to give the established solution, it is this value that we discuss here. An examination of the consequences of choosing the other value is postponed to the next section.

The solutions of {7} are accordingly $y_o' = \pm\cos\eta$ leading to $y = \mp 2q^{\frac{1}{2}} \sin\eta$ as the (known) dominating part of the exponent for the relvant Mathieu functions. With $\beta = 0$, {6} similarly gives $x = \pm j2q^{\frac{1}{2}} \sinh\xi$, leading to the dominant term in the exponents for $Mc_m^{(3)}$ and $Mc_m^{(4)}$, as used in chapter 2. It remains to discuss the validity of the equation for the characteristic numbers particularly for q complex.

III.2 The Characteristic Numbers

Remembering that <u>a</u> (for n even) is considered an even function of q, the asymptotic form for <u>a</u> in {4}

is usually written a ~ $-2|q| + 2(2n+1)|q|^{\frac{1}{2}}$ + --- as $\pm q \to \infty$. This use of $|q|$ is merely a device to select the positive value of q, and is not meant to imply the modulus when q is complex. The important question is: what form should the equation take for complex q? There is nothing in the analysis of the previous section which seems to demand that q be real and positive, other than that which led to the choice of $\beta = 0$ rather than $\beta = 1$. What, then, is wrong with the latter choice? It would correspond to a ~ + 2q as $|q| \to \infty$, and for q negative this is the 'correct'form. But for this relation with q positive an analysis of the number of zeroes of the function (<16> section 12.30), would indicate a number increasing with q in a finite interval, and therefore not agreeing with the established properties of the Mathieu function that the number of such zeroes be independent of q. Either this choice for a is then unacceptable, or it indicates a family of Mathieu functions, different from the established ones, which appears to have been almost overlooked in the literature. We say "almost" because no less an authority than Arscott <35> writes "There are apparently two values of α for which ϕ can have period 2π, namely (i) $\alpha = -2$, $\phi = 2\sin z$ and (ii) $\alpha = 2$, $\phi = 2i\cos z$ ---" (Arscott's is -2 + four times our β, i.e. the coefficient of q in {4}; and his z is our η). But he then goes on to say that the substitutions $q \to -q$, $z \to \pi/2 - z$ transform this second solution into the first so that there is really only the

known, established solution. This conclusion appears as if it may be in error. For if the relationship of $\underline{a}$ to q considered is asymptotically a ~ + 2q (q positive), and q is replaced by -q, then if $\underline{a}$ is even in q, the relationship becomes a = -2 (q negative), and this is not the usual solution. Alternatively, if we retain α = +2, then the relationship is a = + 2q (q negative) and $\underline{a}$ is not then an even function of q. As mentioned earlier, $\underline{a}$ is usually taken as an even function, but this cannot be assumed if it is this feature which is itself under discussion. Of course, the series expansion for $\underline{a}$ does require this, but this expansion is only convergent for $a \leq s_o = 1.4688 \ldots$ and says nothing about the behaviour for large |q|. There exists a continued fraction expansion valid for all q, but since its generation is based on the series solution method it does not necessarily exclude another type of solution. It is as if the expression for $\underline{a}$ involved some such form as $(q^2 + s_o^2)^{\frac{1}{2}}$. This is clearly an even function of q for $q < s_o$, as is seen by the Taylor expansion, but for larger values of q we encounter a branch cut and the value for large q could be $\pm q$ depending on which side of the cut we are. The behaviour for small q does not tell us anything about it.

In the present problem it may seem as if this whole matter could be avoided by simply noting that for a lossless material we are starting out from q real and positive, and therefore we need that solution for which a ~ -2q (or = 0), leaving a discussion of the possible

existence of other types of solution for another occasion. This has been the intention of this Appendix. However, the matter cannot be completely ignored, because the substitutions $q \rightarrow -q$, $\eta \rightarrow \pi/2 - \eta$ leaving Mathieu's equation formally unaltered though it alters the form of solution of {5} and {6} unless we <u>also</u> allow the change $\alpha \rightarrow -\alpha(\beta=0 \text{ to } 1)$; and this is <u>not</u> accomplished if the form $a \sim -2q$ is retained under this substitution. Arscott's comments <35> imply that a change (corresponding to his α going from +2 to -2) <u>is</u> made in his example (corresponding to <u>a</u> even in q), but he seems unaware that he is not then dealing with the standard solution. All this arises because we need to know whether we can use $a \sim -2q$ for q complex, and this forces a consideration of the possible additional solutions stemming from $a \sim +2q$. For the radial functions the two forms lead to different results, since $q \rightarrow -q$, $\xi \rightarrow -j\pi/2 + \xi$, which leaves Mathieu's equation formally unaltered, interchanges $\sinh\xi$ and $-j\cosh\xi$ in the exponent for X. Clearly the latter form is not suitable, since the exponent would then change from $-j2|q^{\frac{1}{2}}|\sinh\xi$ to $-2|q^{\frac{1}{2}}|\cosh\xi$ which represents, for real positive q a damped, not a propagating, wave. But for q pure imaginary, and with $q^{\frac{1}{2}}$ used instead $|q^{\frac{1}{2}}|$ the substitution merely interchanges $\sinh\xi$ and $\cosh\xi$ unless α is also changed. Either form $a \sim \pm 2q$ therefore seems to give rise to a possible solution but they are different, and only one corresponds to the established form of Mathieu function suitable for

use in the analysis of the elliptical waveguide. Which is it? It is suggested that {4} is the basic equation to use, starting out from positive real q, and usable into the fourth quadrant only, as q becomes complex with negative imaginary part. This leads to {6} with $\beta = 0$, and to the results of chapter 2, with the physically acceptable limit for Z_a' and Z_t' as $a/b \to \infty$ for a flattened ellipse. But it has to be admitted that the properties of the Mathieu functions in this domain are not straightforward, and do require a very careful determination if erroneous results are to be avoided.

REFERENCES

< 1 > CLARRICOATS, P.J.B. and SAHA, P.K. : 'Attenuation in corrugated circular waveguide', Electron. Lett., 1970, 6, pp.370-372.

< 2 > CLARRICOATS, P.J.B. and OLVER, A.D. : 'Low attenuation in corrugated circular waveguides', ibid., 1973, 9, pp.376-377.

< 3 > OLVER, A.D., CLARRICOATS, P.J.B. and CHONG, S.L. : 'Experimental determination of attenuation in corrugated circular waveguides', ibid., 1973, 9, pp.424-426.

< 4 > CHONG, S.L. : 'Corrugated waveguides for telecommunication', Ph.D. Thesis, Queen Mary College, University of London, November 1974 (To be submitted).

< 5 > CARLIN, J.W. and D'AGOSTINO, P. : 'Low-loss modes in dielectric lined waveguide', Bell Syst. Tech. Journ., 1971, 50, pp.1631-1638.

< 6 > CARLIN, J.W. : 'A relation for the loss characteristics of circular electric and magnetic modes in dielectric lined waveguide', ibid., 1971, 50, pp.1637-1644.

< 7 > BRYANT, G.H., : 'Propagation in corrugated waveguides', Proc. IEE, 1969, 116, (2), pp.203-213.

< 8 > BRYANT, G.H. : Correspondence and reply by , Proc. IEE, 117, No.5, May 1970, pp.931-932.

< 9 > BALDWIN, R. and McINNES, P.A. : 'Attenuation in corrugated rectangular waveguide', Electron. Lett., 1971, 7, pp.770-772.

<10> BALDWIN, R. : 'A study of rectangular corrugated horns for use as microwave feeds', Ph.D. Thesis, University of Sheffield, June, 1971.

<11> AL-HARIRI, A.M.B. : 'Rectangular corrugated waveguide', Queen Mary College Technical Report AAH/74/2.

<12> DYBDAL, R.B., PETERS, L. and PEAKE, W.H. : 'Rectangular waveguides with impedance walls', IEEE, Trans. Microwave Theory & Technique, Vol. MTT-19, pp.2-9, January 1971.

<13> ABRAMOWITZ, M. and SEGUN, I.A., Ed. : Handbook of Mathematical Functions, New York:Dover, 1968, 5th ed.

<14> CHU, L.J. : 'Electromagnetic waves in elliptic hollow pipes of metal', J. Appl. Phys., Vol.9, pp.583-591, September 1938.

<15> FALCIASECCA, G., SOMEDA, C.G. and VALDONI, F. : 'Wall impedances and application to long-distance waveguides', Alta Freq., Vol.40, pp.426-434, May 1971.

<16> McLACHLAN, N.W. : 'Theory and Application of Mathieu Functions', Oxford, England, Clarendon, 1947.

<17> KRETZSCHMAR, J.G. : 'Attenuation characteristics of hollow conducting elliptical waveguide', IEEE Trans. Microwave Theory & Tech., Vol. MTT-20, pp.280-284, April 1972.

<18> UNGER, H.G. : 'Circular electric wave transmission in a dielectric-coated waveguide', Bell Syst. Tech. Journ., 1957, 36, pp.1253-1278.

<19> CLARRICOATS, P.J.B. and CHAN, K.B. : 'Electro-magnetic-wave propagation along radially inhomogeneous dielectric cylinder', Electron. Lett., 1970, 6, p.695.

<20> BRAYER, M. : 'Principal results obtained by a program of calculations on guided waves within the band 30-150 GHz', in 'Trunk telecommunication by guided waves', IEE Conf. Publ. 1970, pp.45-50.

<21> CHAN, K.B. : 'Electromagnetic wave propagation in optical waveguides', Ph.D. Thesis, Queen Mary College, University of London, March 1972.

<22> BUCKINGHAM, K.A. and REDDISH, W. : 'Low-loss polypropylene for electrical purposes', Proc. IEE, 114, No.11, November 1967, pp.1810-1814.

<23> OLVER, A.D. : 'Low attenuation waveguides- measurement of properties by resonant cavity techniques', Queen Mary College Technical Report ADO/73.1, January 1973.

<24> RAMO, S., WHINNERY, J.R. and VAN DUZER, T. : 'Fields and Waves in Communication Electronics'. Jhon Wiley, 1965.

<25> BLANCH, G. : 'On the computation of Mathieu functions', J. Math. Phys., 25, pp.1-20, 1946.

<26> AL-HARIRI, A.M.B. : Private Communication with C.M. KNOP, Andrew Corporation, Chicago, August 1973.

<27> INCE, E.L. : 'A proof of the impossibility of the coexistence of two Mathieu functions', Cambridge Phil. Soc. Proc. 21, 117, 1922.

<28> LEWIN, L. : 'Advanced Theory of Waveguides', Iliffe, 1951.

<29> COLLIN, R.E. : 'Field Theory of Guided Waves', McGraw-Hill, New York, 1960.

<30> LEWIN, L. and AL-HARIRI, A.M.B. : 'The effect of cross-section curvature on attenuation in elliptic waveguides and a basic correction to previous formulas', IEEE Trans. Microwave Theory & Tech., Vol. MTT-20, pp.504-509, May 1974.

<31> LEWIN, L. : 'Propagation in curved and twisted waveguide of rectangular cross-section', Proc. Inst. Elec. Eng., Vol.102, Pt.B, pp.75-80, January 1955.

<32> KRANK, W. : 'Uber die theorie und technick des elliptischen wellrohrhlleiters', Internal Report Telefunken, Germany.

<33> SAHA, P.K. : 'Propagation and radiation characteristics of corrugated waveguides', Ph.D. Thesis, University of Leeds, March 1970.

<34> CLARRICOATS, P.J.B. and SAHA, P.K. : 'Propagation and radiation behaviour of corrugated feeds, Part I', Proc. IEE, Vol.118, No.9, September 1971.

<35> ARSCOTT, F.M. : 'Periodic Differential Equations', London, England, Pergamon, 1964.

<36> YEH, C.W.H. : 'Electromagnetic surface-wave propagation along a dielectric cylinder of elliptical cross section', California Institute of Technology, Antenna Laboratory Technical Report No.27, January 1962.

<37> KIRCHHOFF, H. : 'Optical wave propagation in self-focusing fibres', IEE Conf. Publ. 71, 1970, pp.69-70.

<38> CLARRICOATS, P.J.B., AL-HARIRI, A.M.B., OLVER, A.D., and CHAN, K.B. : 'Low-attenuation characteristics of dielectric-lined waveguide', Electron. Lett., 1972, 8, pp.407-409.

<39> TAKEICHI, Y., HASHIMOTO, T. and TAKEDA, F. : 'The ring-loaded corrugated waveguide', IEEE Trans. Microwave Theory & Tech., Vol. MTT-19, pp.947-950, December 1971.

<40> GHOSE, R.N. : 'Microwave Circuit Theory and Analysis', McGraw-Hill, New York, 1963.

<41> RAGAN, G.L., Ed. : 'Microwave Transmission Circuits', MIT, Radiation Laboratory Series, 1948.

<42> CHANTRY, G.W., FLEMING, J.W. and PARDOR, G.W.F. (National Physical Laboratories) and REDDISH, W. and WELLIS, H.A., (I.C.I.) : 'Absorption spectra of polypropylene in the millimetre and submillimetre regions', Infrared Physics, 1971, 11, pp.109-115.

<43> KLOPFENSTEIN, R.W. : 'A transmission line taper of improved design', Proc. IRE, pp.31-35, January 1956.

<44> COLLIN, R.E. and BROWN, J. : 'The design of quarter-wave matching layers for dielectric surfaces', Proc. IEE, Monograph. No. 149 R, pp.153-158, September 1955.

<45> FARMER, B.A. : 'Junction admittance between waveguides of arbitrary cross-sections', Proc. IEE, Monograph. No. 148 R, pp.145-152, August 1955.

<46> YOUNG, L. : 'Optimum quarter-wave transformers', IRE Trans. Microwave Theory & Tech., pp.478-482, September 1960.

<47> CLARRICOATS, P.J.B. : 'A new waveguide method for measuring permittivity', Proc. IEE, Vol.109, pp.858-862, 1962.

<48> McBRIDE, J.M.W. : 'Properties of dielectric-rod junction in circular waveguide', Ph.D. Thesis, Queen's University, Belfast, 1964.

<49> BARLOW, H.M., EFFEMEY, H.G. and TAKERI, S.H. : 'A circular H_{01} low-loss waveguide', Electromagnetic wave theory', Vol. II, Part I, pp.399-408, Pergamon Press, 1967.

<50> FALCIASECCA, G., PRANDI, G.M. and SOMEDA, G.G. : 'Attenuation in wall-impedance waveguides : a new approach', Electron. Lett., Vol.8, No.10, 1972.

<51> CLARRICOATS, P.J.B., OLINER, A.A. : 'Transverse-network representation for inhomogeneously filled circular waveguide', Proc. IEE, Vol.112, No.5, pp.883-894, May 1965.

<52> CARLIN, J.W., D'AGOSTINO, P. : 'Normal modes in overmoded dielectric-lined circular waveguide', Bell Syst. Tech. Journ., Vol.52, No.4, pp.453-486, April 1973.

<53> OLVER, A.D. : 'Guided electromagnetic wave propagation in radially stratified media', Ph.D. Thesis, University of Leeds, June 1966.

<54> UNGER, H.G. : 'Lined waveguide', Bell Syst. Tech. Journ., Vol.41, No.2, pp.745-768, March 1962.

<55> BENSON, F.A. : 'Millimetre and Submillimetre Waves', Iliffe, 1969.

<56> RAMSAY, M. : 'Fibre optical communication within the United Kingdom', to be published in Optical Communication, June 1972.

<57> KAO, K.C., DYOTT, R.B. and SNYDER, A.W. : 'Design and analysis of an optical fibers waveguide for communication', IEE Conf. Publ. 71, pp.211-217, 1970.

<58> DYOTT, R.B. and STERN, J.R. : 'Group delay in fiber waveguides', IEE Conf. Publ. 71, pp.176-181, 1970.

<59> SALEMA, C.E.R.C. : 'Theory and design of dielectric cone antennas', Ph.D. Thesis, Queen Mary College, University of London, September 1972.

<60> CLARRICOATS, P.J.B. and SALEMA, C.E.R.C. : 'Antennas employing conical dielectric horns, Part I - Propagation and radiation characteristics of dielectric cones; Part II - The cassegrain antenna', Proc. IEE, 120, pp.741-756, 1973.

<61> GREEN, K.A. and GILL, G.J., 'Lens antennas for millimeter waves', Proceedings of Polytechnic Institute of Brooklyn Symposium on Submillimetre waves, pp.475-485, 1970.

<62> CLARRICOATS, P.J.B. and SLINN, K.R. : 'The numerical solution of waveguide discontinuity problems', Proc. IEE, Vol.114, No.7, 1967.

<63> GLOGE, D. : 'Weakly guided fibers', Applied Optics, Vol.10, No.10, pp.2252-2258, October 1971.

<64> RAVENSCROFT, I. and JACKSON, L.A. : 'Proposals for a dielectric rod transmission system', Proc. of European Microwave Conference, 1973, Paper B.13.2.

<65> CLARRICOATS, P.J.B. and CHANG, D.C. : 'A proposed dielectric waveguide line-feed for a millimetre wavelength radio-telescope', IEEE G-AP International Symposium Digest, 1972, pp.296-298.

<66> LEWIN, L. : 'The local form of the radiation condition: application to curved dielectric structures', Electron. Lett., 1973, 9, pp.468-469.

<67> CLARRICOATS, P.J.B. and CHAN, K.B. : 'Propagation behaviour of cylindrical-dielectric-rod waveguides', Proc. IEE, 1973, 120(11), pp.1371-1378.

<68> DYBDEL, R.B., PETUS, L. and PEAKE, W.H. : 'Rectangular waveguides with impedance walls', IEEE Trans. Microwave Theory & Tech., Vol. MTT-19, pp.2-9, January 1971.

<69> CARLIN, J.W. and D'AGOSTINO, P. : 'Experimental verification of low-loss TM modes in dielectric-lined waveguide', Bell Syst. Tech. Journ., Vol.52, No.4, pp.487-496, April 1973.

<70> CLARRICOATS, P.J.B. : Private communication with W.C. Morgan, 3 December 1971.

<71> BARLOW, H.M. : 'Dipole-mode propagation in hollow tubular waveguides', 1974 URSI Symposium on Electromagnetic Wave Theory, London, 1974.

<72> CLARRICOATS, P.J.B. : 'Low attenuation waveguides', Progress Report No. 13, March 1974.

<73> LAGASSE, P. and VAN BLADEL, J. : 'Square and rectangular waveguides with rounded corners', IEEE Trans. Microwave Theory & Tech., Vol. MTT-20, pp.331-337, May 1972.

<74> JANSEN, J.K.M. and JEUKEN, M.E.J. : 'Propagation and radiation properties of elliptical waveguide with anisotropic boundary', Eindhoven University of Technology, October 1973.

Publications

1. CLARRICOATS, P.J.B., AL-HARIRI, A.M.B., OLVER, A.D., and CHAN, K.B., 'Low-attenuation characteristics of dielectric lined waveguide', Electronics Letters, August 1972, Vol.8, No.16.

2. LEWIN, L. and AL-HARIRI, A.M.B., 'Attenuation in an elliptic waveguide', Electronics Letters, August 1973, Vol.9, No.17.

3. CLARRICOATS, P.J.B., OLVER, A.D. and AL-HARIRI, A.M.B., 'Dielectric waveguide for millimetre-wavelength transmission', Electronics Letters, January 1974, Vol.10, No.1.

4. LEWIN, L. and AL-HARIRI, A.M.B., 'The effect of cross-section curvature on attenuation in elliptic waveguides and a basic correction to previous formulas', IEEE Trans. Microwave Theory Tech., Vol. MTT-22, May 1974.

5. AL-HARIRI, A.M.B., CLARRICOATS, P.J.B. and OLVER, A.D., 'Low attenuation properties of corrugated rectangular waveguide', Electronics Letters, July 1974. Vol.10, No.15.